# Theory of Ultrafast Electron Transfer from Localized Quantum States at Surfaces

Moritz Müller

Universidad del País Vasco

Euskal Herriko Unibertsitatea

eman ta zabal zaz

2019

eman ta zabal zazu

Universidad del País Vasco   Euskal Herriko Unibertsitatea

# Theory of Ultrafast Electron Transfer from Localized Quantum States at Surfaces

## Moritz Müller

Doctoral Thesis Submitted to
the University of the Basque Country
for the Degree of
DOCTOR IN PHYSICS

Thesis Supervisor:
Prof. Daniel Sánchez Portal

Donostia - San Sebastián
February 2019

**Abstract**

The ability of materials to transfer electrons is a basic property controlling the functionality and performance of devices at the nanoscale. Of particular importance is the transfer of electrons at surfaces as a fundamental process in catalytic and photocatalytic applications. This work aims along these lines at a theoretical description of resonant charge injection at surfaces using a combination of density functional theory and Green's functions. A close comparison with available data from core-hole-clock experiments is maintained throughout the work and confirms the validity and predictive power of our first-principles approach. This is demonstrated on the basis of three prototypical systems where we study fundamental aspects of charge transfer providing additional, often complementary information to the interpretation of the experiments.

First, we gauge the effect of structural fluctuations at finite temperatures on the charge transfer dynamics at rutile $TiO_2(110)$ surfaces sensitized by isonicotinic acid molecules in relation to photovoltaic applications. We find that, the inclusion of such fluctuations reconciles the theoretically extracted charge transfer times with the results from core-hole-clock experiments at room temperature. We study in detail how variations in the geometry and the presence of a core hole affect the interfacial level alignment and discuss how the available amount of acceptor states shapes the temperature broadened resonance spectra in our simulations.

Second, we explore spin-dependent charge transfer on ferromagnetic substrates for the example of argon on $Co(0001)$ and $Fe(110)$. Here, recent core-hole-clock experiments reported a strongly spin-dependent charge transfer behavior regarding the injection from core-excited argon atoms. Our calculations reproduce the experimental observation of significantly faster decay of core-excited $Ar^*4s$ resonances in comparison with majority excitations, allowing for a detailed analysis of this phenomenon. We find, in particular, that the position of the $Ar^*4s$ resonance with respect to projected gaps around the $\Gamma$-point of the surface band structure is crucial to explain the spin-dependent behavior, with important implications for spintronic applications.

Third, we closely examine the directionality of charge transfer in relation to sulfur derived resonances at surfaces of the layered transitionmetal dichalcogenide $1T\text{-}TaS_2$. In this joint experimental and theoretical work we analyze the origin of a change from anisotropic to isotropic charge transfer behavior across the phase transition from the nearly commensurate to the commensurate charge density wave phase at low temperatures. Our calculations reveal that the isotropic behavior of the ultrafast electron transfer in the commensurate charge density wave phase is presumably rooted in an increase in interlayer coupling and not the result of a reordering of the charge density wave stacking in subsequent layers of the material.

# Acknowledgments

I would like to express my sincere gratitude to Prof. Daniel Sánchez Portal, who was my direct supervisor. It has been a great privilege to work with such an outstanding scientist over the past years. Thank you Daniel for always having an open ear and time to share. Your uncomplicated, kind, and honest support, both scientifically and personally, made the ups and downs of my life as your PhD student a most valuable and joyful experience. I do not want to miss a second. Thank you for confiding in me in the various collaborations in which I got the opportunity to contribute.

I especially enjoyed my extended stays at the Univeristy of Milano-Bicocca in the group of Prof. Gian Paolo Brivio, whose great spirit and heart for his students have left me deeply impressed. Without the advice and help from Prof. Guido Fratesi my stay in Milan would not have been a success. Thank you Guido for your kind and inspiring words as well as your truly helpful scientific thoughts. I was very lucky to meet Abhilash Ravikumar as a great friend and colleague in Milan and Donostia.

I thank Prof. Pedro Miguel Echenique for the encouragement regarding the work on spin-dependent injection dynamics. I have not forgotten, that whenever I am ready I can on knock on the door of his office.

I would like to thank Prof. Enrique Ortega for the opportunity to work with his experimental group. The professionally relaxed, friendly atmosphere, working with Alejandro Miccio towards the submission deadline, was very pleasant.

Dr. Nick Papior Anderson provided me early on with a version of the *tbtrans* code, which was very helpful during the course of this work.

I would like to thank Prof. Alexander Föhlisch for the great chance I had to get first hand insight into the core-hole-clock experiments at the Helmholtz Zentrum in Berlin, which lead to a great collaboration. I would like to thank him and his group, in particular, Danilo Kühn, Erika Giangrisostomi, and Florian Sorgenfrei, for the warm welcome in Berlin. Danilo, the work with you was one of my highlights during the last years. I feel the difficult topic we worked on somehow bonded us together.

I thank Danilo Kühn, Peter Koval, and Pedro Brandimarte for their careful proof-reading of separate chapters of the manuscript of this work.

I would like to thank Prof. José María Pitarke for tutoring this thesis as well as for hosting Thinface at Nanogune. I want to thank Katharina Rubahn for the excellent coordination of the Thinface network assisted by our speaker Shashank Harivyasi and I thank Itziar Otegui, who managed the network at Nanogune. I am grateful to the people of the Thinface project, in particular to my fellow comrades Mehrad Ahmadpour, Laura Caliò, Antón Fernández, Mattia Farronato, Shashank Harivyasi, Mina Mirsafei, Bernhard Nell, Paola Pellacani, Abhilash Ravikumar, Chloé Rodriguez, Myles Rooney, Golnaz Sherafatipour, and Weike Wang for the great company and support during conferences and project related meetings.

Many thanks to Simune, in particular Monica Garcia Mota and Federico Marchesin for hosting a short-term stay to get a glimpse into the company's workings.

I gratefully acknowledge the EU-FP7 project THINFACE (grant No. 607232) for financial support through Nanogune and training, the Spanish MINECO (grant No.

The wonderful atmosphere here in Donostia has spawned a large amount of witty and refreshingly diverse people, some of which I was lucky enough to get to know and become friends with. Without these people, the time I spent here would not have been half as enjoyable. At the risk of forgetting the most important ones I thank here the following people. The group of scientists gathered by Daniel: Marc Barbry, Pedro Brandimarte, Mads Engelund, Sophie Espert, Federico Marchesin, Natalia Koval, Peter Koval, Masoud Mansouri, Mathias Ljungberg, and Pablo López Tarifa, thank you for your help, friendship, and encouragement. I really appreciate the running motivation and friendly advice by Thomas Frederiksen and Geza Giedke (you were too fast!), I spent fantastic post-race afternoons with you. In the environment of the CFM, Nanogune, DIPC and beyond: Ali Abedi, Unai Aseguinolaza, Nieves Azpiazu, Antton Babaze, Anu Baby, Louis Bigo, Ana Barragan, Miguel Borinaga, Giuseppe Foti, Oihana Galparsoro, Iker Gallardo, Carlos García, Elham Khosravi, Andrea Konečná, Bernhard Kretz, Jon Lasa, Ivor Lončarić, Martin Molezuelas, Tomáš Neuman, Alvaro Nodar, Dino Novko, Alba Pascual, Ignacio Piquero, Jose Reina, Ion Rubio, Patricia Riego, and Aldo Ugolotti. A part of you is missing already since you moved on towards your next destination, all of you keep keeping me on track with life, you have been incredible, wherever you go do not forget about me!

I also want to mention my comrades from studying in Munich: CJ, Fred, Jo, Jochen, Konsti, Klaus, Landvogt, Martin, Nidi, Norb, Roli, and Sebi. The fact that we stick together even though we are now scattered throughout Europe, is proof of how special our group is. Our trips in the past years were the best distraction from PhD-life I could imagine. Your stories often motivate the choices I make.

During my time here in San Sebastián, my "old" friends, Matthias, Maxi, Philipp, and Sebi, and their families, as well as the "Freiligradianer", Quirin and Flo, provided me with a sense of true home. Although my path lead me somewhat distant from yours, whenever we get together, it feels as if we just saw each other yesterday.

Finally, I want to give my heartfelt thanks to my family, my grandma, my parents, and my sister. Your steady and loving support ultimately allows me to reach my personal goals. I just want to let you know how powerful this is, while I do not know how I can possibly make up for it. Thank you so much for your understanding and your patience with me. Cris, thank you for sharing your positivity with me and for bearing with me during this special time. You make my dark days bright and the bright ones shining, no matter what, together we can see the silver linings.

# Contents

# List of Publications

## Publications Covered in this Thesis

- M. Müller, P. M. Echenique, and D. Sánchez-Portal. Theory of Spin-Dependent Electron Transfer Dynamics at Ar/Fe(110) and Ar/Co(0001) Interfaces. (in preparation).

- D. Kühn, M. Müller, F. Sorgenfrei, E. Giangrisostomi, R. M. Jay, R. Ovsyannikov, N. Mårtensson, D. Sánchez-Portal, and A. Föhlisch. Directional Sub-Femtosecond Charge Transfer Dynamics and the Dimensionality of 1T-TaS$_2$. *Scientific Reports.* **9**, 1 , 488 (2019).

- M. Müller, D. Sánchez-Portal, H. Lin, G. P. Brivio, A. Selloni, and G. Fratesi. Effect of Structural Fluctuations on Elastic Lifetimes of Adsorbate States: Isonicotinic Acid on Rutile(110). *The Journal of Physical Chemistry C.* **122**, 14, 7575 (2018).

- L. A. Miccio, M. Setvin, M. Müller, M. Abadía, I. Piquero, J. Lobo-Checa, F. Schiller, C. Rogero, M. Schmid, D. Sánchez-Portal, U. Diebold, and J. E. Ortega. Interplay Between Steps and Oxygen Vacancies on Curved TiO$_2$(110). *Nano Letters.* **16**, 3, 2017 (2016).

## Publications Related to this Thesis

- P. Koval, M. Ljungberg, M. Müller, D. Sanchez-Portal. Towards Efficient *GW* Calculations Using Numerical Atomic Orbitals: Benchmark and Application to Molecular Dynamics Simulations. (in preparation).

- A. Ravikumar, G. Kladnik, M. Müller, A. Cossaro, G. Bavdek, L. L. Patera, D. Sánchez-Portal, L. Venkataraman, A. Morgante, G. P. Brivio, and G. Fratesi. Tuning Ultrafast Electron Injection Dynamics at Organic-Graphene/Metal Interfaces. *Nanoscale.* **10**, 17, 8014 (2018).

## Other Publications

- K. Diller, R. J. Maurer, M. Müller, and K. Reuter. Interpretation of X-Ray Absorption Spectroscopy in the Presence of Surface Hybridization. *The Journal of Chemical Physics.* **146**, 21, 214701 (2017).

- M. Müller, K. Diller, R. J. Maurer, and K. Reuter. Interfacial Charge Rearrangement and Intermolecular Interactions: Density-Functional Theory Study of Free-Base Porphine Adsorbed on Ag(111) and Cu(111). *The Journal of Chemical Physics.* **144**, 2, 024701 (2016).

# Acronyms

The following list defines the acronyms used in this dissertation.

**2PPE**        two-photon photoemission

**ARPES**       angular resolved photoemission spectroscopy

**BOA**         Born-Oppenheimer approximation

**CCDW**        commensurate charge density wave
**CDW**         charge density wave
**CPMD**        Car-Parinello molecular dynamics

**DFA**         density functional approximation
**DFT**         density functional theory
**DOS**         density of states
**DSSC**        dye-sensitized solar cell

**FWHM**        full width half maximum

**GGA**         generalized gradient approximation

**HEG**         homogeneous electron gas
**HF**          Hartree-Fock
**HK**          Hohenberg-Kohn
**HOMO**        highest occupied molecular orbital

**IP**          first ionization potential
**IPES**        inverse photoemission spectroscopy

**LDA**         local density approximation
**LDOS**        local density of states
**LSDA**        local spin density approximation
**LUMO**        lowest unoccupied molecular orbital

| | |
|---|---|
| **MO** | molecular orbital |
| **NCDW** | nearly commensurate charge density wave |
| **NEXAFS** | near edge X-ray absorption fine structure |
| **PBE** | Perdew-Burke-Ernzerhof |
| **PDOS** | projected density of states |
| **PES** | photoemission spectroscopy |
| **PLD** | periodic lattice distortion |
| **QE** | Quantum Espresso |
| **SCF** | self-consistent field |
| **SIESTA** | spanish initiative for electronic simulations with thousands of atoms |
| **STM** | scanning tunneling microscopy |
| **TDDFT** | time-dependent density functional theory |
| **TMD** | transition metal dichalcogenide |
| **tr-2PPE** | time-resolved two-photon photoemission |
| **TranSIESTA** | part of the SIESTA code for the simulation of transport properties of materials |
| **VBM** | valence band maximum |
| **vdW** | van der Waals |
| **vdW-DF** | van der Waals density functional |

# Chapter 1

# Introduction

Living organisms developed efficient pathways in order to extract energy from their natural environment. The most prominent example is the collection of sun light via photosynthesis in plants. During this process the absorbed light energy is chemically stored by capturing carbon. Plants and animals then use cellular respiration to release the stored energy again, allowing their organisms to perform life-sustaining work. Remarkably, at the elementary level these metabolic processes rely on a common scheme: The transfer of electrons in the underlying reduction-oxidation reactions. Very similar and often imitating nature, a wide spectrum of technological applications has been developed that relies on electron transfer at the atomic level. Important catalytic or photo-catalytic applications such as electrochemical cells [1], solar fuel generators [2], and dye-sensitized solar cells [3–5] stand out as promising candidates in the renewable energy sector.

The prospect of such technologies and a fundamental interest in elementary processes explain the ongoing efforts to understand and describe electronic transfer. Initially, many of these efforts were focused on (outer shell) electron transfer reactions in solutions, which lead to the development of Marcus theory and its extensions [6–8], entering many theoretical descriptions up to date. However, experimentally as well as theoretically the scope has changed considerably since then.

While a tendency of catalytic reactions to proceed at interfaces brought the surface into the focus of many studies [9], the advances in the field of laser techniques opened new roads to probe electron dynamics with time and energy resolutions sufficiently precise to address electron transfer at its fundamental time- and length-scales. A cornerstone in this development was the investigation of the decay of electrons trapped in image potential states [10, 11]. These states arise inside potential wells, which are formed between the surface barrier and the attractive image charge mirroring an electron in front of the surface. Their experimental confirmation lead to a series of studies, where in particular the lifetimes of image potential states have been investigated, e.g., by two-photon photoemission (2PPE) [12, 13] and time-resolved two-photon photoemission (tr-2PPE) [14, 15] on various low-index surfaces of metals. Simultaneous theoretical calculations with increasingly realistic descriptions of the band structure of the surfaces backed these experiments [16, 17]. More recently, the

invention of the core-hole-clock method [18–21] enabled investigations of the lifetimes of localized states on adsorbates. This synchrotron technique allows to selectively and locally excite electrons on adsorbates and resolve the associated transfer times with unprecedented time-resolutions down to the sub-femtosecond regime [22].

The interpretation of such increasingly fine-tuned experiments requires in turn precise theoretical tools for their description down to the atomic level. Here, quantum effects are dominant and lead to an exponential increase in complexity with the number of the involved particles. Fortunately, in the absence of known analytical solutions to these complex problems, the developments of approximate first-principles quantum mechanical methods like density functional theory (DFT) [23–25] and their numerical implementations as for example in the SIESTA code [26–29] permit to model realistic systems with up to thousands of atoms with affordable computational effort.

This thesis makes use of DFT and Green's functions to study elastic charge transfer from localized resonance states at surfaces. Wherever possible a direct comparison with available data from core-hole-clock experiments is drawn. We consider an electron transfer process from a core-excited donor atom or molecule $D$ to an extended surface $A$ acting as acceptor, as summarized by the following scheme

$$DA + h\nu \xrightarrow{(1)} D^*A \xrightarrow{(2)} D^+A^-. \tag{1.1}$$
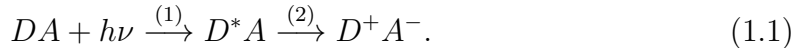
Here, the combined system $DA$ in it's ground state is irradiated by an incoming X-ray beam of energy $h\nu$. (1) This beam excites a core-electron at an atomic site of the donor $D$ preparing the latter in an intermediate (excited) state $D^*$. (2) Subsequently, the excited electron on the donor decays (delocalizes) into the extended surface $A$. The transfer of the electron leaves the donor with a positive $(D^+)$ and the surface with a negative $(A^-)$ partial charge.

In our first-principles DFT approach we model the system in the intermediate (transient) state directly after the core-excitation of an electron [after step (1) in Eq. (1.1)], while we do not explicitly account for the exciting electromagnetic field. The electron in the excited state is instead described by a heuristically determined localized wave-packet on the donor $D$. This wave-packet resembles a discrete energy level of the isolated donor, which typically becomes spread out in energy as a result of the coupling to the continuum of states in the substrate (one speaks of a resonance in the continuum of substrate states) [30–33]. This energy broadening is given by the linewidth $\Gamma$ of the resonance wave-packet. Using the uncertainty relation $\tau \cdot \Gamma = 1$ (in atomic units) the linewidth $\Gamma$ can be translated into the lifetime $\tau$, which represents the characteristic time the electron takes to delocalize into the substrate (the charge transfer time).

In the widely adopted approach to model surfaces by slabs consisting of a few atomic layers, only a finite number of acceptor states is supported by such a finite model of the substrate. This absence of a bulk continuum of states at the surface inhibits a consistent description of the resonant coupling at the interface. To overcome this deficiency we employ a Green's function method based on DFT calculations [34, 35], which is capable of treating surfaces with an infinite amount of atomic layers and therefore supports true resonant coupling of atomic resonances to

a continuum of states, while the methodology can be adapted to treat resonances on molecular adsorbates at surfaces [36].

The extracted resonant linewidths $\Gamma$ (or accordingly the lifetimes $\tau$) are of *elastic* character in our model, in the sense that they do not account for any additional inelastic effects due to, e.g., electron-electron or electron-phonon scattering. In general lifetimes are affected by both, elastic and inelastic processes. The latter arise in a quasiparticle picture through the interaction with, e.g., electron-hole pairs, phonons, magnons, or plasmons. Although methods exist to treat such interactions, these come usually at the expense of elevated computational costs, which restricts their applicability to small systems or reduced models, like simulating the electrons inside the surface as a free electron gas or using DFT-derived model potentials representing realistic surfaces [37, 38]. Examples for such approaches to inelasticity, are the estimation of inelastic electron-electron scattering from the GW self-energy [39] and the treatment of electron-phonon scattering through calculation of the Eliashberg function (cf. Refs. 16, 17). However, here we focus on extremely fast charge transfer processes at surfaces where the role of elastic coherent propagation is dominant.

As soon as a more realistic quantum description of large atomic structures is necessary DFT remains the tool of choice. While we employ in this work a DFT-based Green's function technique [34, 35], a variety of similar techniques to extract resonance widths and positions exists. Closely related is the deconvolution technique which analyzes widths of resonances in finite slab calculations considering a Gaussian broadening of the discrete projected density of states (DOS), which is corrected for later, when extracting the resonance widths [40]. Furthermore, a similar description of charge transfer times can be achieved via direct propagation of wave-packets in the time-domain, however, this requires in practice the introduction of a complex absorbing potential to avoid reflections of the propagating electrons at the boundaries of the simulation cells [17, 41]. Aside from these, a range of techniques have been elaborated to determine the linewidths of resonances at surfaces. Among these are the stabilization method [42], coupled angular momentum technique [43], complex scaling [44], or close-coupling [45], which have been briefly reviewed in Ref. 46. While these techniques provide accurate descriptions of the resonances, they also bring along complications which limit their applicability. However, also these methods do not offer an explicit description of the perturbation (e.g., the incoming electromagnetic field) causing the initial excitation of the resonance.

The thesis is organized in the following way. A brief introduction to the applied theory and the employed tools is provided in Chapter 2, where the required approximations to obtain a tractable theoretical framework are emphasized. In particular, we introduce DFT, where we focus on a formulation in terms of localized orbitals in relation to the numerical implementation in the SIESTA code [26–29], since this is the main tool employed throughout this thesis.

Chapter 3 defines the elastic lifetime of an electronic state within the previously described DFT framework as the central quantity of interest in this thesis. This is achieved by introducing the concept of the single particle Green's function and explaining its role as quantum mechanical propagator. Moreover, it is established how Green's functions can be exploited to treat the effect of a larger environment inside a smaller embedded region of interest. This property is then used to include

the effect of a fully semi-infinite substrate coupled to a finite surface region.

After the introduction to the theoretical tools a brief review of the core-hole-clock method [18–21] in Chapter 4 highlights this X-ray spectroscopic approach to extract lifetimes of localized states on adsorbates or atoms at surfaces experimentally. Experiments using the core-hole-clock technique are later extensively used as a reference for comparison with our simulations. In the literature different implementations of the core-hole-clock are found, these are briefly outlined and a comparison with time-resolved pump-probe measurements is drawn.

Chapter 5 starts with a preface on the interactions of step-edges and vacancies on TiO$_2$, thereby introducing TiO$_2$ as a substrate material. Our simulation suggest a scenario in which vacancies travel to the step edges of the material in support of the observations in curved crystal experiments on reduced TiO$_2$(110) surfaces performed by A. Miccio et al. in the group of Prof. E. Ortega (cf. Ref. 47). This allows us to present the main electronic properties of the TiO$_2$ substrate and how they are influenced by the presence of oxygen vacancies. The density of available acceptor states is an important ingredient for the determination of charge transfer times as discussed in Chapter 3. Subsequently, we turn to the investigation of charge transfer times at a prototypical interface in a dye-sensitized solar cell (DSSC). In particular, we investigate how interfacial structural fluctuations at finite temperatures affect the charge injection from chemisorbed isonicotinic acid molecules into TiO$_2$(110) surfaces. We show that the inclusion of such finite temperature effects can bring the experimentally observed time-scales by Schnadt et al. [48] into agreement with our theoretical estimates. An in-depth discussion of the obtained statistics highlights the role of the DOS in the substrate in shaping the temperature broadened spectra. Finally we attempt to establish a direct connection of the spectral broadening and the extracted lifetimes with specific vibrational modes. While the inhomogeneous broadening of the electronic levels can be explained within a semi-classical harmonic oscillator model involving linear electron-phonon couplings, a similar direct connection between the renormalization of the lifetimes and the excitation of specific vibrations was not possible.

In Chapter 6 we study the influence of the electron spin during charge injection processes at interfaces exhibiting spin polarization. In this context a minimal system that can be thought up is a single atom on a ferromagnetic surface, like argon atoms on Co(0001) or Fe(110) surfaces. For these systems precise and recently confirmed core-hole-clock data on spin dependent charge injection is available [49–51]. We show that our first-principles approach reproduces the experimental findings of faster minority spin charge injection on these surfaces and discuss how a detailed knowledge of the electronic structure in terms of electronic gaps of the surface band structure can explain this behavior, while we argue that explanations solely in terms of the available acceptor DOS in the substrate are bound to fail.

Chapter 7 explores ultrafast charge transfer from chemically bound sulfur atoms at the surface of the transition metal dichalcogenide 1T-TaS$_2$, pushing our methodology to the limits of its applicability. 1T-TaS$_2$ represents a promising candidate for ultrafast optoelectronic switching applications as well as an archetypal system for investigations of the directionality of charge transfer due to its layered two-dimensional structure. In a combined core-hole-clock spectroscopy and DFT study we exploit se-

lectively prepared orbital-polarizations of intermediate wave-packets to determine the directionality and time-scales of the ultrafast electron dynamics at the 1T-TaS$_2$ surface. The experiments conducted in the group of Prof. A. Föhlisch by D. Kühn et al. (see Ref. 52) show a transition from two-dimensional charge transfer behavior in the nearly commensurate charge density wave phase towards three-dimensional charge transfer in the commensurate charge density wave phase. We use our simulations to rationalize the isotropic charge transfer behavior in the low-temperature phase and discuss the effect of variations in the stacking order of the charge density waves in subsequent layers.

Finally, Chapter 8 summarizes the combined results of the investigations in this thesis and provides a general outlook as a perspective to future studies.

# Chapter 2

# The Many-Body Problem in Practice

The aim of this chapter is to outline the tools and models employed in this work while indicating possible short-comings in terms of the approximations made. In order to build on a mathematical foundation the many-body problem is stated and the necessary approximations for a computationally tractable solution are introduced.

## 2.1. The Many-Body Problem in Condensed Matter Physics

The quantum mechanical motion of $N$ particles such as electrons and nuclei is described by the Schrödinger equation [53]. The Schrödinger equation reads in its time-dependent form

$$i\frac{\partial}{\partial t}\Psi = \hat{H}\Psi,\tag{2.1}$$

where $\Psi(\mathbf{r}_1, \mathbf{r}_2, \ldots, \mathbf{r}_{N_e}, \mathbf{R}_1, \mathbf{R}_2, \ldots, \mathbf{R}_{N_n}, t)$ is the full many-body wave-function depending on time $t$ and the $3N$ spatial coordinates of the interacting particles (the electrons are at the positions $\mathbf{r}_i$ with $i = 1, \ldots, N_e$ and the nuclei at the positions $\mathbf{R}_I$ with $I = 1, \ldots, N_n$ and $N = N_e + N_n$). Additionally, the degrees of freedom related to the electron and nuclear spin have to be taken into account, although they are not explicitly appearing in Eq. (2.1). $\hat{H}$ is the Hamiltonian operator and we have written the equation in atomic units

$$\hbar = m_e = (4\pi\epsilon_0)^{-1} = 1.\tag{2.2}$$

Atomic units are used throughout this thesis unless otherwise stated. In the case of a time-independent Hamiltonian $\hat{H}$ one may separate the time degree of freedom and write the time-independent Schrödinger equation

$$\hat{H}\Psi = E\Psi,\tag{2.3}$$

describing a quantum system in a stationary state of an energy $E$. The solutions of the Schrödinger equation are to this level defined up to an arbitrary phase factor $e^{i\alpha}$. The Hamilton operator $\hat{H}$ describing the interactions between the particles

$$\hat{H} = \hat{T}_e + \hat{T}_n + \hat{V}_{ee} + \hat{V}_{en} + \hat{V}_{nn} \tag{2.4}$$

with the kinetic energy operators of the electrons $\hat{T}_e$ and of the nuclei $\hat{T}_n$ defined as

$$\hat{T}_e = -\sum_i \frac{\nabla_i^2}{2}, \qquad \hat{T}_n = -\sum_I \frac{\nabla_I^2}{2M_I}. \tag{2.5}$$

Repulsion between electrons $\hat{V}_{ee}$, attraction between nuclei and electrons $\hat{V}_{en}$, as well as repulsion between nuclei $\hat{V}_{nn}$ are given by the Coulomb terms

$$\hat{V}_{ee} = \sum_{i \neq j} \frac{1}{|\mathbf{r}_i - \mathbf{r}_j|}, \qquad \hat{V}_{en} = -\sum_{i,I} \frac{Z_I}{|\mathbf{r}_i - \mathbf{R}_I|}, \qquad \hat{V}_{nn} = \sum_{I \neq J} \frac{Z_I Z_J}{|\mathbf{R}_I - \mathbf{R}_J|}. \tag{2.6}$$

The analytic solution of Eq. (2.1) is known for a single Hydrogen atom [53]. The task of solving the equation for systems involving more particles has not been achieved analytically and is referred to as the many-body problem. Although up to date analytically intractable, the problem can be approached numerically, if suitable approximations are made. Such a set of approximations is the focus of this chapter.

## 2.2. The Born-Oppenheimer Approximation and the Electronic Problem

As a first step we introduce the Born-Oppenheimer approximation as an important simplification of the many-body problem [54]. This approximation allows to separate the nuclear from the electronic motion and, therefore, to treat electrons and ions independently from each other. It has to be kept in mind that the approximation will break down under certain conditions. The following is based on the discussion in the book chapter by Cederbaum [55].

One can define the electronic Hamiltonian describing the interacting electrons moving in the fixed potential due to the nuclei by

$$\hat{H}_e = \hat{T}_e + \hat{V}_{ee} + \hat{V}_{en} + \hat{V}_{nn}, \tag{2.7}$$

where the effects of the kinetic energy of the nuclei have been omitted. The solution of the Schrödinger equation of the electronic system

$$\hat{H}_e \psi_i(\mathbf{r}, \mathbf{R}) = V_i(\mathbf{R}) \psi_i(\mathbf{r}, \mathbf{R}) \tag{2.8}$$

yields a complete set of electronic eigenstates $\psi_i(\mathbf{r}, \mathbf{R})$ with eigenvalues $V_i(\mathbf{R})$ for a set of fixed nuclear coordinates $\mathbf{R}$ entering parametrically. Note, that exclusively in this section $\mathbf{r} = \{\mathbf{r}\}$ and $\mathbf{R} = \{\mathbf{R}\}$ are interpreted as the entire sets of the electronic and the nuclear coordinates, respectively. In the rest of this work the symbols are used explicitly for the spatial coordinates of single particles. The completeness of the

electronic eigenstates $\psi_i(\mathbf{r}, \mathbf{R})$ allows a formally exact expansion of the full many-body wave function $\Psi(\mathbf{r}, \mathbf{R})$ in terms of the electronic wave functions, such that

$$\Psi(\mathbf{r}, \mathbf{R}) = \sum_i \chi_i(\mathbf{R})\psi_i(\mathbf{r}, \mathbf{R}). \tag{2.9}$$

To this end one may choose the electronic wave-functions to be real by multiplication with a proper phase factor $e^{i\alpha(\mathbf{R})}$. In a periodic solid, the solutions can be classified according to how they transform under translations. This gives rise to a phase factor depending on the so-called Bloch vector quantum number (cf. Section 2.4). However, slowly (adiabatically) transporting the system around a circle by a continuous variation of the coordinates $\mathbf{R}$, the system acquires a well-defined geometrical phase factor. This so-called Berry phase can be correlated to interesting properties of the system [56]. Substituting the ansatz [Eq. (2.9)] into the full Schrödinger equation Eq. (2.3) and multiplying from the left by $\psi_j^*(\mathbf{r}, \mathbf{R})$ yields after integration over the electronic coordinates the expression

$$[\hat{T}_{\mathrm{n}} + V_j(\mathbf{R})]\chi_j(\mathbf{R}) - \sum_i (A_{ji} + B_{ji})\chi_i(\mathbf{R}) = E\chi_j(\mathbf{R}). \tag{2.10}$$

The terms $A_{ji}$ and $B_{ji}$ are known as non-adiabatic couplings. The first term can be identified as

$$A_{ji}(\mathbf{R}) = \sum_I \frac{1}{M_I} \int \psi_j^*(\mathbf{r}, \mathbf{R})\nabla_I\psi_i(\mathbf{r}, \mathbf{R})\nabla_I \, d\mathbf{r} \tag{2.11}$$

and is of derivative nature. The second non-adiabatic coupling term is of scalar character

$$B_{ji}(\mathbf{R}) = \sum_I \frac{1}{2M_I} \int \psi_j^*(\mathbf{r}, \mathbf{R})\nabla_I^2\psi_i(\mathbf{r}, \mathbf{R}) \, d\mathbf{r}\,. \tag{2.12}$$

If the off-diagonal terms of $A_{ji}$ and $B_{ji}$ are negligible, then Eq. (2.8) for the electrons and Eq. (2.10) for the nuclei effectively uncouple and describe a system in which the lighter electrons follow instantaneously the motion of the heavy nuclei. This is the adiabatic or Born-Oppenheimer approximation (BOA) [55]. Since $A_{ji}$ and $B_{ji}$ both are divided by the masses of the heavy nuclei $M_I$, one may assume their contributions to be small. On the other hand, application of $\nabla_I$ to the electronic Schrödinger equation, Eq. (2.8), yields the expression

$$\langle\psi_j(\mathbf{r}, \mathbf{R})|\nabla_I|\psi_i(\mathbf{r}, \mathbf{R})\rangle = \frac{\langle\psi_j(\mathbf{r}, \mathbf{R})|(\nabla_I H_{\mathrm{e}})|\psi_i(\mathbf{r}, \mathbf{R})\rangle}{V_i(\mathbf{R}) - V_j(\mathbf{R})}, \tag{2.13}$$

for $i \neq j$. If two electronic states are nearly degenerate (e.g., at conical intersections of the potential energy surfaces), the denominator in Eq. (2.13) becomes small and the contribution to $A_{ji}$ in Eq. (2.11) explodes so that the BOA breaks down. Nevertheless, assuming the approximation to be valid, it remains to solve the electronic problem Eq. (2.8) for a particular nuclear configuration $\mathbf{R}$ as described in the next sections.

## 2.3.  Density Functional Theory

DFT is currently the tool of choice to simulate and engineer systems consisting of hundreds to thousands of atoms on computers. The idea behind DFT is that the physical properties of a system of interacting electrons are readily defined by its ground state electronic density. This seems surprising since the density is a much simpler object in comparison to the wave function. The density depends only on three spatial coordinates, in contrast to the electronic wave function which is a function of the $3N$ coordinates of the particles in the material of interest. Moreover, the density can be obtained from the hermitian operator

$$\hat{n} = \sum_i \delta(\mathbf{r} - \mathbf{r}_i) \tag{2.14}$$

and hence, is a quantum mechanical observable. The following expression for electronic density $n^\sigma(\mathbf{r})$ of the spin-component $\sigma \in \{\uparrow, \downarrow\}$ emphasizes the reduction of dimensionality when using the density instead of the many-body wave function as the principle variable,

$$n^\sigma(\mathbf{r}) = N \sum_{\sigma_2, \dots, \sigma_N} \int \cdots \int |\psi(\mathbf{r}\sigma, \mathbf{r}_2\sigma_2, \dots, \mathbf{r}_N\sigma_N)|^2 \, d\mathbf{r}_2 \dots d\mathbf{r}_N \,. \tag{2.15}$$

Note, that the symbol $\mathbf{r}$ describes here and from now on a single variable in three spatial coordinates, while it was associated with a set of electronic coordinates $\{\mathbf{r}\}$ in the previous section. The total electronic density $n(\mathbf{r})$ is given as the sum of the two spin components, i.e., $n(\mathbf{r}) = n^\uparrow(\mathbf{r}) + n^\downarrow(\mathbf{r})$. The approach to use the electronic density as the basic variable in quantum mechanical calculations is nearly as old as quantum mechanics itself. The energy density functional proposed initially by Thomas and Fermi [57, 58] is widely seen as a forerunner of modern DFT. Nevertheless, a rigorous mathematical foundation DFT was first provided much later by Hohenberg and Kohn [23]. Finally, the work of Kohn and Sham [24] made DFT applicable in practice.

In the following two sections, DFT is introduced as the standard tool for *ab-initio* modeling of electronic structure, Eq. (2.8). More complete accounts can be found in the books by Martin [59], or Engel and Dreizler [60] on which this chapter is based.

### 2.3.1.  The Hohenberg-Kohn Theorem

Hohenberg and Kohn [23] formulated in their seminal paper the theorem, which builds the basis for modern DFT. The main statements are outlined in this section. Using common nomenclature, we define an external potential $v_{\text{ext}}$, which accounts for the electrostatic interactions of the ions among themselves and with the electrons, thereby incorporating the Born-Oppenheimer approximation into the formalism

$$E_{\text{ext}}[n] = \langle\psi|\hat{V}_{\text{ext}}|\psi\rangle = \langle\psi|\hat{V}_{\text{en}} + \hat{V}_{\text{nn}}|\psi\rangle = \int v_{\text{ext}}(\mathbf{r})n(\mathbf{r}) \, d\mathbf{r} \,. \tag{2.16}$$

In this form the energy contribution $E_{\text{ext}}[n]$ due to $\hat{V}_{\text{ext}} = V_{\text{en}} + \hat{V}_{\text{nn}}$ has been recast as a functional of the density $n(\mathbf{r})$. In general, the external potential may contain further contributions stemming for example from an external electric field. Time-dependent

potentials can be treated in the framework of time-dependent DFT, which is beyond the scope of this section. The Hamiltonian describing electrons subject to a static external potential reads

$$\hat{H}_{\text{e}} = \hat{T}_{\text{e}} + \hat{V}_{\text{ee}} + \hat{V}_{\text{ext}}. \tag{2.17}$$

First, we assume the case of a non-degenerate ground state. Usually, the steps in computing the ground state density corresponding to the above electronic Hamiltonian are: (A) Solving the Schrödinger equation, Eq. (2.8), to obtain the ground state $\psi_0$. (B) Extracting the ground state density using Eq. (2.15). Those steps are indicated by the blue arrows in Fig. 2.1 and give a unique mapping of the Hamiltonian (or the external potential) onto the ground state wave function (in the non-degenerate case).

On the other hand, one can show, e.g., by contradiction (*reductio ad absurdum*), that also the reverse direction (red arrows in Fig. 2.1) of the mapping is unique. One can therefore invert the mappings A and B so that: ($B^{-1}$) The ground state density maps to a unique ground state wave function. ($A^{-1}$) The latter ground state wave function defines the external potential up to a constant term. Therefore, the knowledge of the ground state density $n_0(\mathbf{r})$ is sufficient to determine the external potential $v_{\text{ext}}(\mathbf{r})$ up to a constant term (red dashed lines in Fig. 2.1). In other words, the ground state density is sufficient to define all physical properties (the ones defined by the Hamiltonian) of a system. This is the first statement of the Hohenberg-Kohn (HK) theorem. In light of the mapping ($B^{-1}$) one often writes the following equation

$$|\psi_0\rangle = |\psi[n_0]\rangle, \tag{2.18}$$

which only holds strictly for non-degenerate ground states. The expectation value for the total energy is defined as

$$E[n_0] = \langle\psi[n_0]|\hat{H}_{\text{e}}|\psi[n_0]\rangle. \tag{2.19}$$

Application of Ritz's variational principle leads to the following minimization rule

$$E_0 = E[n_0] \leq E[n], \tag{2.20}$$

where it can be shown that only the exact ground state density $n_0(\mathbf{r})$ minimizes the total energy [23]. This second statement of the HK theorem provides a recipe to determine the ground state density of a system and, therefore, in principle all of its properties. Since the external potential defines the electron density unequivocally, the remaining part of the Hamiltonian in Eq. (2.17) is associated with a universal functional of the density

$$F_{\text{HK}}[n] = \langle\psi[n]|\hat{T}_{\text{e}} + \hat{V}_{\text{ee}}|\psi[n]\rangle. \tag{2.21}$$

The HK theorem can be generalized to include the case of degenerate ground states. A proof of this generalization is analogous to the non-degenerate ground state case but treats a mapping between sets of degenerate wave functions and degenerate densities [60]. In the forward direction (blue arrows in Fig. 2.1) for a given $v_{\text{ext}}$ (plus a constant term) there is a set of degenerate ground-state wave functions (A) which can in turn be mapped onto a set of degenerate ground state densities (B). Two
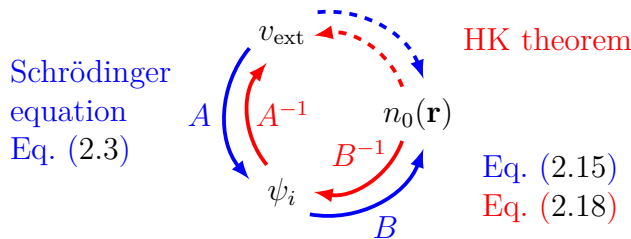
**Figure 2.1.:** Scheme of the Hohenberg-Kohn theorem: The theorem states the existence of a unique mapping $A^{-1} \circ B^{-1}$ of the ground-state density $n_0(\mathbf{r})$ to an external potential $v_{\text{ext}}$.

different but degenerate ground state wave functions may be mapped onto the same ground state density, but a mapping onto distinct degenerate ground state densities is equally possible. In the reverse mapping (red arrows) one set of degenerate ground-state densities pertains to a unique set of degenerate ground-state wave functions. Each wave function in this degenerate set in turn uniquely defines the same external potential up to a constant. Overall, a unique mapping between disjoint sets of wavefunctions belonging to different external potentials (up to a constant) and disjoint sets of densities belonging to sets of degenerate wave functions is established. This extends the HK theorem to the degenerate case.

One may note that the functional $|\psi[n]\rangle$ in Eq. (2.18) is not unique in the degenerate case. However, since the ground state energy is the same for all degenerate ground state wave functions, it is sufficient to pick one wave function from the set of degenerate wave functions corresponding to a given density. This allows to define a unique energy functional $E[n]$ as in Eq. (2.20) recovering the variational principle for the degenerate case. The Hohenberg Kohn theorem can be further generalized as for example to include spin polarization, a proof can be found in [60].

In the original proof of the HK theorem the search for the minimum energy in Eq. (2.20) is performed over all densities $n(\mathbf{r})$, which refer to some external potential $v_{\text{ext}}$ ($v$-representability of the density). In other words, it is assumed that a Hamiltonian with an external potential $v_{\text{ext}}$ exists that produces the trial density. The condition of $v$-representability has not been proven to hold necessarily for any density, but the requirement can be lifted and the domain of the search can be extended by using the constrained search algorithm proposed by Levy [61] and Lieb [62]. Lieb and Levy defined the universal energy functional in a modified way. The Lieb-Levy functional $F_{\text{LL}}[n(\mathbf{r})]$ considers all anti-symmetric wave functions that produce one explicit density integrating to $N$ particles ($N$-representability of the density) and then returns the lowest energy value after performing a minimization over those wave functions. This may be written formally as

$$F_{\text{LL}}[n(\mathbf{r})] = \min_{\psi \to n(\mathbf{r})} \langle \psi | \hat{T} + \hat{V}_{\text{ee}} | \psi \rangle . \tag{2.22}$$

In this definition the search automatically includes degenerate wave functions $\psi$ and it is known that any trial density is actually $N$-representable [63] such that the problem of $v$-representability is circumvented. Since the total energy functional $E[n(\mathbf{r})]$

is minimal for the exact ground state density $n_0(\mathbf{r})$ and $n_0(\mathbf{r})$ is known to be $v$-representable due to the HK-theorem, $F_{\text{HK}}[n_0(\mathbf{r})]$ equals the originally introduced exact universal functional $F_{\text{LL}}[n_0(\mathbf{r})]$ for $n_0(\mathbf{r})$.

## 2.3.2. The Kohn-Sham Equations

An early attempt to use the variational principle in terms of the electronic density Eq. (2.20) was proposed by Thomas and Fermi [57, 58]. In their model the kinetic energy of the electrons was given as a functional of the inhomogeneous electron density $T[n(\mathbf{r})] = \int t_{\text{HEG}}[n(\mathbf{r})]n(\mathbf{r})$ by borrowing the known analytic expression of the kinetic energy density $t_{\text{HEG}}[n(\mathbf{r})]$ from the homogeneous electron gas (HEG), where $n_{\text{HEG}}(\mathbf{r}) = \text{const}$. In the same way known analytic form for exchange energy of a HEG and an approximation for the correlation contribution where introduced. While such an approach yields qualitative results, it does not reproduce basic quantum mechanical behavior like the correct shell structure of atoms and Friedel oscillations. It would be appealing to find a satisfying description of the electronic problem exclusively in terms of the electronic density. However, such orbital-free kinetic energy DFTs lack up to date the desired accuracy [64, 65]. Instead, the Kohn-Sham approach to DFT provides a sufficiently precise alternative for many practical applications.

Kohn and Sham had the idea to make use of an auxiliary system of non-interacting electrons with the same ground state electronic density as the interacting system [24]. The HK theorem is then applied to the auxiliary system as illustrated schematically in Fig. 2.2. The electronic wave function of the auxiliary system can be written in terms of a single anti-symmetric Slater determinant $\phi_{\text{SD}}$ of $N$ independent particle orbitals $\phi_i$ [66]

$$\phi_{\text{SD}}(\mathbf{r}_1\sigma_1, \mathbf{r}_2\sigma_2, \ldots, \mathbf{r}_N\sigma_N) = \frac{1}{\sqrt{N!}} \begin{vmatrix} \phi_1(\mathbf{r}_1\sigma_1) & \phi_2(\mathbf{r}_1\sigma_1) & \cdots & \phi_N(\mathbf{r}_1\sigma_1) \\ \phi_1(\mathbf{r}_2\sigma_2) & \phi_2(\mathbf{r}_2\sigma_2) & \cdots & \phi_N(\mathbf{r}_2\sigma_2) \\ \vdots & \vdots & \ddots & \vdots \\ \phi_1(\mathbf{r}_N\sigma_N) & \phi_2(\mathbf{r}_N\sigma_N) & \cdots & \phi_N(\mathbf{r}_N\sigma_N) \end{vmatrix}. \quad (2.23)$$

Here, each single-particle spin wave function $\phi_i(\mathbf{r}_j\sigma_j) = \phi_i^\sigma(\mathbf{r}_j)\alpha(\sigma_j)$ is a product of a spinor $\alpha(\sigma_j)$ describing the spin state and a spatial function $\phi_i^\sigma(\mathbf{r}_j)$, which may differ for different spins. The total density is then given by the sum of the contributions from both spins $n(\mathbf{r}) = n^\uparrow(\mathbf{r}) + n^\downarrow(\mathbf{r})$.

The introduction of a non-interacting auxiliary system enables the description of the kinetic energy in terms of single-particle wave functions,

$$T_{\text{s}}[n^\uparrow, n^\downarrow] = \langle\phi_{\text{SD}}|\hat{T}|\phi_{\text{SD}}\rangle = -\frac{1}{2} \sum_{\sigma=\uparrow,\downarrow} \sum_i f_i^\sigma \int \phi_i^\sigma(\mathbf{r})\nabla^2\phi_i^\sigma(\mathbf{r}) \, d\mathbf{r}. \quad (2.24)$$

Here, the $f_i^\sigma$ are the occupation numbers, which are given by the Fermi-Dirac statistics

$$f_i^\sigma = f(\varepsilon_i^\sigma) = \frac{1}{e^{\beta(\varepsilon_i^\sigma - E_{\text{F}})} + 1}, \quad (2.25)$$

where $\beta = (k_{\text{B}}T)^{-1}$, $k_{\text{B}}$ is the Boltzmann constant, and $T$ is the electronic temperature. The total energy of the electronic system is then written as a functional of the

electronic density

$$E[n^\uparrow, n^\downarrow] = T_s[n^\uparrow, n^\downarrow] + E_H[n] + E_{xc}[n^\uparrow, n^\downarrow] + E_{ext}[n], \tag{2.26}$$

where $E_H$ is the Hartree term describing the classical electrostatic Coulomb repulsion due to the non-interacting electron density

$$E_H[n] = \frac{1}{2} \iint \frac{n(\mathbf{r})n(\mathbf{r}')}{|\mathbf{r} - \mathbf{r}'|} \, d\mathbf{r} \, d\mathbf{r}' = \frac{1}{2} \sum_{i,j,\sigma,\sigma'} \iint \frac{|\phi_i^\sigma(\mathbf{r})|^2 |\phi_j^{\sigma'}(\mathbf{r}')|^2}{|\mathbf{r} - \mathbf{r}'|} \, d\mathbf{r} \, d\mathbf{r}' \,. \tag{2.27}$$

Importantly, the Hartree term contributes even if only a single electron is considered, e.g., terms with $i = j$. This spurious effect is known as self-interaction of electrons and has to be canceled by the other terms in the exact energy functional. The remaining contributions to the energy of the many-electron system defined by $\langle \psi | \hat{H}_e | \psi \rangle$ (Eq. (2.17)) are included in the exchange-correlation energy

$$E_{xc}[n^\uparrow, n^\downarrow] = E_x[n^\uparrow, n^\downarrow] + E_c[n^\uparrow, n^\downarrow]. \tag{2.28}$$

Here, one may split off the exchange part which is defined analogous to Hartree-Fock theory, with a Slater determinant over the Kohn-Sham orbitals

$$E_x[n^\uparrow, n^\downarrow] := \langle \phi_{SD} | \hat{V}_{ee} | \phi_{SD} \rangle - E_H[n]. \tag{2.29}$$

The spin dependence of the exchange energy follows the spin scaling relation [67]

$$E_x[n^\uparrow, n^\downarrow] = \frac{1}{2}(E_x[n^\uparrow, n^\uparrow] + E_x[n^\downarrow, n^\downarrow]), \tag{2.30}$$

making it an easy task to construct the spin-dependent exchange functional once the spin-independent form is known. With the above definitions, the remaining correlation part of the energy is

$$E_c[n^\uparrow, n^\downarrow] = \langle \psi | \hat{T} | \psi \rangle - T_s[n] + \langle \psi | \hat{V}_{ee} | \psi \rangle - E_x[n^\uparrow, n^\downarrow] - E_H[n] \tag{2.31}$$

The differences between expectation values over the full electronic wave function and the single-particle Slater determinant represent contributions from the kinetic terms (kinetic correlation) and the Coulombic terms (Coulomb correlation).

The functional derivative of the exchange-correlation energy with respect to the density $\epsilon_{xc}[n^\uparrow, n^\downarrow]$ is the exchange correlation potential.

$$v_{xc}^\sigma(\mathbf{r}) = \frac{\delta E_{xc}[n^\uparrow, n^\downarrow]}{\delta n^\sigma(\mathbf{r})} \tag{2.32}$$

$$= \frac{\delta}{\delta n^\sigma(\mathbf{r})} \int n(\mathbf{r}) \epsilon_{xc}[n^\uparrow, n^\downarrow] \, d\mathbf{r} = \epsilon_{xc}[n^\uparrow, n^\downarrow] + n(\mathbf{r}) \frac{\delta \epsilon_{xc}[n^\uparrow, n^\downarrow]}{\delta n^\sigma(\mathbf{r})} \tag{2.33}$$

Although an explicit formula for exact exchange in terms of the Fock operator is known, this term is treated implicitly in the exchange correlation potential in standard DFT as its explicit calculation is in practice computationally too expensive. No explicit analytical form of the exact exchange correlation energy functional is known

and, therefore, further approximations have to be made. Such approximations will be described in the next section. Applying the variational principle, the ground state density can be found in the spirit of the HK-theorem by minimization of the total energy functional. This is formally achieved by functional derivation with respect to the density

$$\frac{\delta}{\delta n^\sigma} \left\{ E[n^\uparrow, n^\downarrow] - \mu \int [n(\mathbf{r}) - N] \, d\mathbf{r} \right\} \bigg|_{n(\mathbf{r}) = n_0(\mathbf{r})} = 0. \qquad (2.34)$$

This can be compared with a system of non-interacting electrons moving in an effective potential $\frac{\partial V_{\text{eff}}}{\partial n}$ where one has similarly $\frac{\partial E_s}{\partial n} = \frac{\partial T_s}{\partial n} + \frac{\partial V_{\text{eff}}}{\partial n} - \mu = 0$. One finds the following single particle equations called Kohn-Sham equations [24]

$$\left[ -\frac{1}{2} \nabla^2 + v_{\text{eff}}^\sigma(\mathbf{r}) \right] \phi_i^\sigma(\mathbf{r}) = \varepsilon_i^\sigma \phi_i^\sigma(\mathbf{r}). \qquad (2.35)$$

where the effective, local and spin-dependent potential $v_{\text{eff}}^\sigma(\mathbf{r})$ is identified as

$$v_{\text{eff}}^\sigma(\mathbf{r}) = v_{\text{H}}(\mathbf{r}) + v_{\text{xc}}^\sigma(\mathbf{r}) + v_{\text{ext}}(\mathbf{r}). \qquad (2.36)$$

Here, we have used the Hartree potential defined as the functional derivative of the Hartree energy Eq. (2.27) with respect to the density $\frac{\partial E_{\text{H}}[n]}{\partial n}$. The Kohn-Sham equations are usually solved iteratively in a self-consistent manner and one speaks then of a self-consistent field (SCF). The solutions $\phi_i^\sigma(\mathbf{r})$ to Eq. (2.35) are the single-particle states, or Kohn-Sham orbitals associated with the Kohn-Sham energy eigenvalues $\varepsilon_i^\sigma$. The Kohn-Sham orbitals form the electronic wave function in terms of a single Slater determinant. The non-interacting electronic density is then given by the sum of the squares of the single-particle energy eigenstates

$$n(\mathbf{r}) = \sum_\sigma n^\sigma(\mathbf{r}) = \sum_{i,\sigma} f_i^\sigma |\phi_i^\sigma(\mathbf{r})|^2, \qquad (2.37)$$

weighted by the occupation number $f_i^\sigma$ [cf. Eq. (2.25)] considering collinear spin $\sigma \in \{\uparrow, \downarrow\}$. The multiplicative character of the effective potential in Eq. (2.35) constitutes the mean-field character of Kohn-Sham DFT. The ground state energy is effectively minimized by solving Eq. (2.35). Using the Kohn-Sham eigenvalues $\varepsilon_i^\sigma$ in Eq. (2.35) the total energy in Eq. (2.26) reads

$$E_0 = \sum_{i,\sigma} f_i^\sigma \varepsilon_i^\sigma - \sum_\sigma \int v_{\text{xc}}^\sigma(\mathbf{r}) n_0^\sigma(\mathbf{r}) \, d\mathbf{r} - E_{\text{H}}[n_0] + E_{\text{xc}}[n_0^\uparrow, n_0^\downarrow]. \qquad (2.38)$$

Although the total energy functional in Eq. (2.26) is in principle exact, no explicit analytic form of the exchange-correlation part Eq. (2.28) is known. The problem of solving the many-body Schrödinger equation has been shifted from finding the real interacting wave-function to the search for an explicit form of the exchange-correlation functional.

## 2.3.3. Exchange-Correlation Functionals and Their Limitations

DFT is in principle an exact theory, however, to apply it in practice one needs to find suitable approximations for the unknown exchange-correlation functional
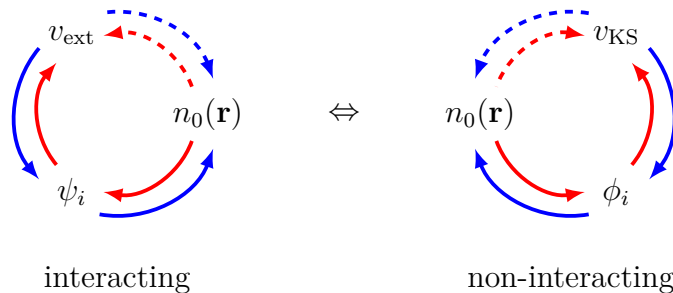
**Figure 2.2.:** Scheme of the Kohn-Sham ansatz. Application of the HK theorem to a system of non-interacting electrons, which yields the same electronic density as the interacting electrons. $\psi_i$ are the full many-body electronic wave-functions while $\phi_i$ are the single-particle Kohn-Sham orbitals.

in Eq. (2.26). In this section the most common approaches are mentioned. These approximate functionals have been associated by Perdew and Schmidt [68] with the first steps on a Jacob's ladder to an imaginative functional heaven, where chemical accuracy is reached.

A first approximation to the exact energy functional is the local density approximation (LDA) or also local spin density approximation (LSDA) if the inclusion of spin is explicitly mentioned. In this approximation the exchange-correlation energy density is treated locally as in a HEG for which accurate expressions are known. The energy density functional becomes therefore a function of the density evaluated at one point in space so that the total exchange correlation energy reads

$$E_{\text{xc}}^{\text{LSDA}}[n^\uparrow, n^\downarrow] = \int \epsilon_{\text{xc}}^{\text{HEG}}(n^\uparrow(\mathbf{r}), n^\downarrow(\mathbf{r})) \, n(\mathbf{r}) \, d\mathbf{r} \,. \tag{2.39}$$

The combined energy density $\epsilon_{\text{xc}}$ is the sum of contributions from exchange and correlation

$$\epsilon_{\text{xc}}(n^\uparrow, n^\downarrow) = \epsilon_{\text{x}}(n^\uparrow, n^\downarrow) + \epsilon_{\text{c}}(n^\uparrow, n^\downarrow). \tag{2.40}$$

The expression for exchange is known analytically [69] and the correlation energy has been parametrized for different densities of a HEG using high accuracy Monte Carlo methods [70, 71]. The LDA can provide a good description of materials, for which the electronic density varies only little over space, as for example in the case of many metallic solids.

As soon as the electronic density exhibits stronger variations in space, the local approximation is no longer accurate enough. From this perspective a natural extension to the LDA is to include the gradient of the density in the description, giving the functional a semi-local character. Unfortunately, the expressions obtained for *low-order* density gradient expansions are not useful [60] since the expansions break down for large density gradients in atoms [72] and violate certain conditions for the exchange-correlation functional [73]. In practice, therefore, *generalized* expressions are used, which have been shown to improve results over LDA [73]. Such generalized gradient approximation (GGA) functionals assume the form

$$E_{\text{xc}}^{\text{GGA}}[n^\uparrow, n^\downarrow] = \int \epsilon_{\text{xc}}(n^\uparrow, n^\downarrow, |\nabla n^\uparrow|, |\nabla n^\downarrow|) \, n(\mathbf{r}) \, d\mathbf{r} \,. \tag{2.41}$$

The two main strategies to create such GGAs are either to empirically fit parametric functionals to a wide range of materials as, e.g., done for the exchange term by Becke [74] or to construct them by exclusively matching known analytic properties of the exact functional. A widely used example of the latter approach is the Perdew-Burke-Ernzerhof (PBE) functional [75] that fulfills a maximum amount of known analytic properties.

Further improvement can be achieved by including higher order contributions of the gradient expansion, e.g., through the kinetic energy density in so-called meta-GGAs [68, 76].

A source of error in local and semi-local functionals is the incomplete cancellation of self-interaction arising in the Hartree term. This spurious self-interaction is completely canceled in Hartree-Fock theory by the Fock operator describing the exchange interaction. Based on this observation hybrid functionals have been constructed which mix some amount of exact exchange into a given local or semi-local density functional approximation (DFA) according to the scheme

$$E_{xc}^{hybrid} = E_{xc}^{DFA} + a(E_x - E_x^{DFA}), \tag{2.42}$$

where the correlation contribution is kept as in the underlying DFA [77].

Evaluating the exchange expression from the definition in Eq. (2.29) leads to the exchange term $E_x[n]$ familiar from Hartree-Fock theory. Here, the term has a slightly different meaning since it is evaluated over the Kohn-Sham orbitals

$$E_x[n] = -\frac{1}{2} \sum_{i,j,\sigma} f_i^\sigma f_j^\sigma \int \int \frac{\phi_i^{\sigma*}(\mathbf{r})\phi_j^\sigma(\mathbf{r})\phi_j^{\sigma*}(\mathbf{r}')\phi_i^\sigma(\mathbf{r}')}{|\mathbf{r} - \mathbf{r}'|} \, d\mathbf{r} \, d\mathbf{r}' . \tag{2.43}$$

The above expression is for the collinear spin case for which Eq. (2.29) holds. Generalizations for the non-collinear case are possible. Looking at Eq. (2.43) it is clear that hybrid functionals are not in the spirit of pure DFTs, as they are based on an orbital-dependent expression. Furthermore, the non-local character of the latter makes numerical work costly. However, the description of materials where self-interaction plays a dominant role is greatly improved. A common example of a hybrid functional is the PBE0 functional, which employs a mixing parameter of $a = 1/4$ in combination with the PBE approximation. This has been rationalized by Perdew et al. [78].

A further drawback of the local or semi-local nature of standard LDAs and GGAs is the absence of long-range effects such as van der Waals forces [79]. More specifically so-called London dispersion forces are not properly described in basic DFAs. Such forces originate from fluctuating dipoles that interact with each other over long distances with a characteristic $1/R^6$ asymptotic behavior [80]. This problem has sparked an extensive discussion about the inclusion of van der Waals (vdW) forces in recent years [79]. A major achievement was the development of van der Waals density functionals (vdW-DFs) with the energy composition [81]

$$E_{xc}^{vdW} = E_x^{GGA} + E_c^{LDA} + E_c^{nl}, \tag{2.44}$$

where the short-ranged correlation part is treated at the level of LDA and the missing fully non-local correlation is described by the correlation functional $E_c^{nl}$. This

functional can be cast in the following simple form [82]

$$E_c^{\mathrm{nl}} = \frac{1}{2} \iint n(\mathbf{r}) \varphi(\mathbf{r}, \mathbf{r}') n(\mathbf{r}') \, d\mathbf{r} \, d\mathbf{r}' , \qquad (2.45)$$

where the non-local character is explicit. The interaction between densities at different positions in space is given by an integration kernel $\varphi(\mathbf{r}, \mathbf{r}')$, which itself depends parametrically on the density and its gradient [81]. The kernel produces the correct asymptotic $-1/R^6$ behavior of dispersion forces and vanishes in the limit of the HEG, whose correlation is already described by $E_c^{\mathrm{LDA}}$. The proposal of an efficient numerical implementation [83] made vdW-DFs applicable to larger more realistic systems, while reducing the computational cost to almost the one of standard GGAs. Apart from the initial proposal, improved descriptions have been put forward [84, 85]. In particular, Klimeš et al. [85] proposed a modified form based on an optimized version of Becke's exchange [74] for reasons of which this vdW-DF is dubbed optB88-vdW. The optB88-vdW functional is employed Chapter 7 for the description of layered two-dimensional materials.

Furthermore, simplified accounts for vdW-interactions in terms of semi-classical corrections have been devised. Such corrections exhibit the pairwise additive form

$$E^{\mathrm{vdW}} = -\frac{1}{2} \sum_{A,B} g(R_{AB}) C_{6,AB} R_{AB}^{-6}, \qquad (2.46)$$

where the sum runs over atomic sites $A$ and $B$ separated by the interatomic distances $R_{AB}$. Each pair of atoms is associated with a $C_{6,AB}$-coefficient, which in the simplest case is a fixed number for each pair obtained from combining atomic species on the periodic table. $g(R_{AB})$ is a damping function, which is used to suppress the singularities in $R_{AB}^{-6}$ and to avoid short-range contributions from $E^{\mathrm{vdW}}$ which are readily captured by standard DFT functionals. Widely used is the scheme proposed by Grimme [86] and its extension [87, 88]. Tkatchenko and Scheffler [89] proposed a method in which the $C_6$-coefficients depend on the chemical environment by employing the density partitioning by Hirshfeld [90]. This scheme has been adapted to include many-body effects beyond pairwise atomic interactions [91] and to provide a description of screened vdW-forces at hybrid organic-inorganic interfaces [92].

### 2.3.4. Kohn-Sham Energy Eigenvalues and Orbitals

In practice, Kohn-Sham energy eigenvalues are often directly compared with the energies of electronic states probed in photoemission experiments. However, such a direct comparison is theoretically not justified, with one exception: the first ionization potential (IP) is identified as the eigenvalue of the highest occupied state $I(N) = -\varepsilon_N$ in an $N$-electron system in exact DFT (Koopman's theorem of DFT). This is known from comparing the asymptotics of the exact density decaying into vacuum as $n(\mathbf{r}) \sim \exp\left(-2\sqrt{2I}\right)$ with the asymptotics of the KS system $n(\mathbf{r}) \sim \exp\left(-2\sqrt{-2\varepsilon_N}\right)$ [93].

It is often pointed out that the fundamental gaps are underestimated by Kohn-Sham energy eigenvalues obtained with local and semi-local DFAs. The fundamental gap $E_{\mathrm{gap}}^{\mathrm{fund}}$ is defined here as the difference between the electron affinity $A$ and the

first ionization potential $I$ of the $N$-electron system[1]

$$E_{\text{gap}}^{\text{fund}} = I(N) - A(N). \tag{2.47}$$

Realizing that the electron affinity of the $N$-electron system is equal to the ionization potential of the $(N + 1)$-electron system one can identify the deviation $\Delta_{\text{XC}}$ of the energy gap in Kohn-Sham DFT $E_{\text{gap}}^{\text{DFT}} = \varepsilon_{N+1}(N) - \varepsilon_N(N)$ from the fundamental gap,

$$E_{\text{gap}}^{\text{fund}} = I(N) - I(N + 1) \tag{2.48}$$

$$= \varepsilon_{N+1}(N + 1) - \varepsilon_N(N) \tag{2.49}$$

$$= \varepsilon_{N+1}(N + 1) - \varepsilon_{N+1}(N) + \varepsilon_{N+1}(N) - \varepsilon_N(N) \tag{2.50}$$

$$= \Delta_{\text{XC}} + E_{\text{gap}}^{\text{DFT}}. \tag{2.51}$$

The quantity $\Delta_{\text{XC}}$ is related to the discontinuity in the exchange correlation functional across integer occupations [Eq. (2.52)]. Due to $\Delta_{\text{XC}}$ even exact DFT underestimates the fundamental gaps of materials. One may use calculations with different amounts of electrons for a better estimate of fundamental gaps as in Eq. (2.48).

DFT approximately accounts for the so-called exchange-correlation hole which describes that in the presence of one electron the probability to find another one in its vicinity is effectively reduced. Therefore unoccupied orbitals (virtual orbitals) in DFT effectively experience $N - 1$ electrons, the $N$ electrons of the system minus the exchange-correlation hole (equivalent of one electron) as if the virtual state were actually occupied.[2] Along this line, it has been argued that the band gap problem in DFT is not a deficiency but a feature of DFT providing a starting point for the estimation of optical excitation gaps, as common functionals like PBE give a relatively good description of the exchange-correlation hole [94].

Apart from this, DFT as a ground state theory is not suited to describe excitations, which are the subject of time-dependent perturbations and can for example be treated with time-dependent density functional theory (TDDFT). Another approach to excited states is finding a solution using the GW-approximation [95] in terms of single-particle Greens functions. The latter provides a good description of electron addition or removal energies. To accurately describe optical excitations it is necessary to account for interactions of the excited electrons with holes (excitons). This can for example be done by solving the Bethe-Salpeter equation [96], which involves the use of two-particle Green's functions.

Unfortunately, these approaches are computationally expensive and not feasible when simulating large, realistic systems with standard computational facilities. Therefore in this thesis we resort to approximate methods based on DFT. A practical approach is adopted for the estimation of lifetimes of excited adsorbate states. The

---

[1]This quantity may be experimentally determined by a combination of photoemission spectroscopy (PES) probing the highest occupied states (ionization potential) and inverse photoemission spectroscopy (IPES) probing the lowest unoccupied state (electron affinity).

[2]On the other hand, Hartree-Fock yields fundamental gaps larger than the experimentally observed ones, since the unoccupied orbitals (virtual orbitals) actually experience an $N$ electron system [94]. The Fock term does not cancel any self-interaction in the Hartree term for unoccupied levels (the sum in Eq. (2.43) runs only over occupied orbitals). Hartree-Fock (HF)-theory does not include any correlation and virtual HF-orbitals are known to be overly delocalized.

excitations are modeled as unoccupied Kohn-Sham states and therefore experience the exchange-correlation of standard semi-local functionals. Additionally and similar to the transition potential method we take into account a certain amount of orbital relaxation by including a core-hole in our calculations (the core-hole is included in the pseudopotential, see Section 2.5).

A further interpretation of the Kohn-Sham eigenvalues is provided by Janak's theorem [97],

$$\frac{\partial E}{\partial f_i} = \varepsilon_i. \tag{2.52}$$

According to this equation, the total energy of the $N$-electron Kohn-Sham system is a continuous function varying piecewise linearly with the fractional occupations $f_i$ of the eigenstates corresponding to the Kohn-Sham energies $\varepsilon_i$. The slopes of the linear segments are the Kohn-Sham energies $\varepsilon_i$ . The abrupt changes of the slope over integer occupations (derivative discontinuities) reflect the non-analytical behavior of the exact functional. Integrating Eq. (2.52) over occupations between systems differing by one electron yields the following approximate relation for the ionization energies

$$E(N) - E(N-1) = \int_0^1 \varepsilon_l \, df_l \approx \varepsilon(f_l = 1/2). \tag{2.53}$$

Here, $f_l$ is the occupation of the lowest unoccupied level of the $N-1$ electron system. The integral has been evaluated at half occupation of the orbital (mid-point approximation). This is known as Slater's transition state method [98] which can be used to estimate excitation energies for transitions from an initial state $i$ to a final state $f$ by evaluating the eigenvalue difference $E_{i \to f} = \varepsilon_f(\Theta_i = 1/2, \Theta_f = 1/2) - \varepsilon_i(\Theta_i = 1/2, \Theta_f = 1/2)$. The notation indicates that the energy eigenvalues have been evaluated self-consistently with the constraint that the initial and final states are half filled (i.e., belong to the family of $\Delta$SCF approaches). In practical implementations suitable methods for constraining the excited state occupations have to be found, as has been done, e.g., in the case of molecular adsorbates on surfaces [99, 100]. Unfortunately, $\Delta$SCF approaches are usually not very practical in solids or large systems with delocalized states, where the obtained corrections are usually negligible. A variation of Slater's transition state method is the transition potential approach proposed by Triguero et al. [101] where only the initial state is half filled (periodic systems need to be neutralized, e.g., by a constant background charge). This approach allows to calculate several transition energies (eigenvalue differences) with one calculation so that near edge X-ray absorption fine structure (NEXAFS) spectra can be simulated. Such simulations agree surprisingly well with experiments as, e.g., results for molecules on surfaces show [102, 103].

## 2.4. DFT with Localized Atomic Orbitals

As soon as an appropriate choice for the exchange-correlation functional has been made, a practical implementation of DFT has to be chosen to solve the Kohn-Sham scheme.

**Self Consistent Field**

The standard approach is to solve the equations self-consistently using the following iterative procedure:

1. Making an initial (educated) guess for the density in the system.
2. Solving the Poisson equation to obtain the Hartree potential from the density.
3. Solving the effective single particle Schrödinger equation, where the Hartree potential and the exchange-correlation approximation enter.
4. Computing a new density and mixing this new density with densities stemming from a number of previous cycles.
5. Jumping to step 2 to repeat the cycle as long as the calculation is not converged. Once the convergence criterion is met the calculation is terminated and the Kohn-Sham equations are considered to be solved numerically.

Depending on the code various convergence criteria may be found. In this thesis the SIESTA implementation is used. The most widely used convergence criterion within the SIESTA code [27–29] refers to the density matrix: a system is considered converged once the elements in the density matrix change less than a specified value with respect to the last cycle.

**Basis Set**

Since the variational space of the energy functional is in principle infinite dimensional useful approximations have to be found to make the involved calculations numerically tractable. In practice the problem is reformulated on a suitable basis spanning the Hilbert space. The used basis set is then truncated to obtain a computationally accessible set of equations. Sufficient terms have to be included which is usually done until convergence of the physical quantities of interest is reached. One possibility is to select a plane-wave basis set and include terms up to a certain wave vector. In the SIESTA code the Kohn-Sham eigenstates $\phi_i^\sigma(\mathbf{r})$ are expanded as linear combinations of numerical atomic orbitals $\varphi_\nu(\mathbf{r})$ [104]

$$\phi_i^\sigma(\mathbf{r}) = \sum_\nu c_{i\nu}^\sigma \varphi_\nu(\mathbf{r}), \tag{2.54}$$

with the expansion coefficients $c_{i\nu}^\sigma$. Those orbitals are localized in space and designed in such a way that they vanish beyond a certain cutoff radius. This efficiently reduces the number of matrix elements that need to be computed and stored.

**Periodic Boundary Conditions**

Using periodic boundary conditions the terms in the above equation depend on the crystal momentum $\mathbf{k}$, hence we write

$$\phi_i^\sigma(\mathbf{k}, \mathbf{r}) = \sum_\nu c_{i\nu}^\sigma(\mathbf{k}) \varphi_\nu(\mathbf{k}, \mathbf{r}). \tag{2.55}$$

The basis set $\{\varphi_\nu(\mathbf{k}, \mathbf{r})\}$ consists of Bloch-type functions $\varphi_\nu(\mathbf{k}, \mathbf{r})$ [105] constructed from the numerical atomic orbitals $\varphi_\nu(\mathbf{r} - \mathbf{t}_\nu - \mathbf{R})$. Here, the $\nu$th atomic orbital

belongs to the atom specified by the vector $\mathbf{t}_\nu$ inside the periodic cell specified by the lattice vector $\mathbf{R}$. The Bloch-type functions read[3]

$$\varphi_\nu(\mathbf{k}, \mathbf{r}) = A_\nu(\mathbf{k}) \sum_{\mathbf{R}} e^{i\mathbf{k}\mathbf{R}} \varphi_\nu(\mathbf{r} - \mathbf{t}_\nu - \mathbf{R}). \tag{2.56}$$

These basis functions are normalized by the normalization constant $A_\nu(\mathbf{k})$ obtained after integration over a single unit cell (see Appendix A). The Kohn-Sham eigenstates in the effective single particle Schrödinger equation can then be expanded in terms of the above defined Bloch-type basis set. Subsequent multiplication from the left with $\varphi_\mu^*(\mathbf{k}', \mathbf{r})$, and integration over $\mathbf{r}$ inside one unit cell leads to the eigenvalue equation,

$$\sum_\nu [H_{\mu\nu}^\sigma(\mathbf{k}) - \varepsilon_i^\sigma(\mathbf{k}) S_{\mu\nu}(\mathbf{k})] c_{i\nu}^\sigma(\mathbf{k}) = 0. \tag{2.57}$$

This expression is readily diagonal in the crystal momentum, such that only the terms $\mathbf{k} = \mathbf{k}'$ contribute. However, the non-trivial solutions to the remaining eigenvalue problem are found by diagonalization of a finite Hamiltonian matrix $H_{\mu\nu}^\sigma(\mathbf{k})$ in the case of a finite basis set. The Hamiltonian matrix is given by

$$H_{\mu\nu}^\sigma(\mathbf{k}) = \int \varphi_\mu^*(\mathbf{k}, \mathbf{r}) \hat{H}_e^\sigma \varphi_\nu(\mathbf{k}, \mathbf{r}) \, d\mathbf{r} = \sum_{\mathbf{R}} e^{i\mathbf{k}\mathbf{R}} H_{\mu\nu}^\sigma(\mathbf{R}). \tag{2.58}$$

This Hamiltonian is obviously spin-dependent, since the exchange-correlation potential entering the effective single particle equations depends on spin. The real-space Hamiltonian $H_{\mu\nu}^\sigma(\mathbf{R})$ describing the interactions between the orbitals in unit cells separated by a lattice vector $\mathbf{R}$ inside the crystal is defined as

$$H_{\mu\nu}^\sigma(\mathbf{R}) = \int \varphi_\mu^*(\mathbf{r} - \mathbf{t}_\mu) \hat{H}_e^\sigma \varphi_\nu(\mathbf{r} - \mathbf{t}_\nu - \mathbf{R}) \, d\mathbf{r} \,. \tag{2.59}$$

Because of the finite range of the numerical atomic orbitals, the interactions between unit cells in the crystal vanish for large separations $\mathbf{R}$. Hence, the infinite sum over lattice vectors $\mathbf{R}$ becomes finite and the problem reveals a tight-binding-like behavior. One finds for the overlap matrix between the basis orbitals

$$S_{\mu\nu}(\mathbf{k}) = \sum_{\mathbf{R}} e^{i\mathbf{k}\mathbf{R}} \int \varphi_\mu^*(\mathbf{r} - \mathbf{t}_\mu) \varphi_\nu(\mathbf{r} - \mathbf{t}_\nu - \mathbf{R}) \, d\mathbf{r} = \sum_{\mathbf{R}} e^{i\mathbf{k}\mathbf{R}} S(\mathbf{R}), \tag{2.60}$$

The overlap is spin-independent in contrast to the Hamiltonian, the spin-dependency is instead carried by the energy eigenvalues $\varepsilon_i^\sigma(\mathbf{k})$.

## 2.5.  Pseudopotentials and Core-Holes

The use of plane wave basis sets has inspired the construction of pseudopotentials as a common ingredient for ab-initio calculations. This additional approximation

---

[3]In the SIESTA code a slightly modified convention is used for the Bloch-type basis. The coefficients $\tilde{c}_{i\nu}(\mathbf{k}) = e^{i\mathbf{k}\mathbf{t}_\nu} c_{i\nu}(\mathbf{k})$, the Hamiltonian $\tilde{H}_{\mu\nu}(\mathbf{k}) = e^{i\mathbf{k}(\mathbf{t}_\mu - \mathbf{t}_\nu)} H_{\mu\nu}(\mathbf{k})$, and the overlap matrix $\tilde{S}_{\mu\nu}(\mathbf{k}) = e^{i\mathbf{k}(\mathbf{t}_\mu - \mathbf{t}_\nu)} S_{\mu\nu}(\mathbf{k})$ carry additional phases. This corresponds to a unitary transformation in the variational space, leaving the eigenvalues $\varepsilon_i^\sigma(\mathbf{k})$ in the Schrödinger equation $\sum_\nu [\tilde{H}_{\mu\nu}^\sigma(\mathbf{k}) - \varepsilon_i^\sigma(\mathbf{k}) \tilde{S}_{\mu\nu}(\mathbf{k})] \tilde{c}_{i\nu}^\sigma(\mathbf{k}) = 0$ unchanged.

aims at reducing the variational space accessed by basis sets as well as the number of electrons that must be treated explicitly, while maintaining the accuracy of the calculations. The idea is originated in the difficulties of plane wave basis sets to reproduce the strong oscillations of the wave functions near the singularities at the ionic cores. The tightly bound core electrons require a large amount of plane wave components to be captured. However, usually the relevant physics is dominated by the behavior of the valence electrons participating actively in the formation of bonds within the chemical environment. The wave functions of core states in contrast stay largely unaffected by the chemical environment and can therefore assumed to be fixed by effectively including them in a pseudopotential. Unfortunately, this is in some cases a strong approximation. Pseudopotentials are employed by the SIESTA code although they are not as vital for localized orbital codes as for plane wave implementations [28]. In the following the construction of pseudopotentials is outlined and the effective inclusion of core-holes in pseudopotentials is described. The latter is used in this thesis to enable the comparison of the theoretical results to core-spectroscopy experiments.

A justification of the pseudopotential theory can be found considering that the wave function of an atomic valence electron is composed by a smooth valence-like pseudo state and a fixed, quickly oscillating part that can be expanded in terms of the wave functions of the core-electrons,

$$|\psi_i^{\mathrm{v}}\rangle = |\tilde{\psi}_i^{\mathrm{v}}\rangle + \sum_j a_j |\psi_j^{\mathrm{c}}\rangle. \tag{2.61}$$

Knowing that the real wave functions of the valence electrons must be orthogonal to the core electrons one may write

$$0 = \langle\psi_k^{\mathrm{c}}|\psi_i^{\mathrm{v}}\rangle = \langle\psi_k^{\mathrm{c}}|\tilde{\psi}_i^{\mathrm{v}}\rangle + \sum_j a_j \langle\psi_k^{\mathrm{c}}|\psi_j^{\mathrm{c}}\rangle = \langle\psi_k^{\mathrm{c}}|\tilde{\psi}_i^{\mathrm{v}}\rangle + a_k, \tag{2.62}$$

finding the expansion coefficients

$$a_k = -\langle\psi_k^{\mathrm{c}}|\tilde{\psi}_i^{\mathrm{v}}\rangle. \tag{2.63}$$

The expansion coefficients reflect the non-orthogonality of the smooth pseudo wave functions to the core states. Substituting the expansion Eq. (2.61) into the Schrödinger equation one obtains a new Schrödinger-like equation

$$(\hat{H} + \hat{V}^{\mathrm{nl}})|\tilde{\psi}_i^{\mathrm{v}}\rangle = \varepsilon_i^{\mathrm{v}}|\tilde{\psi}_i^{\mathrm{v}}\rangle, \tag{2.64}$$

with a pseudo Hamiltonian containing a non-local potential term of the form [106, 107]

$$\hat{V}^{\mathrm{nl}} = \sum_j (\varepsilon_i^{\mathrm{v}} - \varepsilon_j^{\mathrm{c}})|\psi_j^{\mathrm{c}}\rangle\langle\psi_j^{\mathrm{c}}|. \tag{2.65}$$

This non-local term together with the potential of the atomic core $Z_{\mathrm{c}}/r$ is called a pseudopotential.

The actually used pseudopotentials in SIESTA differ from those described by Eq. (2.65). They belong to the so-called class of norm-conserving pseudopotentials

[108, 109], which are given in terms of distinct smooth radial functions for different angular momenta. Norm-conserving pseudopotentials are usually separated into an entirely local component and a semi-local part based on spherical harmonics in the following form

$$\hat{V}^{\mathrm{PS}} = \hat{V}_{\mathrm{loc}}(r) + \sum_{l=0}^{l_{\mathrm{max}}} \sum_{m=-l}^{l} |lm\rangle\, \delta\hat{V}_l(r)\, \langle lm| . \qquad (2.66)$$

The semi-local term in the latter equation only includes a few angular momenta $l \leq l_{\mathrm{max}}$. Higher angular momenta are not occupied by core electrons, so that there are no orthogonality constrains and, in principle, one can assume that the wave function components of larger momenta all interact with the ionic core in a similar way described by the local term.

Kleinman and Bylander rewrote the semi-local part of the pseudopotential as an approximate fully non-local and separable term [110]

$$\hat{V}_{\mathrm{KB}} = \hat{V}_{\mathrm{loc}} + \sum_{lm} \frac{|\delta\hat{V}_l \phi_{lm}\rangle\, \langle\phi_{lm}\delta\hat{V}_l|}{\langle\phi_{lm}|\delta\hat{V}_l|\phi_{lm}\rangle} . \qquad (2.67)$$

This form of the pseudopotential is computationally more efficient as it only requires the computation of two-center integrals in contrast to the three-center integrations required by the semi-local term in Eq. (2.66).

The overall procedure to create an ab-initio norm-conserving pseudopotential of a chemical element follows roughly the following steps. First, one obtains the atomic valence orbitals of the element of interest by solving the radial Schrödinger equation. Then one creates a set of node-less pseudo wave functions (cf. Fig. 2.3). The radial Schrödinger equation can now be inverted, as the pseudo wave functions are node-less, and one receives pseudo potentials for each angular momentum $l$. Finally the Hartree and exchange-correlation contributions due to the pseudo valence density $n^{\mathrm{PS}}$ are subtracted from the total pseudopotential (unscreening). The unscreening procedure avoids a double counting of exchange-correlation contributions by the valence electrons in subsequent calculations. Since the exchange-correlation potential is not linear $V_{\mathrm{xc}}[n^{\mathrm{PS}}+n^{\mathrm{c}}] \neq V_{\mathrm{xc}}[n^{\mathrm{PS}}]+V_{\mathrm{xc}}[n^{\mathrm{c}}]$ a simple subtraction of the contribution by $V_{\mathrm{xc}}[n^{\mathrm{PS}}]$ is usually not sufficient and so-called non-linear core corrections may be applied [112].

During the construction often a set of conditions, put forward by Hamann et al. [108], is fulfilled to ensure the transferability of the pseudopotential into different chemical environments: The pseudo wave functions have the same eigenvalues as the all-electron wave functions for a specific electronic configuration. The real and the pseudo wave function are equal outside the chosen cutoff radius $r_{\mathrm{c}}$ (see also Fig. 2.3). The norm of the pseudo and the real wave function are the same inside the cut off radius $r_{\mathrm{c}}$ (norm-conservation). Finally, the logarithmic derivative of the real and the pseudo wave-function are required to be equal at $r_{\mathrm{c}}$. Importantly, Hamann et al. [108] showed that the condition of norm-conservation leads to the correct scattering properties of the atom and therefore ensures the transferability of the pseudopotential. Nowadays, many plane-wave codes use ultrasoft pseudopotentials, which at the cost of norm-conservation produce even smoother pseudo wave functions [113].
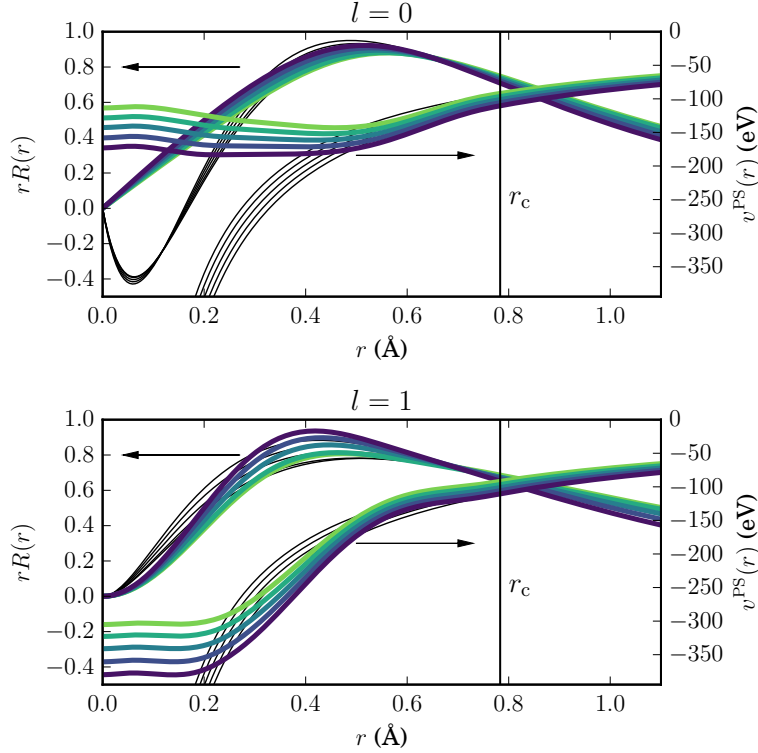
**Figure 2.3.:** Pseudopotentials $v^{\mathrm{PS}}(r)$ and radial parts of the pseudo wave functions $rR(r)$ of Nitrogen as constructed with the ATOM code [111]. The effect of including core-holes in the pseudopotential is shown in colors. Increasing sizes of core-holes (0, 0.25, 0.5, 0.75, and 1.00 electron charges) are depicted in darker colors. The radial part of the all electron wave function (thin black lines) exhibit $n-l-1$ nodes, while the pseudo wave functions are node-less. Beyond the cutoff radius $r_c$ the pseudo wave functions coincide with the all electron wave functions and the pseudopotentials equal the potentials $Z_{\mathrm{c}}/r$ (thin black lines).

The above guidelines to construct a pseudopotential still leave much room for the design of the pseudo wave function inside the core region. The SIESTA code uses pseudopotentials in the Kleinmann-Bylander form [110] that are norm-conserving and based on a construction scheme initially proposed by Troullier and Martins [109]. These pseudopotentials can be created with the ATOM program [111]. The transferability of these pseudopotentials is then tested by comparing the eigenvalues of different valence configurations (e.g., partial occupations mimicking hybridization) from the all electron calculation with the eigenvalues of the pseudo calculation. A further test is the analysis of the logarithmic derivatives defining the scattering properties of the pseudo atom.

Finally, it is possible to consider a configuration that includes a core-hole in the pseudopotential. This is achieved by constraining the occupations when creating the pseudopotential (such a constraint is directly achievable in an isolated atomic system). This method has been used extensively for the calculations in this work since it enables simulations in closer correspondence to core level spectroscopies.

Unlike in Slater's transition state method, where half-filled states are considered, we use mainly full core-holes. We typically perform our calculations including also one additional electron, which is constrained to occupy the excited state of interest in the adsorbate. Empirically we have found that this procedure leads to reasonable positions of the adsorbate electronic resonances on the surface in comparison to experimental information. Furthermore, we tested the effect of different core-hole sizes (cf. Fig. 2.3) on the resulting spectra for isonicotinic acid adsorbed on $TiO_2$ in Chapter 5 (see Appendix C.3) and found no considerable influence onto our results.

# Chapter 3

## Charge Transfer Times from Green's Functions

In this chapter a definition of the elastic lifetime of a localized quantum resonance is given and a theoretical approach to extract such lifetimes on the basis of a time-independent DFT framework is presented. The wording "time-independent DFT" in the context of lifetime calculations appears contradictory, but refers to an idealized time-evolution described by an effective single-particle Hamiltonian that does not explicitly depend on time (static Hamiltonian). In this approach lifetimes of purely electronic origin can be modeled, where dynamic loss-processes, for example due to vibrations (electron-phonon scattering) or due to collective electronic excitations (electron-plasmon scattering), are explicitly excluded.

In the following, first, Green's functions are introduced as the central mathematical tool employed to study the time-evolution of quantum states. Secondly, these single particle Green's functions are used to simulate the electronic structure of a sub-set of atoms inside a small region of a larger atomic structure. The Green's functions are constructed from numerical atomic orbitals as employed in the SIESTA code. Exploiting the localized character of these orbitals, it is possible to simulate atomic structures of infinite spatial extent, i.e., consisting of an infinite amount of atoms. This allows us, in particular, to simulate surfaces terminating an unlimited sequence of stacked atomic layers. Based on such a setup, we employ a suitable procedure to estimate the elastic lifetimes of quantum states at surfaces [34, 35]. These lifetimes are associated with interfacial charge transfer processes, hence, we also speak of charge transfer times. A comprehensive account for Green's functions in general can be found in the book by Economou [114], which provided the basis for part of the following.

# 3.1. Propagators and Green's Functions

The Green's function $G$ associated with the time-independent Schrödinger equation Eq. (2.3) is defined by the following differential equations

$$[z - \hat{H}]G(z) = 1 \quad \text{or} \quad [z - \hat{H}]G(\mathbf{r}, \mathbf{r}'; z) = \delta(\mathbf{r} - \mathbf{r}'), \tag{3.1}$$

where in the first form the Green's function is an operator acting on an abstract Hilbert space and in the second equivalent form the Green's function operator has been recast in real space representation according to $G(\mathbf{r}, \mathbf{r}'; z) = \langle \mathbf{r} | G(z) | \mathbf{r}' \rangle$.

Using the relation $f(\hat{H}) |\phi_i\rangle = f(\varepsilon_i) |\phi_i\rangle$ (the spectral theorem) and inserting a complete set of eigenstates $\sum_i |\phi_i\rangle \langle \phi_i| = 1$ one obtains the Green's function in it's spectral representation

$$G(z) = \sum_i \frac{|\phi_i\rangle \langle \phi_i|}{z - \varepsilon_i} \quad \text{or} \quad G(\mathbf{r}, \mathbf{r}'; z) = \sum_i \frac{\phi_i(\mathbf{r})\phi_i^*(\mathbf{r}')}{z - \varepsilon_i}, \tag{3.2}$$

where the second equation is in turn the real space analogue. The Green's function is defined for all energy values $z$ on the complex plane, except for the poles in the spectral representation, Eq. (3.2). These poles appear for each of the real energy eigenvalues $\varepsilon_i$. Therefore, avoiding these singularities, the following two limiting contours along the real axis are specified

$$G^\pm(\mathbf{r}, \mathbf{r}'; E) = \lim_{\eta \to 0^+} G(\mathbf{r}, \mathbf{r}'; E \pm \mathrm{i}\eta), \tag{3.3}$$

which represent physically relevant Green's functions for real energies $E$. The two limiting cases are referred to as the retarded $G^+$ and the advanced $G^-$ Green's function. One may inspect the spectral representation of the Green's function in Eq. (3.2) by applying the identity

$$\lim_{y \to 0^+} \frac{1}{x \pm \mathrm{i}y} = \mathrm{P}\frac{1}{x} \mp \mathrm{i}\pi\delta(x), \tag{3.4}$$

where P indicates that the principal value has to be taken. The first term in the above formula is therefore an abstract notation, and has to be interpreted in the sense of a distribution like the $\delta(x)$ of the second term. The notation becomes sensible under an integral, where the principal value integral has to be taken. Applying the formula to the real space representation of the spectral decomposition of the Green's function one finds

$$G^\pm(\mathbf{r}, \mathbf{r}'; E) = \mathrm{P}\sum_i \frac{\phi_i(\mathbf{r})\phi_i^*(\mathbf{r}')}{E - \varepsilon_i} \mp \mathrm{i}\pi \sum_i \delta(E - \varepsilon_i)\phi_i(\mathbf{r})\phi_i^*(\mathbf{r}'). \tag{3.5}$$

Here, the second term can be identified for $\mathbf{r} = \mathbf{r}'$ as the local density of states (LDOS) $\rho(\mathbf{r}, E)$ related to the Hamiltonian associated with the Green's function

$$\rho(\mathbf{r}, E) = \mp\frac{1}{\pi} \mathrm{Im}\left\{ G^\pm(\mathbf{r}, \mathbf{r}; E) \right\}. \tag{3.6}$$

Integration over the entire real space yields the DOS $\rho(E)$.

On the other hand, one may start from the time-dependent Schrödinger equation Eq. (2.1), thus defining a time-dependent Green's function $G(\mathbf{r}, \mathbf{r}', t - t')$ as a solution to the following differential equation

$$[\mathrm{i}\frac{\partial}{\partial t} - \hat{H}(\mathbf{r})]G(\mathbf{r}, \mathbf{r}'; t - t') = \delta(\mathbf{r} - \mathbf{r}')\delta(t - t'). \qquad (3.7)$$

The Fourier transform of the Green's function $G^{\pm}(E)$ as specified for the static case, Eq. (3.1), is identified as a solution to the above equation

$$G^{\pm}(t - t') = \frac{1}{2\pi} \int_{-\infty}^{\infty} G^{\pm}(E)\mathrm{e}^{-\mathrm{i}E(t-t')} \, dE = \oint_C G^{\pm}(z)\mathrm{e}^{-\mathrm{i}z(t-t')} \, dz \, . \qquad (3.8)$$

To calculate the Fourier transform of $G^+(E)$ and $G^-(E)$ along the real axis one can extend the integration into the complex plane by closing a contour $C$ along a semi-infinite half-circle. The contour is closed in the lower complex plane for times $t - t' > 0$ following Jordan's lemma. The integral along the infinite half-circle of this contour is then zero due to the asymptotic behavior of the Green's function. Then one can evaluate the Fourier transform along the real axis by applying the residue theorem

$$\oint_C G^{\pm}(z) \, dz = 2\pi\mathrm{i} \sum_k \mathrm{Res}[G^{\pm}(z), a_k], \qquad (3.9)$$

where $\mathrm{Res}[G^{\pm}(z), a_k]$ are the residues of $G^{\pm}(z)$ at the singular points $z = a_k$ of $G^{\pm}(z)$ enclosed by the contour $C$ in the complex plane. One finds that $G^+(t - t')$ is non-zero while $G^-(t - t')$ vanishes for times $t - t' > 0$. Similarly one can close the contour $C$ in the upper complex plane for times $t - t' < 0$, finding instead, that $G^-(t - t')$ is non-zero and $G^+(t - t')$ vanishes. This clarifies the previously introduced nomenclature of retarded and advanced Green's functions.

As a consequence, it is possible to define the difference of the retarded and advanced Green's function $\tilde{G}(t - t') = G^+(t - t') - G^-(t - t')$ with the property,

$$G^{\pm}(t - t') = \pm\theta(\pm t - t')\tilde{G}(t - t'). \qquad (3.10)$$

Since both $G^+$ and $G^-$ satisfy Eq. (3.7), $\tilde{G}$ itself cannot satisfy Eq. (3.7) and hence is not strictly speaking a Green's function. A closer inspection of $\tilde{G}$ reveals instead that $\tilde{G}$ relates to the unitary time evolution operator $\hat{U}(t)$, which can be seen by

$$\tilde{G}(t) = G^+(t) - G^-(t) = \frac{1}{2\pi} \int_{-\infty}^{\infty} [G^+(E) - G^-(E)]\mathrm{e}^{-\mathrm{i}Et} \, dE \qquad (3.11)$$

$$= -\mathrm{i} \int_{-\infty}^{\infty} \sum_i \delta(E - \varepsilon_i) |\phi_i\rangle \langle\phi_i| \, \mathrm{e}^{-\mathrm{i}Et} \, dE \qquad (3.12)$$

$$= -\mathrm{i} \sum_i \mathrm{e}^{-\mathrm{i}\varepsilon_i t} |\phi_i\rangle \langle\phi_i| = -\mathrm{i}\mathrm{e}^{-\mathrm{i}\hat{H}t} = -\mathrm{i}\hat{U}(t). \qquad (3.13)$$

In the second line the spectral decomposition of the Green's function Eq. (3.5) and in the last line the spectral decomposition of the Hamiltonian $\hat{H} = \sum_i \varepsilon_i |\phi_i\rangle \langle\phi_i|$ were used. By plugging the term $\hat{U}(t)$ into the Schrödinger equation, Eq. (2.1) one can verify that it describes a quantum mechanical time-evolution. Consequently, the

retarded Green's function $G^+(t)$ describes a propagation forward in time, whereas the advanced Green's function $G^-(t)$ propagates backwards in time, cf. Eq. (3.10). Finally, a projection of $\hat{U}(t)$ into the coordinate space yields a propagator $K(\mathbf{r}, \mathbf{r}', t - t') = \langle \mathbf{r} | \hat{U}(t - t') | \mathbf{r}' \rangle$ which describes the evolution of a probability amplitude at one point in space $\mathbf{r}'$ and an initial time $t'$, towards a probability amplitude at a point $\mathbf{r}$ and another time $t$.

## 3.2. Lifetimes of Quantum States

Following the introduction about the propagation of probability amplitudes above, we can define the survival amplitude of a wave-packet at some time $t$, which was initially prepared in the state $\psi(t_0)$ at a time $t_0 < t$,

$$A(t) = \langle \psi(t_0) | \psi(t) \rangle = \langle \psi(t_0) | U(t - t_0) | \psi(t_0) \rangle. \tag{3.14}$$

Making use of the Born rule, the square modulus of the amplitude $A(t)$ gives the survival probability

$$S(t) = |A(t)|^2 = |\langle \psi(t_0) | iG^+(t - t_0) | \psi(t_0) \rangle|^2. \tag{3.15}$$

The survival amplitude $S(t)$ is the probability that an initially prepared wave-packet in a state $\psi(t_0)$ is still found in its initial state at a later time $t$. Eq. (3.15) explicitly describes a causal evolution of $\psi$, where the propagation of the wave-packet over a time interval follows the initial preparation of the state (i.e., the propagation is *caused* by the initial preparation). This is achieved by using the retarded Green's function, $iG^+(t) = \hat{U}(t)$ for $t > t_0$, combining Eq. (3.13) and Eq. (3.10). Using the survival amplitude Eq. (3.15), we can define the lifetime $\tau$ as the mean time $\langle t \rangle$ the wave-packet remains in its initial state

$$\tau = \langle t \rangle = \frac{\int_0^\infty t\, S(t)\, dt}{\int_0^\infty S(t)\, dt}. \tag{3.16}$$

If the survival probability exhibits a decaying behavior over time such that the integrals in the fraction converge, the lifetime $\tau$ obtains a finite positive value. In the case of an exponential decay of the survival probability $S(t) = N_0 e^{-\Gamma t}$, where $N_0$ is the initial population of the state one finds the relation

$$\tau = \frac{1}{\Gamma} \tag{3.17}$$

between the lifetime $\tau$ and the rate $\Gamma$ of the exponential decay.

## 3.3. Localized States at Surfaces

In this section Green's functions are applied as a tool to describe smaller systems of atoms inside a larger chemical environment. This allows to simulate localized states of a finite surface region coupled to a substrate consisting of a few atomic layers. In
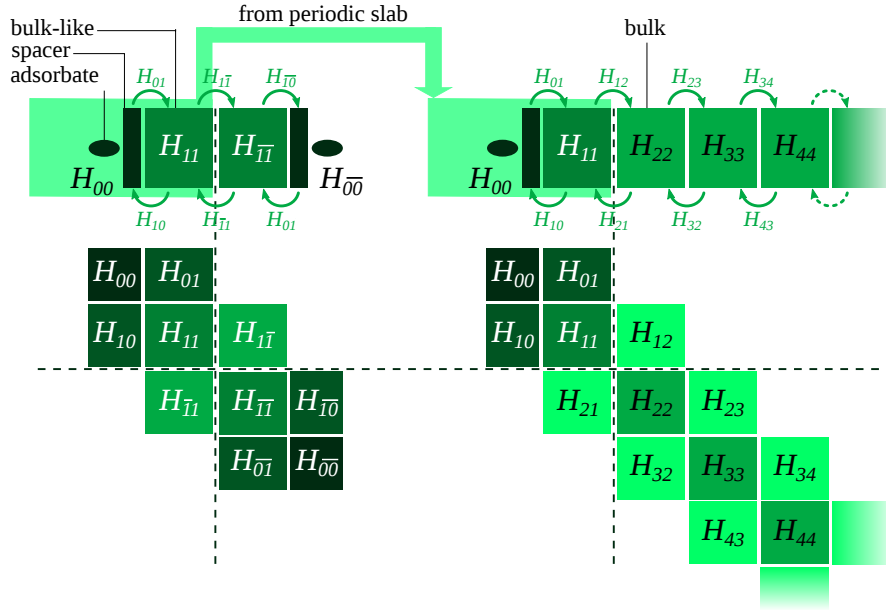
**Figure 3.1.:** Illustration of the scheme used to compute the Green's function of an infinite system in the surface region. In a first step the Hamiltonian of a surface region is obtained from a calculation of periodically repeating slabs with a finite amount of atomic layers separated by vacuum (left side). The surface region is then coupled in a second step to an infinite amount of bulk like atomic layers (right side). The bottom of the scheme shows the block-tridiagonal form of the Hamilton matrices in relation to the structures on top.

a second step the scheme is extended to include the coupling to an infinite amount of stacked atomic layers. The procedure is formulated in the basis of local numerical orbitals used in the SIESTA code.

The starting point is to rewrite the differential equation defining the Green's function, Eq. (3.1), in a the Bloch basis Eq. (2.56),

$$\sum_\mu [z S_{\lambda\mu}(\mathbf{k}_\parallel) - H_{\lambda\mu}^\sigma(\mathbf{k}_\parallel)] G_{\mu\nu}^\sigma(\mathbf{k}_\parallel) = \delta_{\lambda\nu}. \tag{3.18}$$

Here, we consider a system that is periodic in the directions parallel to the surface. Therefore, only wave-vectors $\mathbf{k}_\parallel$ parallel to the surface are taken into account. In the direction perpendicular to the surface no periodicity is assumed, which is equivalent to performing a calculation at the $\Gamma$-point in that direction. The steps in arriving at Eq. (3.18) are shown in the Appendix B. The indices in Eq. (3.18) run over the numerical orbitals at all atomic sites. As in Eq. (2.57) the use of a non-orthogonal basis set requires the consideration of the overlap matrix. Computationally, the Green's function in the energy domain and $\mathbf{k}$-space $G(\mathbf{k}, z)$ can be obtained in two equivalent ways as shown in the formula

$$G_{\mu\nu}^\sigma(\mathbf{k}; z) = \sum_i \frac{c_{i\mu}^\sigma(\mathbf{k}) c_{i\nu}^{\sigma*}(\mathbf{k})}{z - \varepsilon_i^\sigma(\mathbf{k})} = [zS - H^\sigma(\mathbf{k})]_{\mu\nu}^{-1}, \tag{3.19}$$

which follows from Eq. (3.5) for the localized basis set. $c_{i\nu}^\sigma(\mathbf{k})$ are the coefficients of the single particle Kohn-Sham states with energy eigenvalue $\varepsilon_i^\sigma(\mathbf{k})$, cf. Eq. (2.35). In the following the notation for the wave vector $\mathbf{k}$ and spin $\sigma$ are dropped for clarity. The available indices for $\mu$ and $\nu$ are separated into two subsets 0 and 1. Set 0 belongs to the local orbitals of the atoms inside a smaller region (e.g., an adsorbate) connected to a larger environment forming set 1 (e.g., a substrate of a few atomic layers). Introducing this short hand notation we correspondingly rewrite Eq. (3.18) as

$$\begin{bmatrix} zS_{0,0} - H_{0,0} & zS_{0,1} - H_{0,1} \\ zS_{1,0} - H_{1,0} & zS_{1,1} - H_{1,1} \end{bmatrix} \begin{bmatrix} G_{0,0} & G_{0,1} \\ G_{1,0} & G_{1,1} \end{bmatrix} = \begin{bmatrix} 1_{0,0} & 0 \\ 0 & 1_{1,1} \end{bmatrix}. \tag{3.20}$$

Omitting the couplings (the overlap and interaction terms in the Hamiltonian) between the sub-systems, one may define the isolated Green's functions $G_{0,0}^0$ and $G_{1,1}^0$ of the sub-systems

$$G_{0,0}^0 = (zS_{0,0} - H_{0,0})^{-1}, \tag{3.21}$$

$$G_{1,1}^0 = (zS_{1,1} - H_{1,1})^{-1}. \tag{3.22}$$

The parts $H_{0,0}$ and $H_{1,1}$ of the Hamiltonian (called isolated systems here) belong to the Hamiltonian of the combined system and therefore in principle have to be obtained from an explicit self-consistent calculation of the whole set of atoms. Solving for the first column in Eq. (3.20) one obtains

$$(zS_{0,0} - H_{0,0})G_{0,0} + (zS_{0,1} - H_{0,1})G_{1,0} = 1_{0,0}, \tag{3.23}$$

$$(zS_{1,0} - H_{1,0})G_{0,0} + (zS_{1,1} - H_{1,1})G_{1,0} = 0. \tag{3.24}$$

After eliminating the term $G_{1,0}$ by substitution one receives the result

$$(zS_{0,0} - H_{0,0})G_{0,0} - \underbrace{(zS_{0,1} - H_{0,1})(zS_{1,1} - H_{1,1})^{-1}(zS_{1,0} - H_{1,0})}_{(zS_{0,1} - H_{0,1})G_{1,1}^0(zS_{1,0} - H_{1,0}) = \Sigma_{0,0}(z)} G_{0,0} = 1, \quad (3.25)$$

where in the second term one may identify the isolated Green's function $G_{1,1}^0(z)$ and define a new energy dependent quantity $\Sigma_{0,0}(z)$ which is commonly referred to as self-energy. With the definition of $\Sigma_{0,0}(z)$ we rewrite the Green's function inside the reduced space region 0 as [115]

$$G_{0,0}(z) = [zS_{0,0} - H_{0,0} - \Sigma_{0,0}(z)]^{-1}. \quad (3.26)$$

The self-energy term $\Sigma_{0,0}(z)$ effectively introduces the interaction with the set of atoms outside the region 0, so that $G_{0,0}(z)$ describes the region 0 correctly in terms of the coupling to the rest of the system. The main advantage here is that the size of the matrices appearing in Eq. (3.26) is given by the fractional amount of orbitals in region 0.

The above scheme can now be further extended to include the interaction of a primary region belonging to the surface with an infinitely extending substrate. This is achieved by including the coupling to an infinite amount of bulk-like layers.

In the following we assume that the outer surface region is well-described by taking the matrix elements $H_{0,0}$, $H_{1,1}$, $H_{0,1}$, and $H_{1,0}$ from a periodic slab calculation (cf. Fig. 3.1, left side). In this periodic calculation repeating images of the slab are separated by vacuum. The slab is required to consist of a sufficient amount of substrate layers (i.e., it contains a sufficiently large spacer region, cf. Fig. 3.1) so that bulk character is approached in the central region $H_{1,1}$ of the slab. We employed throughout this work ideal structures of perfectly symmetric slabs. In part of the calculations the surfaces of the slab were decorated (symmetrically) with adsorbates. This setup ensures that possible occurrences of spurious surface dipoles on both sides of the slab cancel each other [116].

The bulk-like region of the finite slab $H_{1,1}$ is subsequently coupled to an infinite sequence of blocks $H_{2,2}, H_{3,3}, \ldots$ (cf. Fig. 3.1, right side) representing the bulk material. Considering the periodicity of the system in one half space, one has

$$H_{1,1} \approx H_{2,2} = H_{3,3} = \ldots = H_{n.n} = \ldots, \quad (3.27)$$

where the elements $H_{2,2}, H_{3,3}, \ldots$ are taken from a periodic bulk calculation of the substrate material. Care has to be taken when connecting the bulk and slab systems, since both need to be aligned in practice at a common energy reference. The Fermi energy provides a suitable reference for metallic systems. Semi-conducting materials can be aligned via the (Hartree) potential inside the bulk-like material (see e.g. Section 5.2.2).

The connection of the surface region to the infinite bulk is not treated self-consistently in the approach used in this thesis. We consider here, that the matrix elements from one-shot periodic slab calculations and bulk calculations may be directly connected, assuming therefore that the electronic structures of the separate parts are not mutually affecting each other in a significant way, when they are attached. At

zero bias, in the absence of external fields, this can usually be considered a reasonable assumption, which can be controlled by increasing the thickness of the slab. Generally, self-consistent treatments can be achieved using non-equilibrium Green's functions [117, 118] at significantly higher computational costs.

Due to the limited spatial extent of the orbitals in the basis, the size of the repeating chunks of bulk material (computational bulk unit cell) can be chosen in a way that only neighboring blocks interact with each other. This results in a block tri-diagonal form of the Hamiltonian and overlap matrices (cf. Fig. 3.1). It is therefore possible to write for the defining equations of the Green's function, Eq. (3.18),

$$
\begin{bmatrix} zS_{1,1} - H_{1,1} & zS_{1,2} - H_{1,2} & 0 \\ zS_{2,1} - H_{2,1} & zS_{2,2} - H_{2,2} & \ddots \\ 0 & \ddots & \ddots \end{bmatrix} \begin{bmatrix} G_{1,1} & G_{1,2} & \cdots \\ G_{2,1} & G_{2,2} & \\ \vdots & & \ddots \end{bmatrix} = \begin{bmatrix} 1_{1,1} & 0 & \cdots \\ 0 & 1_{2,2} & \\ \vdots & & \ddots \end{bmatrix}. \quad (3.28)
$$

Equating the first column one obtains the infinite set of equations

$$
\begin{aligned}
(zS_{1,1} - H_{1,1})G_{1,1} + & (zS_{1,2} - H_{1,2})G_{2,1} & = 1_{1,1}, \\
(zS_{2,1} - H_{2,1})G_{1,1} + (zS_{2,2} - H_{2,2})G_{2,1} + & (zS_{2,3} - H_{2,3})G_{3,1} & = 0, \\
& \vdots &
\end{aligned}
$$
$$
(zS_{n,n-1} - H_{n,n-1})G_{n-1,1} + (zS_{n,n} - H_{n,n})G_{n,1} + (zS_{n,n+1} - H_{n,n+1})G_{n+1,1} = 0. \quad (3.29)
$$

Considering the periodicity inside the material [cf. Eq. (3.27)] one may simplify these expressions by writing

$$
\begin{aligned}
(zS_{1,1} - H_{1,1})G_{1,1} + (zS_{1,2} - H_{1,2})G_{2,1} & = 1_{1,1}, \\
(zS_{2,1} - H_{2,1})G_{1,1} + (zS_{1,1} - H_{1,1})G_{2,1} + (zS_{1,2} - H_{1,2})G_{3,1} & = 0, \\
\vdots &
\end{aligned}
$$
$$
(zS_{2,1} - H_{2,1})G_{n-1,1} + (zS_{1,1} - H_{1,1})G_{n,1} + (zS_{1,2} - H_{1,2})G_{n+1,1} = 0. \quad (3.30)
$$

This set of equations can be solved by considering a single transfer matrix $T$ connecting the pairs of the $n$-th and $(n-1)$-th layers [119] in the infinite material, so that

$$
G_{n,1} = TG_{n-1,1}. \quad (3.31)
$$

Using the transfer matrix $T$ the following recursive relation for the transfer matrix can be easily derived,

$$
T = [zS_{1,1} - H_{1,1} + (H_{1,2} - zS_{1,2})T]^{-1}(zS_{2,1} - H_{2,1}). \quad (3.32)
$$

This expression can be solved self-consistently with the initial guess of $T = 0$. The converged result for the matrix $T$ together with the defining equation, Eq. (3.31), and the first line of Eq. (3.30) yields the Green's function belonging to the outermost bulk-like region (for now excluding the termination by the surface associated with $H_{0,0}$)

$$
G_{1,1} = [zS_{1,1} - H_{1,1} + (H_{1,2} - zS_{1,2})T]^{-1}. \quad (3.33)
$$

In a final step the outer surface (adsorbate and spacer, $H_{0,0}$) can be connected via Eq. (3.25) and Eq. (3.26) with the infinite slab, which is now described by the finite matrix in Eq. (3.33). Notice that in order to do this $G_{1,1}^0$ in Eq. (3.25) must be identified with $G_{1,1}$ in Eq. (3.33). Thereby one obtains the Green's function inside the surface region $G_{0,0}$ as desired.

In the practical part of this work (Chapters 5 to 7) we use the TranSIESTA module [117, 118] of the SIESTA code to calculate the Green's function of the surface region (i.e., the combined system of $H_{0,0}$ and $H_{1,1}$ coupled to the semi-infinite substrate). TranSIESTA uses the highly efficient algorithm proposed by Sancho et al. [120, 121] to perform the computations of the semi-infinite substrate. The original purpose of the TranSIESTA code to simulate transport through junctions made it necessary to adopt a setup, where actually two semi-infinite substrates are separated by vacuum (similar to a break junction). The vacuum region is then chosen large enough so that the surfaces, do not interact[1].

## 3.4.   Initial Wave Packets and Resonances

The theoretical estimation of lifetimes of intermediate states that are initially prepared by an excitation (e.g., an external perturbation by light), is at the center of this work [cf. Eq. (1.1)]. So far the intermediate states or wave-packets have not been specified explicitly. In principle, they are defined by the excitation process e.g., the polarization, intensity, and direction of the incoming light. In this work, a direct treatment of the initial excitation process is neglected, as the employed time-independent DFT does not account for the time-dependent field of the excitation. Instead, we adopt a heuristic approach, in which an intermediate wave-packet is constructed from the occupied or unoccupied Kohn-Sham states of a smaller subsystem, e.g., an atom or molecule attached to the surface. These wave-packets may also be calculated considering certain constraints, as for instance the inclusion of a core-hole in relation to core-spectroscopy experiments. Overall, the method leaves room to explore qualitatively different excitations, e.g., spin-selective [122] or polarization-dependent excitations [22, 123], by considering certain orbitals or mixtures thereof.

This heuristic approach to excited states can be justified, since the symmetry and shape of Kohn-Sham states is usually close in comparison to the physically well-motivated Hartree-Fock orbitals, relating to excitations upon electron addition or electron removal. The unoccupied (virtual) or occupied Kohn-Sham orbitals represent even arguably better approximations to *excited* quasi-particle states than Hartree-Fock orbitals due to the approximate inclusion of the exchange-correlation hole in DFT (Hartree-Fock orbitals are known to be too diffuse). We further assume that the lifetime of the resonance wave-packet does only depend weakly on the precise shape of the wave packet allowing for a well-motivated guess.

Using the tools [34, 35] described in the previous two sections, the lifetime of

---

[1]We used a version of the TranSIESTA code carrying the number `trunk-458-ts-npa-57` which was kindly provided by Nick Papior Anderson. We modified this development version for our purposes. In the more recent versions of the TranSIESTA code $n$-electrode calculations, with $n \geq 1$ are feasible [118]. This would in principle allow to directly perform single electrode calculations.

an initially prepared resonance wave packet $|\psi_R\rangle$, which is taken to be the Kohn-Sham state of a smaller subsystem at a surface, can be determined. This can be done by calculating the Green's function of the surface region in the energy domain, Eq. (3.26), and employing it's Fourier transform to propagate the wave packet in time, cf. Eq. (3.8). Alternatively, one first performs a projection of the Green's function onto the initial wave-packet in the energy domain and then executes the Fourier transform $\mathcal{F}$, i.e.,

$$A(t) = \mathcal{F}(\langle \psi_R | iG^+(E) | \psi_R \rangle) = \mathcal{F}[iG_{RR}^+(E)]. \tag{3.34}$$

**Weakly coupled resonances**

In the presence of a single resonance R on an adsorbate attached to a semi-infinite surface, the formula in Eq. (3.26) reflects the Anderson-Grimley-Newns model for chemisorption [31–33] or Fano's description of resonances [30]. These models are based on a Hamiltonian of the form

$$H = \begin{bmatrix} E_R & V_{Rk} \\ V_{Rk} & H_k \end{bmatrix}, \tag{3.35}$$

where the resonant energy level $E_R$ is connected by the coupling elements $V_{Rk}$ to an infinite diagonal matrix $H_k$ with the continuum of energy eigenvalues $E_k$ of the substrate as diagonal elements.

The resonance spectrum $G_{RR}^+(E)$, Eq. (3.26), is therefore of the form $g_{RR}(E)$ described by these models, i.e.

$$G_{RR}^+(E) \approx g_{RR}(E) = \frac{1}{E - E_R - \Sigma(E)}, \quad \text{with} \quad \Sigma(E) = \sum_k \frac{|V_{Rk}|^2}{E - E_k}. \tag{3.36}$$

The complex self-energy $\Sigma(E) = \Lambda(E) - i\Delta(E)$ can be split into a real contribution causing a shift of the resonance energy $E_R$,

$$\Lambda(E) = P \int \frac{\Delta(E')}{E - E'} \, dE', \tag{3.37}$$

where the sum over the discrete energies has been converted to an integral, and an imaginary part, which is known as the *chemisorption function*,

$$\Delta(E) = \pi \sum_k |V_{Rk}|^2 \delta(E - E_k) = \pi |V_{av}|^2 \rho_k(E). \tag{3.38}$$

The chemisorption function is related to the broadening of the resonance peak appearing in the density of states. This can be seen, considering a less general case in which $\Delta(E) \approx \Omega$ is independent of energy, and the real-valued shift $\Lambda(E) \approx 0$ is negligible. This case corresponds formally to the wide band limit in which the DOS of the substrate $\rho(E)$ is constant. The projection of the DOS onto the resonance wave-packet is then given by

$$\rho_R(E) = -\frac{1}{\pi} \text{Im}[G_{RR}^+(E)] \approx -\frac{1}{\pi} \text{Im}[g_{RR}(E)] = \frac{1}{\pi} \frac{\Omega}{(E - E_R)^2 + \Omega^2}. \tag{3.39}$$

Thus, the resulting spectrum is of a Lorentzian lineshape, which has a maximum at the resonance energy $E_\mathrm{R}$ and the linewidth broadening is given by the full width half maximum (FWHM) of $\Gamma = 2\Omega$. Strictly speaking, the Lorentzian distribution does not possess any finite statistical moment of order $k \geq 1$. Hence, instead of the mean and the variance of the distribution, we use the resonance position $E_\mathrm{R}$ the FWHM, respectively.

Taking the Fourier transform $\mathcal{F}[g_\mathrm{RR}(E)] = g_\mathrm{RR}(t)$ one can calculate the survival amplitude $\mathrm{i}g_\mathrm{RR}(t) = \mathrm{i}e^{-(\mathrm{i}E_\mathrm{R}-\Omega)t}$ for $t > 0$. The integral of the Fourier transform is evaluated by extending the integration path into the complex plane. One obtains the result by applying the Cauchy integral formula and Jordan's lemma closing a contour in the lower (upper) plane for t>0 (t<0) . For the survival probability one has

$$S(t) = |\mathrm{i}g_\mathrm{RR}(t)|^2 = \begin{cases} 0, & \text{for } t < 0, \\ e^{-2\Omega t} = e^{-\Gamma t}, & \text{for } t > 0. \end{cases} \tag{3.40}$$

The mean lifetime in relation to the exponential decay is finally $\tau = (2\Omega)^{-1} = 1/\Gamma$, cf. Eq. (3.17). Since $\Gamma$ is a broadening in the energy domain, Eq. (3.17) is identified as an expression for the uncertainty in energy and time.

Hence, if the spectrum in Eq. (3.26) provides a single and sufficiently clear resonance peak, one can extract the associated lifetime by fitting a Lorentzian and determining its width. Such well-defined resonances are found for weakly interacting states in the absence of multiple resonances and without strong contributions from a continuous background. It was possible to apply this approach to the molecular and atomic resonances in chapchap:05 and Chapter 6

In practical calculations the Green's function is evaluated at a slightly complex energy $z = E + \mathrm{i}\eta$ to avoid the poles on the real axis and to facilitate the convergence of the recursive scheme. This results in an additional finite contribution to the width, which we correct for *a posteriori* by subtracting it, so that $\Gamma = 2(\Omega - \eta)$ for the width of the resonance peak.

**Strongly coupled resonances**

If no clear resonance can be determined, i.e., the coupling of the small region to the environment is strong, it is practically not possible to fit a Lorentzian curve and instead an explicit calculation of the time-evolution is necessary. In this case, one has to consider which part of the spectrum $\mathrm{Im}[G_\mathrm{RR}^+(E)]$ in Eq. (3.39) is actually populated by the initial excitation and thus shaping the part of the spectrum associated with the resonance. Here, in principle only unoccupied states are accessible upon excitation, such that the spectrum is in practice cropped by a Fermi distribution $f(E)$ [35]

$$\mathrm{Im}[G_\mathrm{RR,cut}^+(E)] = [1 - f(E)]\,\mathrm{Im}[G_\mathrm{RR}^+(E)]. \tag{3.41}$$

One may further consider the possibility of a separate pumping of distinct features [36] by the incoming light pulse, which further narrows the window of accessible states. To determine the full Green's function describing the causal decay of the resonance wave-packet one obtains the real part $\mathrm{Re}[G_\mathrm{RR,cut}^+(E)]$ by using the Kramers-Kronig relations.

The Kramers Kronig relations can be derived using the residual theorem. Closing a contour $C^+$ in the upper half plane one can relate the real and the imaginary parts of the Green's function $G^+$. Analogously, one can close a contour in the lower half plane for $G^-$. In summary one has in the absence of residues

$$0 = \oint_{C^\pm} \frac{G^\pm(E')}{E' - E} \, dE' = \mathrm{P} \int \frac{G^\pm(E')}{E' - E} \, dE' \mp \mathrm{i}\pi G^\pm(E) \tag{3.42}$$

The above formula may then be split into real and imaginary parts $G^\pm = \mathrm{Re}\, G^\pm + \mathrm{i}\,\mathrm{Im}\, G^\pm$ so that one finds the Kramers-Kronig relations,

$$\mathrm{Re}[G^\pm(E)] = \pm\frac{1}{\pi} \mathrm{P} \int_{-\infty}^{\infty} \frac{\mathrm{Im}\, G^\pm(E')}{E' - E} \, dE' = \mathrm{P} \int_{-\infty}^{\infty} \frac{\rho(E')}{E - E'} \, dE' \,, \tag{3.43}$$

$$\mathrm{Im}[G^\pm(E)] = \mp\frac{1}{\pi} \mathrm{P} \int_{-\infty}^{\infty} \frac{\mathrm{Re}\, G^\pm(E')}{E' - E} \, dE' \,. \tag{3.44}$$

Using Eq. (3.43) we can obtain the real part $\mathrm{Re}[G^+_{\mathrm{RR,cut}}(E)]$ corresponding to the partial spectrum $\mathrm{Im}[G^+_{\mathrm{RR,cut}}(E)]$ . The entire projected Green's function $G^+_{\mathrm{RR,cut}}(E)$ is thereby determined in energy domain. Finally, after Fourier transformation one obtains the survival amplitude $S(t)$ and the mean lifetime $\tau$ of the resonance state can be extracted. Following this route was necessary to explore the evolution of strongly coupled sulfur 3p-resonances excited inside the surface of $TaS_2$ in Chapter 7.

**Resonance states**

To this end we have established the tools to extract lifetimes from heuristically determined resonances on adsorbates (by choosing a suitable projection), which are attached to infinite surfaces. However, a conceptual complication arises, when looking at the Schrödinger equation and the time evolution operator: a hermitian Hamiltonian operator does not admit solutions with an exponentially decaying behavior, since all eigenstates have real eigenvalues. Therefore in principle any eigenstate of the Hamiltonian must oscillate in time with a frequency given by its eigenenergy.

However, in analogy to the use of the Green's function in the surface region above a resonance state of the following shape may be defined

$$\phi_{\mathrm{G}} = \int \frac{1}{\mathrm{i}} \sqrt{\frac{\Omega}{\pi}} \frac{1}{E - E_{\mathrm{R}} + \mathrm{i}\Omega} \, |E\rangle \, dE \,. \tag{3.45}$$

This resonance state is normalized $\langle\phi_{\mathrm{G}}|\phi_{\mathrm{G}}\rangle = 1$ and the DOS in the substrate is considered to be flat, i.e., $\Delta(E) = \Omega$ and the energy shift $\Lambda(E) \approx 0$ to be negligible as in Eq. (3.39). The states $|E\rangle$ are the energy eigenstates belonging to the Hamiltonian of the infinite system (including the adsorbate, where the resonance is localized). Then, Eq. (3.45) does not describe an eigenstate of the (infinite) Hamiltonian in the regular sense, but rather an infinite combination over the continuum of energy eigenstates supported by the latter.

Using a test function $\langle\varphi|$ one can carry out the following steps [124]

$$\langle\varphi|\,\hat{H}\,|\phi_{\mathrm{G}}\rangle = \int \frac{1}{\mathrm{i}}\sqrt{\frac{\Omega}{\pi}}\frac{\langle\varphi|\hat{H}|E\rangle}{E - E_{\mathrm{R}} + \mathrm{i}\Omega}\,dE = \oint \frac{1}{\mathrm{i}}\sqrt{\frac{\Omega}{\pi}}\frac{z\varphi(z)}{z - E_{\mathrm{R}} + \mathrm{i}\Omega}\,dz \qquad (3.46)$$

$$= 2\sqrt{\pi\Omega}(E_{\mathrm{R}} - \mathrm{i}\Omega)\varphi(E_{\mathrm{R}} - \mathrm{i}\Omega) = 2\sqrt{\pi\Omega}\,\langle\varphi|\,(E_{\mathrm{R}} - \mathrm{i}\Omega)\,|E_{\mathrm{R}} - \mathrm{i}\Omega\rangle \quad (3.47)$$

$$= \langle\varphi|\,(E_{\mathrm{R}} - \mathrm{i}\Omega)\,|\phi_{\mathrm{G}}\rangle \qquad (3.48)$$

where $\langle\varphi|E\rangle = \varphi(E)$ is considered a well-behaving function. The integral above was evaluated closing a contour in the complex plane and applying the Cauchy integral formula. Similarly, one finds [124, 125]

$$\langle\varphi|\,\mathrm{e}^{-\mathrm{i}\hat{H}t}\,|\phi_{\mathrm{G}}\rangle = \langle\varphi|\,\mathrm{e}^{-(\mathrm{i}E_R - \Omega)t}\,|\phi_{\mathrm{G}}\rangle \qquad (3.49)$$

The resonance states $\phi_{\mathrm{G}}$ in Eq. (3.45) are sometimes called Gamow vectors and live on an extended (*rigged*) Hilbert space [124–126]. While they represent something like eigenstates of a hermitian Hamiltonian operating on an extended domain, they are not eigenstates in the regular sense, since the wave-packet in Eq. (3.45) consists of a continuum of energy eigenstates. The formulae, roughly outlined here, are not of immediate practical importance for this work but they do provide a consistent picture of decaying resonance states [cf. Eq. (3.49)] in connection with a hermitian Hamiltonian and complex eigenvalues [cf. Eq. (3.46)]. A rigorous introduction is beyond the scope, instead we refer to the literature by Bohm et al. [124, 125, 126].

# Chapter 4

---

# Experimental Determination of Lifetimes of Excited States

---

The realistic simulation of electronic lifetimes can only be ensured through independent experimental validation. The core-hole-clock provides an experimental technique capable of probing ultrafast charge transfer dynamics after electronic excitation with X-rays [18–21]. The method is based on a model that is used to analyze spectroscopic signatures in order to determine the lifetimes of excited electronic states. Core-hole-clock studies therefore provide an important experimental reference for the verification of the theoretically extracted lifetimes in this thesis. Conversely, the simulations presented in the following chapters may add to the interpretation of the experiments. In this chapter the basic principles behind the technique are introduced, while it is not intended to lay out any actual experimental realization. The limitations of the technique are discussed and a concise comparison to laser pump-probe approaches is drawn.

## 4.1.   A Primer on Core-Hole-Clock Measurements

The core-hole-clock technique is predominantly used to analyze data from resonant photoemission maps. A different approach, which utilizes resonant inelastic X-ray scattering is possible (see, e.g., Ref. [127]). The dominant processes in the recorded photoemission spectra are illustrated in Fig. 4.1. The figure comprises different types of Auger-like decays, shown schematically for an Argon adsorbate on a metal surface (see Chapter 6).

Initially, an electron is excited from a core-level into a bound unoccupied state under the absorption of an incident X-ray photon with energy $h\nu$. The excitation energies lie often in the range of soft X-rays (250–1000 eV). The initial excitation is shown in Fig. 4.1a for the electronic transition from the 2p core-level into the 4s-resonance below the vacuum level $E_{\mathrm{vac}}$. The transition happens at an element specific energy and follows dipole-selection rules. Subsequently, two distinct scenarios are possible. In one case the excited electron tunnels into the substrate and the core hole decays in a regular Auger process leaving the system in a two hole final state.

Tunneling into the substrate requires availability of empty DOS around the resonance energy above the Fermi level $E_F$ and sufficient overlap of the resonant state with the substrate. If the excited electron propagates into the substrate (or more generally the environment) one speaks of a delocalized channel (d-channel). The other possibility is that the electron remains initially on the excited atom. It may then either be involved as a passive spectator in a resonant Auger decay (Fig. 4.1c) or as an active participator in a resonant photoemission process (Fig. 4.1d). One speaks in the latter two cases jointly of a localized decay channel (l-channel) or sometimes of auto-ionization [21]. Other authors [22, 123] refer to the entire spectrum due to the processes in Fig. 4.1b-d as auto-ionization spectrum, which will be the nomenclature adopted here. The emitted electrons are collected by a detector quantifying the intensity and kinetic energy of the electrons. With the recorded data it is therefore possible to map out the intensity $I(E_{kin}, h\nu)$ of the electrons as a function of their kinetic energy $E_{kin}$ and the incident photon energy $h\nu$ in a two-dimensional plot. In a subsequent analysis the contributions from all the different decay processes can be disentangled by suitable fitting procedures. In principle, the spectroscopic signatures of the processes can be distinguished as will be pointed out below. Knowing the individual intensity contributions, it is possible to obtain information about the time-scales of the system specific electron dynamics.

Decays via the d-channel appear at constant kinetic energy independent of the photon energy. From the perspective of the Auger electron the information about the energy of the photon is lost during the injection of the excited electron into the substrate (where it is subject to various kinds of scattering processes). Therefore, the initial excitation and the subsequent Auger decay become mutually incoherent processes. Based on this phenomenology the overall decay is often described in an approximate two-step picture of the initial excitation and the subsequent normal Auger decay.

Under so-called Auger resonant Raman conditions the emitted electrons of the l-channel exhibit a linear dispersion of the kinetic energy with the photon energy in contrast to the d-channel,

$$E_{kin} = h\nu - E_B. \tag{4.1}$$

Here, the binding energies $E_B$ of the Auger emitted electron has been taken to be positive. Because of Eq. (4.1) one may equivalently read in literature that the l-channel appears at constant binding energies. The Auger resonant Raman conditions are fulfilled "if the bandwidth of the radiation source is notably narrower than the natural linewidth of the intermediate neutral excited state" [128]. Hence, under these conditions a two-step description of the l-channel is not possible. Excitation and de-excitation have to be interpreted as a single coherent process. Modern synchrotron light sources routinely operate under these conditions producing the described behavior.

Finally, the spectator contributions (resonant Auger) can be distinguished in general from the normal Auger decay, since due to the presence of a spectator electron the core-hole is screened in the subsequent decay. The spectator peak appears therefore blue shifted with respect to the Auger peak in experimental spectra. This is often referred to as spectator shift.
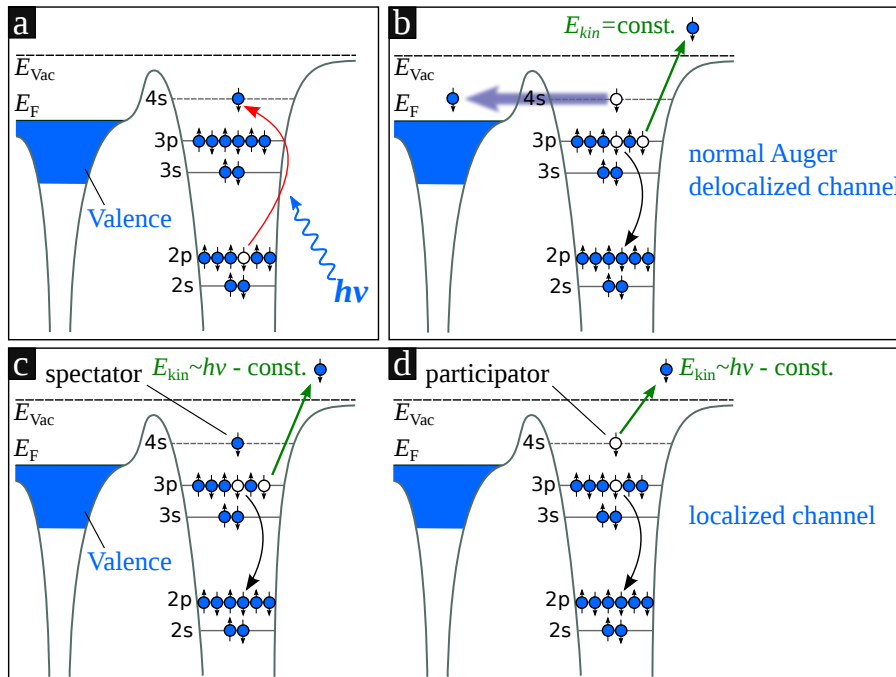
**Figure 4.1.:** Relevant processes in resonant X-ray photoelectron spectroscopy of Argon on a metal surface: (a) Initial excitation of a core electron under absorption of a photon. (b) Decay of the excited (intermediate) electron by tunneling into the substrate, followed by a normal Auger decay leaving the system in a two-hole state (delocalized channel). (c) The intermediate electron stays as a localized spectator during an Auger-like decay leaving the system in two-hole one-electron state. (d) The intermediate electron participates in the decay via resonant photoemission and is ejected. The processes in (c,d) are often referred to as decays via a localized channel.

Knowing the intensities of the separate processes they can be clocked against the lifetime of the core-hole to extract the charge transfer time. In principle this can be achieved using two different types of analysis outlined below. The first approach analyzes the spectrum of the entire localized channel including participant and spectator decays, while the second one is based exclusively on the analysis of participant decay [21].

## 4.1.1. Disentangling l-Channel and d-Channel

The core-hole-clock method is based on the assumption that the excited (intermediate) electron and the core-hole follow independently an exponential decay law. Hence, their populations $N$ obey the differential equation

$$\dot{N}(t) = -\frac{\Gamma}{\hbar} N(t). \tag{4.2}$$

The solution, normalized over all positive times, is the overall probability $P(t) = (\Gamma/\hbar)\mathrm{e}^{-\Gamma t/\hbar}$ of finding an electron in the excited state (or respectively a core-hole). Here $t$ is the time after the initial excitation. Using this assumption one can calculate the probability that a charge transfer happens before the core-hole decay

$$P_{\mathrm{ct}} = \lim_{t\to\infty} P_{\mathrm{ct}}(t) = \lim_{t\to\infty} \int_0^t \frac{\Gamma_{\mathrm{c}}}{\hbar} \mathrm{e}^{-\Gamma_{\mathrm{c}} t_2/\hbar} \int_0^{t_2} \frac{\Gamma_{\mathrm{ct}}}{\hbar} \mathrm{e}^{-\Gamma_{\mathrm{ct}} t_1/\hbar}\, dt_1\, dt_2 = \frac{\Gamma_{\mathrm{ct}}}{\Gamma_{\mathrm{ct}} + \Gamma_{\mathrm{c}}}, \tag{4.3}$$

where the decay of the core-hole was enforced by taking the limit of infinite times $t \to \infty$. The probability that the core-hole decays after charge is transfered is then $P_{\mathrm{c}} = 1 - P_{\mathrm{ct}}$ under the exclusion of other processes such as for example radiative decays (radiative decays are less likely for lighter elements).

The probability for charge transfer before a core-hole decay is then equal to the fraction of the d-channel intensity $I_{\mathrm{d}}$ in the overall spectrum

$$P_{\mathrm{ct}} = \frac{\Gamma_{\mathrm{ct}}}{\Gamma_{\mathrm{ct}} + \Gamma_{\mathrm{c}}} = \frac{I_{\mathrm{d}}}{I_{\mathrm{d}} + I_{\mathrm{l}}}. \tag{4.4}$$

In this picture the rates of the processes $\Gamma_{\mathrm{ct}} = \tau_{\mathrm{ct}}^{-1} = kI_{\mathrm{d}}$ and $\Gamma_{\mathrm{c}} = \tau_{\mathrm{c}}^{-1} = kI_{\mathrm{l}}$ are directly proportional to the measured intensities with a common overall proportionality constant $k$. If the core-hole lifetime $\tau_{\mathrm{c}}$ is known, one can find the charge-transfer time

$$\tau_{\mathrm{ct}} = \frac{I_{\mathrm{d}}}{I_{\mathrm{l}}} \tau_{\mathrm{c}}. \tag{4.5}$$

Here, it is assumed that the core-hole lifetime, is independent of the system under consideration. The value for the core-hole lifetime of the atomic species are usually taken from separate experiments. The decay of the core-hole acts then as an internal clock to the dynamics of competing processes. The approach described in this subsection was applied in the experiments of Blobner et al. [50] and Kühn et al. [52] which we refer to in our theoretical work in Chapter 6 and Chapter 7, respectively.

### 4.1.2. Comparing Participator Decay in Coupled and Uncoupled Systems

In some cases the evaluation of the charge transfer time is difficult using the prescription from the section above and instead a different approach is adopted. This is for example the case if the normal Auger channel cannot easily be distinguished from the l-channel [48, 129]. This can happen for example due to spectral overlap, e.g., if the Auger resonant Raman conditions are not met, or if the background in the spectra does not allow for an unambiguous disentanglement.

In such cases one may exclusively use the participator channel and compare a coupled and an uncoupled system. This can, e.g., be achieved in the case of organic molecules adsorbed on surfaces by comparing a monolayer and a multilayer. In the multilayer case the charge transfer from the molecules to the substrate is efficiently quenched due to the presence of the insulating layer of organic molecules between the absorbing outer layer of molecules and the substrate. Then, the probability that charge transfer happens before the core-hole decay is given by the reduction of the participator intensity comparing the coupled and the isolated system

$$P_{\text{ct}} = \frac{\Gamma_{\text{ct}}}{\Gamma_{\text{ct}} + \Gamma_{\text{c}}} = \frac{I_{\text{iso}} - I_{\text{coup}}}{I_{\text{iso}}}. \tag{4.6}$$

Since two separate measurements of different systems are compared, the intensities need to be normalized by a common reference. This is usually done by dividing the participator spectrum by the overall X-ray absorption spectrum (of the resonance of interest) for each system $I_{\text{coup/iso}} = I_{\text{coup/iso}}^{\text{participator}}/I_{\text{coup/iso}}^{\text{XAS}}$. This adds another complication to the experimental procedure apart from additional assumptions that are made implicitly. The first assumption being that the multilayer system is actually uncoupled from the substrate (i.e., the d-channel is quenched in the isolated system). Secondly, the l-channel must behave similarly in the respective isolated and coupled systems. In particular, the participator channel (in terms of it's matrix elements) should be largely unaffected when isolating the system in a multilayer setting. If these assumptions are fulfilled the charge transfer time is obtained by rearranging Eq. (4.6),

$$\tau_{\text{ct}} = \tau_{\text{c}} \frac{I_{\text{coup}}}{I_{\text{iso}} - I_{\text{coup}}}. \tag{4.7}$$

Such an approach was used by Schnadt et al. [48] to determine the charge transfer time from isonicotinic acid attached to rutile $TiO_2(110)$ as studied theoretically in Chapter 5.

## 4.2. Time Resolution and Applications

The time resolution of the core-hole-clock is limited by the lifetime of the core-hole in a way that the method is only applicable for charge transfer within roughly one order of magnitude deviation from the charge transfer time under investigation, $0.1\tau_{\text{c}} \leq \tau_{\text{ct}} \leq 10\tau_{\text{c}}$ [19].

The core-hole-clock has been used to probe dynamics in the femto-second regime [18] and even slightly below 1 fs charge transfer [130]. Later even faster charge dynamics in the attosecond regime were measured via so-called Coster-Kronig decay [22]. In this type of core-hole decay the hole is filled by an electron of the same shell, a process that is usually an order of magnitude faster than the ordinary decay of the same core-hole. In a fundamental proof of the method, by comparing Coster-Kronig decay and ordinary core-hole decay in one single system, charge transfer times have been shown to be independent of the "clock" taken as a reference [131].

A large number of systems have been studied and continue to be studied with the core-hole-clock up to date. This includes various investigations on organic/electrode interfaces [129, 132], dyes on bulk metals [133–135], and dyes on semiconducting rutile-$TiO_2(110)$ as present in many DSSCs [136–138]. Most recently, charge dynamics in the context of 2d-materials, like metal-adsorbed graphene monolayers [139], interfaces between, e.g., transition metal dichalcogenides (TMDs) and graphene [140, 141], or layered TMDs [142] are starting to be investigated. Along these lines we investigate in Chapter 7 the layered TMD 1T-$TaS_2$.

Moreover, the core-hole-clock has been used to investigate the dependence of interfacial charge injection on different physical aspects such as linker-sizes [143], bonding character [144, 145], and adsorption sites [132] of adsorbed molecules, or spin polarization [49–51] and orbital polarization [123, 131] of the intermediate state.

Recently, the investigation of bi-directional charge dynamics due to additional transfer of electrons in the opposite direction from the substrate to the adsorbate has raised attention [141, 146–148]. Such a scenario becomes possible if the core-hole attraction causes the lowest unoccupied molecular orbital (LUMO) of the studied adsorbate to shift partly below the Fermi level of a metallic substrate, thereby leading to its occupation. The occupation of the LUMO results then in so-called super-Auger or super-participator processes (such processes are summarized in Ref. 148).

## 4.3.   Relation to Laser Pump-Probe Spectroscopy

Although the core-hole-clock method is used widely to probe ultrafast time scales in the femtosecond regime and below, in particular, pump-probe techniques [13, 149–151] are developing fast and present an alternative providing in many ways a more direct access to the fast dynamics of electrons in adsorbates [152]. In such techniques similar to the core-hole-clock initially an electron is excited into an unoccupied state. However, in pump-probe experiments this is done with an incident light pulse of short duration (pump pulse). The system is then probed by a second beam of short duration, such that the temporal evolution of the excited electron can be monitored with photoemission, if the time delay between the two pulses is controlled. This technique is therefore called tr-2PPE.

Due to the additional experimental parameter of the time delay such approaches are often referred to as direct measurements in the time domain, while the core-hole-clock is sometimes seen as a stationary energy domain X-ray technique [153]. However, it has been mentioned by Menzel [154] that in principle the core-hole-clock could also be interpreted as a special type of pump-probe measurement, in which

a continuous light pulse excites the system and subsequently the core-hole decay probes the delocalization of the excited electron with an exponential distribution in the time-domain.

Up to recently tr-2PPE experiments with time resolutions in the femto- and attosecond regime were only realizable for photon energies below the ones of soft X-ray irradiation (optical excitations). These optical beams excite valence states and therefore also electrons from the environment, e.g., from the substrate. In those cases, the hole states are delocalized and evolve independently of the confined excited electrons on the adsorbate. When probing layers of adsorbates under optical excitations, even the final states spread out over the sample as they display a band-like character. Clearly, chemical selectivity is lost in these cases.

In core-spectroscopies, the hole and the excited electron are localized on a single adsorbate, even if dense layers are probed. Moreover, low intensity X-ray beams produce low concentrations of excitations in molecular layers, while the latter is different in laser-pumped systems, where high densities of coherently excited electrons may be present. Such a case corresponds to a collective excitation in contrast to the local character of the core-excitations.

Developments of novel X-ray sources based on free electron lasers are about to allow high time-resolution, low intensity X-ray pump-probe measurements and thus element specific access to electronic time-scales [155–158]. Actual evidence of this can already be seen [159]. Measurements using these novel techniques are expected to be directly comparable to core-hole-clock measurements, while not being constrained by the lifetime of the core-hole.

# Chapter 5

# Lifetimes of Molecular States at TiO$_2$ Surfaces

Titanium dioxide (TiO$_2$) exists abundantly on earth and appears as a component of a wide range of technological applications [160, 161]. Among these are optical and protective coatings, white colorants, and its use in electrical devices or gas sensors. The material's photocatalytic properties [162, 163] promise applications in solar fuel generation like water splitting [164] and in TiO$_2$-based DSSCs directly converting solar energy into electricity [5, 165]. These desirable clean energy applications make TiO$_2$ an extensively studied as well as widely reviewed material in the literature (see the mentioned exemplary references).

Bulk TiO$_2$ materializes predominantly in three structural phases: anatase, brookite, and rutile. All these phases feature large optical gaps at low temperatures with about 3.00 eV [166, 167] for rutile and 3.40 eV [167] for anatase, while for brookite various values up to 3.5 eV [168] (at room temperature) are reported. The thermodynamically most stable phase is rutile, whereas anatase and brookite are metastable undergoing a phase transition to the rutile structure at high temperatures [161]. While the bulk crystal structure of these phases is known, a precise knowledge of the atomic structure at surface terminations of TiO$_2$ is crucial to understand the microscopic processes taking place there. The (110) termination of rutile stands out as a heavily investigated [160], stable, low-index termination of crystalline TiO$_2$ [169, 170] and forms the basic substrate studied in this chapter.

Being a wide band gap material, TiO$_2$ is transparent for visible light and absorbs photons in the ultraviolet range. However, sunlight-driven applications require the absorption of light in the visible range, which is often achieved by depositing dye-molecules on the surface of TiO$_2$ —a process generally known as dye-sensitization. Upon irradiation by light the electrons in sensitized TiO$_2$ devices are excited across the HOMO-LUMO gaps [the electronic gaps between the highest occupied molecular orbital (HOMO) and the lowest unoccupied molecular orbital (LUMO)] of the chemisorbed dye-molecules. Subsequently, the excited electrons can be injected into the conduction band of the TiO$_2$ substrate, where they ideally separate from the left-behind holes before recombination occurs. This is the underlying principle of

charge injection in DSSCs [3–5].

In DSSC devices the injected electrons generate a current, which is converted into consumable electrical energy. Typically the surface ratio in such devices can be increased by employing porous TiO$_2$ electrodes in order to maximize absorption of photons. Due to the use of porous TiO$_2$ various facets of TiO$_2$ crystals coexist in actual devices and surface reconstructions, step edges, or defects (e.g., electron donating oxygen vacancies) may cause disorder at realistic surfaces.

We investigated in particular the formation of vacancies in the vicinity of step edges on rutile TiO$_2$(110) in connection with experiments on curved crystals of TiO$_2$. The results of this combined experimental and theoretical work are presented below (Section 5.1) in modified form[1]. This allows us to introduce the TiO$_2$ substrate which we discuss subsequently in connection with charge transfer dynamics at a prototypical DSSC interface.

The main focus of this chapter is on charge injection from localized states on molecules (isonicotinic acid) sensitizing rutile (110) surfaces, resembling the interface at an electrode inside a DSSC device. We seek to explore the effect of structural fluctuations at finite temperatures on ultrafast charge injection at the interface. This work was performed in direct comparison with available data from core-hole-clock spectroscopy [48]. Using the methodology to extract lifetimes as described in the introductory chapters and sampling the atomic motion at finite temperatures from a Car-Parinello molecular dynamics (CPMD) trajectory, we obtain a consistent description of the charge transfer at the interface in close agreement with the experiment. We discuss the effect of including a core-hole in our model and the role of the density of acceptor states for temperature broadened spectra. The corresponding part of this chapter (Section 5.2) reproduces our original publication in slightly adapted form[2].

Finally, we investigate the electron-phonon coupling of the molecular states of isonicotinic acid on TiO$_2$(110), to trace the influence of structural fluctuations on the interfacial level alignment back to specific vibrational modes. We find that modes stretching the carboxyl group anchoring the molecules to the surface have a dominant effect. Assuming similarly a linear relationship between the structure and the elastic linewidths determining the charge transfer does not allow to single out contributions from specific modes. We discuss the fluctuations of the energy levels in a semi-classical model of harmonic oscillators, rationalizing the Gaussian-type broadening of electronic spectra at finite temperatures.

## 5.1. Interplay Between Steps and Oxygen Vacancies on Curved TiO$_2$(110)[1]

Investigations of TiO$_2$ surfaces at the atomic level are of general importance to understand catalytic processes at these surfaces and to tailor devices through efficient interface engineering. Along this line, experiments on curved crystals in combination with first principles calculations are especially useful to study the formation and the

---

[1]Reprinted (adapted) with permission from [47]. © 2016 American Chemical Society.
[2]Reprinted (adapted) with permission from [171]. © 2018 American Chemical Society.
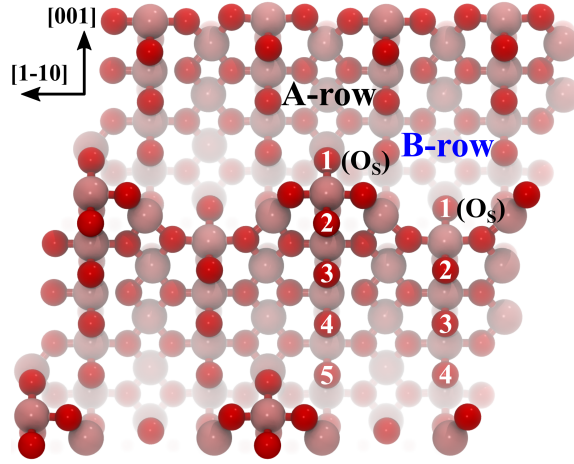
**Figure 5.1.:** Ball-and-stick representation of stoichiometric steps oriented along the [1-10] direction on a TiO$_2$ rutile (110) surface. The O atoms appear in dark red, while the larger Ti atoms appear in a lighter color shade. The image shows $2 \times 2$ computational cells as seen from the top. In our calculations we consider the formation of vacancies along the two rows of bridging oxygens O$_{br}$ and oxygens directly at the step O$_s$ (A-row: positions A1-A5 and B-row: positions B1-B4).

interplay of steps and defects on surfaces systematically.

A curved crystal constitutes a low index surface that has been rounded off along a particular direction. In this way, as one moves away from the center of the sample along the selected direction one enters surface areas that are subject to a larger miscut angle, i.e., corresponding to larger Miller indices. Cutting samples of TiO$_2$(110) in this fashion along the [001] direction leads to the formation of steps with a smoothly growing step density. The sample can subsequently be treated by a sputtering-annealing procedure to introduce oxygen vacancies on the surface. A sample generated in this way allows to investigate the interplay of oxygen vacancies with step-edges on TiO$_2$(110) in a unique fashion. To this end a combination of scanning tunneling microscopy (STM) and angular resolved photoemission spectroscopy (ARPES) measurements was carried out on curved TiO$_2$(110) crystals. The experimental results were obtained by our collaborators (cf. Ref. 47) and will be outlined here, while we concentrate on the theoretically obtained results.

In particular, STM measurements confirmed a smooth variation of the density of step edges on curved TiO$_2$(110) surfaces. Furthermore, step edges and oxygen vacancies can be linked to prominent features in the STM images: (**i**) Vacancies in the rows of bridging oxygens O$_{br}$ (see Fig. 5.1) appear as bright features on TiO$_2$(110) [172, 173] and (**ii**) intense triangular protrusions S$_t$ are characteristic of zigzag edges (cf. Fig. 5.1) of steps on rutile (110) [174].

It has been previously reported that mainly O$_{br}$ vacancies are responsible for the creation of gap states at TiO$_2$ surfaces [175]. These gap states effectively donate charge to the crystal thereby reducing the crystal (doping). Counting the number of O$_{br}$ vacancies and triangular protrusions S$_t$ in areas with varying step densities according to the STM images, reveals that the sum of both features correlates with

the corresponding intensity emitted from gap states in ARPES measurements. Since the measured ARPES intensity is nearly constant across the entire curved sample, both O$_{br}$ vacancies and triangular protrusions S$_t$ need to contribute in a similar way to the ARPES signal and therefore equally donate charge to the crystal doping.

The increasing number of triangular protrusions S$_t$ at higher step densities (going along with a decrease of O$_{br}$ vacancies in the middle of the terraces) points to either of two scenarios: Step edges induce gap states contributing to the crystal doping, while simultaneously the nominal concentration of oxygen vacancies is diminished at higher step densities. Or, vacancies tend to migrate towards the step edges, where they do not perceivably alter the appearance of triangular protrusions in the recorded STM images, but contribute to the crystal doping. As we will see in the following, the latter scenario is strongly supported by our DFT study of gap states at these stepped surfaces, formation energies of oxygen vacancies (Section 5.1.2), as well as simulated STM images (Section 5.1.3).

## 5.1.1.  Computational Setup

In our theoretical approach we assess the formation of O$_{br}$ vacancies in the vicinity of step edges through spin-polarized DFT as implemented in the SIESTA code [28]. We simulate monatomic [1-10] steps according to the model proposed by Luttrell et al. [174]. This type of step edges prevails at high step densities on TiO$_2$(110), as is evident from the recorded STM images [47]. A slab thickness of four oxide layers was employed, while also thinner slabs of three oxide layers were considered to estimate finite size effects (cf. Section 5.1.2). The width of the terraces in the supercell is visible in Fig. 5.1. All atomic positions in the slabs were relaxed using a conjugated gradient scheme with a force tolerance of 25 meV/Ang and a maximum atomic displacement of 0.1 Bohr between consecutive geometry optimization steps.

It is known that an incomplete cancellation of electronic self-interaction in semi-local GGA functionals often leads to a spurious spreading of otherwise localized states. This affects in particular the description of localized gap states stemming from oxygen vacancies at surfaces of TiO$_2$. Such spurious behavior of the gap states can be remedied to some extent using hybrid functionals [176]. Unfortunately, the increase in computational demand coming along with the use of hybrid functionals precludes their use in our current study considering the amount of calculations to be performed and the size of the supercells involved. A possible alternative description by DFT+$U$ methods comes at the expense of introducing an additional empirical parameter ($U$), which favors a localization of the excess electronic charge related to the Ti3d-flavored gap states [177]. Such DFT+$U$ calculations depend strongly on the choice of the $U$ parameter and have been reported to yield qualitatively different charge distributions related to the oxygen vacancy induced gap states in comparison with hybrid functional calculations [177]. Therefore, we opted, in spite of the mentioned short-comings, for employing the semi-local PBE functional [75] in our calculations. This functional has been previously used to simulate stepped stoichiometric surfaces TiO$_2$ [174, 178, 179]. We aim at studying the formation energies of vacancies at varying distances relative to the step edges, i.e., missing oxygens at the positions A1-A5 and B1-B4 in Fig. 5.1. We expect that the employed
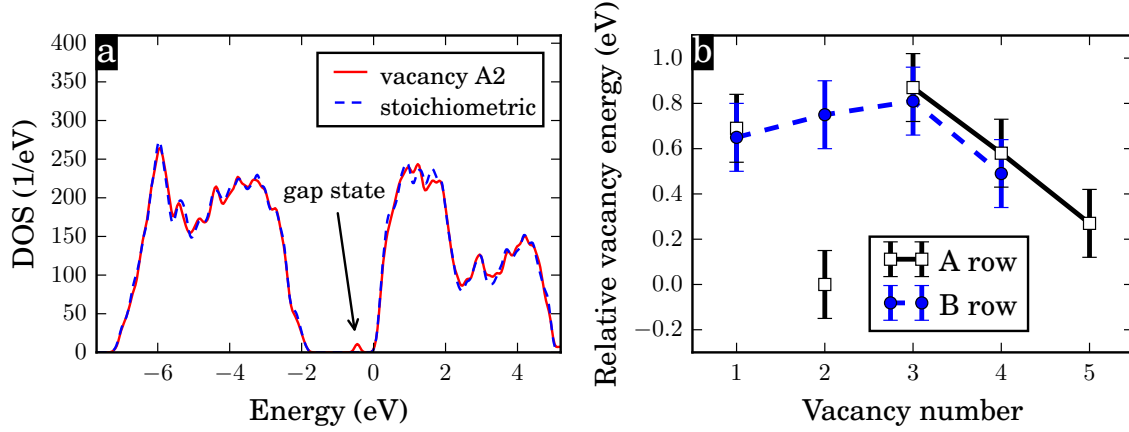
**Figure 5.2.:** Energetics of the vacancy formation at [1-10] steps on rutile TiO$_2$ (110): (a) Majority DOS related to stoichiometric steps and to steps containing a vacancy at the outermost position towards the edges (cf. position A2 in Fig. 5.1). (b) energies related to the formation of vacancies at different inequivalent oxygen positions in the A-row or B-row of oxygens (as specified in Fig. 5.1) inside the computational unit cell.

functional is capable of capturing the correct qualitative trends, which we assume to be governed by the variation of the release of strain for different vacancy positions.

Moreover, we employed norm-conserving Troulier-Martins-type pseudopotentials together with a double-$\zeta$ polarized basis of numerical atomic orbitals, which was generated by using a SIESTA-specific *EnergyShift* parameter of 100 meV. The electronic density was sampled on a real space grid with a fineness equivalent to a plane-wave cutoff of 200 Ry (*MeshCutoff* parameter) in order to compute the Hartree and exchange-correlation potentials. We used a $2 \times 2 \times 1$ Monkhorst-Pack k-point sampling [180] and an electronic temperature of 300 K. The SCF cycle was considered converged, as soon as changes in the elements of the density matrix did not exceed a tolerance value of $10^{-4}$.

### 5.1.2. Energetics of Vacancy Formation

To assess a potential doping of TiO$_2$ crystals by stoichiometric step edges on the surface we inspect the computed DOS plots shown in Fig. 5.2a. It is clearly visible, that stoichiometric steps do not induce any states inside the gap (blue dashed line), while on the contrary a vacancy at, e.g., position A2 (cf. Fig. 5.1) does introduce a state $\sim 400$ meV below the conduction band edge (solid red line) in our calculations. As one expects, both the gap and the distance of the vacancy state to the conduction band minimum are underestimated due to the use of semi-local DFT. Fig. 5.3 shows the DOSs around the edges of the conduction band related to single vacancies at different positions on the terraces (cf. Fig. 5.1, A1-A5 and B1-B4) of a four layer slab in the computational cell. Our analysis confirms that all gap states in our calculations carry a total spin moment of 2 $\mu_B$, where $\mu_B$ is the Bohr magneton. The peaks inside the gap are of Ti3d-type character and are derived from two flat defect bands. The
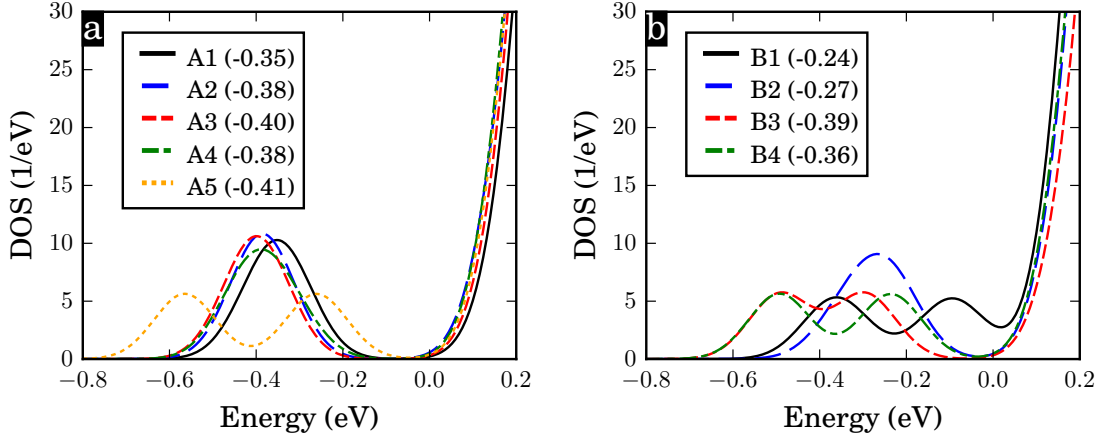
**Figure 5.3.:** Majority channel electronic DOS of [1-10] step edges on TiO$_2$(110) including a single vacancy at different positions inside the oxygen rows on one side of the slab. The subplots refer to vacancies located (a) inside the A-row or (b) inside the B-row as specified in Fig. 5.1. The bracketed values in the legend indicate the corresponding mean energy positions of the gap states with respect to the conduction band edge at the origin of the energy axis.

values in brackets inside the legend indicate the mean energy position of these peaks with respect to the conduction band minimum (the latter has been shifted to 0 eV, taking into account the electronic temperature of 300 K in our calculations). A clear dependency of the energy position of the gap state on the location of the vacancies cannot be stated at this point. The current set of calculations suggests, that the uppermost occupied state inside the gap is lower in energy for vacancies at the centers of the terraces (A3 and B3 in Fig. 5.3 a and b, respectively). However, owing to the possibility that the derived geometries correspond to local minima in the potential energy surface, further calculations are necessary to confirm this observation.

The absence of gap states on stoichiometric steps and the experimental finding that the sum of the O$_{br}$ vacancies and triangular protrusions S$_t$ correlates with the ARPES intensity from gap states, suggests that a migration of vacancies towards step edges takes place. To further investigate this presumption we examine the (relative) vacancy formation energies when moving the O$_{br}$ vacancy along the rows of the bridging oxygens on the surface. Here, a migration of vacancies towards step edges seems plausible, since the vacancies in the middle of terraces are less stable in our calculations. This can be read from the relative vacancy formation energies along the rows of the bridging oxygens in Fig. 5.2.

We considered in our calculations a single vacancy on one side of the slab in the computational supercell. However, this creates an asymmetry with respect to the two surfaces of the slab. To estimate the effect of this asymmetry we additionally conducted calculations with vacancies on both sides of the slab for the positions A1, A2, A4, A5 (cf. Fig. 5.1). Likewise, the finite size of the slabs in our model may affect the results. Therefore, we also conducted calculations with three layers in order to assess the corresponding errors. According to these tests we estimate an uncertainty of about ±50 meV. Additionally, some of our calculations were fairly sensitive
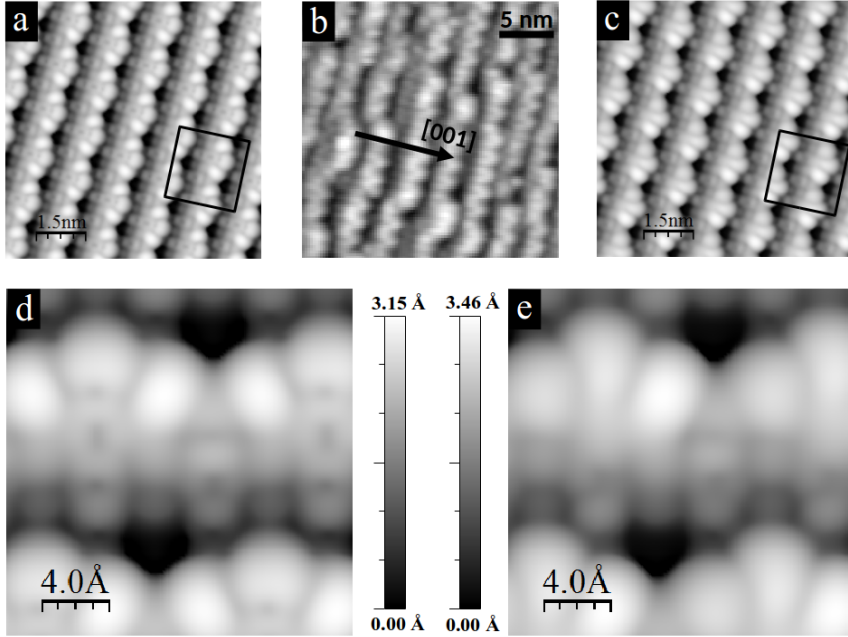
**Figure 5.4.:** Simulations of STM images according to the Tersoff-Hamann approach (a, c, d, e) in comparison with the experimental STM image (b) of tightly packed [1-10] steps on rutile TiO$_2$(110): (a, d) Simulation cell containing a single vacancy at the theoretically most stable position next to the step edge (position A2, Fig. 5.1) and (c, e) stoichiometric step edges. The figures (a, c) closely resemble the experiment (b) exhibiting the triangular protrusions S$_t$ characteristic of [1-10] edges. Even the corresponding zoomed sections (d, e) as indicated by black boxes in (a, c) are hardly distinguishable despite the missing oxygens in (d). The images were created using the WSXM tool [183] and the STM tool of the SIESTA package.

regarding the geometry relaxation of the structures, which sometimes converged to different minimum energy structures. This was in particular the case for the most stable vacancies at A2 or A5 positions. Based on these results we raised the overall error bars to an estimated ±150 meV.

These errors were consequently assigned to all values in Fig. 5.2. Accordingly, we read from Fig. 5.1 that the formation of a single vacancy at the upper edge of the step (position A2) is energetically most favorable, closely followed (with overlapping error bars) by the formation of vacancies at the lower edges of the steps (position A5, Fig. 5.1). In contrast, all other examined positions are substantially less stable. Hence, our calculations support a view in which vacancies tend to migrate towards [1-10] step edges, in line with a similar tendency for vacancy formation in the vicinity of [1-11] step edges [181, 182]. A migration of $O_{br}$ towards step edges might also explain why water molecules dissociate in an analogous way at oxygen bridging vacancies and at [1-10] steps in our experiments on reduced TiO$_2$ surfaces [47].

### 5.1.3. Appearance of Vacancies in Simulated STM Images

Overall, the absence of a doping effect by stoichiometric step edges in combination with a tendency of O$_{br}$ vacancies to form at step edges suggests that triangular protrusions in STM images are to a large extent populated by oxygen vacancies. On the other hand it has previously been demonstrated that triangular protrusions in experimental STM images are closely resembled by simulated STM images of stoichiometric step edges in the Tersoff-Hamann approximation [174]. This apparent inconsistency can be resolved, if the triangular protrusions in STM images containing a vacancy are not perceivably different from triangular protrusions due to stoichiometric step edges.

We investigate this presumption by carrying out simulations of constant current STM images within the Tersoff-Hamann approximation [184, 185]. In particular we simulate empty state imaging with energies up to 1.0 eV above the conduction band minimum, imitating the experimental bias voltage range from 0.7 V to 1.8 V. Both types of step edges in Fig. 5.4, the ones containing a vacancy (a) and the stoichiometric ones, closely resemble the experimental image (b). A zoom onto the single triangular protrusions S$_t$ in the images (d, e) further corroborates that the minor differences induced by missing oxygens at the step edges in Fig. 5.4d) do not alter the overall appearance of the protrusions.

We note that our STM simulations possibly underestimate contributions from the titanium rows on the surface, which are known to appear as bright lines in experimental STM images [160, 175]. Likely, this deficiency is due to the finite support of the numerical orbitals employed by the SIESTA code, which leads to a vanishing LDOS at realistic tip-to-sample distances in comparison with actual STM experiments. This deficiency can be cured by extrapolating the finite-ranged orbitals into the vacuum region starting from a plane above the surface using the STM tool of the SIESTA code. However, since it is difficult to define a plane with respect to the stepped surfaces, we performed the extrapolation starting from two different planes parallel to the corrugated surface. The final images in Fig. 5.2 were obtained as the average of the two extrapolations.

The pronounced contributions from the oxygens at the step edges in our STM simulations seem to mask the contributions of the titaniums. However, we do not expect that possible additional weight from the titaniums will alter our observation that missing oxygens at step edges have a negligible effect on the appearance of the STM images. The latter is unlikely, since the signatures of triangular protrusions are predominantly due to twofold coordinated oxygens at the step edges [174].

### 5.1.4. Conclusion and Outlook

In this section we described theoretical calculations of [1-10] step edges and O$_{br}$ vacancies on TiO$_2$(110) and the implications of our results for corresponding curved crystal experiments. In particular, our findings strongly suggest that stoichiometric step edges do not introduce additional states inside the electronic gaps of TiO$_2$(110) and therefore are not donating excess charge to the crystal. Instead our results indicate that oxygen bridging vacancies tend to migrate to the edges of the steps,

where they contribute to the reduction of the crystal. This appears plausible, since the corresponding triangular signatures of such reduced step edges in STM images appear unaltered with respect to the ones from stoichiometric step edges, as backed by our Tersoff-Hamann simulations of STM images.

These findings provide a possible explanation for a similar tendency of water molecules to dissociate at step edges or at $O_{br}$ vacancies on reduced $TiO_2(110)$ surfaces (as observed in the experiments [47]). Presumably, this is due to the presence of $O_{br}$ vacancies at the step edges and not due to an intrinsic reactivity of the $O_s$ atoms at these edges (cf. Fig. 5.1). However, we believe further investigations are necessary to substantiate this interpretation.

## 5.2. Effect of Structural Fluctuations on Elastic Lifetimes of Adsorbate States: Isonicotinic Acid on Rutile(110)[3]

After the introductory discussion about steps and vacancies on $TiO_2(110)$, we turn now to the study of dye-molecules attached to perfect $TiO_2(110)$ surfaces. Making use of the methodology introduced in Chapter 3 we investigate how structural disorder caused by temperature influences charge transfer at the interface.

We sample *ab initio* molecular dynamics trajectories to address the impact of structural fluctuations on elastic lifetimes of adsorbate states at room temperature focusing on heterogeneous charge injection from isonicotinic acid as a key anchoring unit in dye-sensitized energy devices. Complementing related theoretical studies, we employ a Green's function technique based on density functional theory to account for a fully semi-infinite substrate of rutile $TiO_2(110)$. We address the effect of a core-excitation enabling direct comparison with soft X-ray experiments. We find that room temperature fluctuations drastically improve the agreement with experimental lifetime measurements while the core-hole plays an important role shifting the spectra and reducing the electron vibrational coupling of the adsorbate states. Ultimately, the emerging resonance spectra highlight the role of the continuum of acceptor states in temperature broadened Voigt-type profiles.

### 5.2.1. Introduction

Ultrafast electronic processes at surfaces are at the heart of many applications in photochemistry, catalysis, and molecular electronics. After an initial excitation by light, ultrafast electron transfer takes place during generation of solar fuel, [2] as well as from photo-excited dyes towards semiconducting substrates in DSSCs [3–5]. Although the original design of the DSSC has been challenged in recent years by perovskite-based solar cells, [186, 187] electronic charge injection remains the basic physical process behind these sunlight harvesting energy devices.

Among a variety of candidates, isonicotinic acid is a common anchoring unit in DSSCs as, for instance, in the high-performing N719-dye [188]. Isonicotinic acid has

---

[3]Reprinted (adapted) with permission from [171]. © 2018 American Chemical Society.

been investigated extensively, from an experimental and theoretical point of view. In particular many studies have examined isonicotinic acid on different facets and structural phases of TiO$_2$, which is the preferred material for the anode of DSSCs due to its stability, high mobility, mesoporous structure and high availability.

A series of core-spectroscopy studies by Schnadt *et al.* [48, 189–192] investigated the structural and electronic properties of mono- and multilayers of isonicotinic acid on rutile TiO$_2$(110). Using core-hole-clock spectroscopy, [19, 21, 154] they extracted electron injection times from core-excited isonicotinic acid (identified as LUMO+2) into the substrate at an ultrafast time-scale below 5 fs at monolayer coverage [48]. The employed core-hole-clock technique can be pushed to measure charge-transfer times in the attosecond domain [22].

From a theoretical point of view, the calculation of charge-transfer times from adsorbates has been approached using different techniques [34, 36, 193]. For example, starting from standard DFT calculations, Fermi's golden rule was used to estimate charge-transfer rates from the computed Hamiltonian matrix elements between the extended states in the substrate and the localized states in the adsorbate. In principle, the relatively short range of these interactions (proportional to the overlaps between adsorbate and substrate wave functions) can be exploited to design efficient algorithms to screen dyes for optimal charge injection [193] as carried out by Martsinovich and Troisi [194]. These authors estimated lifetimes below 1 fs for isonicotinic acid in its equilibrium geometry (no core-excitation included) on rutile (110) and on anatase (101) [194].

While the calculations described above analyze static structures, some groups have already tried to incorporate the effect of temperature on the electron injection process. This has been done at different levels of theory. For example, Prezhdo *et al.* [195–197] have used a combination of non-adiabatic molecular dynamics based on fewest switches surface hopping [198] and DFT. Employing this technique they found for the LUMO of isonicotinic acid on rutile (110) at 50 K a lifetime of 28 fs averaging over 10 different trajectories [199]. In a subsequent work using a derivative of isonicotinic acid functionalized with silver cyanide, they found that the lifetime of the LUMO dropped to 5 fs when the temperature was increased to 350 K and 100 initial configurations were considered. Although it is difficult to obtain a precise picture of the effect of temperature from these simulations, since the data are not directly comparable (different derivatives and statistics are used), the authors make the interesting observation that the increased transfer rate is mostly due to adiabatic effects.

Batista *et al.* [200, 201] studied the effect of thermal fluctuations, focusing on the case of catechol on anatase (101). They used *ab initio* molecular dynamics to generate trajectories at a given temperature in combination with extended Hückel theory to model the electron dynamics along the trajectory. They found lifetimes of the LUMO around 38 fs at 0 K, [200] while an ensemble average of fixed initial configurations from a trajectory at 300 K reduces the injection time to about 6 fs [200]. Additional non-adiabatic effects due to nuclear motion during electronic decay lead to further reduction of the lifetime to about 2.5 fs [201]. This observation seems consistent with the one mentioned above concerning the relative importance of adiabatic and non-adiabatic effects. After the ultrafast initial injection to an interfacial charge state,

Batista *et al.* also followed the delocalization of the electron into extended substrate states.

The approaches mentioned so far treat the ions as classical particles, which is usually necessary for such complex systems. However, there have been model calculations that use a full quantum treatment to study electron dynamics at the DSSC interface [202–205].

Along similar lines, in this work, we investigate the elastic lifetimes of the frontier orbitals of isonicotinic acid on rutile $TiO_2(110)$ in the presence of structural fluctuations by sampling static nuclear configurations from *ab initio* molecular dynamics at room temperature [206]. Thereby we extended previous work considering the equilibrium structure (0 K) [36] to include the effect of temperature. This approach does not include non-adiabatic effects explicitly. However, the sampling of the configurational space at a given temperature is included. Such sampling has been identified as a key ingredient to determine the temperature dependence of charge-transfer rates. The adopted Green's function technique improves the description of the electronic structure of the substrate over that provided by finite slabs and cluster models [34, 36]. Thus, our method is suitable to describe charge-transfer into fully delocalized states in the substrate. Additionally, and importantly, we include a core-hole in our simulations to obtain charge-transfer rates comparable with core-hole-clock experiments by Schnadt *et al.* [48]

We performed a detailed analysis of the cumulative theoretical spectra. Our results indicate that the inhomogeneous broadening due to the fluctuating energy positions of the resonances is not sufficient to explain their shapes. It is crucial to take into account the variation of the average elastic width with energy. The latter reflects the energy dependence of the density of states in the substrate.

The presentation of the results below is organized in two parts, the first considering the adsorbate in its electronic ground-state and the second the core-excited case.

## 5.2.2. Computational Methods

In this work we analyze the effect of thermal structural fluctuations on the elastic linewidths of the molecular resonances. We access a set of structures representative of the configurational space sampled by the adsorbed molecule at finite temperature. Extending our previous study for the equilibrium configuration, we consider a number of snapshots generated along a previously calculated CPMD trajectory [206] of isonicotinic acid ($C_5H_4NCOOH$) adsorbed on rutile (110). The CPMD trajectory was computed at a constant temperature of 300 K using a Nosé thermostat, a slab containing four $TiO_2$ trilayers, a $3 \times 2$ $TiO_2$ supercell in the lateral directions and one molecule per supercell adsorbed on one of the surfaces of the slab. The trajectory covers 10 ps after an initial equilibration period of 2 ps. As described in detail in Appendix C.1, we devise a matching procedure that allows us to model an infinitely extended $TiO_2$ substrate starting from the finite-slab CPMD geometries.

In the present work we have selected a total of 161 snapshots (at a constant sampling rate of one frame every 62.5 fs) and recomputed electronic structure of each configuration using the SIESTA/TranSIESTA package [28]. As a first step, for each original structure we generated a new structure employing the above mentioned
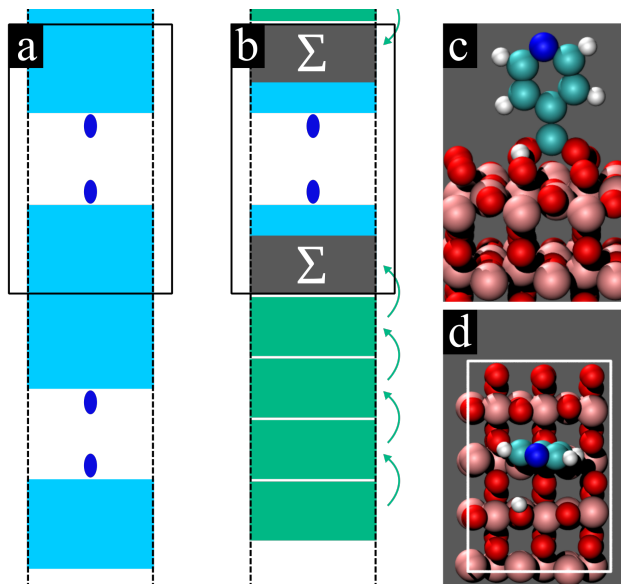
**Figure 5.5.:** (a) As described in the text, a symmetric slab containing nine TiO$_2$ trilayers plus one adsorbate in each surface is constructed starting from selected snapshots of the CPMD simulation in Ref. 206. (b) The coupling of the structure to a semi-infinite bulk support is included in the Green's function of the central region via self-energies $\Sigma$. Blue ovals represent adsorbates, light blue areas stem from finite slab calculations, while green areas refer to bulk calculations. The self-energies due to the bulk are added to the slab in the $\Sigma$-regions. The coupling of the adsorbed isonicotinic acid to the continuum of states in rutile(110) yields then the lifetime broadening. (c) Side view and (d) top view of the system. The black and white boxes refer to the computational unit cell.

matching procedure (described in Appendix C.1). The idea is to construct geometries with a larger number of layers and approaching the perfect bulk phase inside the material. This is necessary to provide a smooth connection with the self-energies that describe the semi-infinite TiO$_2$ substrate in our Green's function technique. In the final geometries only the two outermost trilayers of TiO$_2$ and the adsorbate move according to the original CPMD simulation. Hence, the third trilayer provides a smooth transition to the fixed bulk configuration, that is assumed in the inner layers. To cancel spurious dipoles the final slab is symmetrical and contains nine TiO$_2$ trilayers in total. Periodic images are separated by at least 24.4 Å of vacuum in order to avoid interaction between replicas. This setup is illustrated schematically in Fig. 5.5a, while Fig. 5.5c, d shows the details at the organic-semiconductor interface.

Our SIESTA calculations utilized a double-$\zeta$ polarized basis set of numerical atomic orbitals [104] to expand the wave functions, whose radii were determined using a 100 meV *energy shift* [28]. The exchange-correlation functional by Perdew, Burke and Ernzerhof [75] was employed in combination with norm-conserving Troullier-Martins pseudopotentials [109] to perform closed shell simulations (a separate discussion about the influence of spin for the core excited case can be found in Ap-

pendix C.5, where we show that the explicit inclusion of the spin degree of freedom does not alter our conclusions). We used $3\times2\times1$ k-point sampling and a mesh cutoff value of 250 Ry, respectively, for the reciprocal and real-space grids. A tolerance of $10^{-4}$ was used for the changes of the density matrix in order to stop the self-consistent cycle.

In a final step we include the coupling of the scattering region (enclosing the decorated surfaces) to the fully semi-infinite $TiO_2$ support (Fig. 5.5b) in an embedding approach [207–209]. The coupling is accurately simulated inside the scattering region by adding self-energies ($\Sigma$) due to the semi-infinite substrate (Fig. 5.5b) that connect to four trilayers (layers 3 to 6) of the initially calculated nine-trilayer slab. We use the Green's function procedure implemented in the TranSIESTA transport code [117]. The $TiO_2$ electrode was defined using $1\times2\times4$ bulk unit cells with a k-point sampling of $9\times2\times2$. To compute the Green's function an imaginary part of $\eta =0.02$ eV was added to the energies.

The Hamiltonian and self-energy matrices coming from bulk calculations (green areas, Fig. 5.5b) and slab calculations (light blue areas, Fig. 5.5a) were aligned at a common reference to correctly include the coupling to bulk $TiO_2$ in the Green's function procedure. This is important, since the Fermi level commonly used to align transport calculations for metallic systems cannot be used for calculations of semiconducting materials, which produce in practice arbitrary positions of the Fermi level inside the electronic gap. Additionally, the zero of potential in periodic systems is known to be arbitrary [210]. To overcome both issues, the energy levels of bulk and slab calculations were aligned at the Hartree potential of the bulk $TiO_2$ assuming that the bulk value of the Hartree potential is reached deep inside the slabs. We determine the macroscopically averaged Hartree potentials applying the smoothing method of Junquera *et al.* [211, 212] in the direction perpendicular to the surface. Subsequently, the two values are aligned at the transition towards the bulk region, making the bulk DOS a common energy reference for all calculations. Such a common reference also enables the comparison of peak positions from different snapshots. For plotting purposes, the origin of the spectra was shifted to the valence band maximum (VBM) of bulk $TiO_2$. This appeared to be a reasonable choice since the total DOS of the 9 trilayers and symmetrically attached adsorbates only showed small fluctuations of the VBM across different snapshots of the CPMD simulation.

We extract (resonant) elastic lifetimes of initial wave-packets derived from single molecular orbitals (MOs) of isonicotinic acid following the procedure in Refs. 34, 35 and extensions to MOs in Refs. 36, 147. For the calculation of the MOs the hydrogen atom dissociated upon adsorption is added back to the molecule in order to saturate free bonds. The reference wave-packet $\Phi$ is then obtained by setting the basis set coefficients related to the added hydrogen to zero and normalizing. This is expected to give good results as the coefficients for the hydrogen atom's orbitals are negligible for the MOs of interest here [36]. We subsequently calculate the projected density of states (PDOS) on the reference wave-packets [cf. Eq. (3.39)]:

$$\rho_\Phi(E) = -\frac{1}{\pi}\,\mathrm{Im}\left[\int\int \Phi^*(\mathbf{r})G(E,\mathbf{r},\mathbf{r}')\Phi(\mathbf{r}')d\mathbf{r}d\mathbf{r}'\right] \approx \frac{1}{\pi}\frac{\Omega}{(E-E_R)^2+\Omega^2}, \quad (5.1)$$

where $G(E,\mathbf{r},\mathbf{r}')$ is the Green's function of the scattering region. The resulting spec-

tra are fitted in an energy window of $\pm 0.8$ eV around their maxima by a Lorentzian function with a proportionality coefficient, and the resonance energy $E_R$ and the full width at half maximum of $2\Omega$ as fitting parameters. The elastic linewidth $\Gamma$ of the resonance is extracted as $\Gamma = 2(\Omega - \eta)$ considering that the Green's function was calculated at an imaginary energy $E + i\eta$. We found that the use of $\eta = 20$ meV is sufficient to determine the linewidth of narrow peaks within an accuracy of $\sim 1$ meV (for a more detailed discussion on this issue please refer to Appendix C.2). Employing the uncertainty relation we obtain the lifetime $\hbar/\Gamma$ ($\hbar = 658.21$ fs $\cdot$ meV in the relevant units).

In CPMD simulations ionic and electronic degrees of freedom are strictly separated due to the Born-Oppenheimer approximation. Non-adiabatic effects such as electronic transitions caused by ionic movement are hence explicitly excluded. As a result the electronic properties are governed by the electronic structure at every instance of time. In that spirit, considering a Lorentzian line shape as in Eq. (5.1) implies that the populations of the instantaneous initial states $P(t)$ decay exponentially with time. In regions of strong coupling, where deviations from the Lorentzian line shapes occur, we still expect that the width will give a reasonable estimate of the time scale for charge transfer (for further discussion of the fitting procedure refer to Appendix C.2). The dependence on temperature is then included in the statistical ensemble $\langle P(t)\rangle = \langle \exp(-\Gamma t/\hbar)\rangle$, where $\langle \dots \rangle$ denotes the arithmetic average over all snapshots. This model is well-placed for fast processes, where the structural configuration remains virtually unchanged, while the electron is transferred. For larger charge transfer times the expression becomes approximate [213]. To simplify the forthcoming discussion, unless otherwise stated we approximate $\langle P(t)\rangle \approx \exp(-\langle\Gamma\rangle t/\hbar)$, where $\hbar/\langle\Gamma\rangle$ plays the role of an approximate average lifetime. The limit to this approximation is discussed at last.

To compare our simulations with core spectroscopy experiments, we effectively introduce a core-hole in our calculations by reducing the occupation of the 1s state of the nitrogen atom during the construction of the pseudopotential. In the slab calculations this core-hole is neutralized by adding back the removed electron to the valence. The model represents a metastable situation with a strongly localized hole on the nitrogen 1s level, and an electron has been excited into a molecular resonance. The transfer of this electron into the TiO₂ support is the main process whose time-scale we aim to study.

## 5.2.3. Elastic Lifetimes in the Electronic Ground State

We start by analyzing isonicotinic acid adsorbed on rutile (110) in its electronic ground state. The corresponding spectra computed according to Eq. (5.1) are presented in Fig. 5.6. To investigate the dependency of the elastic linewidths on the adsorption and molecular geometry we calculated the projections of the Kohn-Sham DOS onto the adsorbate states ranging from the HOMO-1 to the LUMO+2 at different snapshots along a CPMD simulation at a constant temperature of 300 K, as well as in the equilibrium geometry. The latter case is shown in Fig. 5.6a, and Table 5.1 presents the corresponding extracted linewidths $\Gamma_{\text{eq}}$ and peak positions of the molecular resonances $E_R$. These values are in good overall agreement with previously

reported values by Fratesi *et al.* [36] (shown in brackets). The observed deviations are attributed to the larger unit-cell in the present calculations ($3\times2$ instead of $3\times1$). Another difference with respect to the model in Ref. 36 lies in the chosen adsorption site for the dissociated hydrogen, that is put closer to the molecule in the current work, following the CPMD study [206]. However, we explicitly checked that this choice has negligible effect on the reported results.

We now compare the case of the equilibrium structure with instantaneous snapshots from our CPMD simulation. We sample the 10 ps trajectory taking 161 snapshots after an initial equilibration time of 2 ps. Under the effect of temperature the resonance peaks move around their equilibrium positions and relative to the DOS of the bulk $TiO_2$ (Fig. 5.6b). The overall picture suggests a correlated motion of the energy position of the different levels across time (peak ordering and distances between peaks tend to keep constant), although deviations from a rigid shift can be observed. In Fig. 5.6b it is visible that the HOMO lies within the band gap for most of the snapshots. Just in a few cases it is severely downshifted, which is most clearly seen in Fig. 5.7. The LUMO splits into two peaks corresponding to a bonding (lower energy peak) and an antibonding (higher energy peak) interaction with the substrate [36]. This is particularly apparent for the equilibrium geometry as shown in Fig. 5.6a. For most of the snapshots the bonding component of the LUMO melts into an extended tail towards the edge of the conduction band of the $TiO_2$ substrate and it does not give any distinct peak in the cumulative spectrum in Fig. 5.6c. Contributions to the spectrum from the antibonding part dominate the LUMO's PDOS, and the reported values in Table 5.1 and Fig. 5.7 correspond to this antibonding peak. The LUMO+1 is uncoupled from the substrate in the equilibrium geometry and structural fluctuations preserve the single peak shape, only causing a small increase in width. Peak broadening during the dynamics is also visible in the case of the LUMO+2, where already at the equilibrium structure coupling to

**Table 5.1.:** Computed values of the linewidths $\Gamma_{eq}$, associated lifetimes $\hbar/\Gamma_{eq}$, and resonance positions $E_R$ of the molecular states at the equilibrium adsorption geometry. These values are to be compared with the corresponding averages obtained using the structures visited during the CPMD trajectory: Mean energy positions of the molecular resonances $\langle E_R \rangle$ and their standard deviations $\sigma(E_R)$, average linewidths $\langle \Gamma \rangle$ and their relative standard error $\delta(\langle \Gamma \rangle)$, lifetimes $\hbar/\langle \Gamma \rangle$. The values for the equilibrium adsorption shown in brackets are taken from Ref. 36. All quantities are further defined in the text. All energies are referred to the VBM of $TiO_2$.

| | equilibrium (0 K) | | | thermal average (300 K) | | | | |
|---|---|---|---|---|---|---|---|---|
| | $E_R$ (eV) | $\Gamma_{eq}$ (meV) | $\hbar/\Gamma_{eq}$ (fs) | $\langle E_R \rangle$ (eV) | $\sigma(E_R)$ (eV) | $\langle \Gamma \rangle$ (meV) | $\delta(\langle \Gamma \rangle)$ (%) | $\hbar/\langle \Gamma \rangle$ (fs) |
| HOMO | 0.27 | 0 (0) | $\infty$ ($\infty$) | 0.27 | 0.45 | 11 | 43 | 62 |
| LUMO | 3.53 | 218 (186) | 3 (4) | 3.47 | 0.30 | 280 | 5 | 2 |
| LUMO+1 | 4.61 | 1 (0) | 657 ($\infty$) | 4.61 | 0.27 | 6 | 10 | 105 |
| LUMO+2 | 5.93 | 35 (15) | 19 (44) | 5.83 | 0.29 | 57 | 5 | 12 |
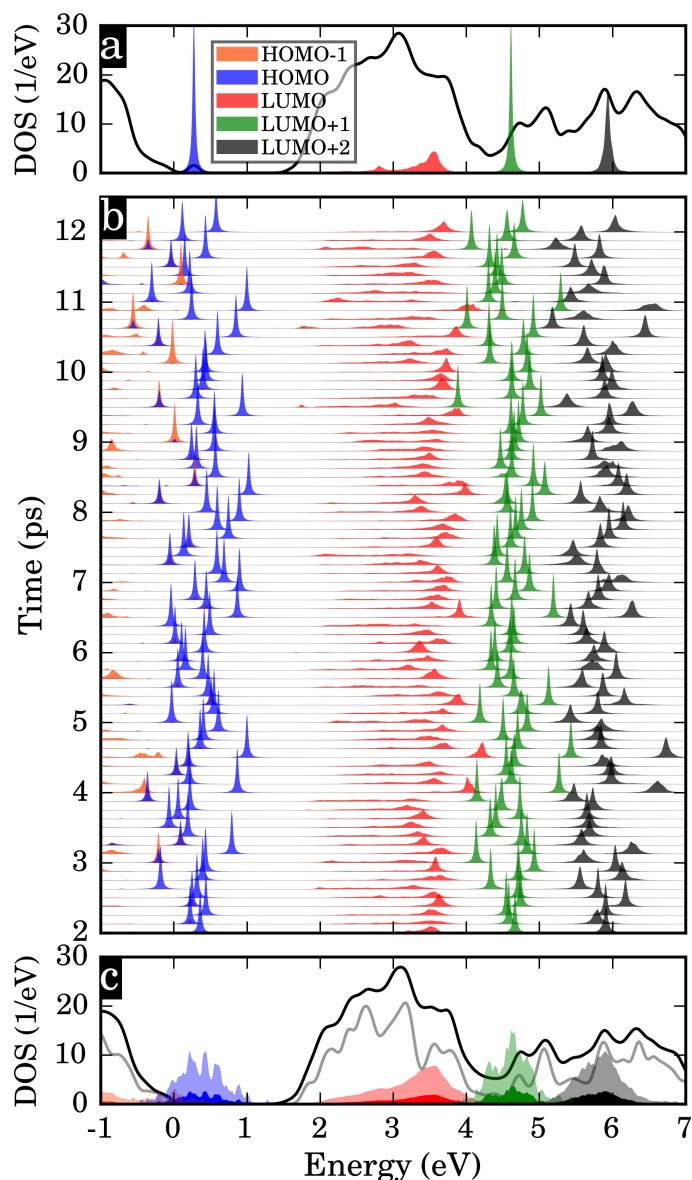
**Figure 5.6.:** Density of states projected onto the frontier orbitals (HOMO-1 up to LUMO+2) of isonicotinic acid [Eq. (5.1)]: (a) Spectrum for the equilibrium structure. (b) 81 snapshots during 10 ps of the CPMD at 300 K (every second snapshot of the full sampling shown). (c) Cumulative spectra after averaging all 161 snapshots (colored areas), additionally repeated after rescaling ($\times 4$) to facilitate visualization (light shaded areas). Black lines in (a) and (c) show the DOS ($\times 0.14$) from finite slab calculation. The gray line in (c) shows the bulk TiO$_2$ DOS ($\times 0.6$). The origin of all the spectra was shifted to the VBM of the bulk DOS as a common energy reference.

the substrate yields a finite width. Strong couplings to the substrate for distorted configurations induce additional deviations from the Lorentzian line-shape as visible in several snapshots in Fig. 5.6b.

In spectroscopy experiments probing the density of states under typical conditions, thermal averages of spectra are recorded. Even at zero temperature such spectra usually correspond to an ensemble of different structures, as the configuration may vary from molecule to molecule. In analogy to such experiments we average our set of calculated spectra from different snapshots. The resulting cumulative spectra are shown in Fig. 5.6c. While the finite sampling still leads to spiky features for the weakly interacting HOMO and LUMO+1 states (reflecting the need of a larger statics), for the more strongly coupled LUMO and LUMO+2 the spectra approach a smooth profile. Regarding the LUMO resonance, its bonding component is smeared out in the cumulative spectrum reducing the possibility of a separate experimental measurement of its lifetime at room temperature, as was suggested for the zero temperature case [36]. We note that the width of the peaks in the cumulative spectrum cannot be directly related to electronic charge-transfer times, as the latter depend on the instantaneous electronic couplings, while the former are dominated by the fluctuations of the MO energies at room temperature. Hence, thermally broadened spectra do not provide direct access to electronic lifetimes. Instead, more sophisticated experimental techniques such as the core-hole-clock method or high resolution pump-probe experiments are required.

For a quantitative statistical analysis, we examine the mean value $\langle E_R \rangle$ of the MO resonance positions $E_R$ and its standard deviations $\sigma(E_R)$. All extracted values are listed in Table 5.1. A binning procedure allows us to analyze the distribution of $E_R$ during the dynamics, as reported in Fig. 5.7c. The number of sampled configurations is sufficient to approximately reproduce a Gaussian shape of the distributions. As expected, the thermal averages $\langle E_R \rangle$ are found to be in close agreement with the peak positions in the equilibrium geometry $E_{R,\text{eq}}$. However, the spreads of the values of $E_R$ are relatively large, as evidenced both by the plot in Fig. 5.7c and by their standard deviations $\sigma(E_R)$ that reach about 0.3 eV (even 0.45 eV for the HOMO). Overall, the size of the fluctuations in our study is consistent with observations in related works. For example, Prezhdo and coworkers find slightly smaller energy fluctuations at 50 K for the evolution of the excited state (state with the highest occupation after initial filling of the Kohn-Sham LUMO) in non-adiabatic molecular dynamics simulations of isonicotinic acid on rutile (110) [199]. Furthermore, for a structurally strongly related compound (consisting of isonicotinic acid with an added AgCN group) on $TiO_2$ they report an energy range of up to 1 eV for the resonance position at 350 K [214]. Similarly, for alizarin on $TiO_2$ they report a standard deviation of 0.39 eV [165, 215] at ambient temperature.

To further assess the statistical distribution of the resonance positions $E_R$ we compare the results for the HOMO with those related to the highest occupied electronic state following its evolution during the CPMD simulation, where more than 5000 steps were recorded. A Gaussian-like distribution is even more apparent in the latter case, as can be seen from the histogram in Fig. 5.7c (to facilitate comparison to the other plots, its area is also normalized to $N = 161$). It is interesting to see that the position and shape of both distributions is very similar. Indeed, we can see that the
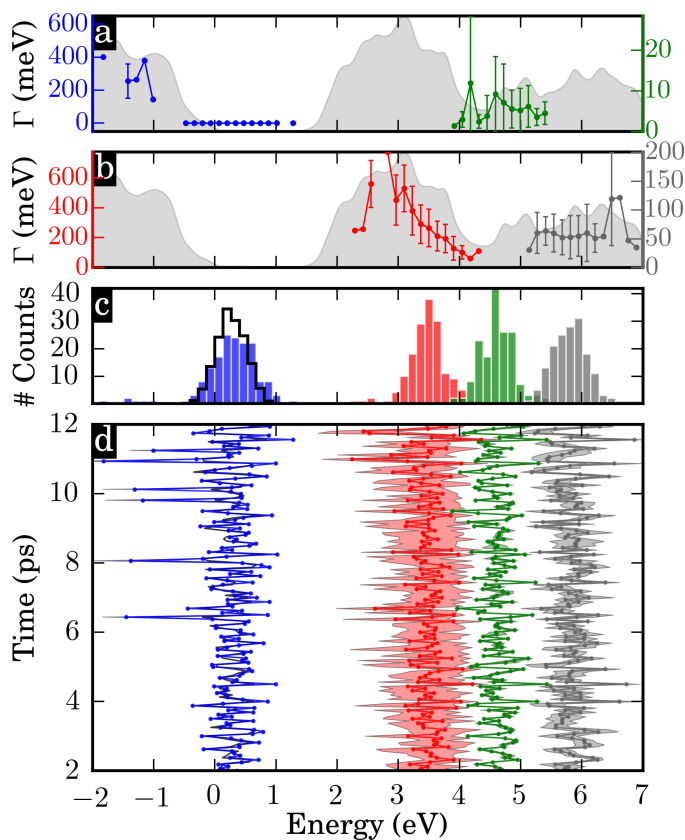
**Figure 5.7.:** Fluctuations of the positions and widths of the molecular resonances for 161 snapshots of the CPMD trajectory. The values were extracted from a Lorentzian fit to the PDOS of the frontier orbitals of isonicotinic acid (cf. Fig. 5.6b): (d) Evolution of the peak positions. Shaded areas indicate the corresponding widths ($\sqrt{\Gamma}$ plotted instead of $\Gamma$ to make small changes in the width more visible) (c) Histograms of the resonance positions. (a,b) Mean widths of the Lorentzian fits and their standard deviations (error bars) in each of the energy bins of the histograms in (c), highlighting the importance of the DOS in the substrate (light shaded areas). Two separate plots (a,b) are presented to allow the use of different scales on the y-axes for each set of data (colored dots) and to avoid the overlapping of the data in energy. Black lines in (c,d) show the highest occupied state during CPMD trajectory (corresponds, in principle, to the HOMO) for which larger statistics regarding its energy position are available.

energies of the highest occupied level during the CPMD (computed using a finite slab and plane-waves, thin black line in Fig. 5.7d) and the mean position of the HOMO projection of the surface Green's function (calculated using a semi-infinite surface and the SIESTA/TranSIESTA package, blue line in Fig. 5.7d) agree very well at most of the 161 snapshots selected. They only deviate in a few snapshots where the HOMO and the HOMO-1 projections cross (e.g., at 9 ps in Fig. 5.6b). This supports the reliability of the procedure used to match (Appendix C.1) the fluctuating structures of the adsorbate and surface layers (from the slab calculation) to the static semi-infinite bulk necessary to incorporate the effect of the substrate.

To quantitatively assess our theoretical results for elastic lifetimes, we extracted the linewidth of the MO peaks for each snapshot of Fig. 5.6b by Lorentzian fitting as illustrated in the methods section. The average widths presented in Table 5.1 follow the trend $\langle \Gamma^{\text{LUMO+1}} \rangle < \langle \Gamma^{\text{HOMO}} \rangle < \langle \Gamma^{\text{LUMO+2}} \rangle < \langle \Gamma^{\text{LUMO}} \rangle$, which is similar to that found for the equilibrium geometry apart from $\langle \Gamma_{\text{HOMO}} \rangle$. Unlike for the equilibrium structure, the HOMO state enters the valence band at several simulation times where it couples strongly to the substrate and we get a finite average electronic width of $\langle \Gamma_{\text{HOMO}} \rangle \sim 11$ meV (i.e., an average lifetime $\hbar/\langle \Gamma \rangle \sim 62$ fs). Also the linewidth of the other analyzed peaks increases in comparison to the equilibrium structure. For example, the LUMO+1 state is strongly broadened leading to a reduction of about half a picosecond in its charge transfer time. Overall the effect of the structural fluctuations clearly shows that it is indispensable to take into account an extended set of geometries in order to obtain a realistic picture of the charge transfer times in a device.

We stress that structural fluctuations not necessarily tend to increase the average linewidths of adsorbate levels, although we observed such behavior here. For example, the opposite effect may occur for a molecular resonance whose energy in the equilibrium geometry overlaps with a large peak of the DOS of the substrate. In that case, deviations of the peak position may result in a reduction of the average linewidth due to the reduced availability of final states in the substrate in the configurations visited during the dynamics.

The coupling to a continuum of states in the substrate is usually described by Fermi's golden rule [194, 216]

$$\Gamma_R = \Gamma(E_R) = 2\pi |M_{RS}(E_R)|^2 \rho_S(E_R), \tag{5.2}$$

where $M_{RS}(E_R)$ is the Hamiltonian matrix element coupling the resonance $R$ to the electronic states $S$ in the substrate at a given energy $E_R$, and $\rho_S(E_R)$ is the density of states in the substrate. Here, by averaging $\Gamma$ over the various snapshots, we effectively deal with a thermally averaged version of this equation, $\langle \Gamma(E_R) \rangle = 2\pi \langle |M_{RS}(E_R)|^2 \rho_S(E_R) \rangle$. We note that the density of states $\rho_S(E_R)$ depends on the adsorption configuration only through the resonance energy $E_R$. However, the couplings $M_{RS}(E_R)$ are in general dependent on fine structural details and on $E_R$, since the character (e.g., symmetry, shape, decay into vacuum, ...) of the states from the substrate is also depending on energy. For a more intuitive understanding of the results it is desirable to separate the role of $\rho_S(E_R)$ and $|M_{RS}(E_R)|^2$. In particular, the above expression simplifies if both ingredients entering Eq. (5.2) behave as statistically independent, i.e., $\langle |M_{RS}(E_R)|^2 \rho_S(E_R) \rangle \approx \langle |M_{RS}(E_R)|^2 \rangle \langle \rho_S(E_R) \rangle$, leading

to

$$\langle\Gamma(E_R)\rangle \approx 2\pi\langle|M_{RS}(E_R)|^2\rangle\langle\rho_S(E_R)\rangle. \tag{5.3}$$

The validity of this approximation in our specific case was investigating separately $\langle\rho_S(E_R)\rangle$ and $\langle|M_{RS}(E_R)|^2\rangle$, operatively defined as $\langle\Gamma(E_R)/[2\pi\rho_S(E_R)]\rangle$. The excellent agreement between the values of $\langle\Gamma(E_R)\rangle$ and of $2\pi\langle|M_{RS}(E_R)|^2\rangle\langle\rho_S(E_R)\rangle$ (see Table 5.2) confirms their approximate statistical independence for isonicotinic acid on rutile TiO$_2$.

This indicates that the average character of the substrate states does not change dramatically within the energy windows explored by the resonances as the system fluctuates at room temperature and, thus, $M_{RS}(E_R)$ does not exhibit a strong variation as a function of $E_R$ (note that this is still compatible with a strong dependence on other variables, e.g., structural ones, which however do not exhibit a one-to-one correspondence with $E_R$). We are then enabled to disentangle the role of the matrix elements and the DOS, and to analyse the average coupling matrix $\langle|M_{RS}|^2\rangle$ as a physically meaningful quantity.

Additional insight into this aspect is provided by evaluating subset averages of $\Gamma$ within narrow energy intervals, for which we take the bins of Fig. 5.7c. The resulting $\langle\Gamma\rangle_{bin}$ values are shown in Fig. 5.7a and b), where it is apparent that the average widths scale with the amount of available acceptor states. Thus, structural fluctuations at the interface affect the coupling matrix $|M_{RS}|^2$ in a way that is on average independent of the energy $E_R$ at which the molecular resonance appears. Nevertheless, fluctuations of the width $\Gamma$ of single snapshots even within the bins are relatively large as shown by their standard deviations (error bars in Fig. 5.7a and b).

To summarize the discussion of isonicotinic acid in its ground-state electronic configuration, we return to the cumulative spectra in Fig. 5.6c. Those spectra are the result of two broadening mechanisms. The electronic coupling leads to approximately Lorentzian-like peaks for the molecular resonances in each snapshot, with some ex-

**Table 5.2.:** Separate evaluation of time averages of the different terms in Fermi's golden rule for the ground state and core-excited molecular resonances of isonicotinic acid on rutile (110). Here, $\rho_S$ is the density of states of the nine trilayer slab computed with SIESTA. The core-excited case is further discussed in Section 5.2.4.

| Ground state | $2\pi\langle|M_{RS}|^2\rangle \equiv \langle\Gamma_R/\rho_S\rangle$ ($10^{-3}$eV$^2$) | $\langle\rho_S\rangle$ (eV$^{-1}$) | $2\pi\langle|M_{RS}|^2\rangle\langle\rho_S\rangle$ (meV) | $\langle\Gamma_R\rangle$ (meV) |
|---|---|---|---|---|
| LUMO | 1.87 | 145.66 | 272.05 | 279.89 |
| LUMO+1 | 0.10 | 65.40 | 6.58 | 6.29 |
| LUMO+2 | 0.63 | 94.29 | 59.19 | 56.94 |
| Core-excited | $2\pi\langle|M_{RS}|^2\rangle \equiv \langle\Gamma_R/\rho_S\rangle$ ($10^{-3}$eV$^2$) | $\langle\rho_S\rangle$ (eV$^{-1}$) | $2\pi\langle|M_{RS}|^2\rangle\langle\rho_S\rangle$ (meV) | $\langle\Gamma_R\rangle$ (meV) |
| LUMO | 0.01 | 15.23 | 0.18 | 0.19 |
| LUMO+1 | 0.05 | 185.09 | 9.22 | 9.19 |
| LUMO+2 | 1.61 | 69.13 | 111.39 | 105.57 |
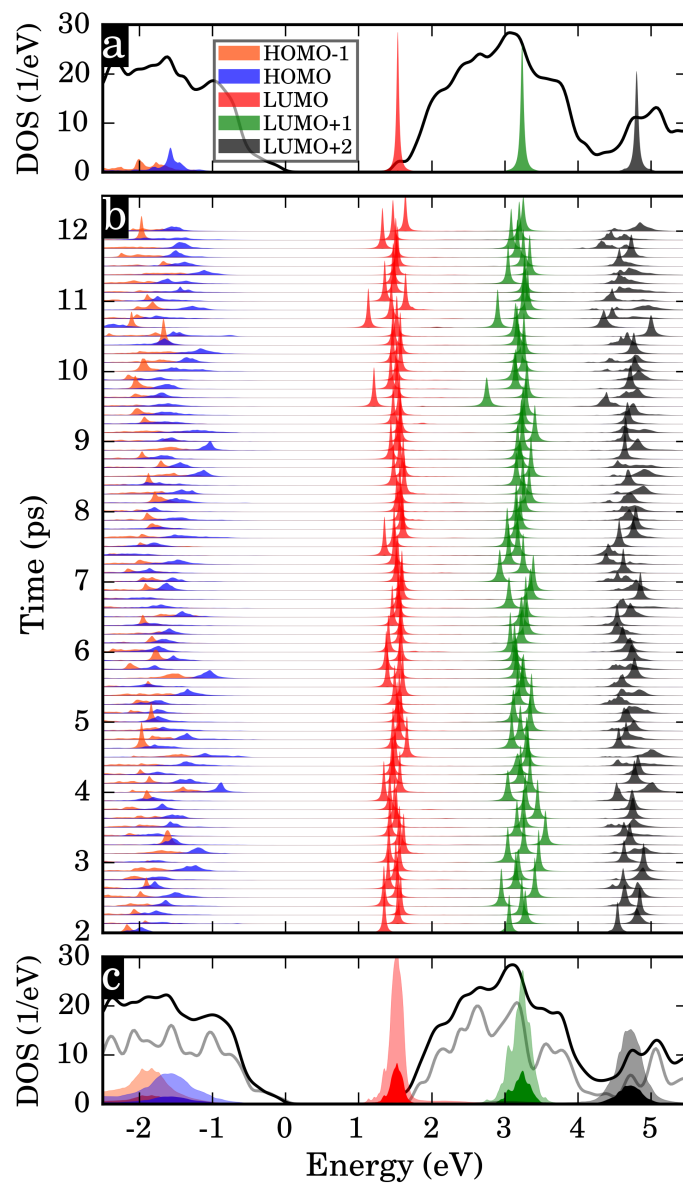
**Figure 5.8.:** Spectra as in Fig. 5.6 but including an N 1s core-hole in the calculations.

ceptions to this behavior depending on the details of the electronic structure around the resonances and the strength of the coupling to the substrate. Within our classical treatment of the dynamics of ions, thermal fluctuations result in a Gaussian-like distribution of the resonance positions. Then, neglecting deviations from the two approximations described above, the cumulative spectra (see Fig. 5.6c) of the MO PDOS may be approached by a sum of Voigt curves, i.e., convolutions of Gaussians with Lorentzian profiles. Such Voigt or Pseudo-Voigt curves are routinely used to fit experimental spectra, [217] where additional broadening due to the resolution of detector and broadening of incident beams must be also taken into account in order to extract relevant electronic couplings. A detailed discussion of such a fitting of the computed cumulative spectra with Voigt-type curves can be found in the Appendix C.6. As described there, we find that the quality of the fit is improved if the energy dependence of the average elastic width is taken into account. This energy dependence describes mostly the variation of the DOS of the substrate.

## 5.2.4. Elastic Lifetimes upon Inclusion of the N1s Core-Hole

In this second part of our analysis we include a core-hole in our calculations as necessary to quantitatively compare our theoretical charge-transfer times with available data from core-hole-clock experiments [36, 48]. The core excited (Fig. 5.8a) and the ground state systems (Fig. 5.6a), both computed in the ground-state equilibrium structure, exhibit striking differences since the levels shift downwards in energy due to the presence of the positive core-charge. The HOMO level is now positioned inside the valence band of the substrate and consequently is strongly broadened so that it overlaps with the HOMO-1 level. Furthermore, the LUMO gets pinned to the edge of the conduction band, where the added electron (excited from the core N 1s level) gets localized and screens the positive charge of the nitrogen core-hole. Although the LUMO+1 peak of the core-excited spectrum is located at energies comparable to those of the LUMO peak in the ground-state spectrum, the LUMO+1 remains largely decoupled from the substrate. This is in contrast to the case of the LUMO of the unexcited molecule, where interaction with the substrate is favored by the symmetry and spatial distribution of the MO [36]. Similarly, the width of the LUMO+2 peak in the core-excited system is smaller than in the ground-state case. The extracted values of the linewidths at the equilibrium geometry and the corresponding lifetimes can be found in Table 5.3, the values for the equilibrium adsorption structure from Ref. 36 are given in brackets. We find a good agreement between the two sets of data. As pointed out by Fratesi *et al.* [36], coincidentally the energy level alignment of the adsorbate and substrate states compare well with those reported experimentally [48]. This can be considered as a fortuitous cancellation of errors in this specific case, given that semi-local DFT functionals tend to misdiagnose the gaps of semi-conductors and the HOMO-LUMO gaps of adsorbates, as well as their relative level alignment.

We now turn towards investigating the effect of structural fluctuations in the presence of the core-hole, paralleling our previous discussion for the ground state case. We discuss the evolution of the spectra along the CPMD trajectory (Fig. 5.8b), in
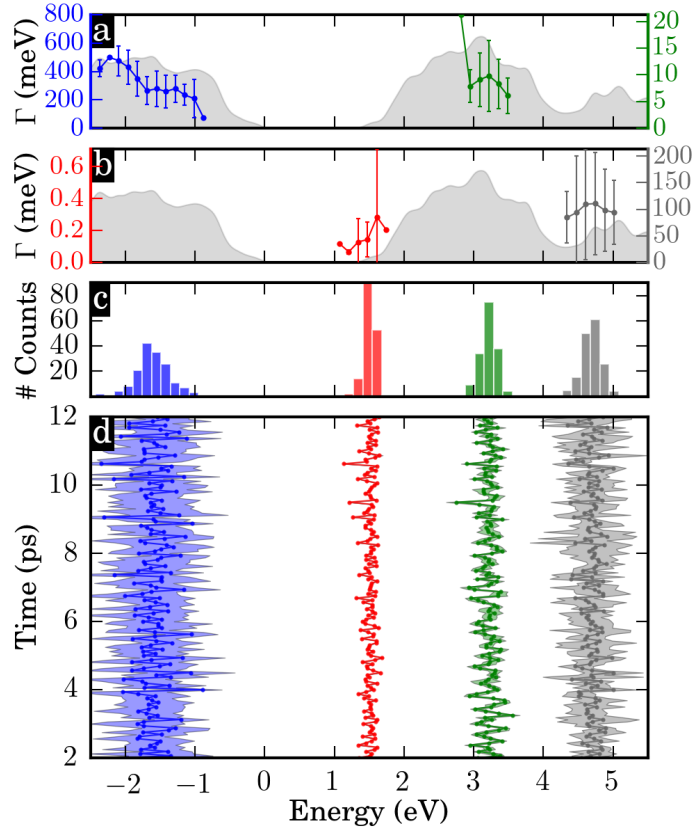
**Figure 5.9.:** Energy positions of the resonances and associated elastic linewidths for the core-excited case. The figure is organized analogously to Fig. 5.7.

comparison to the spectrum at the equilibrium structure (Fig. 5.8a), and address the cumulative spectrum (Fig. 5.8c) including the effect of the finite temperature fluctuations. The shift of the molecular levels to lower energies due to the presence of the core-hole is similar for all the snapshots along the CPMD trajectory (Fig. 5.8b). The HOMO-1 and the HOMO level are strongly hybridized with the substrate and show overlapping distributions in the density of states. In a few simulation snapshots these two resonances exchange their relative energy positions. The situation is different for the LUMO and LUMO+1 states showing only a weak coupling to the surface during the whole CPMD simulation. This is particularly true in the case of the LUMO state spending most of its time inside the substrate's gap. Thus, these peaks keep a predominantly Lorentzian shape in the successive spectra displayed in Fig. 5.8b. In contrast, the LUMO+2 is found to hybridize strongly with the substrate in many snapshots, to the extent that the resonance splits into more than one peak in some cases. This is also in contrast to the case of the ground-state equilibrium structure, for which the LUMO+2 state of the core-excited molecule is more weakly coupled than in most of the CPMD snapshots (compare the values of $\Gamma_{eq}$ and $\langle \Gamma \rangle$ in Table 5.3).

For the LUMO, LUMO+1 and LUMO+2 we observed considerably smaller fluctuations of the peak positions along the CPMD trajectory than in the ground state. This is reflected by smaller values for $\sigma(E_R)$ in Table 5.3 as compared to those in Table 5.1. As a consequence of this and the moderate coupling to the substrate,
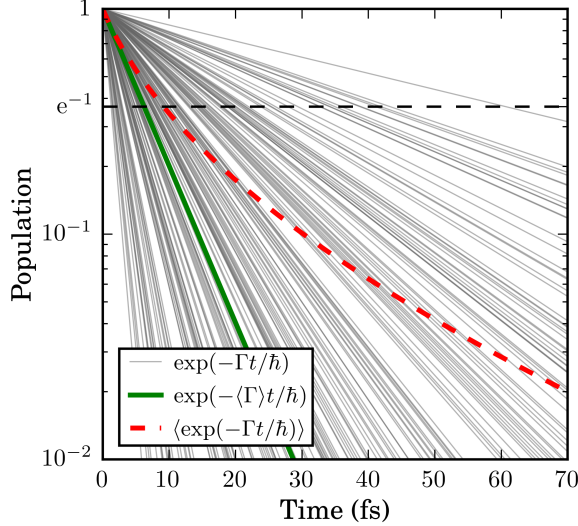
**Figure 5.10.:** Exponential decays corresponding to the calculated LUMO+2 linewidths $\Gamma$ for the sampled snapshots during the CPMD trajectory (gray lines). The lifetime $\tau$ of the state, defined as the time to decay to a population of $1/e$, is slightly increased when considering the average of the exponential decays (broken red line) instead of the exponential determined by the averaged linewidth $\langle\Gamma\rangle$ (thick green line).

we find well separated peaks for each of these resonances in the cumulative spectra in Fig. 5.8c. This clearly differs from the ground-state case shown in Fig. 5.6c.

As in the section covering the electronic ground-state configuration, we carry out a quantitative analysis by extracting the maximum peak positions $E_R$ and the width $\Gamma$ (using Lorentzian fitting) for a large number of snapshots during the CPMD simulation. The data is visualized in Fig. 5.9d and the corresponding values summarized in Table 5.3. The scaled widths displayed in the plot Fig. 5.9d show the trend $\langle\Gamma^{\mathrm{LUMO}}\rangle < \langle\Gamma^{\mathrm{LUMO+1}}\rangle < \langle\Gamma^{\mathrm{LUMO+2}}\rangle < \langle\Gamma^{\mathrm{HOMO}}\rangle$, which coincides with the trend for the equilibrium geometry (see Table 5.3).

Regardless of the finite temperature fluctuations, the LUMO maintains a vanishing ($< 1$ meV) width and is approximately pinned to the conduction band edge. The coupling to the substrate of the LUMO+1 resonance is similar during the CPMD steps than for the equilibrium structure. Indeed, the average $\langle\Gamma^{\mathrm{LUMO+1}}\rangle$ equals $\Gamma_{\mathrm{eq}}^{\mathrm{LUMO+1}}$, although the estimated relative error of $\delta(\langle\Gamma\rangle) = \sigma(\Gamma)/(\langle\Gamma\rangle\sqrt{N}) = 5\%$ for $N = 161$ snapshots (sample size) indicates that the width slightly fluctuates along the trajectory ($\sigma(\Gamma)$ refers to the standard deviation of the linewidths). The average linewidths of the HOMO, LUMO, and LUMO+1 states retain the same order of magnitude when including the influence of fluctuations. Conversely, the LUMO+2 peak is significantly broadened from $\Gamma_{\mathrm{eq}}^{\mathrm{LUMO+2}} = 15$ meV to $\langle\Gamma^{\mathrm{LUMO+2}}\rangle = 110$ meV. Correspondingly, its lifetime decreases from $\hbar/\Gamma_{\mathrm{eq}} = 45$ fs to $\hbar/\langle\Gamma\rangle = 6$ fs, to be compared to an experimental value of 5 fs [48]. Therefore, the inclusion of structural fluctuations improves considerably the agreement to available experimental data.

In Fig. 5.10 we explore two possible definitions of the mean lifetime of an electronic state under the effect of structural fluctuations. So far we have identified

the average lifetime $\hbar/\langle\Gamma\rangle$ in connection with the average elastic linewidth, i.e., giving rise to the exponential decay of the molecular orbital occupation $\exp(-\langle\Gamma\rangle t/\hbar)$. A reasonable alternative would be to extract the elastic lifetime $\tau'$ from the average of the exponential decays for all the snapshots along the molecular dynamics, $\langle\exp(-\Gamma t/\hbar)\rangle$. The lifetime would then be defined as the solution of the equation $\langle\exp(-\Gamma t/\hbar)\rangle = \exp(-1)$, which we solve graphically in Fig. 5.10 for the LUMO+2 resonance. We find that such alternative analysis produces larger lifetimes, although the difference is moderate and it does not change the results qualitatively. For example, in the case of the LUMO+2 this increases the computed elastic lifetime from 6 fs to 9 fs, thus retaining the improved agreement with the experiment. Table 5.4 compares the analysis of the lifetimes $\tau'$ from this alternative approach to the previous estimate $\tau = \hbar/\langle\Gamma\rangle$.

It can be seen in Table 5.4 that no changes in the trends occur, while the absolute values of the lifetimes $\tau'$ are somewhat larger. In the ground-state case the width of the LUMO is always very close to zero, since it is located inside the gap. The HOMO enters the valence band of the $TiO_2$ substrate only at a few simulation times. In those cases it has a rather large width, which is the reason we report in Table 5.4 only a finite value for $\hbar/\langle\Gamma\rangle$. However, it is impossible to extract a meaningful value for $\tau'$ in the case of the HOMO in the ground-state.

The observation that, for core-excited isonicotinic acid on $TiO_2$, only the LUMO+2 resonance features a significant increase in width upon inclusion of structural fluctuations can be rationalized in terms of the symmetry and spatial distribution of the MOs. Only the LUMO and the LUMO+2 state exhibit a significant overlap with the substrate ($\pi$-type bonding visible in Fig. S7) and, thus, making the coupling very sensitive to interfacial structural fluctuations. However, the LUMO appears in an energy position with a low density of acceptor states (spending a large amount of time inside the substrate gap), resulting in the quenching of the corresponding decay channel [48] and leaving the elastic width of the LUMO+2 resonance as the only one largely affected by the dynamics.

Analogously to the ground state case we analyze the distributions of the resonance

**Table 5.3.:** Energy positions and linewidths of the electronic levels extracted from the spectra calculated for the core-excited molecule. The values presented in brackets are taken from Ref. 36 and were computed only at the equilibrium adsorption structure. The values in this Table can be contrasted with those presented in Table 5.1 for the molecule in its ground-state electronic configuration.

|  | equilibrium (0 K) | | | thermal average (300 K) | | | | |
|---|---|---|---|---|---|---|---|---|
|  | $E_R$ (eV) | $\Gamma_{\mathrm{eq}}$ (meV) | $\hbar/\Gamma_{\mathrm{eq}}$ (fs) | $\langle E_R\rangle$ (eV) | $\sigma(E_R)$ (eV) | $\langle\Gamma\rangle$ (meV) | $\delta(\langle\Gamma\rangle)$ (%) | $\hbar/\langle\Gamma\rangle$ (fs) |
| HOMO | -1.57 | 152 | 4 | -1.60 | 0.24 | 292 | 3 | 2 |
| LUMO | 1.53 | 0 | $\infty$ | 1.51 | 0.08 | 0 | 11 | $\infty$ |
| LUMO+1 | 3.24 | 9 (7) | 75 (93) | 3.21 | 0.12 | 9 | 5 | 72 |
| LUMO+2 | 4.80 | 15 (15) | 45 (44) | 4.69 | 0.13 | 106 | 7 | 6 |

positions of the MOs and compare their standard deviations during dynamics. The respective values in Table 5.3 show in general a significant decrease of the standard deviations $\sigma(E_R)$ of the unoccupied state's energy upon inclusion of the core-hole, with respect to the case without the core-hole in Table 5.1. Most significantly the fluctuations of the LUMO's energy level are decreased upon pinning to the conduction band edge leading to a low standard deviation of 0.08 eV. Approximately reduced by a factor of two appear the fluctuations of the HOMO, the LUMO+1, and the LUMO+2 which have standard deviations of 0.24 eV, 0.12 eV, and 0.13 eV, respectively. This reduction of the temperature broadening can be rationalized as a result of the localization of the adsorbate states on isonicotinic acid due to the attractive interaction with the core-hole, making them less susceptible to the structural fluctuations at the surface-molecule interface and to low energy fluctuations of the molecular structure.

Fig. 5.9 analyzes the distribution of the resonance positions and widths over energy. Consistent with the observations made in the previous paragraph, the distributions of both the LUMO+1 and LUMO+2 states can be described by narrow Gaussian-like curves (see Fig. 5.9c). In contrast, HOMO and LUMO states do not present such symmetric energy distributions exhibiting tails towards the band edges. Similarly to the ground-state case, we find that also in the excited state the average widths of the peaks referring to each of the energy bins in Fig. 5.9c follow approximately the DOS of the substrate as shown in Fig. 5.9a and b. This suggests that the energy dependence of the DOS plays a key role in determining the average coupling of each resonance and the shape of the cumulative spectra in Fig. 5.8c.

## 5.2.5. Discussion on Different Estimates of Average Lifetimes

The two estimates for the lifetimes $\hbar/\langle\Gamma\rangle$ and $\tau'$ presented in Table 5.4 can be seen as upper and lower limits to the charge transfer times as we discuss here. We assume that a rather general description of the rate of the population decay is given by

$$\dot{P}(t) = -\Gamma(t)P(t) \tag{5.4}$$

**Table 5.4.:** Estimation of the lifetime at room temperature from the average linewidth $(\hbar/\langle\Gamma\rangle)$ and alternatively from an ensemble average of exponential decays $(\tau')$. All values are given in femtoseconds.

|          | ground-state | | core-excited | |
|----------|:---:|:---:|:---:|:---:|
|          | $\hbar/\langle\Gamma\rangle$ | $\tau'$ | $\hbar/\langle\Gamma\rangle$ | $\tau'$ |
| HOMO     | 62  | -   | 2        | 3        |
| LUMO     | 2   | 3   | $\infty$ | $\infty$ |
| LUMO+1   | 105 | 220 | 72       | 84       |
| LUMO+2   | 12  | 14  | 6        | 9        |

with the solution

$$P(t) = P_0 \, e^{-\int_0^t \Gamma(s+t_0)ds} \tag{5.5}$$

where the initial population $P_0 = 1$ is normalized and $\Gamma(t)$ is the decay rate at each instance of time $t$. However, Eq. (5.5) is a simplification of the quantum propagation with $\hat{U}(t,0) = \hat{T} \exp[-\frac{i}{\hbar} \int_0^t \hat{H}(s) \, ds]$, where $\hat{T}$ is the time-ordering operator.

Under the assumption Eq. (5.4) and a statistical distribution of decays we show that the average population decay $\langle P(t) \rangle$ is confined by upper and lower averages according to, so that

$$\left\langle e^{-\Gamma t} \right\rangle \geq \langle P(t) \rangle \geq e^{-\langle \Gamma \rangle t}. \tag{5.6}$$

This implies that the lifetime $\tau$ is bounded by the two estimates $\hbar/\langle \Gamma \rangle$ and $\tau'$,

$$\tau' \geq \tau \geq \frac{\hbar}{\langle \Gamma \rangle}, \tag{5.7}$$

which is consistent with the values extracted before, as can be seen in Table 5.4.

We provide now a simple proof of Eq. (5.6) employing the relation

$$\int e^{g(x)} \rho(x) \, dx \geq e^{\int g(x)\rho(x)dx}, \tag{5.8}$$

where $g(x)$ is any real valued function and $\rho(x)$ is some probability distribution. Eq. (5.8) is a special case of Jensen's inequality that can easily be derived by expanding in a Taylor series,

$$\left\langle e^{-X} \right\rangle = e^{-\langle X \rangle} \left\langle e^{-X+\langle X \rangle} \right\rangle \geq e^{-\langle X \rangle} \left\langle 1 - X + \langle X \rangle \right\rangle = e^{-\langle X \rangle}, \tag{5.9}$$

where we have considered in analogy to the current case [Eq. (5.4)] a negative sign and we introduced a short hand notation with angle brackets for expected values of the stochastic variable $X$.

We may then calculate the ensemble average over Eq. (5.5) by writing

$$\langle P(t) \rangle = \left\langle e^{-\int_0^t \Gamma(s+t_0)ds} \right\rangle = \frac{1}{T} \int_0^T e^{-\int_0^t \Gamma(s+t_0)ds} \, dt_0 \,, \tag{5.10}$$

where we employed ergodicity $\langle \ldots \rangle = \frac{1}{T} \int_0^T \ldots dt$ after the second equality sign.

Then there are two ways in which we can apply the inequality in Eq. (5.8) to the ensemble average in Eq. (5.10). The first way consists in moving the inner integration outwards, so that

$$\begin{aligned} \langle P(t) \rangle &= \frac{1}{T} \int_0^T e^{-\frac{1}{t}\int_0^t \Gamma(s+t_0)\cdot t \, ds} \, dt_0 \\ &\leq \frac{1}{T} \int_0^T \frac{1}{t} \int_0^t e^{-\Gamma(s+t_0)\cdot t} \, ds \, dt_0 = \frac{1}{T} \int_0^T e^{-\Gamma(t_0)\cdot t} \, dt_0 = \left\langle e^{-\Gamma t} \right\rangle \end{aligned} \tag{5.11}$$

Since $\Gamma$ depends equally on $s$ and $t_0$ the double integral can be reduced to a single ensemble average. Secondly, we move the outer integration inside the exponential function, so that we receive

$$\langle P(t) \rangle \geq e^{-\frac{1}{T}\int_0^T \frac{1}{t}\int_0^t \Gamma(s+t_0)\cdot t \, ds \, dt_0} = e^{-\langle \Gamma \rangle t}. \tag{5.12}$$

All together one obtains the final result Eq. (5.6) under the assumption of statistical distributions of the decays and a generalized exponential decay law [Eq. (5.4)].

## 5.2.6. Conclusions

We investigated ultrafast electron injection from a prototype dye to a rutile TiO$_2$(110) substrate by DFT slab calculations and Green's function techniques. To include the effect of thermal fluctuations we computed the resonant lifetimes of the molecular states by sampling a Car-Parinello molecular dynamics trajectory at room temperature. We studied both the molecular ground state and an excited case with a core-hole in the nitrogen 1s shell as occurring in core-hole-clock experiments [48].

We find temperature effects to be substantial: The LUMO+2 channel, dominating the experimental spectrum, couples more strongly to the substrate in configurations far from equilibrium. At room temperature this resulted in a computed lifetime in the range of 6 to 9 fs in agreement with the experimental observation [48] –a result that cannot be reproduced by only considering the relaxed structure. The LUMO and LUMO+1 are less affected by temperature and remain weakly coupled to the substrate. We observe a reduction of thermal broadening in comparison to the ground-state and explain this by a stronger localization of the molecular states in the core-excited case.

The presented thermally averaged spectra can be described by Voigt-type profiles obtained by convolving a Lorentzian peak describing the electronic resonance with a Gaussian distribution modeling the temperature broadening. The description is substantially improved by taking into account the energy dependence of the configurationally averaged electronic width. We find this energy dependence to be governed by the variation of the density of acceptor states in the substrate.

Our study shows that the description of fast processes at finite temperatures, where an electron is transferred while the underlying ionic configuration remains virtually unchanged, requires detailed knowledge of the instantaneous configuration and the electronic excitation. Here, a statistical sampling of the configurations available at finite temperatures is instrumental. Yet, to access the dynamics of faster processes in the attosecond domain further considerations have to be made. In such strongly coupled cases discernible resonance features are absent and approaches like real time propagation of wave packets, possibly including an explicit treatment of the external exciting field, become necessary. Current developments of experimental techniques such as free electron lasers [155, 157, 158] to probe ever faster electron dynamics require combined theoretical models for their interpretation.

## 5.3. Vibrational Analysis of Isonicotinic Acid Adsorbed on TiO$_2$(110)

In order to further characterize the influence of the atomic motion and its effect onto the molecular levels, we analyze the computed spectra of isonicotinic acid on TiO$_2$ in the vibrational eigenmode basis of the adsorbed molecule. Our intent is to determine the modes which have the largest impact on the spectra, i.e., the modes along which the energetic positions of the molecular orbitals change most significantly. This is achieved by estimating the diagonal elements of the electron-phonon coupling.

We introduce a semi-classical harmonic oscillator model of the spectral broadening

at finite temperatures. In this framework the electron-vibrational couplings and the corresponding eigenfrequencies determine the inhomogeneous broadening at a given temperature. An a priory prediction of the modes with the strongest effect on the electronic spectra is not possible, since the thermalization of the modes leads to a broad range of contributions. However, after a detailed analysis, particular vibrational modes can be identified, which affect the spectra most strongly. A similar linear coupling between the computed electronic widths (instead of the energetic positions) and a few selected modes is not apparent. Instead, a broad range of modes affects the matrix elements related to the electronic widths in a simple linear coupling model like the one we assume.

In the analysis carried out in this section, we use mainly data from the molecular dynamics simulations (cf. Section 5.2), which is readily at hand. A separate calculation of the electron-vibrational (electron-phonon) couplings in terms of other methods (e.g. density functional perturbation theory [218]) is technically not necessary.

The section is organized in the following way: First, we briefly describe the extraction of a vibrational eigenmode basis from ab initio forces. Then we use the mode vectors in a semi-classical model to describe their effect in temperature broadened spectra. Subsequently, we look at the effect of particular modes and address the question of whether a subset of vibrational modes is useful to determine the position of the electronic level for each particular geometry.

### 5.3.1. Semi-Classical Model of Spectral Broadening in a Normal Mode Basis

We start by deriving the broadening of the electronic levels from a semi-classical model giving rise to Gaussian line shapes. Applying the Born-Oppenheimer approximation we treat the $N$ nuclei classically so that their effective energy is given by the Hamiltonian

$$H = \sum_{i=1}^{3N} \frac{1}{2} M_i \dot{R}_i + V(\mathbf{R}). \tag{5.13}$$

Here, $V(\mathbf{R})$ is the potential energy, which depends on the complete set of the $3N$ coordinates $\mathbf{R} = (R_1, \ldots, R_{3N})$ specifying the positions of the nuclei with the corresponding masses $M_i$.

We follow the common approach (e.g., Ref. 219) introducing a mass-scaled set of coordinates $q_i(t) = \sqrt{M_i}[R_i(t) - R_{i,0}]$ describing the displacements from the equilibrium positions $R_{i,0}$. In this new set of coordinates the Hamiltonian can be rewritten as

$$H(\mathbf{p}, \mathbf{q}) = \sum_{i=1}^{3N} \frac{p_i^2}{2} + V_0 + \sum_{i,j=1}^{3N} \frac{1}{2!} \left( \frac{\partial^2 V}{\partial q_i \partial q_j} \right)_{\mathbf{q}=0} q_i q_j, \tag{5.14}$$

where the kinetic energy depends quadratically on the momentum $\dot{q}_i = \frac{\partial H}{\partial p_i} = p_i$. The potential energy is given up to second order by a Taylor expansion around the equilibrium configuration at $\mathbf{q} = 0$, where all linear terms vanish. As already above, we use boldface typesetting to indicate the full set of the coordinates. The equilibrium contribution to the potential energy $V_0$ is set to zero without loss of generality.

By Newtons law $\dot{p}_i = \ddot{q}_i = -\frac{\partial H}{\partial q_i}$ and the vibrational ansatz $q_{i,k}(t) = A_{i,k}\cos(\omega_k t + \phi_k)$ one has for the time-evolution of the coordinates

$$\sum_{i=1}^{3N} \left( D_{ij} - \omega_k^2 \delta_{ij} \right) q_{i,k} = 0, \tag{5.15}$$

which is an eigenvalue equation describing a set of $3N$ independent harmonic oscillators. We have defined the dynamical matrix

$$D_{ij} = \frac{1}{\sqrt{M_i M_j}} \left( \frac{\partial^2 V}{\partial R_i \partial R_j} \right)_{\mathbf{R}=\mathbf{R}_0} = \left( \frac{\partial^2 V}{\partial q_i \partial q_j} \right)_{\mathbf{q}=0}. \tag{5.16}$$

The dynamical matrix can be set up, by computing the change in the forces upon displacements of single atoms from the Hellman-Feynman theorem (frozen phonon approximation). The solution of the eigenvalue problem Eq. (5.15) yields a complete set of vibrational eigenmodes with the corresponding frequencies $\omega_k$.

The dynamical matrix can be extended by considering Bloch-like distortions in periodic crystal structures. This allows to analyze phonon spectra along phononic wavevectors $\mathbf{k}'$, very much like the $\mathbf{k}$-points related to the Bloch waves described by the Hamiltonian in Eq. (2.57). However, here we consider exclusively atoms moving identically in the periodically repeating unit cells of the structure, this corresponds to vibrations with a phononic wave-vector of $\mathbf{k}' = 0$.

Defining the set of the normal coordinates $Q_k$ by the orthogonal transformation

$$q_i = \sum_{k=1}^{3N} A_{i,k} Q_k, \tag{5.17}$$

allows for a more convenient treatment. The columns $\mathbf{a}_k$ of the matrix with the elements $A_{jk}$ are given by the eigenvectors of the dynamical matrix $D_{ij}$, that correspond to $3N$ vibrational eigenmodes including three translations with zero frequency and, for finite systems also, rotations. The nuclear Hamiltonian can be rewritten in a separable form using the normal mode basis

$$H(\mathbf{P}, \mathbf{Q}) = \frac{1}{2} \sum_{k=1}^{3N} \left( P_k^2 + \omega_k^2 Q_k^2 \right), \tag{5.18}$$

where the momenta are given by $P_k = \dot{Q}_k$.

Employing the above introduced classical harmonic oscillator formalism one can derive the effect of the vibrations onto an electronic level of a molecule. We assume that the energetic position $E$ of the molecular level depends linearly on the coordinates $Q_k$ of the normal modes (i.e. neglecting higher order terms),

$$E(\mathbf{Q}) = E_0 + \sum_{k=1}^{3N} \alpha_k Q_k, \qquad \text{with} \qquad \alpha_k = \left( \frac{\partial H_{\mathrm{e}}}{\partial Q_k} \right)_{\mathbf{Q}=0}. \tag{5.19}$$

Here, the coupling constant $\alpha_k$ quantifies the energy shift of a molecular level $E_0$ (i.e., an eigenstate of the electronic Hamiltonian $H_{\mathrm{e}}$ or of a part of the latter) after

a displacement with respect to the equilibrium position at $\mathbf{Q} = 0$ along the normal coordinate $Q_k$. The $\alpha_k$ correspond hence to the diagonal terms of the electron-phonon coupling matrix, which are the most relevant coupling terms for molecular levels with sufficiently large energy spacings.

A way to compute the coupling $\alpha_k$ is by displacing the molecule along a single eigenmode $\mathbf{a}_k = \sum_{j=1}^{3N} A_{jk}\mathbf{e}_j$ with a forward difference scheme

$$\alpha_k = \left(\frac{\partial E}{\partial Q_k}\right)_{\mathbf{Q}=0} = \lim_{Q_k \to 0} \frac{E\left(\mathbf{R}_0 + Q_k \sum_{j=1}^{3N} A_{jk} M_j^{-1/2}\mathbf{e}_j\right) - E_0}{Q_k}, \qquad (5.20)$$

where three standard basis vectors $\mathbf{e}_j$ span the real space at each of the $N$ atoms and thus the $3N$-dimensional space in total. We note that this one-sided differencing scheme avoids ambiguities when identifying the average coupling of degenerate eigenstates. The crossing of degenerate energy levels requires to identify the corresponding states at energies below and above the crossing point, since the crossing changes the order of the energy levels, which is in practice not trivial. Performing a one sided average avoids this complication and an average couplings of the degenerate levels can be determined.

Using the definitions above one can derive the spectral broadening of the electronic level $E$ in the following statistical average (canonical ensemble, with a fixed volume and number of particles at a constant temperature)

$$\langle \delta(E - E(\mathbf{Q})) \rangle = \frac{1}{Z} \iint \delta(E - E(\mathbf{Q})) e^{-\beta H(\mathbf{P},\mathbf{Q})} \, d\mathbf{P} \, d\mathbf{Q}, \qquad (5.21)$$

with

$$Z = \iint e^{-\beta H(\mathbf{P},\mathbf{Q})} \, d\mathbf{P} \, d\mathbf{Q} = \prod_{k=1}^{3N} \frac{2\pi}{\beta \omega_k}. \qquad (5.22)$$

Where we defined $\beta = k_{\mathrm{B}}T$, the product of the Boltzmann constant $k_{\mathrm{B}}$ with the temperature $T$. The two integrations run over all $3N$ degrees of freedom, as indicated by the short hand notation $\int \ldots d\mathbf{Q} = \int \ldots dQ_1 \cdots dQ_{3N}$ and $\int \ldots d\mathbf{P} = \int \ldots dP_1 \cdots dP_{3N}$. We make use delta function in the Fourier representation

$$\delta(E - E(\mathbf{Q})) = \frac{1}{2\pi} \int e^{-\mathrm{i}(E - E(\mathbf{Q}))t} \, dt, \qquad (5.23)$$

to recast the numerator of Eq. (5.21) in the following form

$$\frac{1}{2\pi} \iiint \exp\left[\sum_{k=1}^{3N}\left(-\frac{\beta}{2}P_k^2 - \frac{\beta}{2}\omega_k^2 Q_k^2 + \mathrm{i}\alpha_k Q_k t\right)\right] e^{-\mathrm{i}(E-E_0)t} \, d\mathbf{P} \, d\mathbf{Q} \, dt. \qquad (5.24)$$

The system consists of $3N$ independent oscillators, i.e., $H(\mathbf{P}, \mathbf{Q})$ is separable, and therefore we can factor the exponentials and execute the Gaussian integrals over the momenta $P_k$. This yields the constant factors $\prod_{k=1}^{3N}\left(\frac{2\pi}{\beta}\right)^{\frac{1}{2}}$, which cancel with the corresponding terms from the integrations over momenta in the denominator $Z$. In the following steps we drop the Fourier transform related to the integral over time

for readability. We are left with

$$\int \exp\left[\sum_{k=1}^{3N}\left(-\frac{\beta}{2}\omega_k^2 Q_k^2 + i\alpha_k Q_k t\right)\right] d\mathbf{Q} = \prod_{k=1}^{3N}\left(\int e^{-\frac{\beta}{2}\omega_k^2 Q_k^2 + i\alpha_k Q_k t}\, dQ_k\right)$$
$$= \prod_{k=1}^{3N}\sqrt{\frac{2\pi}{\beta\omega_k^2}}\exp\left(-\frac{\alpha_k^2 t^2}{2\beta\omega_k^2}\right). \tag{5.25}$$

Here, we carried out the Fourier transform of a Gaussian in $Q_k$ after the final equality sign. As before the resulting prefactors $\prod_{k=1}^{3N}(\frac{2\pi}{\beta\omega_k^2})^{\frac{1}{2}}$ cancel the remaining terms from the integration over the coordinates $Q_k$ in the denominator $Z$. Restoring the Fourier transformation previously dropped for readability in Eq. (5.24) we receive the spectral density in a statistical average

$$\langle\delta(E - E(\mathbf{Q}))\rangle = \frac{1}{2\pi}\int \exp\left(\frac{1}{2\beta}\sum_{k=1}^{3N}\frac{\alpha_k^2}{\omega_k^2}t^2\right)e^{-i(E-E_0)t}\, dt\,. \tag{5.26}$$

This is just the Fourier transform of a Gaussian, which can be equated to the final result

$$\langle\delta(E - E(\mathbf{Q}))\rangle = \frac{1}{\sqrt{2\pi\sigma^2}}e^{-\frac{(E-E_0)^2}{2\sigma^2}}, \qquad \text{where} \qquad \sigma = \left(k_{\mathrm{B}}T\sum_{k=1}^{3N}\frac{\alpha_k^2}{\omega_k^2}\right)^{\frac{1}{2}}. \tag{5.27}$$

According to this semi-classical description, an electronic level $E$ is vibrationally broadened into a Gaussian peak, where the standard deviation $\sigma$ is given by the coupling constants $\alpha_k$, the frequencies of the independent oscillations $\omega_k$, and the temperature $T$.

The steps carried out here are similar to the ones of Sevian and Skinner [220] [cf. the standard deviation in Eq. (2.27) of Ref. 220] . However, we discuss here explicitly the relation to normal modes considering a linear coupling with the electronic levels.

The result for the standard deviation $\sigma$ can be interpreted applying the equipartition theorem considering the Hamiltonian in Eq. (5.18), so that one has

$$k_{\mathrm{B}}T = \left\langle Q_k\frac{\partial H}{\partial Q_k}\right\rangle = \omega_k^2\langle Q_k^2\rangle. \tag{5.28}$$

Using this one can see that $\sigma$ is given by the root of the summed squared energy fluctuations along each mode [compare to Eq. (5.19)],

$$\Delta E_k = \alpha_k\langle Q_k^2\rangle^{1/2}. \tag{5.29}$$

The energy fluctuations themselves are due to the standard deviations in each of the independent normal coordinates $\langle Q_k^2\rangle^{1/2} = (k_{\mathrm{B}}T)^{1/2}/\omega_k$.

## 5.3.2. Characterization of the Molecular Motion in the Vibrational Eigenmode Basis

We have extracted the vibrational eigenmodes of isonicotinic acid on rutile (110) in an effort to relate the observed lifetimes to specific structural changes at finite

temperatures. In particular, we computed the mode vectors related to the atoms of the adsorbed molecule and the two Ti atoms, where the molecule is attached to the surface (15 atoms, 45 modes). For this purpose we diagonalized the dynamical matrix Eq. (5.16). Although we computed the dynamical matrix at this stage in the frozen phonon approximation [218], one can alternatively determine an effective normal mode basis directly from the trajectory by performing a principal component analysis of the dynamics (see e.g. [221]).

Once a set of normal mode vectors spanning all possible molecular positions is available, one can project the mass-scaled trajectory of the molecule into this complete basis. Thereby one obtains the coefficients $Q_k$ for the mode number $k$ at each instance of time in the CPMD simulation.

Fig. 5.11a displays the time evolution of the normal mode coordinates $Q_k(t)$ during 10 ps of the CPMD simulation. The evolutions along each mode vector are not perfectly harmonic, nevertheless their oscillatory character with a dominant frequency is clearly visible. The modes in the plot are ordered according to increasing eigenfrequencies $\omega_k$, as obtained from our frozen phonon calculations (blue dots in Fig. 5.11b). The blue dashed line in Fig. 5.11b represents the average frequencies $\tilde{\omega}_k$ of each mode, obtained from the extracted normal mode coordinates $Q_k$ using Eq. (5.28), $\tilde{\omega}_k = (k_\mathrm{B}T/\langle Q_k^2 \rangle)^{-1/2}$. It is visible that some reordering of the frequencies occurs in the CPMD calculation, while the overall trend of $\omega_k$ and $\tilde{\omega}_k$ coincide.

Looking at the variances of the normal mode coordinates $\langle Q_k^2 \rangle$ (bar plot in Fig. 5.11b, logarithmic scale) one sees that, as expected at thermal equilibrium, the contributions from larger frequencies bring about smaller structural fluctuations. Again the trend agrees roughly with the frozen phonon estimate $k_\mathrm{B}T/\omega_k^2$ (red dots). The jump in the plots after mode number 40 occurs since the four highest frequency modes strongly involve the light hydrogen atoms around the pyridin cycle.

To get an impression of the overall motion of the molecule on the surface, we analyze the three lowest frequency modes, i.e., the modes producing the largest structural fluctuations along the CPMD trajectory in Fig. 5.11c-e. The main motion can be characterized by three angles, which are related to (c) tilting, (d) twisting, and (d) sidewards bending of the molecule as the figure shows. The mode displacement vectors related to these angles are displayed by yellow arrows in the top panels. Correspondingly one can see in the bottom panels that the respective evolutions of the normal coordinates $Q_k(t)$ (black lines) match the evolutions of the three angles (red lines).

However, a comparison of the evolution of the angles in Fig. 5.11 with the energetic positions (or also the linewidths) of the resonances (Figs. 5.7 and 5.9) shows that higher frequencies significantly couple to the molecular levels and cannot be neglected. Therefore, the evolution of the electronic states cannot be described by a set of low frequency modes, although they represent the largest structural displacements.

81
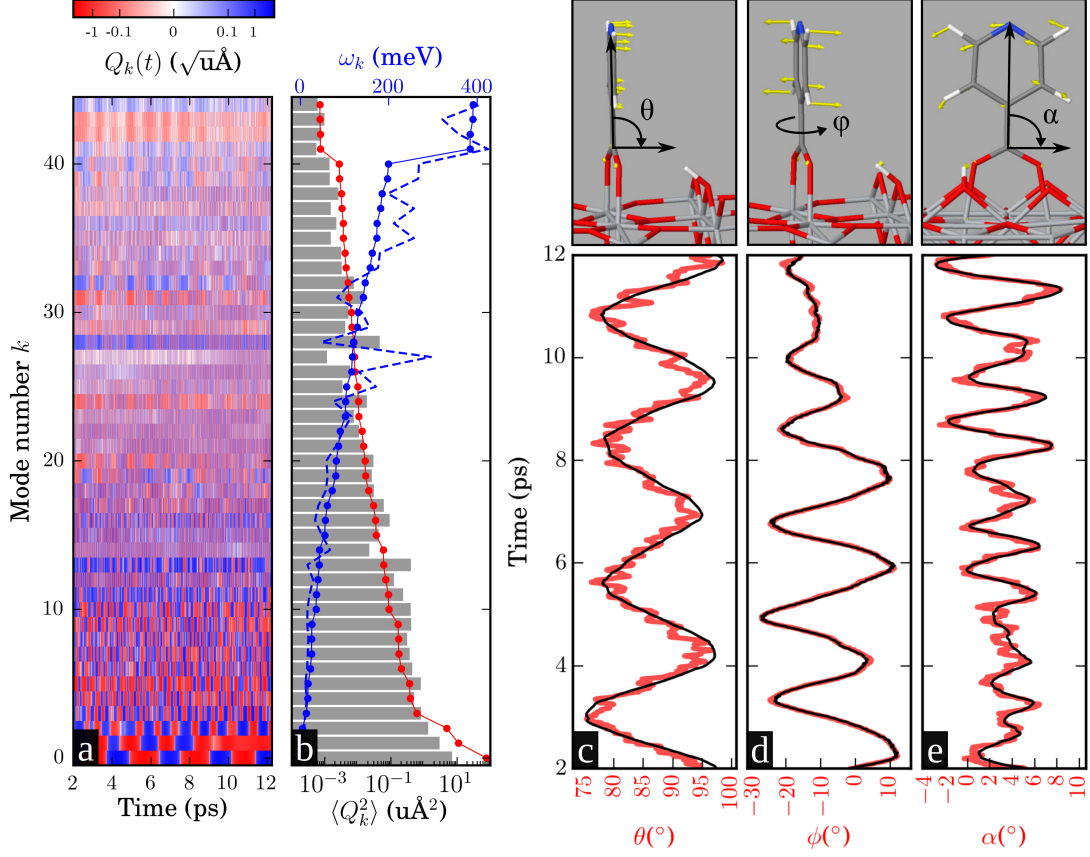
**Figure 5.11.:** Analysis of the CPMD trajectory of isonicotinic acid on TiO₂ in the normal mode basis of the adsorbate's atoms and the two Ti atoms, where the adsorbate is attached. (a) Color plot of the time evolutions of the normal mode coordinates $Q_k(t)$. (b) Corresponding bar plot showing the variance of the normal mode coordinates $\langle Q_k^2 \rangle$ in comparison with the quantity $k_B T / \omega_k^2$ (connected red dots). Additionally shown are the frequencies $\omega_k$ from a frozen phonon calculation (connected blue dots) in comparison with the frequencies $\tilde{\omega}_k = (k_B T / \langle Q_k^2 \rangle)^{-1/2}$ [cf. Eq. (5.28)]. (c-e) Visualization of the three lowest frequency mode vectors (yellow arrows) in the top panels. The displayed displacement vectors of the modes refer to (c) tilting, (d) twisting, and (e) sidewards bending with respect to the angles $\Theta$, $\phi$, and $\alpha$. The evolutions of the angles are shown in the bottom panels (red lines), they coincide with the evolutions of the coordinates $Q_k$ (black lines).

### 5.3.3. Mode Specific Analysis of the Electron-Vibrational Coupling

Employing a basis of vibrational eigenmodes $\{\mathbf{b}_k\}$ as introduced in Section 5.3.1,

$$\mathbf{b}_k = \sum_{j=1}^{3N} \frac{A_{jk}}{\sqrt{M_j}} \mathbf{e}_j \tag{5.30}$$

one can expand a chosen quantity $w(\mathbf{R})$ around the equilibrium position $\mathbf{R}_0$ along the normal coordinates $Q_k$ [cf. Eq. (5.19)]. If this is done to first order one obtains the following linear model

$$\Delta w = w(\mathbf{R}) - w(\mathbf{R}_0) = w \left( \mathbf{R}_0 + \sum_k Q_k \mathbf{b}_k \right) - w(\mathbf{R}_0)$$

$$\approx \sum_k Q_k \left( \frac{\partial w}{\partial Q_k} \right)_{Q_k=0} = \sum_k Q_k m_k = \mathbf{Q} \cdot \mathbf{m}, \tag{5.31}$$

where we defined the couplings $m_k = \left( \frac{\partial w}{\partial Q_k} \right)_{Q_k=0}$ and adopt a vector notation in the last step.

Assuming that the approximation in Eq. (5.31) holds for each of the $i = 1, \dots, N_\mathrm{s}$ snapshots in a molecular dynamics trajectory, one can write $\Delta w_i \approx \sum_k Q_{i,k} m_{i,k}$. If we further assume there exists a constant effective coupling $\overline{m}_k$ for all the snapshots, we can write $\Delta w_i \approx \sum_k Q_{i,k} \overline{m}_k = \Delta w_i'$, which reads in matrix notation

$$\mathbf{\Delta w} \approx \mathbf{C} \cdot \overline{\mathbf{m}} = \mathbf{\Delta w'}. \tag{5.32}$$

Here, $\mathbf{\Delta w}$ is a vector containing the deviations $\Delta w_i$ of the quantity $w_i$ from the equilibrium value $w(\mathbf{R}_0)$ for each of the $N_\mathrm{s}$ snapshots. Further we have introduced the effective vector $\overline{\mathbf{m}}$ containing the average couplings $\overline{m}_k$ corresponding to each of the $3N$ modes ($k = 0, \dots, 3N-1$). $\mathbf{C}$ is the $N_\mathrm{s} \times 3N$-matrix containing the corresponding $3N$ normal coordinates $Q_{i,k}$ specifying the geometry of the molecule at each snapshot $i$.

If the number of snapshots $N_\mathrm{s}$ is larger than the number of modes $3N$, Eq. (5.32) is overdetermined. In this case one can perform a *pseudoinversion* of the problem in search of an optimal solution $\overline{\mathbf{m}}$. This can be achieved by performing a singular value decomposition [222] of the normal mode coefficient matrix $\mathbf{C} = \mathbf{U}\mathbf{\Sigma}\mathbf{V}^\mathrm{T}$, where $\mathbf{U}$ is a $N_\mathrm{s} \times 3N$-matrix (the columns of $\mathbf{U}$ are orthonormal), $\mathbf{\Sigma} = \mathrm{diag}(s_1, \dots, s_{3N})$ is a diagonal $3N \times 3N$-matrix, and $\mathbf{V}$ is a $3N \times 3N$-matrix. The pseudoinverse of the matrix $\mathbf{C}$ in terms of the singular value decomposition is defined as $\mathbf{C}^+ = \mathbf{V}\mathbf{\Sigma}^+\mathbf{U}^\mathrm{T}$. Here, the pseudoinverse of $\mathbf{\Sigma}$, is given by the diagonal matrix $\mathbf{\Sigma}^+ = \mathrm{diag}(1/s_1, \dots, 1/s_{3N})$, where the diagonal elements $1/s_i$ are set to zero for all $s_i = 0$ with $i = 1, \dots, 3N$. Making use of the pseudoinverse $\mathbf{C}^+$ one can compute the effective couplings $\overline{\mathbf{m}}$ by

$$\overline{\mathbf{m}} = \mathbf{C}^+ \cdot \mathbf{\Delta w}. \tag{5.33}$$

The obtained effective coupling $\overline{\mathbf{m}}$ minimizes the Euclidian norm $\|\mathbf{C}\overline{\mathbf{m}} - \mathbf{\Delta w}\| = \|\mathbf{\Delta w'} - \mathbf{\Delta w}\|$ and hence is the best solution to the linear problem given by Eq. (5.32)
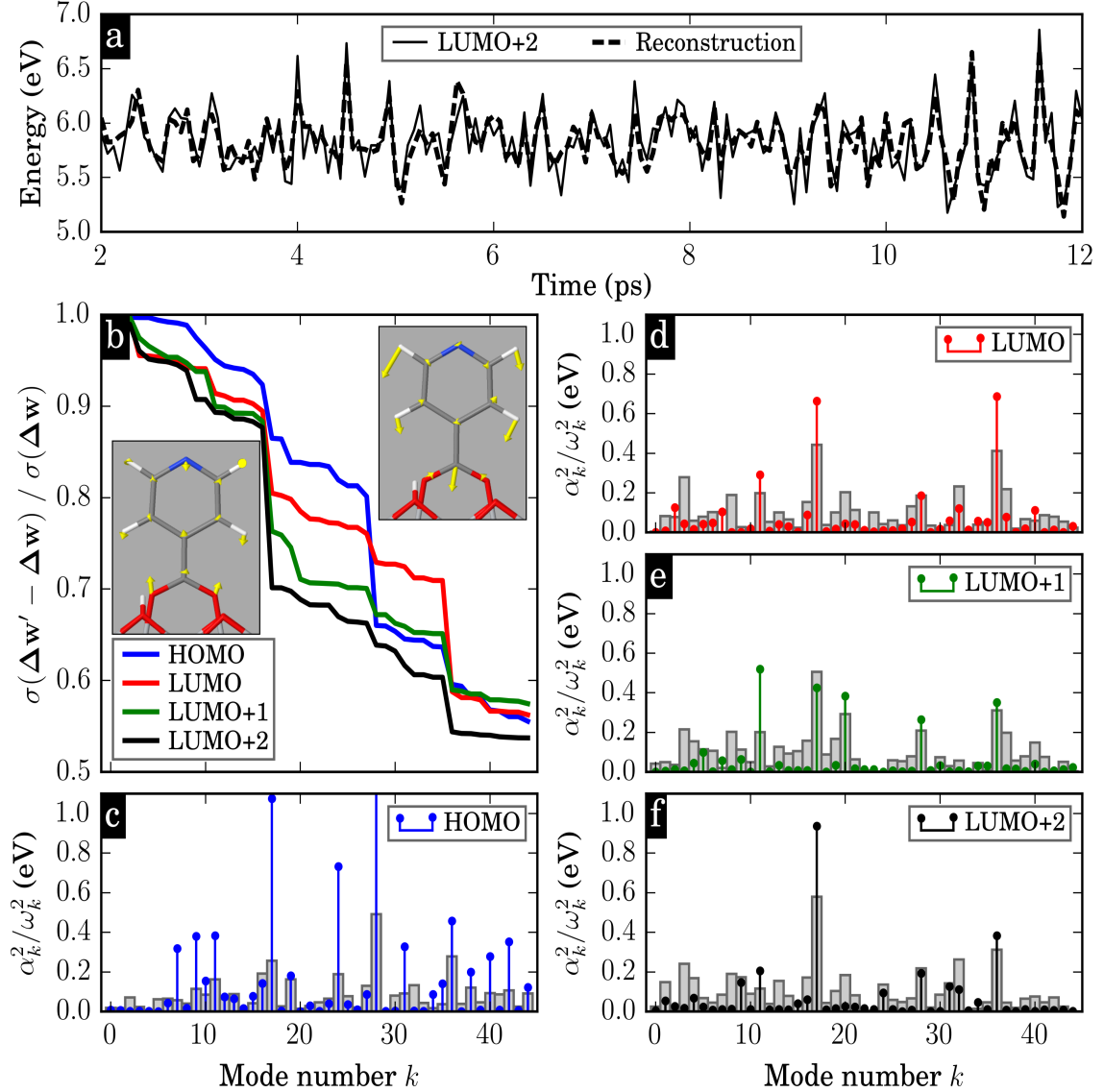
**Figure 5.12.:** Analysis of the electron vibrational coupling for the HOMO, LUMO, LUMO+1, and LUMO+2 resonances of isonicotinic acid on TiO$_2$(110) in the ground state. (a) Reconstruction of the energy fluctuations $\mathbf{\Delta w'}$ of the LUMO+2 (thick dashed line) in comparison with the fluctuations of the original resonance positions $\mathbf{\Delta w}$ (solid line) around the equilibrium energy position [cf. Eq. (5.32)]. (b) Quality of the reconstructed energy positions of the molecular resonances of isonicotinic acid (HOMO to LUMO+2) in terms of the ratio between the standard deviation $\sigma(\mathbf{\Delta w'} - \mathbf{w})$ of the reconstructed energy fluctuations $\mathbf{\Delta w'}$ from the original ones $\mathbf{\Delta w}$ and the standard deviation of the original resonance positions $\sigma(\mathbf{\Delta w}) = \sigma(\Delta E_R)$. Including only the lowest frequencies up to mode number $k$ and incrementally raising $k$, leads to an increasingly more accurate reproduction of the original data. In particular, mode 17 [(b) left inset] and mode 36 [(b) right inset] improve the description substantially, as can be seen from the sharp drops of the lines upon their inclusion. This observation coincides with the contributions from the couplings $\alpha_k^2/\omega_k^2$ (with $\alpha_k^2 = \overline{m_k^2}$) of the corresponding modes $k$ (c-e). The gray bar plots in (c-e) refer to the Pearson correlation of the energy positions $\mathbf{\Delta w}$ of the molecular resonances at each snapshot with the normal mode coordinates $Q_k$.

in the sense of a least square optimization [222]. Therefore, Eq. (5.33) provides a way to extract effective mean couplings $\overline{m}_k$ of the vibrational modes to some quantity $w$ by fitting a linear model to the snapshots of a molecular dynamics simulation.

We have applied this model to the CPMD trajectory from Section 5.2 ($N_\mathrm{s} = 161$) in order to extract the effective electron-phonon couplings of the molecular levels of isonicotinic acid on TiO$_2$(110). For this purpose, we set the quantity $w$ in Eq. (5.31) to the energy positions $E_R$ of the molecular resonances at each of the snapshots in Figs. 5.7 and 5.9. The results for the electron-phonon couplings related to the HOMO to LUMO+2 in the ground state are summarized in Fig. 5.12.

In Fig. 5.12a the fluctuations of the original positions of the resonances $\mathbf{\Delta w}$ for snapshots of the CPMD trajectory are displayed for the LUMO+2, which can be compared with the reconstructed fluctuations of the energy level $\mathbf{\Delta w}'$ [cf. Eq. (5.32)]. The overall correspondence is visibly good. The quality of the reconstruction can be estimated by calculating the ratio $\sigma(\mathbf{\Delta w}' - \mathbf{\Delta w})/\sigma(\mathbf{\Delta w})$, where $\sigma(\mathbf{\Delta w}' - \mathbf{\Delta w})$ is the standard deviation of the reconstructed fluctuations $\mathbf{\Delta w}'$ from the original fluctuations $\mathbf{\Delta w}$ in the snapshots. We emphasize here that $\sigma(\mathbf{\Delta w}) = \sigma(E_R)$ corresponds to the standard deviation of the original energy positions $E_R$ discussed in Section 5.2. We calculated the ratio $\sigma(\mathbf{\Delta w}' - \mathbf{\Delta w})/\sigma(\mathbf{\Delta w})$ for the HOMO up to the LUMO+2 while successively increasing the amount of the considered vibrational modes in the description (following the order of the modes specified in Fig. 5.11). In Fig. 5.12b one can see that a large part of the standard deviation is captured by the linear model upon the inclusion of all 45 vibrational modes related to the molecule on the surface. The remaining deviations are due to non-linearities not captured by the model or vibrations inside the substrate.

Furthermore, it is clearly visible in Fig. 5.12b that the modes number 17 and number 36 couple most strongly to the LUMOs (i.e. LUMO up to LUMO+2). The corresponding displacement vectors are shown in the insets of Fig. 5.12b (mode 17 left inset, mode 36 right inset). It can be seen that both modes involve strongly the carbon atom or the two oxygen atoms linking the molecule to the surface.

Also a direct assessment of the frequency-scaled electron phonon couplings $\alpha_k^2/\omega_k^2$ [with $\alpha_k = \overline{m}_k$, cf. Eq. (5.27)] in the subplots Fig. 5.12d-f (colored stem plots) shows clearly that the modes 17 and 36 exhibit the highest coupling strength with respect to the examined LUMOs. It is also visible, that mode 28 –a breathing mode of the

**Table 5.5.:** Broadening of the molecular resonances of isonicotinic acid on TiO$_2$ based on the extracted electron phonon couplings in comparison with the standard deviations from the original data.

|  | ground-state | | core-excited | |
|---|---|---|---|---|
|  | $\sigma$ [Eq. (5.27)] | $\sigma(E_R)$ | $\sigma$ [Eq. (5.27)] | $\sigma(E_R)$ |
| HOMO | 0.37 | 0.45 | 0.21 | 0.24 |
| LUMO | 0.30 | 0.30 | 0.06 | 0.08 |
| LUMO+1 | 0.22 | 0.27 | 0.12 | 0.12 |
| LUMO+2 | 0.23 | 0.29 | 0.11 | 0.13 |

pyridin cycle– strongly affects the HOMO (cf. Fig. 5.12c) but has a considerably lower effect upon the LUMOs.

The bar plots, which are additionally shown in Fig. 5.12, represent the Pearson correlation of the normal coordinates $Q_k$ with the energy levels $E_R$ (the Pearson correlations are plotted on the same axes, while they assume as usual dimensionless values ranging from zero to one). As one expects, strong electron-vibrational couplings are linked to strong correlations between $Q_k$ and $E_R$.

We conducted the above analysis of the electron-phonon couplings analogously for the resonance positions $E_R$ of the core-excited isonicotinic acid molelecule (including an N1s-core-hole in the calculations). The results of this analysis can be found in the Appendix C.7. There, it is visible that the vibrational mode 17 is also noticeably influencing the core-excited molecular levels and in particular the LUMO+2 which is the level probed by the core-hole-clock experiments. However, overall it is harder to single out a dependence on particular modes in the core-excited state.

A dependency on particular modes (as in Fig. 5.12) is even less apparent, when investigating a connection of the modes with the electronic widths $\Gamma(E_R)$ at each snapshot [or equally with the matrix elements $\Gamma(E_R)/\rho(E_R)$]. Reasons for this may be an increasingly non-linear behavior of these quantities, additional influences from the motion of the atoms in the substrate, or merely a simultaneous dependence of $\Gamma(E_R)$ on a broad range of modes.

As a final consistency check one may sum up the extracted electron phonon couplings $\alpha_k^2/\omega_k^2$ with $\alpha_k = \overline{m}_k$ from all vibrational modes according to Eq. (5.27) and compare the obtained standard deviation with the one from the original data set $\sigma(E_R)$. This can be done by inspecting Table 5.5. The table shows a good agreement of the two values of standard deviations, while non-linear behavior or fluctuations in the substrate may be possible sources of deviations.

## 5.3.4. Conclusion and Outlook

In this section we have discussed the role of specific vibrational modes in broadening the electronic spectra of isonicotinic acid adsorbed on rutile(110). We set up a semi-classical model, which describes the spectral broadening in terms of linear electron-phonon couplings and explains the Gaussian character of the emerging line shapes.

While in general the largest structural deviations at finite temperatures are due to low-frequency modes, a broad range of eigenmodes may contribute to the spectral broadening of the energy levels. This makes it hard to narrow down the sources of the level fluctuations to a few dominant modes, instead it is necessary to study all vibrational modes coupling to the molecular levels. We find in the case of isonicotinic acid on TiO$_2$(110) that stretching modes involving the anchoring carboxyl groups of the dye-molecules on the surface exhibit particularly large electron-phonon couplings and therefore are a primary source of the fluctuations in the molecular levels. Because of their strong contributions to these fluctuations, these modes are expected to affect the lifetimes of the states to which they couple. However, a direct connection of the vibrational modes with the lifetimes of the molecular states could not be established.

Further theoretical studies on isonicotinic acid at TiO$_2$(110) or similar systems may aid in designing future combined experiments, where the activity of single vi-

brational modes can potentially be driven by infrared beams, while simultaneously charge transfer is monitored by core-hole-clock spectroscopy. Comparably, but less specific, temperature dependent core-spectroscopy studies could be used to gain further insight into the effects of structural fluctuations on charge transfer, although measuring at higher temperatures may introduce considerable noise in such experiments. Another possibility in order to investigate similar effects could be to conduct core-hole-clock experiments on molecules containing different isotopes of the constituting atoms to tune the vibrational frequencies.

# Chapter 6

# Spin-Dependent Charge Transfer on Magnetic Surfaces

Argon atoms on magnetic substrates played in recent years an important role for the investigation of spin-dependent charge injection using core-hole-clock spectroscopy [49–51]. These measurements revealed that electrons promoted from corestates to unoccupied resonances on Argon are significantly longer-lived for majority spin than for minority spin on Fe(110) and Co(0001) surfaces. Up to date these experimental results have not been reproduced by independent theoretical calculations and the origin of the spin dependency of the charge transfer is subject to ongoing discussion.

In this chapter we simulate spin-dependent charge injection by applying the Green's function technique described in Chapter 3 to core-excited Argon atoms on magnetic Fe(110) and Co(0001) surfaces. We find a good agreement with the experiments in terms of the overall trends and the absolute values of the experimentally detected charge transfer times.

It has been suggested, that the difference in the charge transfer time between the two spin channels could possibly explained by the available DOS of d-symmetry at the interface [50] and the need for theoretical studies to discuss this in detail has been mentioned at various places [19, 50, 223]. We argue here on the basis of our first-principles calculations, that such a picture would be incomplete if not misleading in the case of Ar on the studied surfaces: While there exists an inverse proportionality relation between the charge transfer times and the amount of d-type DOS at a given energy, this does not provide a consistent reasoning to explain the phenomenology.

In fact, for Cs on Fe(110) theoretical calculations by Muiño et al. [122] indicated the opposite relation between the line widths and the available DOS of d-type symmetry at the resonance position. In connection with this initial result, Blobner et al. [50] suggested to extrapolate such a relation to the case of Ar on Fe(110) and Co(0001), finding a contradiction. However, we want to stress that there is a conceptual difference between those two works. The discussion in Ref. [122] is made in terms of the angular momenta of the atomic states giving rise to the substrate bands at the resonance position, thus, distinguishing bands of different symmetry (i.e., flat d bands

as opposed to dispersive sp bands of Fe and Co). However, Ref. [50] used a decomposition of the DOS around the resonance position into different angular momentum components by means of a projection scheme, which leads to the appearance of a non-zero partial DOS of d-symmetry with respect to the atomic centers. However, in the latter case, the d bands of Fe and Co (following traditional nomenclature) appear at lower energies than the Ar*4s resonance and, thus, do not play a crucial role in the measured charge transfer process. Therefore, although both references used a similar nomenclature, in practice they referred to different concepts.

We demonstrate, that the differences in the line widths are instead related to the spin-dependent sizes of the electronic gaps at the energy of the Ar resonance in the surface-projected band structures of the magnetic surfaces. It has been emphasized before that the presence of such electronic gaps is important to characterize charge transfer processes at interfaces [34, 35, 41, 224–226]. Here, the effect of the gaps is studied by mapping out the line shapes of the relevant 4s-resonances of Argon in reciprocal space. Subsequently, a simplified model [35] incorporating the effect of the electronic gaps is used to explain the spin-dependent behavior for Fe(110) and Co(0001) at a semi-quantitative level. Generally, the effect of electronic gaps on charge transfer depends strongly on the particular interface being considered.

The chapter is structured in the following way: First, we analyze the simplest approach, where the initial wave packet of the 4s-resonance of the core-excited argon on Fe(110) and Co(0001) is described in terms of the 4s orbitals of an isolated Ar* atom. Secondly, we attempt an improved description considering the polarization of the initial wave-packets at the interface by the admixture of $4p_z$-components. Subsequently, we study the competing effects of the spatial overlap of the resonance wave packet with the states inside the surface, the energetic position of the resonance, and the presence of electronic gaps in surface projected band structures. Finally, we wrap the observations up by employing a simplified model [35], explaining the spin-dependent behavior.

## 6.1.  Argon on Co(0001) and Fe(110) - Computational Settings

For the investigation of the resonances of Argon adsorbed on magnetic Fe(110) and Co(0001) the following computational set-up was employed. In order to obtain relaxed crystal structures we computed bulk Fe in the body centered cubic (bcc) primitive lattice and Co in the hexagonal close packed (hcp) primitive lattice. The primitive cell of bulk Co contains two atoms. The lattice constants of the primitive cells were determined by periodic bulk calculations relaxing the forces and stresses. The underlying SCF cycles were considered converged if the elements in the density matrix changed by less than $10^{-4}$. All geometry relaxations used a force tolerance of 25 meV/Å and a maximum atomic displacement of 0.1 Bohr in consecutive relaxation steps.

The calculations employed the PBE functional and a double-$\zeta$ basis set, unless otherwise stated. Moreover, we make use of norm-conserving Troullier-Martins pseu-

dopotentials [109]. The basis was constructed with a SIESTA specific energy shift parameter of 0.1 eV and the calculations were run at an electronic temperature of 300 K.

The lattice constants converged within $\pm 0.01$ Å for a mesh cutoff of 250 Ry and a Monkhorst Pack grid of $10 \times 10 \times 10$ to a value of $a = 2.88(2)$ Å for Fe and $a = 2.51(0)$ Å and $c = 4.09(8)$ Å for Co. The magnetic moments showed a much slower convergence: At a k-point sampling of $20 \times 20 \times 20$ we obtained a converged bulk magnetic moment per atom of 2.28 $\mu_B$ for Fe and of 1.64 $\mu_B$ for Co using a $22 \times 22 \times 14$ k-point grid. Wherever an even number of k-points along one direction in the reciprocal lattice was used, the sampling in that direction was shifted by 0.5 diminishing the amount of irreducible points in the Brillouin zone [28, 180].

We modeled clean surfaces using 11-layer slabs where the outermost layer on each side was allowed to relax. We used a mesh cutoff of 250 Ry and a k-point sampling of the surface Brillouin zone of $20 \times 20 \times 1$ for Fe and $22 \times 22 \times 1$ for Co, consistent with the values used for the bulk calculations. With these settings the total energies converged within $\pm 10$ meV. The change of the outer Fe layer was barely noticeable leaving the interlayer distance of 2.04 Å unchanged. The outermost Co layers relaxed slightly outwards changing the interlayer spacing of equally 2.04 Å by less than 2 %.

To quantify the magnetization of the surfaces we extracted the magnetic moment inside the slab and at the surface. At the surface we obtained 2.82 $\mu_B$ for Fe and 1.78 $\mu_B$ for Co. The magnetic moment of the innermost layers of the slabs was found to be 2.29 $\mu_B$ per atom for Fe and 1.64 $\mu_B$ for Co. These values agree with those from our periodic bulk calculations stated above. We note, that this is important in order to ensure a good alignment of the spin-polarized band structure deep inside the slab with that of the bulk material. Such a matching is necessary for the subsequent connection of the slabs to the semi-infinite bulk electrodes. Increasing the size of the slab further to 15 layers did neither change the magnetic moment on the surface atoms nor the magnetic moments of the inner atoms of the slab by more than $\pm 0.01$ $\mu_B$. The values for the magnetic moments agree well with experimental values of 2.22 $\mu_B$ for Fe and 1.72 $\mu_B$ for Co [227], as well as with calculations, e.g., Refs. 228–231 for Fe and Refs. 229, 231 for Co.

The ideal surface structures are depicted in Fig. 6.1 showing the hexagonal Co(0001) and the non-hexagonal Fe(110) surfaces from the top and side view. Both materials follow an ABAB stacking scheme. The Argon atoms were attached to the Fe or Co surfaces in top-position in Fig. 6.1 with varying adsorption heights $h$. In the Appendix D other possible adsorption sites are taken into account. As shown there, charge-transfer times are rather insensitive to the adsorption site and, thus, in the following we will focus only on the results obtained for the top configuration. We considered $4 \times 4$ unit cells in single point calculations and employed a k-point sampling of $5 \times 5 \times 1$ and $6 \times 6 \times 1$ for Fe and Co, respectively.

Regarding the bulk calculations needed to construct the self-energy terms entering the surface Green's functions we considered a smaller $1 \times 1$ unit cell of the electrode with 6 layers and a k-point sampling of $20 \times 20 \times 5$ and $24 \times 24 \times 5$ for Fe and Co, respectively. The four-fold k-point sampling parallel to the surface allows to expand the Bloch-waves of the electrodes and to connect with the $4 \times 4$ supercell of the scattering regions. This feature is implemented in recent versions of the TBTrans/TranSIESTA
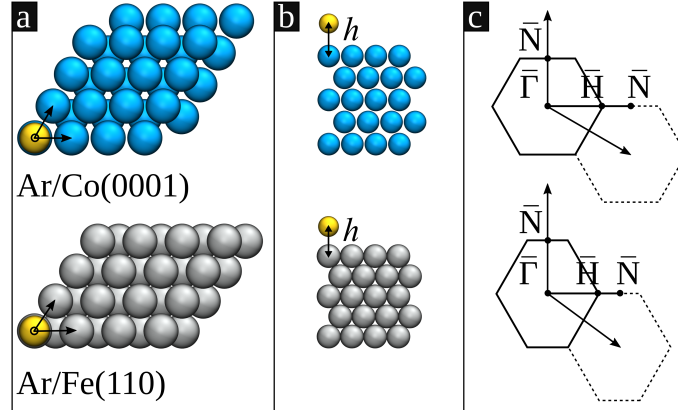
**Figure 6.1.:** Geometric properties of our models for Ar/Co(0001) (top panels) and Ar/Fe(110) (bottom panels) interfaces in real space and in reciprocal space. (a) Top views of the computational unit cells of the slabs showing the primitive lattice vectors of the clean surfaces. (b) Side views of slabs of five layers. The core-excited argon atom is attached to the metallic surfaces in top position (directly on top of an atom in the surface) at an adsorption height $h$. (c) Schemes of the respective surface Brillouin zones showing the reciprocal lattice vectors and the high symmetry points $\bar{\Gamma}, \bar{H}$, and $\bar{N}$. The non-hexagonal surface structure of Fe(110) is reflected in its Brillouin zone.

code.

As in the case of isonicotic acid on TiO$_2$ (Chapter 5) we modeled the decorated surfaces as tunneling junctions (two electrodes separated by vacuum) owing to the version of TranSIESTA we are using. In the case of Fe(110) we analyze a surface region of 6 layers where the last 3 layers are connected to the self-energy of the semi-infinite substrate. For the simulations of Co(0001) a larger surface region of 8 layers was required, where the last 4 layers carried the self-energy of the semi-infinite substrate. This resulted from careful checks regarding the amount of bulk layers included. In both cases the vacuum between the metal surfaces was $\sim 40$ Å. The infinite slabs were not treated self-consistently regarding the calculation of the Green's functions. For the small imaginary broadening parameter used to calculate the Green's functions in this chapter we employed a value of $\eta = 5$ meV, which we have tested to yield converged results for the lifetimes.

## 6.2. Constrained Model to Account for Excitations

In relation to the experiment, we consider as in Chapter 5 a core-excited system, including a 2p-hole in the pseudopotential. In contrast to the previously studied systems the localized charge of the excited electron tends to delocalize over the entire system, because the populated state is resonant with the conduction band of the substrate. We prevent the latter by using a constrained approach. The system is effectively modeled in an intermediate state, where the core-excited electron is

located on the Argon atom before it relaxes to the surface. In the following such a core-excited Argon atom is denoted by Ar*. The excited electron is constrained by fixing the occupation of the first $\zeta$-component of the 4s-orbital of the Argon atoms to a value of one, following the procedure in Ref. 35. This means that the population of the 4s1$\zeta$-orbital is not allowed to relax during the SCF cycle. In our case two Argon atoms are present at the positions $\mathbf{R}_1$ and $\mathbf{R}_2$: one on each side of the slab in order to obtain a symmetric system. The total density is then constructed from the relaxed Kohn-Sham density $\rho^{N_e-2}$ of the $(N_e - 2)$-electron system plus the density of the two constrained 4s orbitals

$$\rho(\mathbf{r}) = \rho^{N_e-2}(\mathbf{r}) + \rho^{4s1\zeta}(\mathbf{r} - \mathbf{R}_1) + \rho^{4s1\zeta}(\mathbf{r} - \mathbf{R}_2) \tag{6.1}$$

$$= \sum_{i=1}^{N_e-2} |\phi_i(\mathbf{r})|^2 + |\varphi^{4s1\zeta}(\mathbf{r} - \mathbf{R}_1)|^2 + |\varphi^{4s1\zeta}(\mathbf{r} - \mathbf{R}_2)|^2. \tag{6.2}$$

Here, the $\phi_i(\mathbf{r})$ are the $N_e - 2$ self-consistently computed Kohn-Sham states of lowest energy, while the $\varphi^{4s1\zeta}(\mathbf{r} - \mathbf{R}_1)$ are the 4s1$\zeta$ orbitals of the two core-excited Ar* atoms on each side of the slab. The basis set of each Ar*-atom consisted of 16 pseudo atomic orbitals: the double-$\zeta$ components of 4s- and 3p-shells as well as the single-$\zeta$ bases of the 4p- and 3d-shells. The spin of the constrained electron was specified explicitly in the simulations to mimic the excitation of a particular spin.

## 6.3.  Spin Dependence of the Charge Transfer Time

In the following the results for the 4s-resonance spectra of Ar* adsorbed on Fe(110) and Co(0001) surfaces are analyzed, the spin-dependent charge injection times are extracted, and the observed behavior is discussed in comparison with the experiment.

Fig. 6.2a, b show the imaginary part of the projection of the Green's function $-\frac{1}{\pi} \text{Im}[\langle \phi_R | G^+(E) | \phi_R \rangle]$ onto the initial wave packet $\phi_R$ for the Ar*4s-resonances on Fe(110) and the two spin channels. The spectra are shown for varying adsorption heights starting from 2.4 Å up to 3.6 Å changing in steps of 0.3 Å (Fig. 6.2a, b). It is visible that a closer positioning of the adsorbate towards the surface leads to a stronger confinement of the resonance wave packet causing an upwards shift towards higher energies.

Examining the shapes of the resonance peaks, deviations from an ideal Lorentzian lineshape and the associated purely exponential decay are visible. The Lorentzian fits to the resonances are indicated by narrow black lines in the plots. In the case of the majority channel in Fig. 6.2a an extended tail towards the Fermi level (at 0 eV) is visible at all adsorption heights, while the peak shape becomes increasingly asymmetric at lower adsorption heights. For the minority channel in Fig. 6.2b the resonances exhibit shoulders around 2 and 3 eV as the onset of the more localized d-bands around 2 eV is approached (see also the band structure in Fig. 6.8 introduced further below). This leads to some deviations from the Lorentzian line shape that complicate the analysis. Readily, after the inspection of the graphs, it is evident that
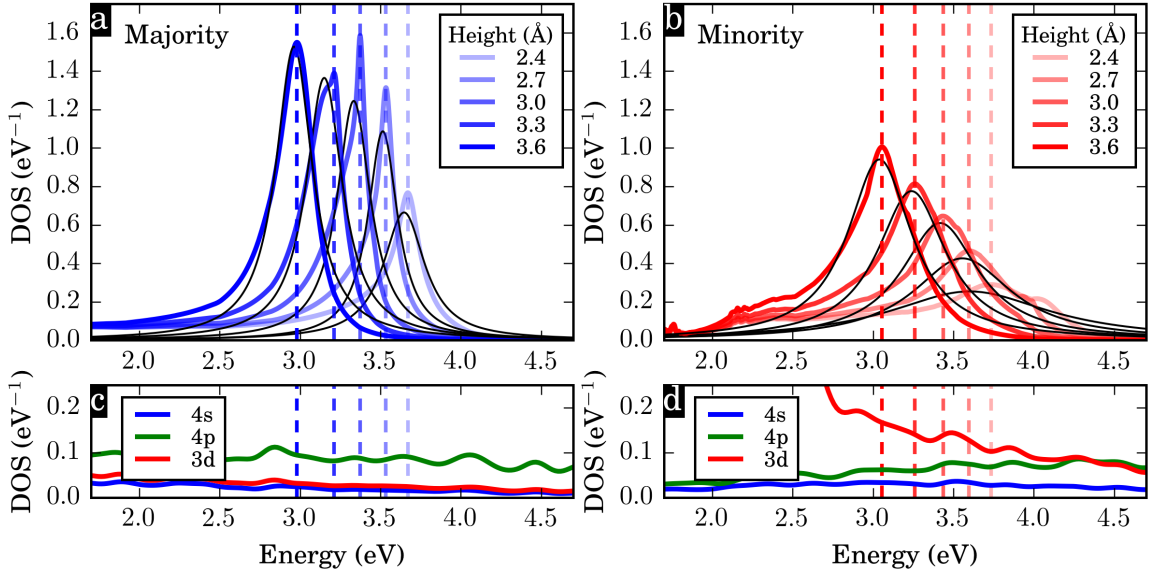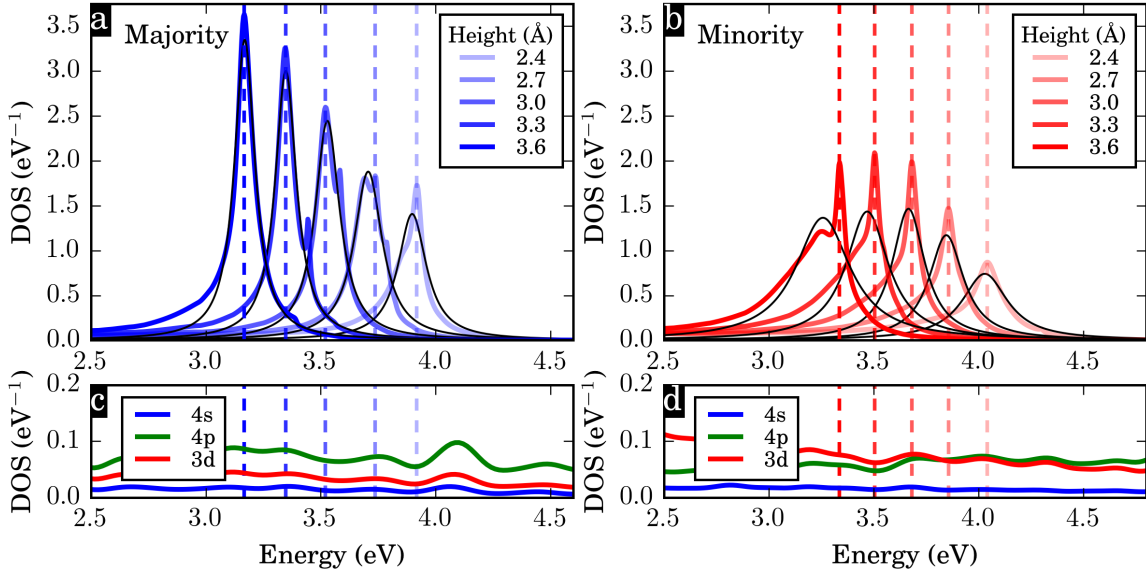
**Figure 6.2.:** Resonance peaks appearing in the imaginary part of the Ar*4s projected Green's function for Ar*/Fe(110). The majority (a) and minority (b) channels are shown for various adsorption heights. The thin black lines represent Lorentzian fits to the resonance spectra. The DOS projected onto different components of the angular momentum of the surface atoms of clean Fe(110) is shown in (c) and (d) for the respective spin channels. The resonance positions (peak maxima) are indicated by dashed lines in (a, c) and (b, d). The energies in the subplots refer to the Fermi level.

the broadened minority channel is associated with faster charge transfer than the majority channel.

The interaction with the d-states in the substrate has been mentioned as a possible source of the difference between the majority and minority lifetimes, while a connection to the sp-states would result in opposite trends [50]. At first sight, this interpretation holds in a direct comparison of different angular contributions to the DOS of a clean surface at the respective resonance positions, as can be seen in Fig. 6.2c, d. The DOS projected onto d-symmetry orbitals for minority spin exceeds that of the majority spin over the whole range of the Ar* resonance positions (dashed lines in the plots). However, it has already been pointed out that such a relation between an available DOS of strong d-character and a larger coupling to the substrate is somehow counterintuitive since d-states are typically localized in nature and contribute less to charge transfer [19]. The latter is indeed, what we see in our calculations. Moreover, there are no bands of clear d-type atomic character (i.e., derived from the atomic 3d states) in the energy range of interest where the Ar* resonances appear.

In this context, it is important to consider the origin of labeling states by their symmetries (s, p, d, f, etc.). From a chemists point of view the band-like states in solids are formed by the orbitals of the constituent atoms and their overlaps determine the dispersions of the bands [232]. Thus, localized d-states constitute less dispersive bands than s- or p-bands. The concept of associating bands with symmetries is straightforwardly applied in DFT-codes employing atomic orbital basis-sets. On the

**Figure 6.3.:** Majority (a) and minority (b) resonance peaks appearing in the imaginary part of the Ar*4s projected Green's function for Ar*/Co(0001). The surface projected DOS of the clean Co(0001) slab due to different components of the angular momentum is shown in (c) and (d). The figure is organized analogously to Fig. 6.2.

other hand, analyzing the electronic structure by projecting into localized orbitals can lead to misleading results. An example of this occurs when using projection routines to analyze states of predominant plane-wave character. The higher the energy of the plane-wave state the stronger it's variation in space, which is eventually captured best by projections onto more localized (e.g., d-type) states in a finite atomic orbital basis-set. However, in this case an interpretation of highly dispersive plane-wave states as d-type states is not very meaningful.

An example of the projection of dispersive bands onto states labeled by a d-type symmetry can be seen in Fig. 6.2d (compare also with the surface band structure of Fe(110) in Fig. 6.8 on Page 103, where the flat d-bands, following traditional nomenclature, appear at energies below the resonance positions). Here the d-type DOS dominates the s- and p-contributions over an extended energy range associated with the underlying dispersive bands. Moreover, since the employed projection schemes vary from code to code, a unique identification of the bands' symmetries is not guaranteed.

The adsorption of Ar* on Co(0001) leads qualitatively to a similar picture, as can be seen in Fig. 6.3a, b. Here, both spin channels reveal long tails towards the Fermi level. For 2.7 Å to 3.3 Å small peak splittings are visible in the majority channel. The minority peak shows a growing shoulder that splits for larger adsorption heights at around 3.6 Å. Readily from the plots it is visible that the sharp peaks of the majority channel will lead to significantly longer lifetimes than the minority channel, as it has been observed in core-hole-clock experiments [50]. As before the contributions from different angular momenta to the DOS projected onto the surface in Fig. 6.3c, d indicates that the difference in peak widths between the spin channels appears to correlate with the amount of DOS projected onto the d-orbitals. However,
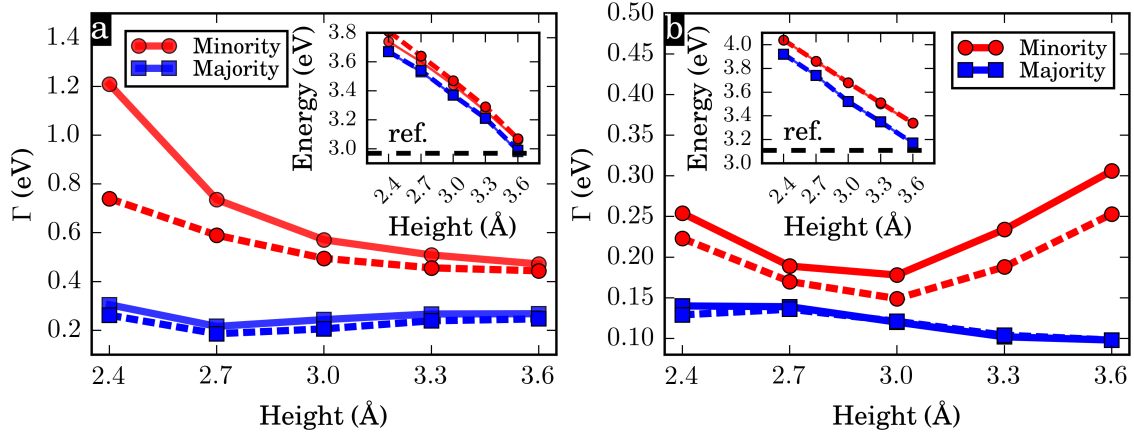
**Figure 6.4.:** Extracted line widths of the Ar*4s resonances from Lorentzian fits and energy positions of peak maxima with respect to different adsorption heights (insets). Minority and majority channels are displayed. Subplot (a) refers to Ar*/Fe(110) and subplot (b) shows the case of Ar*/Co(0001). The dashed lines in the insets refer to the resonance energies determined in the experiment [50]. The dashed lines in the main panels display the values obtained using optimized wave packets to describe the Ar*4s-resonance, which take into account polarization effects in the presence of the surface (see also Section 6.4). Continuous lines correspond to values obtained using a single atomic Ar*4s orbital to model the resonance wave function.

as explained above this should not be interpreted as an indication that a larger amount of available d-states leads to shorter lifetimes (larger coupling). This rather indicates that the highly dispersive bands of Co(0001) (see also the band structure of Co(0001) in Fig. 6.9 on Page 104) in this energy range present a large contribution from d-symmetry basis orbitals. The inspection of the DOS at the interface across different adsorption heights (Fig. 6.3d) shows that the variations of the peak widths at different energetic positions (Fig. 6.3b) do not resemble the d-type DOS.

To get a quantitative picture of the theoretically determined data and the associated trends on both substrates, the extracted line widths associated with the 4s-resonance are displayed in dependence of the adsorption height in Fig. 6.4 (continuous lines). Here, the line widths have been determined from the FWHM of a Lorentzian fitting (cf. Section 3.4).

For the minority channel on Fe(110) one observes that the line widths increase as the adsorbate approaches the surface. This is expected due to the increasing overlap of the adsorbate states with the surface states at lower adsorption heights. However, on Co(0001) the opposite trend is observed for the minority channel: The widths increase at larger distances from the surface and a minimum at around 3 Å adsorption height is observed. This behavior can be explained by considering the dispersion of the peaks in energy (cf. insets in Fig. 6.4) and the interplay with electronic gaps: the resonances become increasingly confined when approaching the surface, this leads to an up-shift of their energetic positions into regions with a different amount of available DOS. Importantly, the accessible DOS is determined by the interaction of the resonances with projected band gaps, as discussed in detail

in Section 6.5. As a result of this the line widths are controlled by the competing effects of the spatial overlap of the adsorbate wave function with the surface states, and the resonance position with respect to the surface band structure. Both effects are entangled through the adsorption height.

Also in the case of the majority channel opposite trends on both substrates are visible. On the Fe(110) substrate the widths show a minimum at around 2.7 Å adsorption height and the widths increase again at larger distances. On the Co(0001) substrate we find a continuously decreasing width upon increase in the adsorption height. While the trends on the two substrates behave rather oppositely, the majority channel exhibits independently of the distance and the substrate material smaller peak widths than the minority channel.

To complete the quantitative analysis we compare directly with the experimental results from core-hole-clock spectroscopies. In the setup by Blobner et al. [50] charge transfer dynamics from core-excited $Ar^*(2p_{3/2}^{-1}4s)$ adatoms on the magnetic surfaces Fe(110), Co(0001), and Ni(111) were probed using spin-selective core-excitation by circularly polarized light. Values for lifetimes of the $Ar^*4s$-resonance in a range from 2 to 3.3 fs have been reported [50]. In a follow-up work spin-selective core-hole-clock measurements using spin-independent excitation in combination with spin-selective detection of the decay spectra were proposed [49]. In a series of measurements this technique was shown to provide consistent results with the earlier measurements for Ar/Co(0001). In particular, the reported final average of this second type of measurements agrees with the first study by Blobner et al. [50] within the errorbars [51]. The experimentally reported quantities of these studies are summarized in Table 6.1.

We have determined the values for the lifetimes of the $Ar^*4s$-resonances by extracting peak widths from Lorentzian fits as well as with the direct approach by Fourier transformation (see Section 3.4) to the time-domain and estimating the lifetime by integrating Eq. (3.16) up to 30 fs (using larger integration ranges did not affect the results). Although the Lorentzian fits (shown by slim lines in Figs. 6.2 and 6.3) are not always optimal –since the peak shapes may exhibit long tails, shoulders, or peak splits– the agreement between the two methods is remarkable as the values in Tables 6.2 and 6.3 suggest.

For a quantitative comparison in-between the two substrates, and in-between the two spin-channels, as well as with the experiment [50] we display the extracted values

**Table 6.1.:** Majority and minority decay times $\tau_{\mathrm{maj.}}^{\mathrm{exp.}}$ and $\tau_{\mathrm{min.}}^{\mathrm{exp.}}$ of core-excited $Ar^*$ and the energetic position of the corresponding $Ar^*4s$-resonances $E_{\mathrm{R}}^{\mathrm{exp.}}$ on different magnetic metal substrates, as determined by core-spectroscopy experiments [50, 51].

|  | | $\tau_{\mathrm{maj.}}^{\mathrm{exp.}}$ (fs) | $\tau_{\mathrm{min.}}^{\mathrm{exp.}}$ (fs) | $E_{\mathrm{R}}^{\mathrm{exp.}}$ (eV) |
|---|---|---|---|---|
| Ar/Fe(110) | [50] | $2.67 \pm 0.15$ | $2.08 \pm 0.15$ | 2.97 |
| Ar/Co(0001) | [50] | $3.24 \pm 0.15$ | $2.63 \pm 0.15$ | 3.11 |
| Ar/Co(0001) | [51] | $3.1 \pm 0.20$ | $2.4 \pm 0.10$ | – |
| Ar/Ni(111) | [50] | $3.12 \pm 0.15$ | $3.12 \pm 0.15$ | 3.14 |

**Table 6.2.:** Various extracted quantities for Ar* resonances on Fe(110) related to the majority and minority spin channels. Values obtained using an Ar*4s1$\zeta$ orbital to model the resonance wave function and values obtained using an optimized wave packet containing a 4p$_z$ component: the peak maximum at $E_R$, the width $\Gamma$ extracted by a Lorentzian fitting, the related lifetime $\hbar/\Gamma$, and the lifetime $\tau_{FFT}$ obtained by the Fourier transform method described in Section 3.4. In the case of the optimized wave packet additionally the mixed-in percentages $|c_p|^2$ of 4p$_z$ contributions are given.

| Fe(110) | | $\|\phi_R\rangle = \|\varphi^{4s1\zeta}\rangle$ | | | | $\|\tilde{\phi}_R\rangle = c_s\,\|\varphi^{4s1\zeta}\rangle + c_p\,\|\varphi^{4p_z}\rangle$ | | | | |
|---|---|---|---|---|---|---|---|---|---|---|
| Height (Å) | | $E_R$ (eV) | $\Gamma$ (meV) | $\hbar/\Gamma$ (fs) | $\tau_{FFT}$ (fs) | $E_R^{opt.}$ (eV) | $\Gamma^{opt.}$ (meV) | $\hbar/\Gamma^{opt.}$ (fs) | $\tau_{FFT}^{opt.}$ (fs) | $\|c_p\|^2$ (%) |
| Majority | 2.4 | 3.67 | 305 | 2.16 | 2.14 | 3.67 | 262 | 2.51 | 2.52 | 63 |
| | 2.7 | 3.53 | 216 | 3.05 | 3.01 | 3.54 | 186 | 3.53 | 3.43 | 56 |
| | 3.0 | 3.37 | 244 | 2.70 | 2.81 | 3.37 | 206 | 3.18 | 3.21 | 50 |
| | 3.3 | 3.21 | 267 | 2.46 | 2.43 | 3.21 | 239 | 2.74 | 2.76 | 43 |
| | 3.6 | 2.98 | 268 | 2.45 | 2.36 | 2.99 | 247 | 2.66 | 2.64 | 33 |
| Minority | 2.4 | 3.74 | 1209 | 0.54 | 0.76 | 3.81 | 740 | 0.89 | 1.08 | 65 |
| | 2.7 | 3.60 | 736 | 0.89 | 0.99 | 3.64 | 590 | 1.12 | 1.26 | 57 |
| | 3.0 | 3.44 | 571 | 1.15 | 1.19 | 3.47 | 495 | 1.33 | 1.41 | 49 |
| | 3.3 | 3.26 | 509 | 1.29 | 1.30 | 3.29 | 456 | 1.44 | 1.51 | 41 |
| | 3.6 | 3.06 | 472 | 1.39 | 1.40 | 3.07 | 444 | 1.48 | 1.55 | 32 |

**Table 6.3.:** Extracted quantities for Ar* resonances on Co(0001) related to the majority and minority spin channels. The table is organized completely analougous to the case of Fe(110) in Table 6.2.

| Co(0001) | | $\|\phi_R\rangle = \|\varphi^{4s1\zeta}\rangle$ | | | | $\|\tilde{\phi}_R\rangle = c_s\,\|\varphi^{4s1\zeta}\rangle + c_p\,\|\varphi^{4p_z}\rangle$ | | | | |
|---|---|---|---|---|---|---|---|---|---|---|
| Height (Å) | | $E_R$ (eV) | $\Gamma$ (meV) | $\hbar/\Gamma$ (fs) | $\tau_{FFT}$ (fs) | $E_R^{opt.}$ (eV) | $\Gamma^{opt.}$ (meV) | $\hbar/\Gamma^{opt.}$ (fs) | $\tau_{FFT}^{opt.}$ (fs) | $\|c_p\|^2$ (%) |
| Majority | 2.4 | 3.92 | 140 | 4.69 | 4.24 | 3.92 | 129 | 5.10 | 4.61 | 60 |
| | 2.7 | 3.74 | 139 | 4.73 | 4.28 | 3.74 | 136 | 4.82 | 4.52 | 52 |
| | 3.0 | 3.52 | 120 | 5.46 | 4.76 | 3.52 | 121 | 5.43 | 4.94 | 43 |
| | 3.3 | 3.35 | 102 | 6.39 | 5.08 | 3.35 | 104 | 6.31 | 5.20 | 37 |
| | 3.6 | 3.17 | 98 | 6.67 | 5.29 | 3.17 | 98 | 6.66 | 5.42 | 30 |
| Minority | 2.4 | 4.04 | 254 | 2.59 | 2.56 | 4.04 | 223 | 2.94 | 2.96 | 63 |
| | 2.7 | 3.86 | 189 | 3.46 | 3.27 | 3.86 | 170 | 3.87 | 3.67 | 56 |
| | 3.0 | 3.68 | 178 | 3.69 | 3.65 | 3.68 | 149 | 4.41 | 4.13 | 50 |
| | 3.3 | 3.50 | 234 | 2.80 | 3.11 | 3.51 | 188 | 3.48 | 3.58 | 44 |
| | 3.6 | 3.34 | 306 | 2.14 | 2.65 | 3.34 | 253 | 2.59 | 3.10 | 38 |
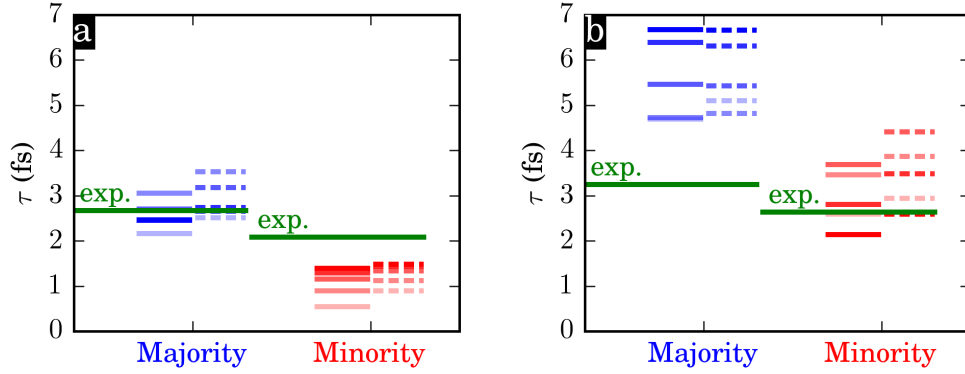
**Figure 6.5.:** Ab-initio lifetimes and comparison to the experimental values (green solid lines) from core-hole-clock spectroscopy experiments [50] for the case of Ar*/Fe(110) in (a) and Ar*/Co(0001) in (b). It is clearly visible that electrons in the majority channel are longer-lived than their minority excited counterpart. Dashed lines represent the values obtained using optimized wave packets to describe the Ar*4s-resonance, which take into account polarization effects in the presence of the surface (see Section 6.4). Continuous lines correspond to values obtained using a single atomic Ar*4s orbital to model the resonance wave function.

for $\hbar/\Gamma$ in Fig. 6.5. It is visible that our calculations reproduce the characteristic of faster minority channel decay in comparison with the majority channel, and an overall faster charge transfer regarding both spin-channels on the Fe(110) substrate in comparison with Co(0001). Also a good quantitative agreement with the experimental values can be stated. Here we consider exclusively the top adsorption site. A significant dependence of the line widths on the adsorption site could be ruled out by additional simulations: The trends and the time-scales across different sites are conserved (compare with the results in Appendix D).

The relatively small deviations from the experimental results may stem from several factors. Among these we list: (**i**) The deficiency of GGA functionals to describe the localized states causing a possible shift of the resonance positions with respect to the substrate's bands in combination with the sensitivity of the resonance's width on the energetic position [36, 122], which is in principle entangled with the adsorption height (see also Fig. 6.4 and the attempt to disentangle the effects in Section 6.5.2). (**ii**) We simulate elastic lifetimes excluding any effects of structural fluctuations or scattering with phonons and other inelastic processes, which might shorten lifetimes further. (**iii**) The calculations are based on static Hamiltonians, dynamic effects of screening during the electron transfer are not considered.

We have additionally performed calculations for the unconstrained system, thus, relaxing the electron occupying the Ar*4s1$\zeta$-orbital. The extracted lifetimes of these unconstrained calculations in Table 6.4 show surprisingly an opposite trend in one instance: The majority channel for an adsorption height of 3.3 Å on Fe(110) is faster than the minority channel. This coincides with the behavior reported for constrained and unconstrained calculations of Cs/Fe(110) [122]. We note that this behavior is opposite to what would be expected, when comparing with the amount of d-type DOS (cf. Fig. 6.2) around the resonance positions $E_R$. Indeed, in the region of the
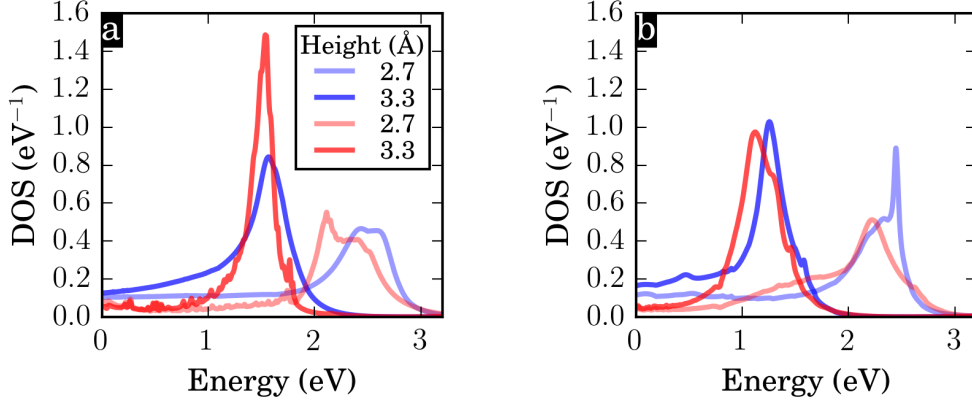
**Figure 6.6.:** Calculations without the constraint described in Section 6.2: Ar*-resonance spectra for (a) Ar*/Fe(110) and (b) Ar*/Co(0001). The blue lines represent the majority spin channel and the red lines the minority spin channel.

largest d-type contributions the line widths are reduced, supporting the idea that more localized states contribute less to charge transfer [19]. The remaining values of $\hbar/\Gamma$ in Table 6.4 show about equal charge transfer times for both spin channels. The positions of the resonances are comparable with the ones reported for the case of Cs/Fe(110) between 2 and 2.5 eV [122]. However, the energy range in which the resonances occur in the unconstrained case is far lower than the experimentally observed resonance position, so that this case is irrelevant for a direct comparison with the experiment by Blobner et al. [50]. The main purpose of the unconstrained calculations is to illustrate the effect of an overlap of the resonance wave packet with the flat minority d-bands and to emphasize the importance of the resonance position with respect to the surface band structure.

So far we have considered a resonance wave packet of pure 4s-character in our calculations. However, indeed it can be expected that in the presence of the surface the excited wave-packet is polarized in the direction perpendicular to the surface. This possibility is examined in the next section.

## 6.4. Polarization of the Resonance Wave Packet

The approximately spherical shape of the Ar*4s wave function is reflected in the spatially resolved DOS integrated over an energy window of 1 eV around the resonance positions in Fig. 6.7. However, due to the presence of the surface the spherical shape is slightly distorted, so that the DOS deforms towards the Fe or Co atoms, where the adsorbate is attached to the surface. Independently of the spin-channel and the substrate the behavior is similar. It is also visible that the DOS around the surface atoms is increased in the case of the minority channels in Fig. 6.7b, d.

In search of a wave packet capturing the above described polarizing effect onto the resonance, we employ an optimization scheme considering the additional inclusion of a $p_z$-orbital in the description of the resonance wave-packet

$$|\tilde{\phi}_{R}\rangle = c_{s} |\varphi^{4s1\zeta}\rangle + c_{p} |\varphi^{4p_z}\rangle. \tag{6.3}$$
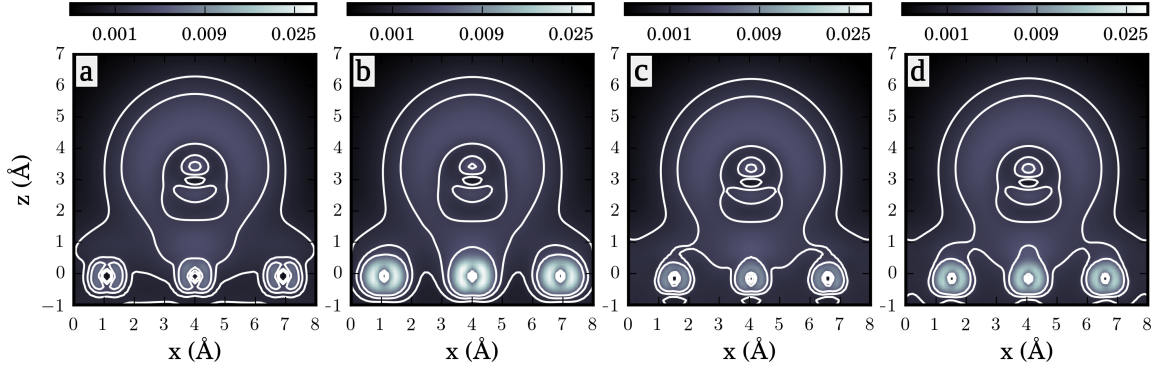
**Figure 6.7.:** Spatially resolved DOS integrated in a range of $\pm0.5$ eV around the maximum peak position of the Ar*4s resonance: Ar/Fe(110) for majority (a) and minority (b) electrons, as well as Ar/Co(0001) for majority (c) and minority (d) electrons. Shown are sections through the Argon adsorbate in the xz-plane. The surface's atoms are centered at a height of $z = 0$ Å. The color code follows a square root dependency to highlight the differences for small densities.

Here, the 4p$_z$-orbital is one of the pseudo-atomic orbitals obtained for Ar*, which is contained in the basis set employed in the calculations.

The optimized wave-packet is then chosen such that it maximizes the spectral density inside of a small energy region around the position of the resonance for the real coefficients $c_s$ and $c_p$. This is achieved by finding the maximum of the integral

$$I(c_s, c_p) = \int_{E_R - \frac{\Gamma}{2}}^{E_R + \frac{\Gamma}{2}} \text{Im} \, \langle \tilde{\psi}_R | G(E) | \tilde{\psi}_R \rangle \, dE \,, \tag{6.4}$$

under the constraint that the resonance wave packet is normalized $c_s^2 + c_p^2 = 1$. The integration range $[E_R - \Gamma/2, E_R + \Gamma/2]$ is centered around the energy $E_R$ and

**Table 6.4.:** Extracted values of the lifetimes $\hbar/\Gamma$ and the resonance positions $E_R$ with respect to the 4s-resonances of Ar* adsorbed on Fe(110) and Co(0001). Both (majority and minority) spin channels are shown. In these calculations the electron occupying the Ar* resonance was allowed to relax so that it is transfered to the metal substrate, thereby leading to an excited ion on top of the surfaces. Under this condition our DFT-GGA calculations predict too low energetic positions for the Ar *4s-resonance as compared to the experiment [50].

|  | $h$ | Majority | | Minority | |
|---|---|---|---|---|---|
|  |  | $\hbar/\Gamma$ | $E_R$ | $\hbar/\Gamma$ | $E_R$ |
|  | (Å) | (fs) | (eV) | (fs) | (eV) |
| Fe(110) | 2.7 | 1.19 | 2.44 | 1.16 | 2.11 |
|  | 3.3 | 1.42 | 1.57 | 3.28 | 1.54 |
| Co(0001) | 2.7 | 1.45 | 2.45 | 1.04 | 2.22 |
|  | 3.3 | 1.78 | 1.26 | 1.74 | 1.12 |

has a length of $\Gamma$, which correspond to the extracted values for the resonance position $E_{\mathrm{R}}$ and the line width $\Gamma$ in the calculations discussed above where a pure Ar*4s wave packet was considered. The finite region of integration ensures that the feature related to the resonant charge transfer process of interest is maximized. A formal derivation of the optimized coefficients $c_{\mathrm{s}}$ and $c_{\mathrm{p}}$ can be found in Appendix E.

The optimized wave packets result overall in larger lifetimes $\tau_{\mathrm{FFT}}^{\mathrm{opt.}}$ than the pure Ar*4s resonances ($\tau_{\mathrm{FFT}}$), reflecting a closer match with the physical character of the systems under study –at the current level of theory. For a quantitative comparison all values are listed in Tables 6.2 and 6.3. The change in the lifetimes is rather small (a few tenths of a femtosecond), as can be seen from the dashed lines in Fig. 6.5 which show the values of the optimized resonances.

Studying the qualitative trends across different adsorption heights with the ones observed for the pure Ar*4s resonance, no significant changes are found, cf. Fig. 6.2 and Fig. 6.3, the largest difference being a smaller increase in the resonance width towards lower adsorption distances in the minority channel of Ar/Fe(110).

It is interesting to analyze the amount of the $p_z$-component, which is mixed into the wave packet by the optimization prescription. The percentages $|c_{\mathrm{p}}|^2$ of the admixture of $p_z$-components are displayed in Tables 6.2 and 6.3. For the largest distances (3.6 Å) we find that the contribution from the $p_z$-components amounts to one third, this steadily increases to about two thirds at close proximity to the surface (2.4 Å). This increase in polarization upon approaching the surface is found regardless of the two substrates or the spin-polarization under consideration with nearly the same quantitative behavior. Considering the large amount of polarization in proximity to the surfaces, the marginal changes in the lifetimes are surprising and verify a certain robustness of the resonant line widths.

## 6.5. Interplay with Electronic Gaps of the Surface Band Structure

As discussed above, a characterization of the Argon-surface interaction cannot only rely on arguments based on the total DOS or on a rather arbitrary partition of the DOS into symmetry components. Instead, additionally a careful analysis of the electronic coupling is necessary. In particular, the interaction with projected gaps in the surface band structure has been studied in this context [41, 224–226]. Projected band gaps are known to lead to a blocking effect regarding the charge transfer [34, 35, 233]. A discussion of this blocking effect of electronic band gaps in connection with Ar* on magnetic substrates is the subject of this section.

We start by inspecting the alignments of the resonance positions with respect to the band structure of the clean substrates in Figs. 6.8 and 6.9 for Fe(110) and Co(0001), respectively. In both plots the majority (a) and minority (c) spin-channels are analyzed. The resonance positions at different adsorption heights (compare also the insets in Fig. 6.4) are indicated by horizontal lines. It is directly visible that band gaps are opening around the $\overline{\Gamma}$-points at the positions of the resonances. The band gaps are framed by the highly dispersive free-electron-like bands of the metal
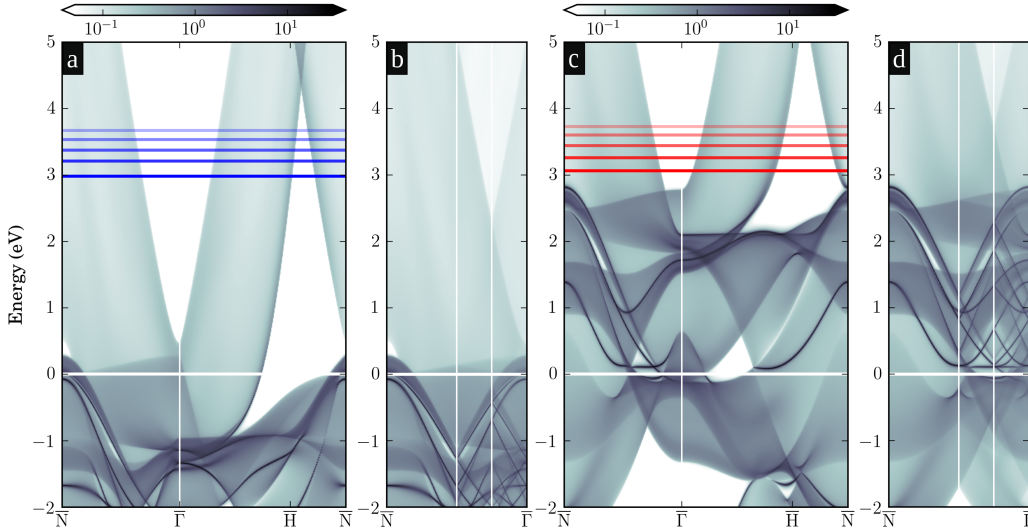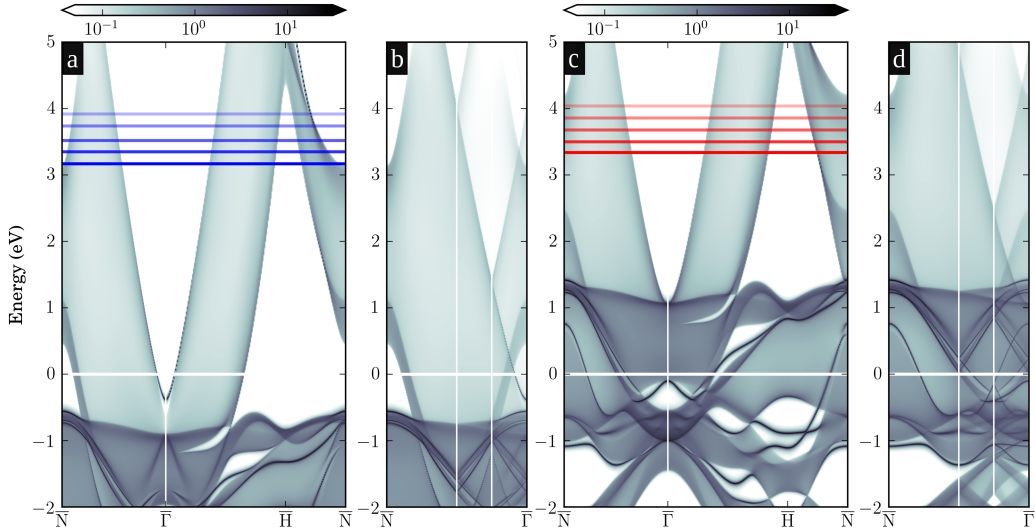
**Figure 6.8.:** Band structure (**k**-resolved DOS) of clean Fe(110) computed using the surface unit cell (a, c) and highlighting the effects of band folding in a $4 \times 1$-supercell (b, d). The band structures of the $4 \times 1$-supercell are found by folding twice along the vertical white lines: The corresponding result is shown in the rightmost quarter of the panels b and d. The energies are referred to the Fermi energy. The grey scale in the plots represents the magnitude of the imaginary part of the Green's function of the semi-infinite substrate projected on to the surface region. Majority states are shown in (a, b) and minority states in (c, d). The horizontal blue lines in (a) and red lines in (b) indicate the Ar*4s-resonance positions. The five resonance positions in each of the two spin channels correspond to different adsorption heights from 2.4 Å to 3.6 Å. Lighter shadings represent smaller adsorption heights (cf. Fig. 6.2). Note, that the flat d-bands occur away from the resonance positions at energies roughly below $\sim 0.2$ eV for majority spin and below $\sim 2.9$ eV for minority spin.

surfaces.

The Fe(110) surface differs qualitatively from the Co(0001) surface in two points: the gaps are less isotropic around the $\overline{\Gamma}$ points due to the geometry of the Fe(110) surface, and in the case of the minority channel of Fe(110) the resonances approach the flat localized d-bands below 2 eV in the band structure (cf. Fig. 6.8c).

To study the effect of the identified gaps more directly, we computed the Ar*4s projected DOS along the high-symmetry lines between the $\overline{N}$ and $\overline{\Gamma}$-points of the $4 \times 4$ unit cell (**k**-resolved DOSs in Figs. 6.10 and 6.11c-f). The resonances on the excited Argon map out the underlying band structures of the substrates in reciprocal space. For a straightforward comparison, we folded the band structures of the $1 \times 1$ unit cells twice along the direction of the corresponding wave vectors to obtain the equivalent electronic structure in a $4 \times 1$ cell. The folding procedure is illustrated in Figs. 6.8 and 6.9b, d. The resulting folded bands are displayed rotated and magnified for the relevant energy range in Fig. 6.10a, b and Fig. 6.11a, b.

The resonant line shapes in Figs. 6.10 and 6.11c-f clearly reflect the areas of larger spectral density and lower density due to the folding of the free-electron-like bands around the surface projected band gap. In regions of lower DOS the resonances

**Figure 6.9.:** Band structure (**k**-resolved DOS) of clean Co(0001) obtained from the Green's function approach to describe a semi-infinite surface. The figure is organized analogously to Fig. 6.8.

appear sharply peaked while in regions of larger surface density the broadening is stronger, so that the resonances mirror the folded band structure in **k**-space. Away from the $\overline{\Gamma}$-point towards the boundary of the Brillouin zone (e.g., at $\overline{N}$) the intensity of the resonance peaks decreases rapidly, indicating that larger crystal momentum components have a smaller contribution to the localized wave packet of the Ar*4s resonances.

For a smaller adsorption height of 2.7 Å (Fig. 6.10e, f and Fig. 6.11e, f) the resonances shift up in energy and thus deeper into the gaps. This locates the Ar*4s resonances in regions of low substrate DOS in reciprocal space. At the same time the spatial overlap of the resonance wave-packet with the surface wave functions is increased leading to stronger interaction reflected in broadened peaks and a decrease of the intensity around the maximum peak position.

In some cases, as we move along $\overline{\Gamma} - \overline{N}$, the resonances enter into regions with reduced DOS leading to sharp changes in the shapes of the resonances. The positions of these sharp changes in the DOS are determined by the folding of the lower threshold of the gap in the supercell. An example of this situation can be found around 4.0 eV at the $\overline{N}$-point for the minority channel on Fe(110) when reducing the adsorption height of Ar* from 3.3 Å in Fig. 6.10d to 2.7 Å in Fig. 6.10f.

The correspondence of the band structure to the **k**-resolved DOS of the resonance obtained from simulations in a $4 \times 4$ unit cell is less apparent, when comparing with the actual surface band structure of the $4 \times 4$ unit cell in Fig. 6.10g, h and Fig. 6.11g, h. Additional bands appear due to the folding along the perpendicular direction in the Brillouin zone complicating a direct comparison. However, looking closely at the band like features of the $4 \times 4$ supercell one can only see for this supercell a perfect agreement with the different features in the resonances. The latter is very apparent for the d-type contributions at energies below 2 eV for the minority channel on Fe(110) in Fig. 6.10f.
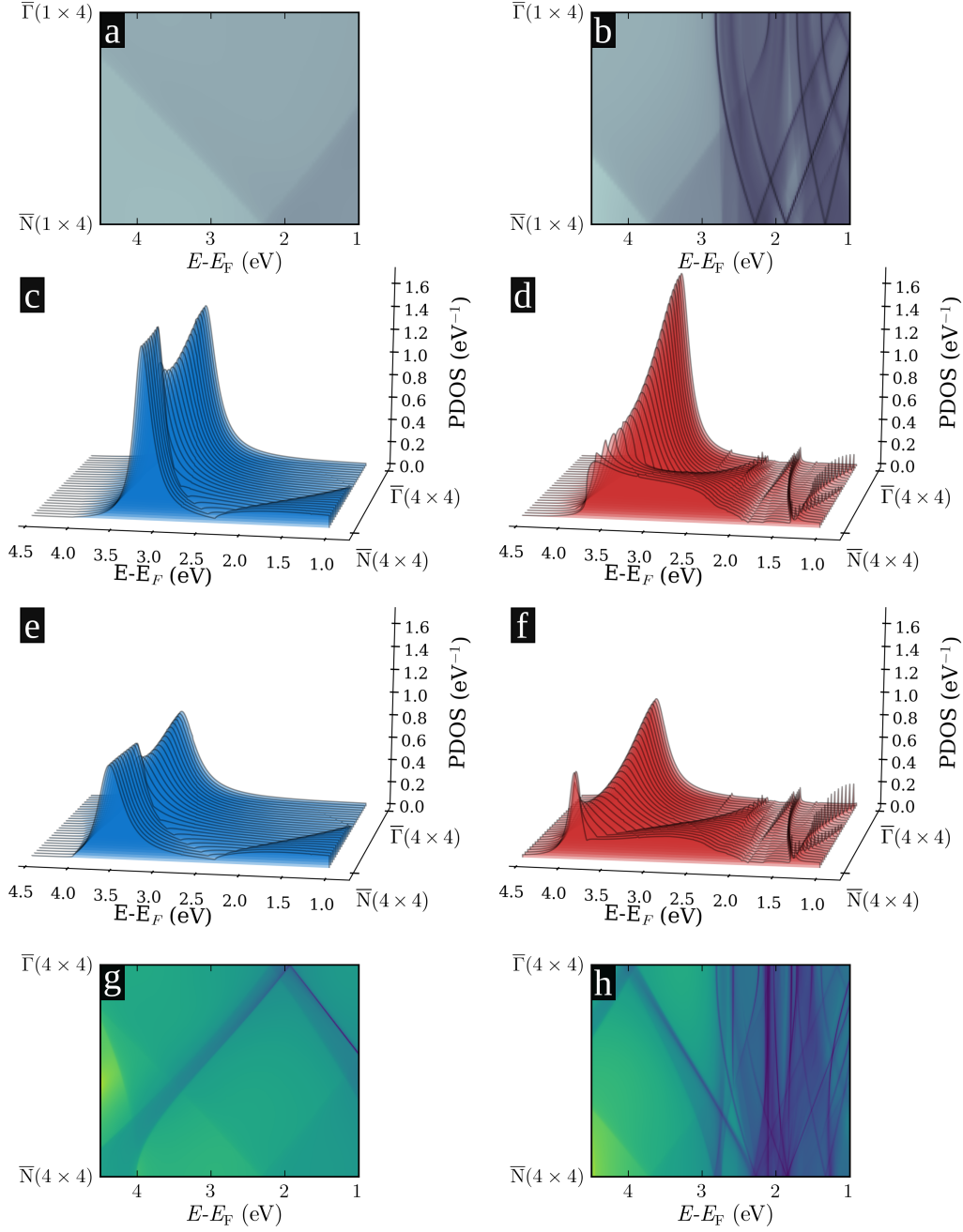
**Figure 6.10.:** (a, b) Relation of the folded surface band structure of the $1 \times 4$ cell (magnified and rotated from Fig. 6.8b, d) to the **k**-resolved resonance spectra obtained by projecting the Green's function of the decorated Ar*/Fe(110) $4 \times 4$ slabs onto the Ar*$4s1\zeta$ state for each spin (c-f). Panels (c, d) refer to an adsorption height of 3.3 Å and panels (e, f) to 2.7 Å. Clearly, the resonances map out the surface bands as can be seen for the majority (a, c, e, g) and the minority (b, d, f, h) channels. The presence of band gaps leads to weak coupling regions with low DOS, where the resonances become sharper. A comparison with the folded bands of the $4 \times 4$ unit cells (g, h) is less straightforward due to the additional amount of features, but is in better agreement with the curves mapped by the resonances in (c, f).
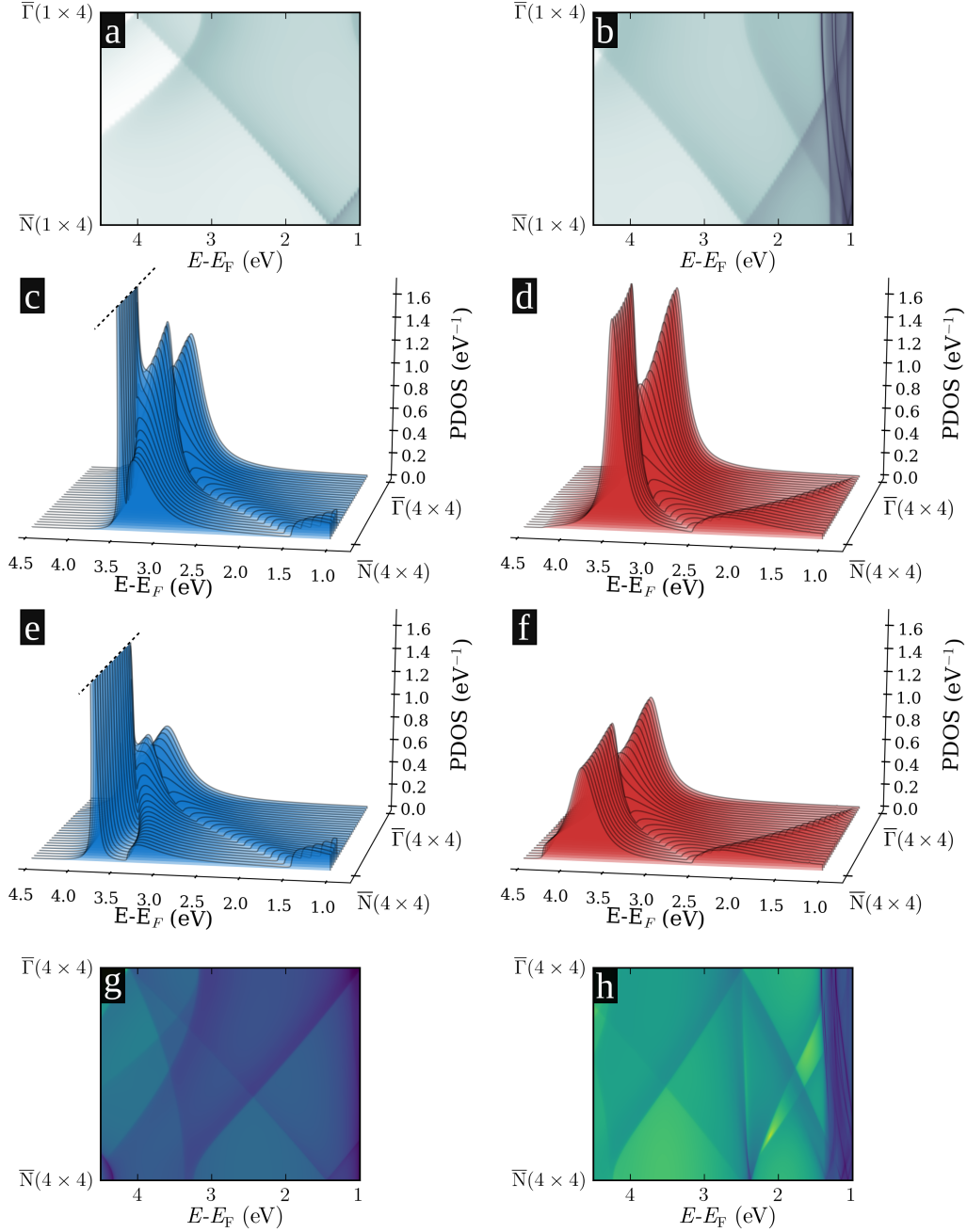
**Figure 6.11.:** Relation of the folded surface band structure in Fig. 6.9 (b,d) to the **k**-resolved resonance spectra obtained from the Ar*4s-projected Green's function of the semi-infinite Ar*/Co(0001) surfaces in analogy to the case of Fe(110) in Fig. 6.10. The dashed lines in (c, e) indicate that very sharp and tall peaks have been cropped along these lines.

## 6.5.1. Effect of Surface Projected Gaps: Descriptive Tunneling Model

At this point, it is instructive to devise a simplified model to understand the effect of the band gaps as proposed in Ref. [35]. The model proposed there maps out the coupling $V(\mathbf{k}_\parallel)$ of the resonance state (Ar*4s) in reciprocal space to get a qualitative picture of the line widths $\Gamma$. Assuming, that at the energy of the resonance the onset of the bands contributing to the otherwise homogeneous DOS is at a distance $k_0$ from the $\overline{\Gamma}$-point (i.e., the bands start, where the gap ends). The value of $k_0$ defines a circle in the two-dimensional surface Brillouin zone. The tunneling rate is then related to the available phase space by the equation [35]

$$\Gamma \approx 4\pi^2 \int_{k_0}^{\infty} |V(k_\parallel)|^2 k_\parallel \, dk_\parallel \,. \tag{6.5}$$

Secondly, it is assumed, that the coupling in reciprocal space $V(\mathbf{k}_\parallel)$ is given in terms of the overlap of the resonance state $\varphi^{4s1\zeta}(\mathbf{r})$ with the wave functions of the states $\psi_{\mathbf{k}_\parallel}$ belonging to the surface,

$$V(\mathbf{k}_\parallel) \approx \int \psi_{\mathbf{k}_\parallel}(\mathbf{r})\varphi^{4s1\zeta}(\mathbf{r}) \, d\mathbf{r} \approx \int f(\mathbf{k}_\parallel, d)\mathrm{e}^{-i\mathbf{k}_\parallel \mathbf{r}}\varphi^{4s1\zeta}(\mathbf{r}) \, d\mathbf{r} \approx f(\mathbf{k}_\parallel, d)\tilde{\varphi}^{4s1\zeta}(\mathbf{k}_\parallel) \tag{6.6}$$

Finally, the components of the surface wave functions can be factored independently from the rest of the terms into a plane wave contribution with a wave vector $\mathbf{k}_\parallel$ parallel to the surface and a contribution $f(\mathbf{k}_\parallel, z = d)$, which accounts for the tunneling behavior perpendicular to the surface. We evaluate the tunneling behavior at a distance from the surface $z$ equal to the adsorption height $d$ of the Ar* atom. The highly dispersive (parabolic) nature of the surface bands justifies the plane wave character of the corresponding states in parallel to the surface.

To estimate the coupling $V(\mathbf{k}_\parallel)$ we identify the three-dimensional Fourier transform of the spherical (pseudo-)wave function $\varphi^{4s1\zeta}(\mathbf{r})$, which we evaluate using the Fourier-Bessel transform (see Appendix F), by writing $f(\mathbf{k}_\parallel, d)\tilde{\varphi}^{4s1\zeta}(\mathbf{k}_\parallel) \approx f(k_\parallel, d)\tilde{\varphi}^{4s1\zeta}(k_\parallel)$.

The factor $f(k_\parallel, d)$ describes the tunneling behavior in front of the surface in terms of the expression for the wave functions in the semi-classical WKB-approximation. This equals the characteristic exponential dependence on the distance $d$, which is assumed to set in at some value $d = d_0$

$$f(d, E_\mathrm{R}, k_\parallel) = \exp\left[-(d - d_0)\sqrt{2(\Phi - E_\mathrm{R}) + k_\parallel^2/m^*}\right]. \tag{6.7}$$

The contribution of this factor to the tunneling probability $|f(d, E_\mathrm{R}, k_\parallel)|^2$ depends on the work function of the surface $\Phi$, the energy position of the resonance $E_\mathrm{R}$ with respect to the Fermi level, and the momentum of the injected electron parallel to the surface $k_\parallel$. The effective masses $m^*$ depend on the dispersion of the surface bands.

Adopting a homogeneous DOS inside the bands, the resonance width can be estimated by

$$\Gamma(d, E_\mathrm{R}) \approx \int_{k_0}^{\infty} |f(d, E_\mathrm{R}, k_\parallel)\tilde{\varphi}^{4s1\zeta}(k_\parallel)|^2 k_\parallel \, dk_\parallel \,. \tag{6.8}$$

In this equation, the spread in reciprocal space of, both, the Ar*4s resonance state and the substrate wave functions (i.e., the electronic gaps), are taken into account.
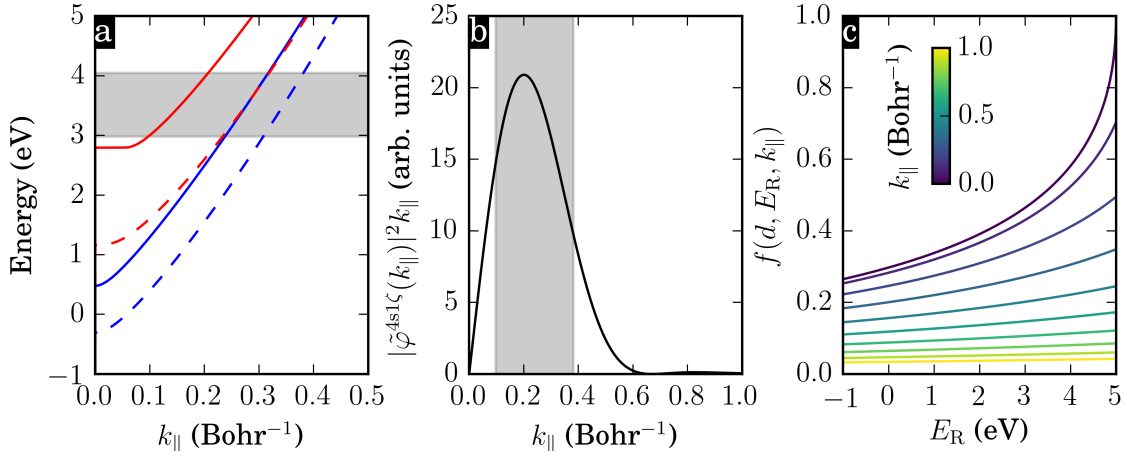
**Figure 6.12.:** Ingredients of a simplified model of spin-dependent charge injection at surfaces. (a) Approximate description of the projected electronic gaps around $\overline{\Gamma}$ as a function of $k_\parallel$ (i.e., $k_0(E)$ following the nomenclature in Eq. (6.5)), for Fe(110) (solid lines) or Co(0001) (dashed lines) and majority (blue) or minority (red) electrons. The shaded area indicates the region, where the resonances occur (for adsorption heights $d$ from 2.4 Å to 3.6 Å). (b) Weighting $|\tilde{\varphi}^{4s1\zeta}(k_\parallel)|^2 k_\parallel$ of the contributions to the line widths due to the structure of the Ar*$4s1\zeta$ orbital $\varphi^{4s1\zeta}(\mathbf{r})$ in reciprocal space. The shaded region indicates the range of values $k_0$ at the resonance energies, where the gaps are opening. (c) Filtering effect due to $f(d, E_R, k_\parallel)$ at a constant adsorption height ($d = 5$ Bohr, $d_0 = 2.0$ Bohr) for varying resonance energies $E_R$, varying momenta $k_\parallel$, and a fixed effective mass of $m^* = 0.4$ .

In the following we apply the model to the present case of Ar* on Fe(110) and Co(0001). We explain the differences in charge transfer times for minority and majority spins in terms of the gap sizes in the surface band structure. The same argumentation explains the differences between the two substrates.

The ingredients of the model are shown in Fig. 6.12 for both spins and materials. The average gap size along $\overline{\Gamma}$–$\overline{N}$ and $\overline{\Gamma}$–$\overline{H}$ in Fig. 6.12a varies strongly around the resonance energies (gray shaded area). Simultaneously, the weighting in reciprocal space due to the spread and shape of the Ar*4s wave function in Fig. 6.12b changes rapidly at the edge of the projected band gap $k_0$. The region of the gap edges $k_0$ at the relevant energies is marked by the gray shaded in Fig. 6.12b. Due to these strong variations the coupling $V(k_\parallel)$ in Eq. (6.6) is very sensitive to the size of the gap.

In Fig. 6.12c it can be seen that $f(d, E_R, k_\parallel)$ decays strongly for larger values of the momentum $k_\parallel$ parallel to the surface. Therefore $f(d, E_R, k_\parallel)$ has a filtering effect on contributions with larger parallel momenta. This is reasonable in the sense that higher values of $k_\parallel$ lead to less available momentum in the tunneling direction perpendicular to the surface [note that we are taking the free-electron dispersion with an effective mass $m^*$ as a simple approximation for the dispersive bands of Fe(110) and Co(0001) ]. Equivalently, one may think of an increase of the effective barrier to $2(\Phi - E_R) + k_\parallel^2/m^*$ for non-zero parallel momenta. At the same time higher resonance energies $E_R$ render tunneling processes more likely by reducing the effective barrier.

In contrast to the increase in tunneling rate with rising values of $E_R$, the widening
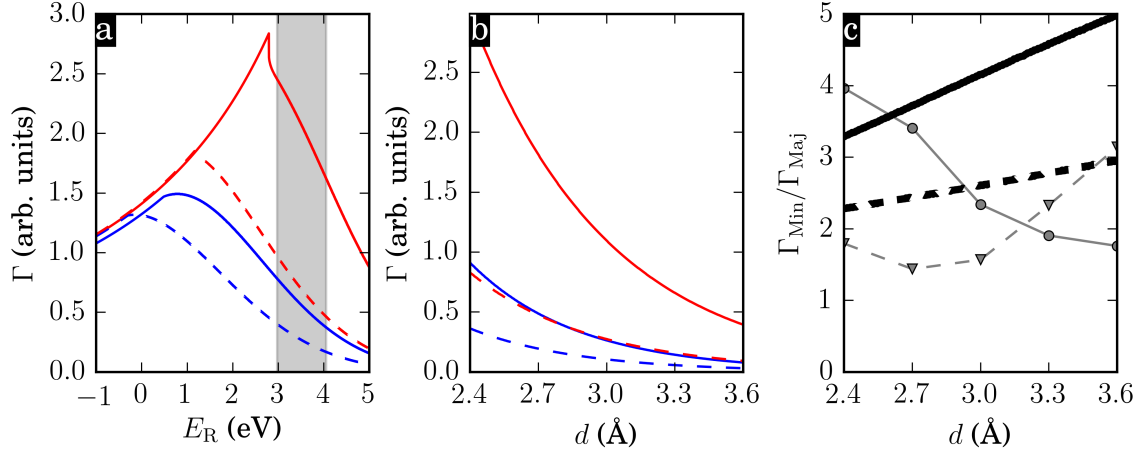
**Figure 6.13.:** Simplified model of spin-dependent line widths. (a) Behavior for a constant adsorption height of $d = 5$ Bohr as a function of the resonance energy $E_R$. The shaded area indicates the region, where the resonances occur (considering adsorption heights from $d = 2.4$ Å to 3.6 Å). (b) Line widths $\Gamma$ in dependence of adsorption heights $d$ considering the height-dependent resonance energies $E_R(d)$. (c) Ratios of the line widths $\Gamma_{Min}/\Gamma_{Maj}$ between both spin-channels (thick black lines). All quantities in the plot are shown for Ar*4s resonances on Fe(110) (solid lines) or Co(0001) (dashed lines), and minority (red) or majority (blue) spins. The gray data points in (c) display the results from our DFT calculations (cf. Fig. 6.4). The effective masses $m^*$ were extracted for each spin channel and material by analyzing shapes of the gaps in Fig. 6.12a using Eq. (6.9). We adopted a distance parameter of $d_0 = 3.0$ Bohr and a work function of $\Phi = 5$ eV.

of the electronic gaps at higher resonance energies leads to a decrease of the tunneling probability. Putting together the ingredients illustrated in Fig. 6.12 we obtain the curves shown in Fig. 6.13a, choosing the parameters $\Phi = 5$ eV and $d_0 = 3$ Bohr. The model shows clearly how the line widths $\Gamma$ increase exponentially until the point where the gaps open, which causes the immediate decay of the line widths.

Here, we have estimated the material- and spin-dependent effective masses based on the energy difference $\Delta E$ of the resonance position (at $E_R = 4$ eV) minus the bottom of the band gap and the gap size $\Delta k_\parallel$ at $E_R = 4$ eV,

$$m^* = \frac{\Delta k_\parallel^2}{2\Delta E}. \tag{6.9}$$

The extracted values for the effective masses of the majority (minority) electrons are 0.38 (0.46) for Fe(110) and 0.45 (0.48) for Co(0001).

In a second step, we incorporate the dependence of the width on the adsorption height by letting the resonance positions $E_R$ vary with $d$. To do so, we fit the trends of the DFT-based resonance energies $E_R$ (cf. Fig. 6.4) linearly across different widths. The fits match the original data well, as can be seen in Fig. 6.14a. Additionally, one has to consider that the gap sizes $k_0$ change with the resonance energy, so that one
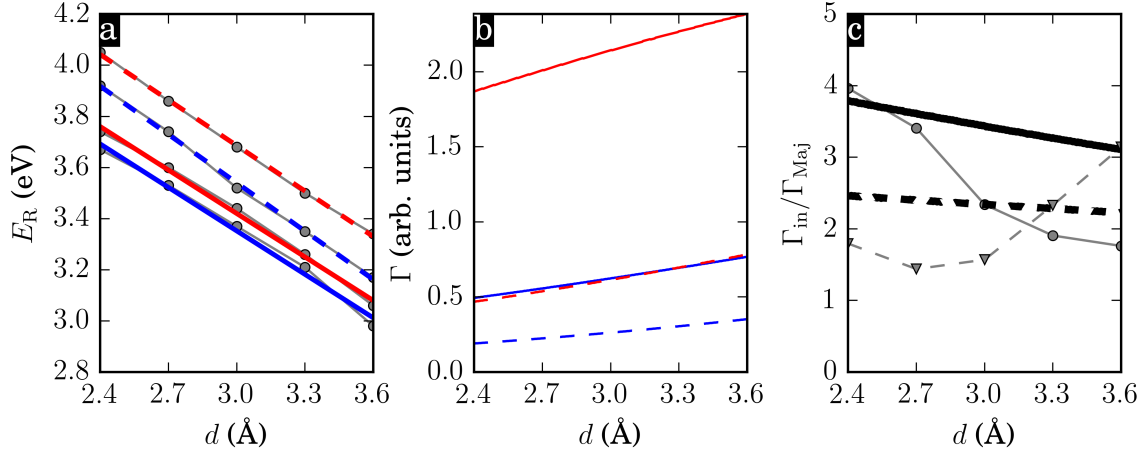
**Figure 6.14.:** Model of the resonant line widths for distance dependent resonance positions $E_R(d)$, while simultaneously fixing the distance in the pre-factor $d - d_0 = 2.0$ Bohr of the exponential tunneling behavior $f(d, E_R, k_\parallel)$: (a) Distance dependence of resonance energies. (b) Resulting line widths. (c) Ratios of the line widths $\Gamma_{\mathrm{Min}}/\Gamma_{\mathrm{Maj}}$ between both spin-channels. The lines are defined as in Fig. 6.13: Fe(110) (solid lines) or Co(0001) (dashed lines) and minority (red) or majority (blue) spins. The connected gray data points display the data from our DFT calculations in (a,c). The values of $m^*$ and $\Phi$ equal those in Fig. 6.13.

receives the adapted formula

$$\Gamma(d) \approx \int_{k_0[E_R(d)]}^{\infty} |f(d, E_R(d), k_\parallel)\tilde{\varphi}^{4s1\zeta}(k_\parallel)|^2 k_\parallel \, dk_\parallel \,. \tag{6.10}$$

The behavior described by Eq. (6.10) is shown in Fig. 6.13b. Overall, the model resembles qualitatively the line widths of the DFT calculations (cf. Figs. 6.4 and 6.5): In particular, the minority channels relate to faster charge transfer (i.e., broader line widths), the charge transfer on Fe is faster than on Co, and the minority channel on Co exhibits the same time scales as the majority channel on Fe. However, all line widths in Fig. 6.13 decrease for larger distances $d$ due to the dominant exponential dependence in Eq. (6.7). This exponential distance dependence can explain the decreasing line widths for the Fe(110) minority electrons and Co(0001) majority electrons, but does not account for the behavior of the other two spin channels in Fig. 6.4. Most importantly the increase of $\Gamma$ at larger distances for Fe(110) minority electrons cannot be explained.

To eliminate the unknown scaling between the model and the DFT output it is useful to compare them in terms of the ratios $\Gamma_{\mathrm{Min}}/\Gamma_{\mathrm{Maj}}$ of the minority and majority line widths. The plots of $\Gamma_{\mathrm{Min}}/\Gamma_{\mathrm{Maj}}$ in Fig. 6.13c show that the ratios are captured very well for both materials. However, a description of the trends across different adsorption heights is not feasible. Although the ratios related to Co(0001) in Fig. 6.13c (dashed lines) follow an overall increase as in the DFT results, the corresponding separate quantities $\Gamma_{\mathrm{Min}}$ and $\Gamma_{\mathrm{Maj}}$ do not agree with the trends of the DFT data in Fig. 6.4, where the minority widths increase significantly at larger distances $d$. In the case of Fe(110) (solid lines, Fig. 6.13c) opposite trends are found

already for the ratios $\Gamma_{\text{Min}}/\Gamma_{\text{Maj}}$.

Inspecting Fig. 6.13a, an increase of the line width $\Gamma$ as the adsorbate's distance to the surface $d$ is increased can be easily justified: $E_{\text{R}}$ decreases (from about 4 eV to 3 eV, gray shaded region) with increasing $d$ and, correspondingly, the size of the projected band gap encountered at $E_R$ also decreases. The reason we only find a decrease of $\Gamma$ with increasing $d$ stems from the exponential dependence assumed for the prefactor $f(d, E_{\text{R}}, k_{\|})$ cf. [Eq. (6.7)]. However, while such exponential dependence is expected in the tunneling regime (large values of $d$), the values of $d$ we consider here are relatively small and assuming such exponential decay may not be justified[1]. Therefore, we consider now the opposite extreme in Fig. 6.14: a modified model where the explicit dependence on the distance in $f(d, E_{\text{R}}, k_{\|})$ is canceled by fixing $d - d_0 = 2$ Bohr in Eq. (6.7), so that the distance only enters through $E_{\text{R}}(d)$. The plot in Fig. 6.14b shows now an increasing behavior of $\Gamma$ as a function of $d$.

This saturation of the exponential decay or at least a milder distance dependence of the wave-function overlaps, at small values of $d$ can explain the increase in line width as the adsorption height increases for minority spin on Co(0001). This behavior can be seen in Fig. 6.4b. Equally, fixing the factor $d - d_0$, changes the slope of the ratios in Fig. 6.14, which now display decreasing trends. In summary, the simple model presented here can explain the main features of the spin dependence observed in the detailed ab initio calculations and in the experiments in a satisfactory manner. In particular, our model highlights the important roles of the energy position of the resonance and the size of the projected band gaps for the cases of argon on Fe(110) and Co(0001) considered here.

## 6.5.2. Disentangling the Effect of Energetic Position and Adsorption Height in the Ab Initio Model

As discussed above, the position of the resonance and the adsorption height appear entangled in the ab initio calculations, therefore a separate analysis of their effect is not directly possible. In the previous section a descriptive model was used to analyze their effects. In this section we explore the separate effects using the full Green's function based model for the case of the Ar*/Fe(110) interface. This is achieved by varying the resonance positions through modifications of the Hamiltonian. In particular we shift the matrix elements of the Hamiltonian $H_{ij}$ which belong to the excited Ar atom by an energy $\Delta\varepsilon$ multiplied with the overlap matrix $S_{ij}$,

$$H'_{ij} = \begin{cases} H_{ij} + S_{ij}\Delta\varepsilon & \text{for } \{i, j\} \in \text{Argon atom}, \\ H_{ij} & \text{otherwise.} \end{cases} \tag{6.11}$$

In principle, this modification allows to move the energetic position of the Argon projected DOS nearly at will. However, due to the overlaps in the non-orthogonal

---

[1]Similarly, in STM experiments a saturation of the current with distance is observed in the contact regime. Also here the donor/acceptor state's position (on the tip) with respect to the substrate band structure may vary further due to confinement as the tip approaches the surface. This may affect the measurements.
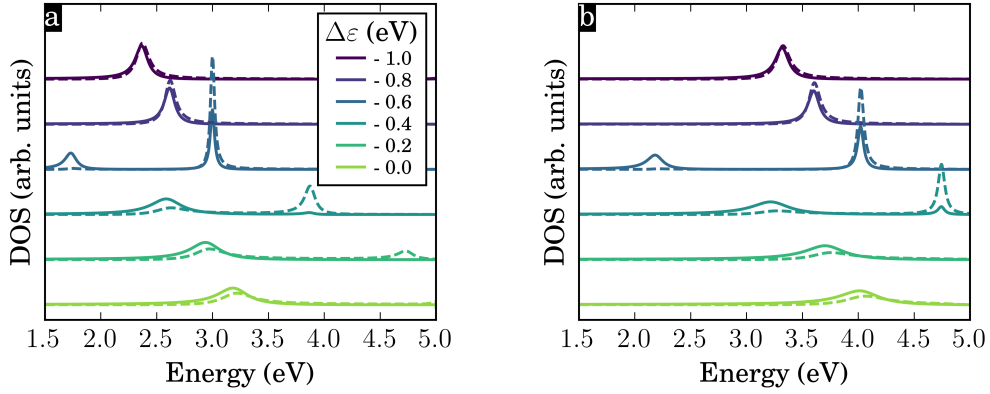
**Figure 6.15.:** Effect of the energy shift $\Delta\varepsilon$ on the Ar*4s (solid lines) and Ar*4p$_z$ (dashed lines) resonance spectra for Ar* adsorbed at a distance of 3.0 Å on Fe(110). The spectra show the energy ranges from 1.5 eV to 5.0 eV above the Fermi level.

basis set of SIESTA also neighboring sites may be affected, e.g., contributions to the DOS related to the Fe-atom where the Ar-adsorbate is attached.

We employ the shift in Eq. (6.11) for the case of Ar* adsorbed on Fe(110). The more complete basis set used so far for Argon does not allow for an unambiguous interpretation of the peaks, since the character of the peaks changes as we apply the energy shift $\Delta\varepsilon$ complicating the interpretation considerably. This can be seen in Fig. 6.15: The contributions from 4s and 4p$_z$ orbitals to the resonances move downwards in energy with increasing negative shifts (up to $-1.0$ eV). Around $\Delta\varepsilon = -0.6$ eV a jump occurs where the anti-bonding 4p$_z$-contribution crosses with the 4s resonance resulting in a sharp peak. The bonding 4p$_z$-contribution almost coincides with the 4s-peak for small shifts $\Delta\varepsilon$ (this goes along with our previous results for the optimized wave-packets, where the 4p$_z$-component was shown to have a large contribution, see Section 6.4). These effects are related to the simple procedure used to shift the resonance energy in Eq. (6.11): Ar* resonances of distinct symmetries hybridize each in a particular way with the substrate and carry therefore different weights on the orbitals of the Ar* atom and the Fe substrate. This gives rise to different behaviors as a function of $\Delta\varepsilon$.

In an effort to avoid mixing with Ar*4p states, we restrict ourselves to a limited basis set for Argon, where only 3p-contributions and the 4s1$\zeta$-component are taken into account. Using this restricted basis set we apply shifts $\Delta\varepsilon$ in steps of 0.2 eV. The resulting line widths $\Gamma$ for varying shifts can then be mapped out for combinations of resonance positions $E_R$ and adsorption heights $d$. This is shown in Fig. 6.16.

In the plot it is visible that increasing the adsorption height, while keeping simultaneously the resonance at a constant energy position, leads to a decay of the line widths as it is expected from the exponential decay in Eq. (6.7). On the other hand one can also see the effect of changing the resonance position at a constant adsorption height. This reveals the effect of the band gaps. In particular, for the majority spin channel in Fig. 6.16a a decrease in the line widths can be seen for increasing resonance energies $E_R$ at constant adsorption heights.

Along the red dashed line for zero energy shifts ($\Delta\varepsilon$=0) we see a decrease of the line
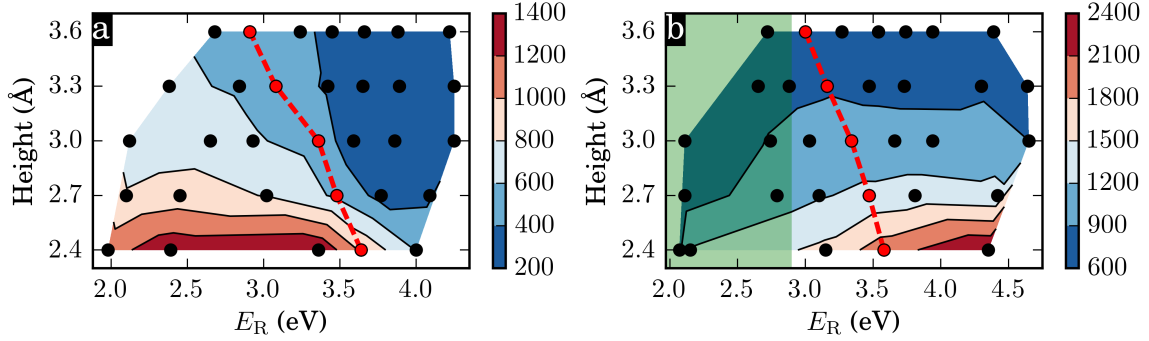
**Figure 6.16.:** Disentangling the effects of the adsorption height $d$ and the energy position of the resonance $E_R$ for Ar*/Fe(110), a reduced basis set is used to describe of Ar* in this case, as explained in the text. The extracted widths are shown in colors and are in units of meV. The connected red dots are the data points for $\Delta\varepsilon = 0$ eV. The black dots represent the data points for which calculations with positive and negative shifts have been performed. (a) Shows the majority spin channel and (b) the minority channel. The green shaded area in (b) indicates schematically the energy region of the 3d bands.

widths at growing distances as observed for the calculations using a more complete basis set for Argon (cf. Fig. 6.4). Because of the description of the Argon resonance in a restricted basis, the line widths from the model calculations differ from the previously calculated values. However, the effect of the band gap is clearly visible along the variation of the resonance energies for the majority spin channel. For the minority channel the behavior as a function of the energy is somewhat different since in the energy range covered by Fig. 6.16b the dominant character of the bands in the Fe substrate changes in from the 3d manifold for energies below $\sim 2.9$ eV (green shaded area) towards dispersive 4sp bands at the energies above.

## 6.6. Conclusions and Outlook

In this chapter we discussed spin-dependent charge injection from core-excited Argon adsorbates into magnetic surfaces from a theoretical perspective. The Green's function technique [34, 35] introduced in the first chapters was used to estimate the elastic lifetimes of the lowest-energy bound resonance on core-excited Argon.

Our results corroborate the experimental finding that minority spin electron transfer is significantly faster in comparison with the majority spin on Fe(110) and Co(0001) substrates [50]. As in the experiment the injection is faster on Fe(110) regarding each separate spin channel, while minority charge transfer on Co(0001) is about as fast as majority charge transfer on Fe(110). The absolute charge transfer times are of the order of a few femtoseconds and hence in good agreement with the time-scales from core-hole-clock experiments [50].

We explore the character of the resonances in front of the surfaces by employing an optimization scheme mixing $p_z$-components into the initially considered pure Ar*4s-resonance. While we find that the optimized wave-packets describing the resonances

become strongly polarized when approaching the surface, this has only a small effect on the extracted lifetimes.

We explain the spin-dependency by the interplay with electronic gaps in the surface's band structures. The variation of the gap sizes for the investigated materials and different spin channels controls the effective injection time. We qualitatively illustrated the behavior in reciprocal space using the output from our first-principles calculations. Subsequently, we employed a descriptive model to give a consistent explanation in terms of the electronic gaps. While the model captures the effects of the gaps, it can also be adapted to reproduce the dependence of the lifetimes on the adsorption height as observed in our DFT-based Green's function calculations.

We find a discussion of the lifetimes in terms of the angular momenta of the acceptor states misleading, considering the highly dispersive character of the substrate states in the energy range of interest. Although contributions from d-type components and larger angular momenta can be expected to grow with increasing energies (as it happens e.g., for a simple plane-wave with respect to an arbitrary center), this does not reflect and should not be confused with the traditional nomenclature, where 3d-bands are associated with flat bands directly derived from bound 3d-type atomic orbitals. Therefore, we claim that the correlation between the spin-dependent charge-transfer times and the amount of DOS labeled by a d-type symmetry found in Ref. 50 is mostly coincidental and does not reflect the ultimate cause of the observed effect. Instead the spin-dependence of the size of the projected band gaps around $\overline{\Gamma}$ at the resonance positions explains the behavior for the studied substrates.

In general charge transfer times at surfaces are primarily controlled by a combination of the coupling matrix, accounting for the symmetry and the spatial overlap of the states, and the available density of acceptor states in reciprocal space (Fermi's golden rule). To determine the availability of acceptor states, the energetic position of the resonances with respect to electronic gaps in the surface band structures is crucial. In the case of Ar* on Fe(110) or Co(0001) the resonance position is strongly influenced by the increasing confinement of the resonance wave-packets as one reduces the adsorption height. This shifts the resonances up in energy and forces them deeper into the projected band gaps. Hence, the effect of the electronic gaps competes with simultaneously growing overlaps at decreasing adsorption heights. Overall, at the level of time-independent semi-local DFT the agreement with the experiment is good, even considering that the alignment of the adsorbate states with the substrate's electronic structure might be misrepresented.

Aside from performing explicit time-propagations in order to investigate dynamic effects, a continuation of the current study for the magnetic Ni(111) substrate to complete the comparison with all three experimentally studied surfaces is desirable for future investigations. Furthermore, a potential extension of prevailing tunneling models like the Tersoff-Hamann approximation [184] for STM simulations to incorporate the effect of band gaps along the lines of the descriptive model [35] employed in this chapter provides an interesting perspective. This requires the use of a reasonable model for the wave function of the tip in order to assign relative weights to the contributions from the DOS at different k-points.

# Chapter 7

## Polarization Dependence of Electron Dynamics on 1T-TaS$_2$

In the preceding chapters we explored the lifetimes of resonances on adatoms and molecules that were attached to surfaces. In this chapter we take it a step further and study charge transfer in the outer atomic layers of surfaces. In particular, we are interested in the TMD 1T-TaS$_2$, which we study by first-principles modeling in combination with a core-hole-clock analysis. This work is the result of a close collaboration with the experimental group lead by Prof. A. Föhlisch and, in particular, D. Kühn et al., who conducted the core-hole-clock experiments. The chapter is based on the publication in Ref. 52.

TMDs are materials of the chemical composition $MX_2$, where each transition metal atom ($M$ = Mo, W, Ta, etc.) is sandwiched between two chalcogen atoms ($X$ = S, Se, Te). They often exhibit a layered structure and in many cases TMDs can be synthesized as few- or monolayer structures. They comprise semi-conducting 2D-materials with promising electronic properties for technological applications like switching, sensing, energy storage, and opto-electronics [234–237]. The pronounced spin-orbit coupling in TMDs allows to address spin or valley degrees of freedom in electronic applications (i.e., spintronics, valleytronics) [238–240]. TMDs typically preserve quasi-two-dimensional properties in the bulk phase, where individual layers are joined by vdW forces. They often exhibit various electronic and structural phases. An especially rich phase diagram is observed for 1T-TaS$_2$ featuring charge density waves (CDWs) with varying degrees of commensurability, superconducting behavior, and metal-insulator transitions [241, 242]. This offers the possibility to study specific physical processes, like electronic excitations or charge transfer, in different electronic phases of one material.

At the same time 1T-TaS$_2$ can be seen as a prototypical system for investigations of the directionality of charge transfer. The layered structure of the material supports delocalization of electrons into in-plane directions, while it hampers delocalization into out-of-plane directions (with respect to the material's layers). Such directionality can be probed by polarization-dependent excitations of oriented wave-packets in core-hole-clock experiments [22, 123]. The promotion of electrons into in-plane polarized

resonances that overlap strongly with orbitals of the neighboring atoms of the same layer favors in-plane charge transfer. Equivalently, out-of-plane orbital-polarization favors out-of-plane charge transfer. This picture is paralleled in this chapter by first-principles calculations of 1T-TaS$_2$ surfaces, where we study spectral projections onto different orbital-orientations.

Our polarization dependent core-hole-clock experiments with respect to the sulfur $2s \rightarrow 3p$ transitions in 1T-TaS$_2$ indicate a surprising change in the charge transfer behavior across different electronic phases, when varying the temperature. In the nearly commensurate charge density wave (NCDW) phase out-of-plane polarized excitations yield twice slower charge transfer times, than in-plane excitations. This reflects the layered structure of the material and is in line with comparable results for SnS$_2$ [142]. In striking contrast to this, the commensurate charge density wave (CCDW) leads to isotropic behavior, where the out-of-plane charge transfer proceeds equally fast as its in-plane counterpart, whose time-scale remains unaffected by the NCDW to CCDW transition.

In order to explore the possible sources of the observed behavior, we perform Green's function calculations of 1T-TaS$_2$ surfaces in the CCDW. Our theoretical model reproduces the invariance of the charge transfer times with respect to different orbital-polarizations of the excited wave-packets. In combination with the experiment, we conclude therefore, that an increased interlayer coupling causes isotropic three-dimensional charge transfer behavior in the CCDW phase. The experimentally observed breakdown towards anisotropic charge transfer in the NCDW phase is not easily addressed in our fully periodic calculations (due to the incommensurations in the structure). However, it is has been suggested that variations with respect to the stacking of the CDWs in subsequent layers can critically affect the electronic structure around the Fermi level [243, 244]. Here, we study the effect of such variations in the stacking onto the unoccupied electronic structure. Our results indicate, that these variations are not the responsible mechanism for the differences in the charge transfer behavior across the NCDW–CCDW transition.

The chapter is organized as follows: First, we set up a theoretical model of 1T-TaS$_2$ in the CCDW phase, which captures previously observed experimental properties of the material. Secondly, we briefly introduce some aspects of excitations in atoms by linearly polarized light and their effect onto the spectra in our calculations and experiments. Then we summarize the experimental core-hole-clock results. To further investigate the origin of the experimental results, we study the calculated unoccupied electronic structure of 1T-TaS$_2$ above the Fermi level. Here, we focus on the effect of different stackings and orbital-projections of the extracted spectra in relation to the polarization-dependent experiments. We relate the features of the experimental spectra to semi-empirical two-dimensional maps derived from our DFT calculations. The correspondence between experiment and theory allows us to extract estimates of the lifetimes of the identified features in the energy ranges probed by the experiment. We use our results to rationalize the invariance of the experimental charge transfer times with respect to different polarizations of the excitation in the CCDW. The chapter is concluded with a summary and a brief outlook onto possible future investigations.

# 7.1.  1T-TaS$_2$ in the Commensurate Charge Density Wave Phase

A CDW is a periodic modulation of the electron density, which arises commonly in low-dimensional electron systems in combination with a periodic lattice distortion (PLD) [242, 245]. The period of these two modulations can be expressed by rational or integer multiples of the lattice vectors in the case of a CCDW, or by irrational multiples of the lattice vectors in the case of a NCDW. Either way the original translational symmetry of the underlying crystal lattice is broken. The mechanism behind the formation of CDWs is frequently illustrated using the example of Peierls distortions in one-dimensional chain-like systems [246].

Regarding a Peierls distortion a doubling of the lattice constant by displacing every second atom in the one-dimensional chain leads to the opening of a gap around the Fermi energy (for half-filled bands, i.e., every ion contributes one electron). This opening of a gap translates into an effective energy gain due to the shift of the occupied band next to the Fermi level to lower energies, driving a metal-insulator transition. A Peierls distortion can be observed, whenever the gain in energy due to the opening of gaps around the Fermi energy is larger than the energy required to distort the lattice. This happens usually below a characteristic transition temperature. A more general analytic description of CDWs is achieved in terms of model Hamiltonians taking electron-electron and electron-phonon interactions into account, such as the Fröhlich Hamiltonian [247].

At ambient pressure 1T-TaS$_2$ exhibits a CCDW at temperatures below $\sim$ 180 K. The super lattice is rotated by 13.9° with respect to the original crystal lattice and exhibits a PLD, where clusters of 13 Ta atoms form the so-called Star-of-David reconstruction [248]. Above the critical temperature of $\sim$ 180 K a transition to a NCDW occurs. Here, the CDW vector is rotated by 12° with respect to the fundamental lattice and multiple Star-of-David reconstructions agglomerate into clusters separated by domain walls [249]. At even higher temperatures above $\sim$ 350 K the CDW becomes incommensurate [241]. Incommensurations and domain walls are not easily simulated in periodic calculations as the simulation cells become quickly intractably large. However, recently DFT has been used to model the appearance of domain wall reconstructions related to the NCDW [250].

In our calculations we restrict ourselves to fully periodic 1T-TaS$_2$ in the CCDW phase. We employ the SIESTA/TranSIESTA code and in particular the tbtrans module to extract Green's functions in relation to semi-infinite surfaces as described in Chapter 3. Since the repeating layers of 1T-TaS$_2$ are joined by vdW-interactions, we apply the vdW-DF by Dion et al. [81] with the optimized exchange by Klimeš et al. [85] (optB88-vdW) to account for dispersion forces in-between the layers. The optB88-vdW functional has been reported to yield a good performance for layered materials in comparison with accurate RPA calculations, in particular when investigating energetic variations related to different stackings [251]. To generate the required relativistic Troullier-Martins pseudopotentials [109], we used the semi-local density functional BLYP [74, 252], which is based on the exchange by Becke [74], as is the optB88-vdW functional [85]. Furthermore, we employed an atom centered
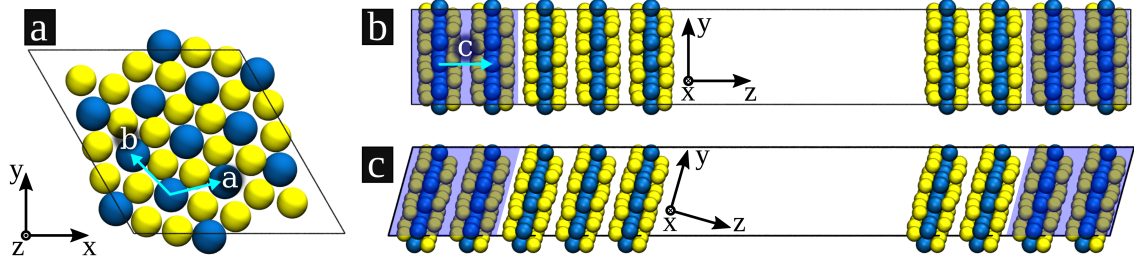
**Figure 7.1.:** Geometries employed in the simulations presented in this chapter. (a) Unit cell of the distorted structure of TaS$_2$ in the CCDW. The black box indicates the $\sqrt{13}a \times \sqrt{13}a$ supercell in which the blue Ta atoms are slightly displaced towards the central Ta atom (displacements not discernible in the figures) by a periodic lattice distortion in the CDW-phase. The light blue vectors **a**, **b**, and **c** in the subplots depict the unit cell vectors of 1T-TaS$_2$ in the undistorted structure. (b, c) Set-ups for simulations of 9-layer slabs of 1T-TaS$_2$ with respect to different CDW stackings: (b) according to a stacking vector $\mathbf{T}_s = \mathbf{c}$ and (c) according to $\mathbf{T}_s = 2\mathbf{a} + \mathbf{c}$. The stacking in (c) results in a tilted computational cell. The blue shaded areas indicate the layers carrying the self-energies to connect the slab on each side of the cell to infinite 1T-TaS$_2$ substrates.

basis set including double-$\zeta$ and polarization orbitals [104] with a SIESTA-specific energy-shift of 0.1 eV for the confinement of the orbitals.

This level of theory is not expected to reproduce every detail of the band structure around the Fermi level as for example the accurate size of the experimentally observed pseudogap [253]. Nevertheless, a rather good overall agreement with spectroscopic results has been reported for comparable simulations [243, 244].

To simulate the bulk phase of 1T-TaS$_2$ in the CCDW state, we set up the well-known $\sqrt{13}a \times \sqrt{13}a$ hexagonal super cell containing 13 Ta atoms in the Star-of-David reconstruction [248, 254], see Fig. 7.1a. This is achieved by an initial displacement of the surrounding Ta atoms towards a central one. A subsequent geometry relaxation produces the Star-of-David reconstruction, where the sulfurs around the center of contraction buckle slightly outwards. The distortion of the lattice simultaneously stabilizes a CDW [243]. The forces were relaxed within a threshold of 25 meV/Å and a maximum displacement of 0.1 Bohr was allowed between subsequent relaxation steps. We used a $5 \times 5 \times 9$ Monkhorst-Pack k-point sampling, a Mesh cutoff of 200 Ry, and an electronic temperature of 300 K. Convergence was assumed when the elements of the density matrix changed by less than $10^{-4}$ in consecutive SCF steps.

In order to set up the $\sqrt{13}a \times \sqrt{13}a$ super cell of the layered bulk material the lattice parameters of the undistorted material's cell containing a single unit of TaS$_2$ were used. The corresponding in-plane lattice vectors **a** and **b** of the undistorted material are shown in Fig. 7.1a (light blue arrows). The lattice parameters $a = 3.398$ Å and $c = 5.910$ Å were obtained from relaxation runs with a stress tolerance of 0.1 GPa and a k-point sampling of $20 \times 20 \times 10$. These values are in good agreement with the ones determined experimentally ($a = 3.360$ Å and $c = 5.897$ Å) [249].

The final slab calculations with a fixed cell employed nine layers, where the outer
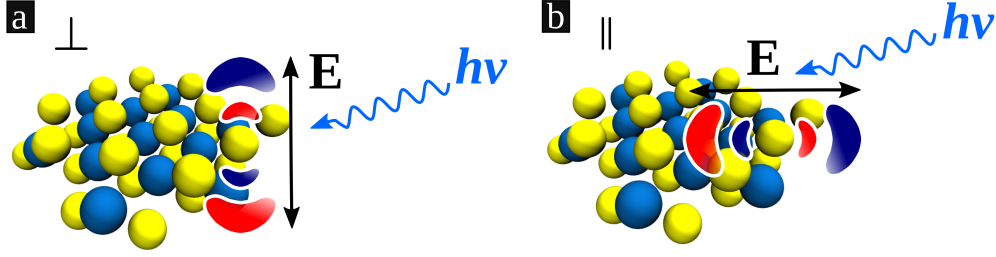
**Figure 7.2.:** Perspective sketch of the selective excitation of S2s-electrons into S3p-states inside a single layer of 1T-TaS$_2$ by linearly polarized light with an electrical field vector **E**: Shown are the dipole transitions into (a) out-of-plane and (b) in-plane polarized orbitals.

two layers on each side have been relaxed. The surface Brillouin zone was sampled with $5 \times 5$ k-points and 30 Å of vacuum were added. Moreover, we used two types of cells to simulate different stackings of the CDW/PLD in consecutive layers: Hexagonal super cells (Fig. 7.1b) to simulate the CDW stacking given by the stacking vector $\mathbf{T}_s = \mathbf{c}$ [249, 255] and triclinic super cells (Fig. 7.1c) for the $\mathbf{T}_s = 2\mathbf{a}+\mathbf{c}$ stacking. The outer two layers on each side of the cells carried the selfenergies connecting the slab to an infinite amount of layers representing the bulk substrate (see blue shaded areas in Fig. 7.1b, c). These selfenergies were extracted from separate bulk calculations considering a computational cell with just two TaS$_2$-layers.

In the Tables 7.1 and 7.2 we compare the distorted $\sqrt{13}a \times \sqrt{13}a$ unit cell from our bulk calculations with the experimental observations [255, 256]. Our calculations produce reasonable structures as can be seen from the displacements with respect to the undistorted crystal structure in Table 7.1 and the distances between pairs of neighboring atoms Table 7.2. Considering the experimentally reported standard deviations and the slightly larger simulation cell in comparison to the experimental lattice, the calculated values agree well with the geometry in the experiment.

## 7.2. Selective Excitation with Polarized Light

In the experiment the X-ray excitation causes an electronic transition from an occupied S2s state into an unoccupied S3p orbital. According to atomic dipole selection rules the polarization of the incident electromagnetic field **E** with frequency $h\nu$ can be used to formally select the orientation of the intermediate S3p states, i.e., a preparation of the initial wave packet or the excited electron in terms of a particular linear combination of the p$_x$, p$_y$, and p$_z$ orbitals is possible. Accordingly, we write for the resonance states in our calculations [22]

$$|\phi_R\rangle = |\phi_R(t=0)\rangle = e_x |p_x\rangle + e_y |p_y\rangle + e_z |p_z\rangle = |\phi_R(\vartheta, \varphi)\rangle, \qquad (7.1)$$

where $e_{i=x,y,z}$ are the components of the normalized polarization vector **e** of the electromagnetic field $\mathbf{E} = |\mathbf{E}|\mathbf{e}$. The polarization of the resonance state can be expressed in terms of polar coordinates $|\phi_R(\vartheta, \varphi)\rangle$ with the azimuthal angle $\varphi$.

**Table 7.1.:** Displacements in Å of different atoms in the Star-of-David reconstruction with respect to the undistorted substructure of 1T-TaS$_2$ in comparison with the experimental findings [255, 256]. The inequivalent atomic sites are numbered in the drawing on the left in analogy to the Refs. 255, 256. The values in brackets refer to the standard deviations in units of the last displayed digit.
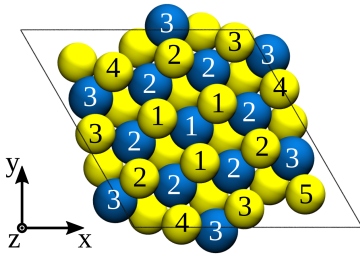


| | theo. | exp. | | theo. | exp. |
|---|---|---|---|---|---|
| Ta1 | 0.001 | 0.0 | S1 | 0.112 | 0.11(4) |
| Ta2 | 0.192 | 0.215(5) | S2 | 0.092 | 0.09(3) |
| Ta3 | 0.245 | 0.236(6) | S3 | 0.084 | 0.10(1) |
| | | | S4 | 0.090 | 0.13(2) |
| | | | S5 | 0.073 | 0.07(2) |

**Table 7.2.:** Distances between neighboring atoms in the Star-of-David reconstruction in comparison with the experimental values [255, 256]. Shown are values for Ta—Ta and Ta—S pairs in Å. The theoretical values show three decimal places to put emphasis on chemically different and equivalent sites. The integers before the numbered atoms refer to the amount of equivalent neighbors. We note, that the theoretical values for the two Ta2—1S1 distances might be swapped with respect to the experimental ones as it was not possible to identify the atoms unequivocally. The same holds for the two Ta2—1S2 distances.

| | theo. | exp. | | theo. | exp. |
|---|---|---|---|---|---|
| Ta1—6Ta1 | 3.207 | 3.15(1) | Ta1—6S1 | 2.528 | 2.50(3) |
| Ta2—1Ta1 | 3.207 | 3.15(1) | Ta2—1S1 | 2.456 | 2.39(3) |
| —2Ta2 | 3.207 | 3.15(1) | —1S1 | 2.462 | 2.41(3) |
| —1Ta2 | 3.268 | 3.27(1) | —1S2 | 2.541 | 2.48(3) |
| —1Ta3 | 3.305 | 3.29(1) | —1S2 | 2.537 | 2.45(3) |
| | | | —1S3 | 2.568 | 2.54(3) |
| | | | —1S4 | 2.583 | 2.57(3) |

The spectral density is then given by the expectation value of the Green's function operator over the resonance state $\rho_R(E, \vartheta, \varphi) = -1/\pi \, \mathrm{Im} \, G_{RR}^+(E)$ [cf. Eq. (3.39)]. We split the spectrum $G_{RR}^+(E)$ into two parts: an in-plane $G_\parallel^+(E)$ and an out-of-plane $G_\perp^+(E)$ contribution. The in-plane contribution is given by an average over the azimuthal angles $\varphi$ (the z-direction is perpendicular to the surface)

$$
\begin{aligned}
G_\parallel^+(E) &= \frac{1}{2\pi} \int_0^{2\pi} \langle \phi_R(\vartheta = \pi/2, \varphi) | G^+(E) | \phi_R(\vartheta = \pi/2, \varphi) \rangle \, d\varphi \\
&= \frac{1}{2} \langle p_x | G^+(E) | p_x \rangle + \frac{1}{2} \langle p_y | G^+(E) | p_y \rangle ,
\end{aligned}
\tag{7.2}
$$

whereas the out-of-plane contribution is simply given by the contribution from the $p_z$ orbitals

$$
G_\perp^+(E) = \langle p_z | G^+(E) | p_z \rangle .
\tag{7.3}
$$

Using Eqs. (7.2) and (7.3) one can in principle extract estimates of the ultrafast time-scales of the charge transfer in different directions inside the material (cf. Chapter 3 and Section 7.6 below).

Additionally, and in analogy to the core-level spectroscopy experiments presented below (see also the introduction in Chapter 4), we generate pseudopotentials for excited sulfur atoms considering an electronic configuration with a hole in the 2s core state. In our periodic calculations the positive charge due to the hole is subsequently balanced by an additional electron in the valence. We assume that there are only two excited sulfur atoms inside the simulation cell, i.e., one on each of the two outermost sulfur layers of 1T-TaS$_2$ facing each other (cf. Fig. 7.1b, c). The excited sulfurs are placed symmetrically on both sides of the slab in a dipole canceling set-up. We take into account the five inequivalent sulfur sites in the outermost sulfur layers in separate calculations. It can be seen in the drawing in Table 7.1, that there are three of each of the sulfurs numbered 1 to 4 and only one with the label 5. To obtain the overall spectra we perform correspondingly weighted averages.

## 7.3. Polarization Dependence of the Resonant Photoemission Spectra

The core-hole-clock analysis of resonant photoemission spectroscopy (see Chapter 4) is a uniquely powerful tool to investigate the atomic origin and directionality of charge transfer. This is rooted in the chemical selectivity, surface sensitivity, defined knowledge about the involved electronic transitions, and sub-femtosecond time resolution of the technique. As illustrated in the previous section, atomic dipole selection rules allow in such experiments to selectively populate oriented orbitals such as $p_x$, $p_y$, and $p_z$ components of the sulfur 2s→3p transition (see Fig. 7.2). This has been established for the directional attosecond charge transfer from adsorbed sulfur atoms into a Ru(0001) [22, 123] surface. This section summarizes new results from polarization dependent core-hole-clock experiments probing directional charge transfer for different electronic phases of layered 1T-TaS$_2$. The experiments have been carried out by D. Kühn et al. in the group of Prof. A. Föhlisch at the BESSY II
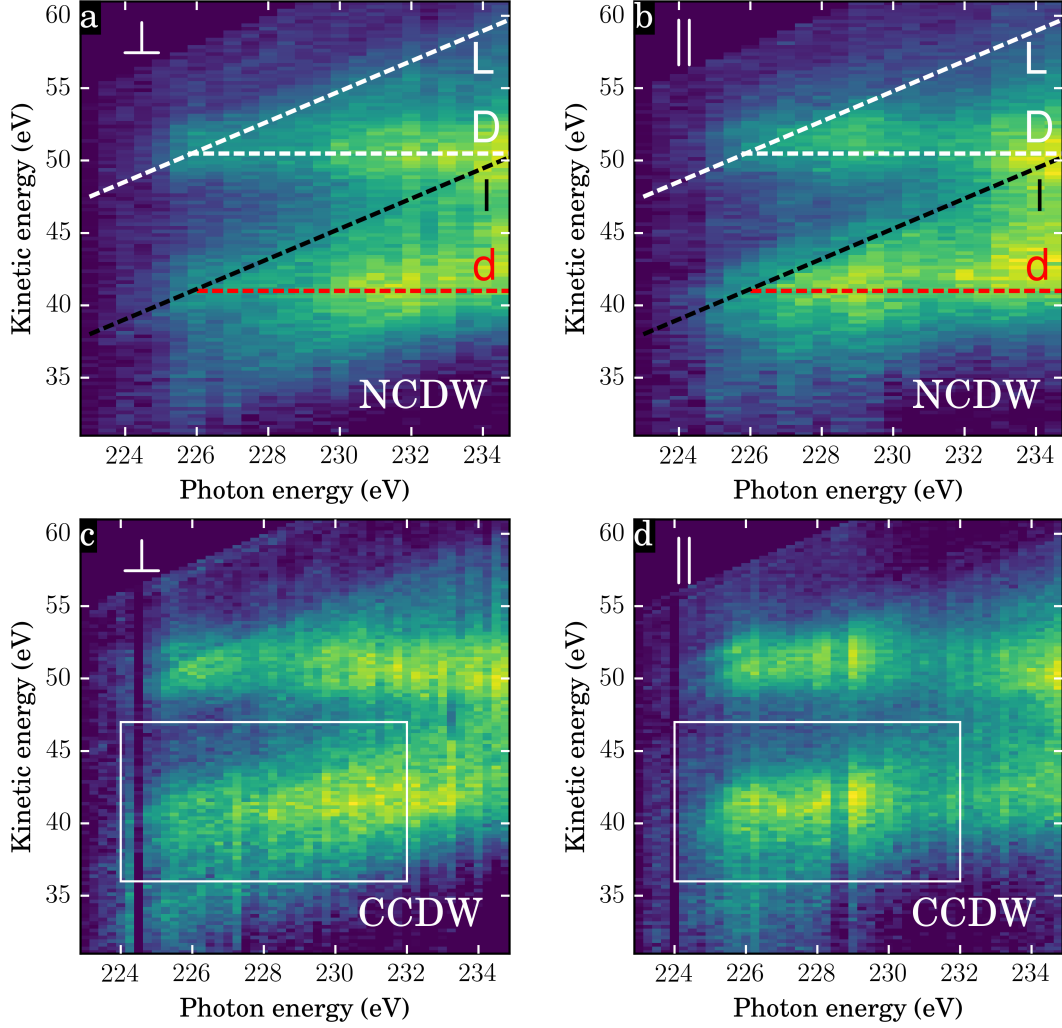
**Figure 7.3.:** Experimentally recorded Coster-Kronig auto-ionization spectra of 1T-TaS$_2$ in the NCDW (a, b) and CCDW (c, d) phase for the S2s→S3p transitions. In both cases the spectra are shown for excitation into in-plane orbitals ($\parallel$) and out-of-plane orbitals ($\perp$) of p-type. Lighter colors show higher intensities. The lines in (a, b) indicate the linear dispersion of the localized Auger-Raman decay channels for S2p$^{-1}$3p$^{-1}$3p$^{1}$ (L) and S2p$^{-1}$3s$^{-1}$3p$^{1}$ (I) final states. In contrast, the delocalized Auger decay channels with the final states S2p$^{-1}$3p$^{-1}$deloc$^{1}$ (D) and S2p$^{-1}$3s$^{-1}$deloc$^{1}$ (d) do not disperse with the incoming photon energy. The delocalized channels appear above the resonance frequency of $h\nu = 226$ eV. For clarity, the lines indicating the channels are not repeated in (b, d), where instead the boxes indicate the rough energy ranges of the simulated spectra presented below in Fig. 7.9.
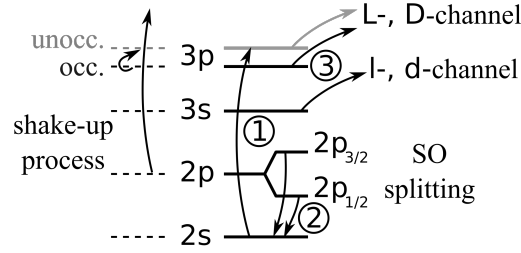
**Figure 7.4.:** Scheme showing the various transitions during resonant photoemission in sulfur contributing to the auto-ionization spectra in Fig. 7.3. In particular, ① initial excitation by incoming radiation, ② decay of the core-hole, and ③ ejection of the Auger(-like) electron. In the presence of the excited electron localized channels (l, L) contribute, after delocalization of the excited electron delocalized channels (d, D) contribute. The Shake-up process shown on the left side leads to an equivalent final state as the decay via the L-channel. Note that the numbering of the transitions is not meant to imply a strict chronological order of the processes. In particular, the Auger-like decay via ② and ③ is often considered as one process. Regarding the localized l, L-channels also the excitation cannot be seen as entirely independent from the decay, which is evident from the dispersion of the kinetic energy of the emitted electron with the incident photon energy in the experiments.

in Berlin. More details regarding the specifics of the experiment can be found in Ref. 52.

Fig. 7.3 shows the experimental auto-ionization spectra for the room temperature NCDW phase and the low temperature CCDW phase ($\sim 30$ K, cryogenic temperature) of 1T-TaS$_2$. The spectra have been recorded for excitations with in-plane ($\parallel$) and out-of-plane ($\perp$) polarized X-rays, referring to the surface plane. The dashed lines in Fig. 7.3a, b indicate the various decay channels appearing in the spectra.

After the initial excitation (S2s→S3p), the excited electron has the possibility to stay localized at the excited atom during the core-hole decay. In this case the Auger decay proceeds via emission from an occupied 3s-level via the so-called l-channel or via emission from an occupied 3p level via the L-channel. The associated final state configurations are S2p$^{-1}$3s$^{-1}$3p$^1$ (l) and S2p$^{-1}$3p$^{-1}$3p$^1$ (L), respectively. The localized channels show the typical linear dispersion of the features towards higher kinetic energies with increasing energy of the incoming photons.

The excited electron has also the possibility to decay (delocalize) into the substrate before the core-hole decays, leading to delocalized decay channels via Auger processes. This involves the possible final states S2p$^{-1}$3p$^{-1}$deloc$^1$ (D-channel) and S2p$^{-1}$3s$^{-1}$deloc$^1$ (d-channel) for decays involving the occupied 3p or 3s levels, respectively. Clearly, for the delocalized channels the energy is not locally conserved. In other words the coherence between the initial excitation process and the subsequent Auger decay is lost so that the Auger emission lines appear at constant kinetic energies of 41 eV (d-channel) and at 50, 6 eV (D-channel).

A scheme showing all the possible transitions contributing to the auto-ionization spectra can be seen in Fig. 7.4. The scheme additionally shows that shake-up pro-
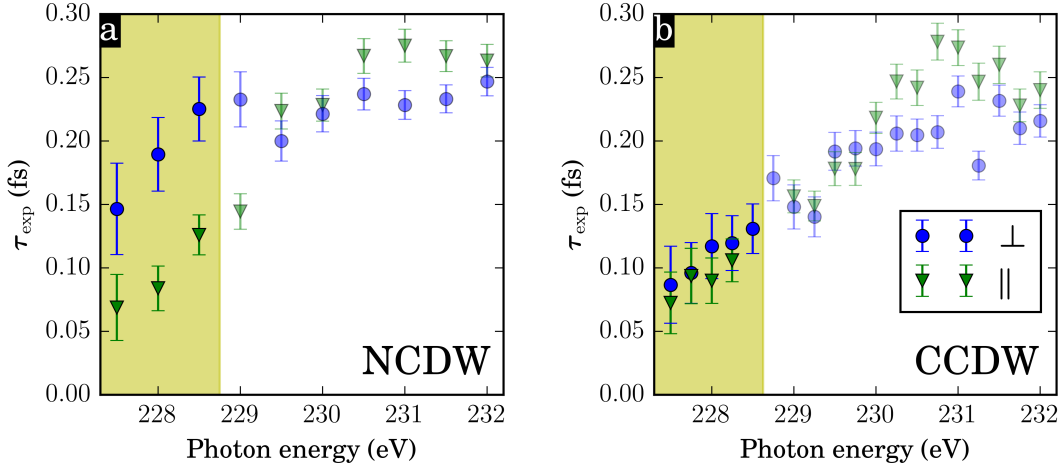
**Figure 7.5.:** Experimentally obtained charge transfer times for in-plane ($\parallel$) and out-of-plane ($\perp$) polarization of the incoming radiation: (a) results for the NCDW and (b) for the CCDW of 1T-TaS$_2$. Due to the appearance of a second resonance between 229 eV and 230 eV only the extracted value below 228.5 eV can be directly interpreted as charge transfer times. The values above those energies, which are shown here as shaded data points, result from a superposition of the intensities from the first and the second resonance (see Section 7.5 below) and hence are difficult to interpret, i.e., to analyze in terms of absolute charge transfer times using the core-hole-clock technique.

cesses involving an excitation of the 3p-level and direct photoemission from the 2p-level coincide with the final states of decays via the L-channel. These shake-up processes are allowed through monopole selection rules [22]. Their presence makes the analysis of the L-channel unsuitable for the core-hole-clock analysis, since they prevent a direct identification of the localized channels and thus inhibit an unambiguous extraction of the Raman fraction. Therefore, we examine instead the pure auto-ionization feature of the l-channel in order to extract information about the lifetimes of the excited resonances.

The resonances appear at photon energies of $\hbar\omega = 226$ eV. The intensities of all the channels (l, L, d, D) can be unambiguously extracted for photon energies ranging from 227.5 eV to 235 eV, probing states above the Fermi level. At 235 eV the l- and D-channels cross. Nevertheless, the charge transfer analysis of the experimental data had to be further restricted to the range of photon energies from 227.5 to 228.5, where the l-channel and the d-channel are ideally separable. The reason for this is, that between 229 eV and 230 eV a second resonance appears making an unambiguous identification of the separate channels difficult (see the description in Section 7.5 below).

To extract the lifetimes from the experimental data, a set of Lorentzian peaks was fitted for each photon energy (see [52] for details of the fitting procedure). This allows to extract the Raman fraction in dependence of the photon energy from the intensities of the localized and delocalized decay channels. The charge transfer time is then determined relative to the core-hole lifetime ($\tau_c = 0.5$ fs) of the sulfur 2s state
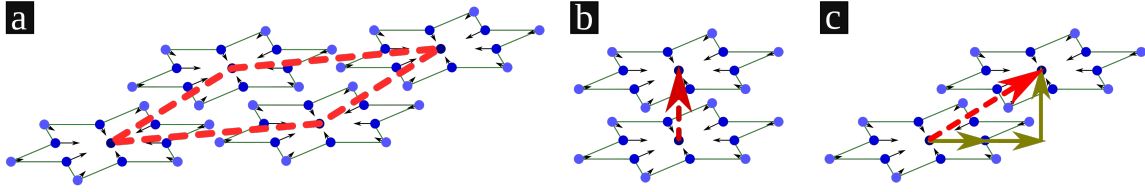
**Figure 7.6.:** Ta planes of 1T-TaS$_2$ in the CCDW: (a) Star-of-David reconstructions, where 12 surrounding Ta atoms contract towards a central one. The red dashed line marks the $\sqrt{13}a \times \sqrt{13}a$ cell. Different stacking vectors $\mathbf{T}_s$ (red dashed arrows) control the alignment of the reconstructions in adjacent layers: (b) Pairing of the Star-of-David centers in subsequent layers $\mathbf{T}_s = \mathbf{c}$ and (c) avoiding such paring in subsequent layers $\mathbf{T}_s = 2\mathbf{a} + \mathbf{c}$.

[cf. Eq. (4.5)]. Fig. 7.5 displays the extracted lifetimes for all combinations of the two investigated CDW phases and the two polarizations of the X-ray excitation in the relevant energy range.

In the NCDW phase in-plane charge transfer is twice as fast as out-of-plane charge transfer (cf. Fig. 7.5a), emphasizing the two-dimensional character of the material. A similar, but more pronounced anisotropy regarding the charge transfer in quasi-two-dimensional materials has been reported for core-hole clock experiments on layered SnS$_2$ [142]. In the latter work, the anisotropy was related to different spectral ranges with varying composition of orbital orientations (in-plane and out-of-plane), as obtained from DFT-calculations. The measurement on TaS$_2$ presented here, directly assess the anisotropy in the material by probing different orbital orientations via selective initial excitation.

Surprisingly, and in contrast to the NCDW phase, the CCDW phase (cf. Fig. 7.5b) exhibits no dependence on the polarization of the initial excitation. We observe thus an isotropic charge transfer behavior. Both, the in-plane and the out-of-plane charge transfer being as fast as the in-plane charge transfer in the NCDW phase. The nominal time-scale is about 100 as. This lines up with several previous experimental findings: The appearance of domain walls in the NCDW phase [249]. The increase of CDW ordering along the *c*-axis during the NCDW to CCDW transition. The presence of a metallic band at the Fermi level in the direction perpendicular to the crystal layers observed in ARPES experiments [257].

## 7.4. Influence of Stacking on the Electronic Structure of 1T-TaS$_2$

The electronic structure of low-dimensional materials depends strongly on a variety of parameters like pressure, doping, and stress. Similarly, the electronic structures of 1T-TaS$_2$ [243, 244, 258] and TaSe$_2$ [259] are known to be sensitive to the stacking sequence of the CDW/PLD in subsequent layers. In particular, the formation of a metallic band along the out-of-plane direction [257] has been linked to a particular stacking order in several studies of CCDW phase. To investigate the possibility of

similar effects at energies further above the Fermi level (where the 3p-resonances of interest live, i.e., in the range up to $\sim 2$ eV above the Fermi level), we study the influence of stacking in the CCDW phase within our DFT model.

We examine in particular two different stackings, which appear in the CCDW phase of 1T-TaS$_2$ according to theoretical considerations [260, 261] and diffraction experiments [262–264]. The first one is defined by the stacking vector $\mathbf{T}_s = 2\mathbf{a}$ and aligns the centers of the Star-of-David reconstructions within adjacent layers (Fig. 7.6b). This first stacking is energetically less favorable, since it pairs the outwards buckling sulfur atoms around the Star-of-David centers in the neighboring TaS$_2$ sheets. The second stacking according to $\mathbf{T}_s = 2\mathbf{a} + \mathbf{c}$ pairs weakly displaced Sulfur atoms in-between the centers of contraction in one layer with strongly displaced Sulfur atoms at the Star-of-David centers in a neighboring layer.

At the Fermi level, our bulk calculations of 1T-TaS$_2$ in the CCDW phase show clearly the observed metallic band for the $\mathbf{T}_s = \mathbf{c}$ stacking along the out-of-plane Γ—A direction of the band structures displayed in Fig. 7.7a, b. The band is almost entirely flat in the in-plane directions of the Brillouin zone, where the electronic structure is pseudogapped around the Fermi level, making the material a semiconductor along these directions. Interestingly, changing the stacking to $\mathbf{T}_s = \mathbf{c}$ in Fig. 7.7c, d switches the material to a metallic phase along all directions in the calculations. This reproduces the observations from comparable DFT-based studies [243, 259].
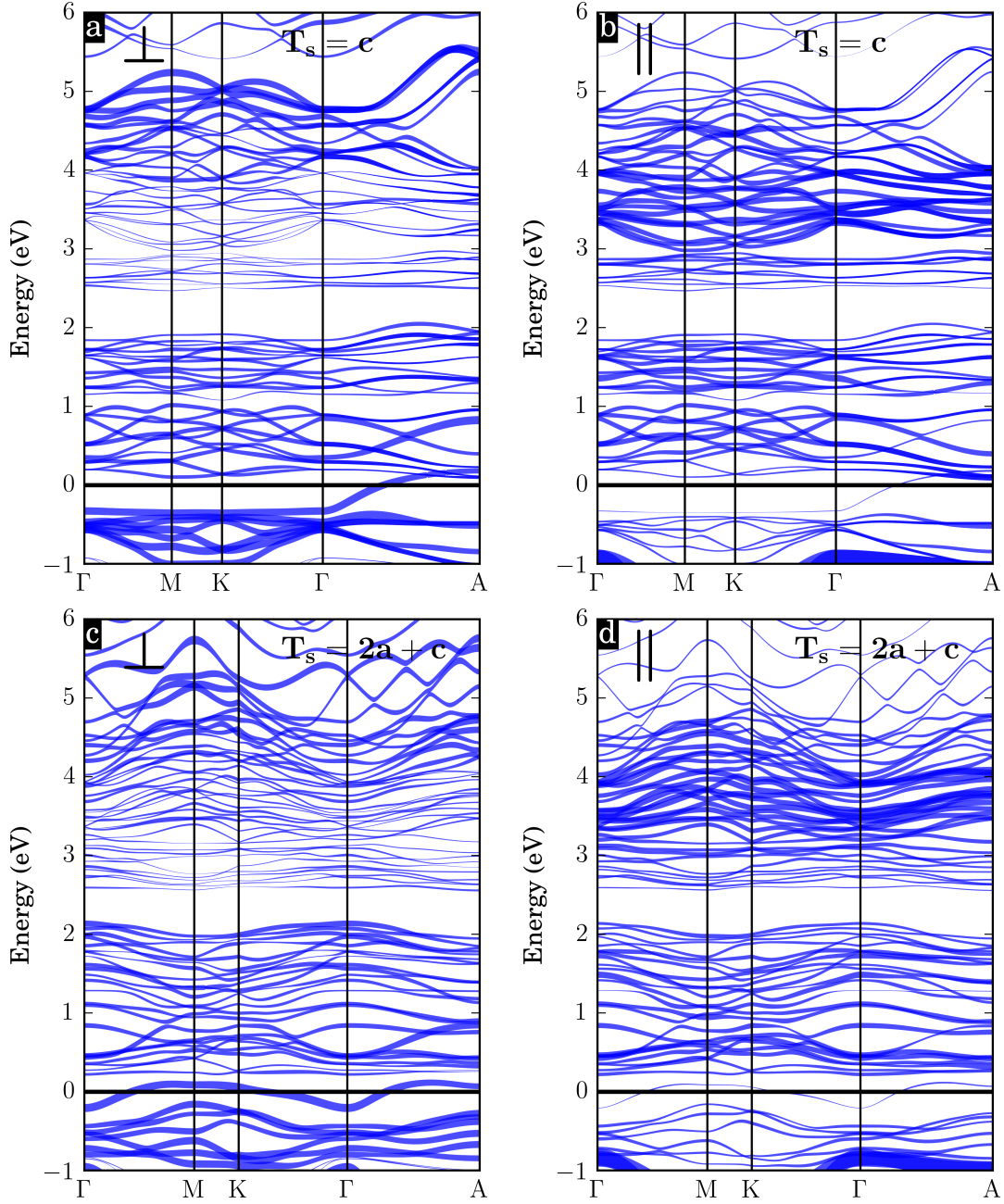
Above the Fermi level the band structure from our bulk calculations appears split by an electronic gap at around $\sim 2$ eV. This is in line with the observations from IPES experiments [265, 266]. The IPES spectroscopic results in both of these studies show a splitting into two bands around $\sim 2$ eV. Another slight splitting of the bands is also visible for the $\mathbf{T}_s = \mathbf{c}$ stacking in Fig. 7.7a, b around 1 eV, whereas it is absent in the second stacking.

Additionally, we study the contributions to the different bands from in-plane polarized ($\parallel$, p$_{x,y}$-orbitals, Fig. 7.7b, d) as well as from out-of-plane polarized ($\perp$, p$_z$-orbitals, Fig. 7.7a, c) p-type orbitals. This is indicated by the widths of the bands in the plots. The weights of the in-plane polarizations have been determined by an average between the $p_x$ and $p_y$ contributions [compare to Eq. (7.2)] and the ones of the out-of-plane polarizations by the $p_z$ contributions. It is clearly visible that the dispersive metallic band crossing the Fermi level is related to out-of-plane polarized orbitals, while the weight stemming from in-plane polarized contributions is negligible.

The block of bands between the Fermi level and the gap around $\sim 2$ eV is overall rather similar regarding the weights on in-plane and out-of-plane components in the Γ—A direction. However, a few dispersive bands appear, which pertain mainly to out-of-plane oriented p-orbitals. Above the electronic gap around $\sim 2$ eV the contributions are less homogeneously distributed: Contributions from in-plane polarized orbitals are centered around roughly 3.5 eV, while the out-of-plane contributions dominate at higher energies around roughly 5 eV for both stackings.

In comparison with experiments and further theoretical studies, we have so far established a model of the geometry and the electronic structure of 1T-TaS$_2$ in the bulk CCDW phase. This allows us to move on to surface calculations using Green's functions to describe the semi-infinite substrate (see the geometric setup in Fig. 7.1b, c).

**Figure 7.7.:** Band structures of bulk 1T-TaS$_2$ for different stackings of the CDW around and above the Fermi energy (used to define the zero of energy): (a, b) stacking according to $\mathbf{T_s} = \mathbf{c}$ and (c, d) according to $\mathbf{T_s} = 2\mathbf{a} + \mathbf{c}$. The thickness of the bands reflects the weight of the states on the in-plane p$_{x,y}$-orbitals ($\parallel$) in (a, c) and the out-of-plane p$_z$-orbitals ($\perp$) in (b, d). Our results reproduce the transition from an in-plane semi-conducting material for $\mathbf{T_s} = \mathbf{c}$ towards an in-plane conductor for $\mathbf{T_s} = 2\mathbf{a} + \mathbf{c}$ in agreement with Ref. 243.
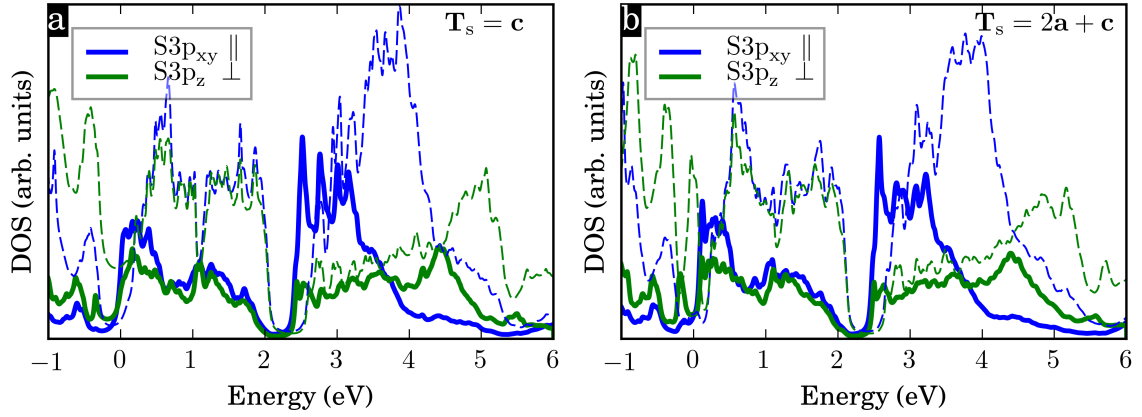
**Figure 7.8.:** Spectral densities from weighted averages across inequivalent sulfur sites in relation to different polarizations of S3p orbitals: in-plane $p_{xy}$-polarization ($\parallel$) and out-of-plane $p_z$-polarization ($\perp$). Shown are two different stackings of CDWs in consecutive layers. In (a) the stacking is according to a stacking vector $\mathbf{T}_s = \mathbf{c}$ and in (b) according to $\mathbf{T}_s = 2\mathbf{a} + \mathbf{c}$. The thick lines refer to the core-excited case and the thin dashed lines belong to the ground state case. To obtain the average core-excited spectra, we performed five distinct calculations, each considering a hole in the 2s shell of the pseudopotentials of one of the inequivalent sulfurs at the surface.

We also introduce the core-excited sulfur atoms by considering modified pseudopotentials as described in Section 7.2.

Fig. 7.8 shows the spectral densities related to in-plane [Eq. (7.2)] and out-of-plane [Eq. (7.3)] polarized S3p-orbitals in the outer atomic layer of a 1T-TaS₂ surfaces. We also consider the two readily introduced stacking schemes $\mathbf{T}_s$ in the plot. All spectra have been calculated from weighted averages over the inequivalent sulfur sites. The thick lines refer to the core-excited simulation, while the dashed lines refer to the ground state. In the core-excited case the main weights of the two blocks of bands which can be observed above the Fermi level are shifted towards lower energies. However, the splitting of the DOS shortly above 2 eV, which we already observed for the ground state bulk band structures in Fig. 7.7, is preserved in the averaged spectra of the core-excited case (thick lines). Regarding both stackings, the DOS is spread out over a broad energy range, as a consequence of the covalent bonding of the sulfur atoms inside the material. The appearance of the spectra in the two subplots Fig. 7.8a, b is not critically affected by $\mathbf{T}_s$.

The broad appearance of the spectra in Fig. 7.8 makes an assignment of spectral features to the resonances studied in the core-hole-clock experiment difficult. This is in contrast to the previously studied molecules (Chapter 5) and atoms (Chapter 6) adsorbed on surfaces, where the adsorbate states appeared as peaked resonances in the spectra. To relate the resonances observed in the experiment to the calculations we perform a post-processing of the data in the next section.
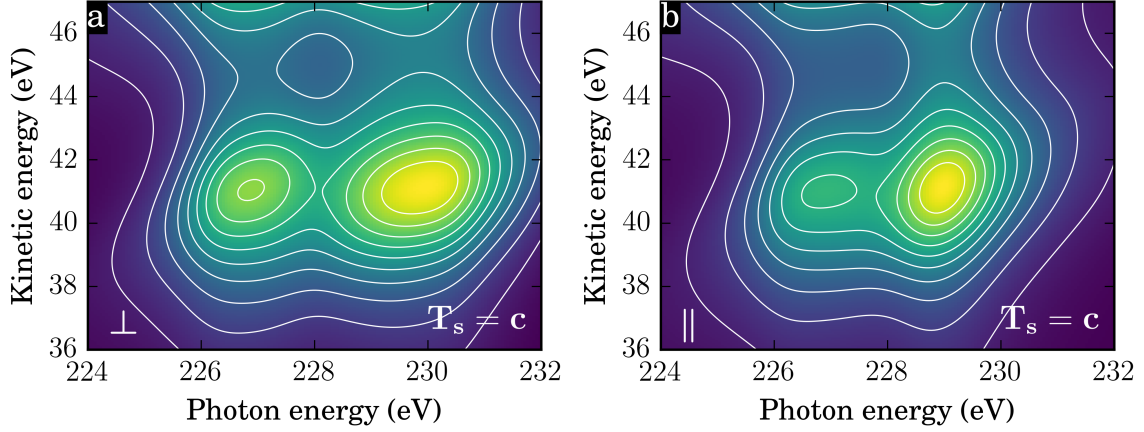
**Figure 7.9.:** Simulated spectra of the auto-ionization processes according to the semi-empirical formula in Eq. (7.4). The spectra are derived from the spectral densities related to the stacking vector $\mathbf{T}_s = \mathbf{c}$ in Fig. 7.8a. Shown are the results for out-of-plane excitations (a) and in-plane excitations (b).

## 7.5. Semi-Empirical 2D Intensity Maps

In order to achieve a more immediate comparison with the experimental autoionization spectra for the CCDW phase of $1T\text{-}TaS_2$, we map the intensity of the localized decay channels (l- and L-channels) after S2s$\rightarrow$S3p excitation in the plane of the kinetic energy of the outgoing Auger-like electrons $E_A$ and the photon energy $\hbar\omega$. Therefore, we employ an adapted semi-empirical model following Drube et al. [267] and Föhlisch et al. [268], which we use to simulate the localized autoionization channels shown in Fig. 7.4,

$$I(E_A, \hbar\omega) \sim \int_{E_F}^{\infty} dE \int_{-\infty}^{E_F} dE' \frac{\rho^{3p}(E)}{(\hbar\omega - E - E_{2s})^2 + (\Gamma_{2s}/2)^2} \\ \times \frac{\rho_{SO}^{3s/3p}(E')}{(\hbar\omega - E - E_A - E_{2p_{3/2}} - E')^2 + (\Gamma_{3s,3p}/2)^2}. \tag{7.4}$$

The first fraction below the double integral refers to the probability of the transition S2s$\rightarrow$S3p of the excitation process (Fig. 7.4, ①), where the denominator ensures the conservation of energy taking into account a broadening due to the lifetime of the sulfur 2s core-hole of $\Gamma_{2s} = 1.5$ eV. The electron is excited into the unoccupied DOS of the 3p-orbitals $\rho^{3p}(E)$ at the energy $E$. This DOS is taken from our core-excited surface calculations shown by the thick lines in Fig. 7.7a. We use exclusively the data for the $\mathbf{T}_s = \mathbf{c}$ stacking since the differences with respect to the other stacking are negligible.

The Auger-like decay is described by the second fraction in Eq. (7.4) and proceeds via the transitions ② and ③ in Fig. 7.4. In this schematic view the 2s core-hole is filled by electrons from the energetically higher lying 2p-levels and the thereby released energy is used to eject electrons from the occupied DOS of the sulfur 3s-states (l-channel) or 3p-states (L-channel) at the energy $E'$. We denote the corresponding

occupied DOS by $\rho_{\text{SO}}^{\text{3s/3p}}(E')$ and adapt it, to account for the spin-orbit splitting of the 2p level in the following way,

$$\rho_{\text{SO}}^{\text{3s/3p}}(E') = \int [\rho^{\text{3s}}(E') + \rho^{\text{3p}}(E')][\delta(\epsilon - E') + 2\delta(\epsilon - E' + \Delta E_{\text{SO}})]\, d\epsilon\,. \qquad (7.5)$$

Here, we have taken into account the ratio between the multiplicities of the spin-orbit split 2p levels by placing a factor of 2 in front of the second $\delta$-function (i.e., $2p_{3/2}$ has four, while $2p_{1/2}$ has only two states corresponding to different values of the projection of the total angular momentum quantum number $M_J$ ). The spin-orbit splitting is given by the energy $\Delta E_{\text{SO}} = E_{2p1/2} - E_{2p3/2} = 1.2$ eV. The experimental determined binding energies of the $E_{2p1/2}$ level and $E_{2s}$ level are around 162.4 eV and 226 eV, correspondingly (considering a single-hole final state). $E_{\text{A}}$ is the energy at which the Auger electron is emitted. All energies in Eq. (7.4) are with respect to the Fermi level $E_{\text{F}}$, so that in order to obtain the kinetic energy $E_{\text{kin}}$ in the plots one has to subtract the experimentally estimated work function of $\sim 4.2$ eV from A.

Furthermore, we employ in Eq. (7.4) a broadening $\Gamma_{\text{3s,3p}} = 3.3$ eV, corresponding to the phenomenological width which was used for the experimental fittings of the autoionization spectra. In order to match the experiment, the final spectra have been shifted to lower kinetic energies by $\sim 2.6$ eV. This discrepancy may be due to additional coulomb interaction between the two holes in the final states (S2p$^{-1}$3s$^{-1}$ and S2p$^{-1}$3p$^{-1}$) of the localized decay channels.

Fig. 7.9 shows the resulting semi-empirical spectra for the $\mathbf{T}_{\text{s}} = \mathbf{c}$ stacking and the two polarizations (in-plane and out-of-plane). The features in the spectra, resemble the experimental data in Fig. 7.3c, d closely. The corresponding energy ranges in the experimental data (Fig. 7.3) are marked by white frames. The splitting of the bands around 2 eV (cf. Fig. 7.8) causes two features in the semi-empirical spectra around $\sim 228$ eV in both subplots of Fig. 7.9. However, for the out-of-plane polarization (Fig. 7.9b) the second feature above $\sim 228$ eV appears strongly broadened along the axis of the photon energies as in the experimental data. This establishes a good correspondence between the two separate features above the Fermi level in the theoretical spectra with the features in the experimental auto-ionization spectra. Due to the presence of two resonance features (one below and the other above $\sim 2$ eV with respect to the Fermi Level) a reliable analysis of the charge transfer times in terms of the core-hole-clock method can only be performed for photon energies below the appearance of the second resonance, while at energies above the spectra contain information about two distinct 3p-resonances.

## 7.6. Lifetime Extraction from S3p-Resonances in 1T-TaS$_2$: Facing Limitations

The theoretically determined S3p-projected spectra in Fig. 7.8 are rather broad and exhibit multiple features, reflecting the strongly hybridized character of the sulfur atoms. Such strong broadening inhibits the direct extraction of lifetimes from peak widths, which are associated with well-defined resonances. However, the correspondence of the experimental and the semi-empirical spectra in (Figs. 7.3 and 7.9),

respectively, allows us to identify the spectral features related to the energy ranges for which an unequivocal determination of the lifetimes by the core-hole-clock method is possible.

We identify in particular, the DOS between the Fermi energy $E_F = 0$ eV and the gap around 2.2 eV in Fig. 7.8a, b with the first resonance in the experimental spectra at 226 eV. Readily upon inspection with the bare eye, the calculated spectral densities in this energy range do not depend significantly on the orbital polarization in this energy range. One can also see that a strong dependence of the spectra on variations related to the stacking $\mathbf{T}_s$ can be ruled out.

In order to estimate values for the lifetimes related to separate features in the theoretical spectra $\rho(E)$ (cf. Fig. 7.8), we transform these to the time domain. We consider here a window function $W(E)$ to isolate the spectral feature corresponding to a resonance living on an energy interval $[E_{\min}; E_{\max}]$,

$$W(E) = [1 - f(E - E_{\min})]f(E - E_{\max}), \tag{7.6}$$

where $f(E)$ is the Fermi distribution at room temperature (300 K). The imaginary part of the projected resonance spectrum is then given by

$$\rho_R^W(E) = -\frac{1}{\pi} \operatorname{Im} \langle \phi_R | G(E) W(E) | \phi_R \rangle. \tag{7.7}$$

Here the resonance wave-packets $\phi_R$ may be any of the polarizations of the S3p-orbitals (p$_x$, p$_y$, or p$_z$).

To extract the lifetimes related to the spectral features $\rho_R^W(E)$ living on different energy intervals, we apply the procedure for the case of strongly coupled resonances outlined in Section 3.4; reconstructing the real part of $\rho_R^W(E)$ via the Kramers-Kronig relations and subsequently Fourier transforming to the time-domain. The value for the lifetime of a resonance at one site $\tau_i$ is taken to be the smallest time $t$ for which the population of the initial state drops below e$^{-1}$ (we correct a posteriori for the small energy broadening $\eta = 20$ meV used in Green's function calculations by multiplying the time-evolution of the population with a factor e$^{2\eta t}$). The overall lifetime $\tau_R$ is computed by the expression $\frac{1}{\tau_R} = \sum_i \frac{w_i}{\tau_i}$, where the $w_i$ are the weights

**Table 7.3.:** Theoretically extracted lifetimes in units of fs for the resonance feature in the energy intervals from 0 to 2.2 eV and from 2.2 to 5.7 eV. In both cases two distinct stacking orders $\mathbf{T}_s$ of the CCDW are analyzed as well as different polarizations of the sulfur 3p orbital (p$_x$, p$_y$, and p$_z$) defining the initial wave-packet after excitation with a correspondingly polarized X-ray.

| interval (eV) | $\mathbf{T}_s$ | $\tau_{3p_x}$ (fs) | $\tau_{3p_y}$ (fs) | $\tau_{3p_z}$ (fs) |
|---|---|---|---|---|
| $[0.0; 2.2]$ | $\mathbf{c}$ | $1.21 \pm 0.15$ | $1.19 \pm 0.15$ | $1.19 \pm 0.06$ |
| | $2\mathbf{a} + \mathbf{c}$ | $1.20 \pm 0.15$ | $1.19 \pm 0.14$ | $1.18 \pm 0.08$ |
| $[2.2; 5.7]$ | $\mathbf{c}$ | $1.17 \pm 0.19$ | $1.27 \pm 0.09$ | $0.80 \pm 0.11$ |
| | $2\mathbf{a} + \mathbf{c}$ | $1.19 \pm 0.19$ | $1.27 \pm 0.08$ | $0.82 \pm 0.11$ |

of the inequivalent sulfur sites in the super cell. The extracted values are listed in Table 7.3 together with their standard deviations due to the inequality in the sulfur sites.

The theoretical lifetime values for the first spectral feature living on the energy interval from $E_{\mathrm{F}} = 0$ eV to 2.2 eV are listed in Table 7.3. They agree qualitatively with the experimentally observed isotropic charge transfer behavior, reflected by the constant time-scales for the delocalization into the in-plane directions $\tau_{3\mathrm{p_x}}$ and $\tau_{3\mathrm{p_y}}$ and into the out-of-plane direction $\tau_{3\mathrm{p_z}}$. However, the absolute values for the theoretically determined charge transfer times depart from the experimental values (cf. Fig. 7.5) by an order of magnitude.

The charge transfer times for the second resonance in the DOS (cf. Fig. 7.8) living on the energy range from 2.2 eV to 5.7 eV show a different trend. The lifetimes $\tau_{3\mathrm{p_x}}$ and $\tau_{3\mathrm{p_y}}$ related to in-plane orbital-polarizations even exceed the lifetime $\tau_{3\mathrm{p_z}}$ related to the out-of-plane orbital-polarization [cf. Table 7.3]. Although this trend is seemingly reflected by the lifetimes in Fig. 7.5b, these extracted values are the result of a fitting procedure that assumes a single pair of l- and d-channels corresponding to a single resonance, hence a direct comparison is not possible. An extension of the applied fitting procedure, e.g., assuming another pair of l'- and d'-channels branching off at the second resonance, would require further assumptions to extract lifetimes in the energy range above $\sim 230$ eV, where the contributions from both resonances overlap.

## 7.7. Conclusions and Outlook

In this chapter we presented combined theoretical and experimental evidence that 1T-TaS$_2$ exhibits in spite of its layered structure surprisingly strong electronic interlayer coupling in the CCDW phase. We employed in our study a core-hole-clock analysis of resonant photoemission data in conjunction with Green's function based calculations at the level of semi-local DFT.

We studied in our theoretical model the dependence of the charge transfer times on different orbital-polarizations reflecting the selective excitation into in-plane and out-of-plane polarized sulfur 3p orbitals (wave-packets) by linearly polarized X-rays in the experiments. Although, the absolute ultrafast time-scales probed by the experiments are challenging for our model, we find that it supports the experimentally observed qualitative behavior: Resonances related to both in-plane and out-of-plane polarized orbitals produce equal charge transfer times, revealing the isotropic, three-dimensional character of the ultrafast charge transfer inside the material in CCDW phase.

We started by setting up a model of 1T-TaS$_2$ in the CCDW which reproduces the known Star-of-David reconstruction of the material and important features of the electronic structure, such as a splitting of the conduction bands and a metallic band crossing the Fermi level.

The projected DOS that we derive from our Green's function calculations of 1T-TaS2$_2$ surfaces show two prominent features. We relate these to the measured two-dimensional spectra by similarly mapping out our theoretical spectra using a

semi-empirical formula. A good qualitative correspondence is found. The feature living on the first $\sim 2$ eV above the Fermi level can be related to the observed isotropic charge transfer behavior. The second feature centered $\sim 3$ eV above the Fermi level, is linked to an even faster out-of-plane than in-plane charge transfer. However, a direct comparison with the experimental values in the corresponding energy range is difficult due to an overlap of the intensities stemming from the two resonances.

Finally, our results are invariant with respect to different stacking schemes of the commensurate charge density waves in subsequent layers of 1T-TaS$_2$. This suggests that a variation of the stacking is not the prevalent mechanism for the deviations in the charge transfer behavior across the NCDW–CCDW transition, although in general the band structures of TMDs are sensitive to these.

In contrast to the CCDW, the experimentally observed charge transfer behavior in the NCDW phase is anisotropic and of two-dimensional character, the in-plane charge transfer being twice as fast as the out-of-plane charge transfer. This corresponds to the expected behavior for a layered material like 1T-TaS$_2$. Unfortunately, the NCDW cannot be directly addressed in our fully periodic calculations due to the occurrence of CDW clusters separated by domain walls, which bring along prohibitively large simulation cells.

In conclusion our theoretical model rationalizes the isotropic charge transfer behavior in the CCDW, but it is not suited to make predictions about the NCDW nor to reproduce the absolute time-scales of the measured charge transfer in 1T-TaS$_2$.

Future studies involving explicit time-propagations of the initial wave-packets could provide a more immediate picture of the delocalization of excited electrons inside the material. This could be used to trace the path of the electrons in the material to gather information about the evolution of the initially three-dimensional behavior charge transfer behavior at larger time-scales.

Another interesting perspective is provided by simulations involving spin-orbit coupling in the material to address spin-dependent applications. We note that here our combined experimental and theoretical approach is especially useful since both methods can be adapted to incorporate spin-dependency. Finally, multi-scale methods may be able to address the electronic behavior and disorder in the NCDW phase in future.

# Chapter 8

# Summary and Outlook

Electronic charge transfer is a fundamental process in nature and elementary to many technological applications. A thorough understanding of its workings at the atomic level is of great importance for the design of new materials and devices. In particular, electron transfer takes place in catalytic and photocatalytic applications, like DSSCs, solar fuel generators, and electrochemical cells. In such applications the transfer of the electron commonly proceeds at or across interfaces, while it originates at a chemical donor unit, like an atom or a molecule. Modern experimental techniques are able to address such interfacial electron transfer at their fundamental time and length scales. However, in complex and large systems multiple processes can interfere, hence at a basic level electron transfer at surfaces is best studied in prototypical systems of minimal models that can be addressed theoretically and experimentally.

This thesis is concerned with a theoretical treatment of elastic electron transfer at surfaces by means of first-principles methods. In particular, a combination of Green's functions and DFT calculations was employed to describe resonant electron transfer at surfaces in terms of the delocalization of a wave-packet towards a continuum of states inside a substrate consisting of an infinite amount of layers. We studied a variety of electron donors at interfaces ranging from relatively weakly coupled chemisorbed dye-molecules, over atomic argon adsorbates, to strongly chemically bound sulfur atoms. The corresponding speeds of the charge transfer observed in core-hole-clock experiments progressively increased from a few femtoseconds to the sub-femtosecond domain. In connection with this, a variety of solid substrates of different character were explored from semi-conducting $TiO_2$ (Chapter 5) over ferromagnetic metallic Co(0001) and Fe(110) (Chapter 6) to layered two-dimensional 1T-$TaS_2$ (Chapter 7), respectively. Our results illustrate the versatility of the approach in addressing various physical aspects, such as the inclusion of finite temperature effects (Chapter 5) as well as modeling of charge transfer after spin-selective (Chapter 6) or orbital-selective (Chapter 7) excitations, which allowed us to maintain a close relationship to core-hole-clock experiments throughout this thesis.

We started by introducing semi-conducting $TiO_2$ substrates with an investigation of [1-10] steps and oxygen bridging vacancies on vicinal rutile(110) facets in relation to curved crystal experiments. The theoretically extracted vacancy formation

energies and Tersoff-Hamann STM simulations support a scenario in which oxygen bridging vacancies tend to migrate towards step edges, where they are difficult to detect, since their presence does not essentially alter the appearance of the [1-10] step edges in STM images. Furthermore, an analysis of bridging-oxygen vacancy induced gap states in the computed DOSs, suggests that vacancies at step edges contribute equally to the crystal doping as vacancies in the middle of the (110) terraces, while stoichiometric step edges do not bring about additional gap states in the material. Therefore, a tendency of oxygen vacancies to migrate to step edges can explain the experimentally observed decrease in the amount of oxygen vacancies in areas with higher step densities on curved crystal surfaces alongside a simultaneously homogeneous doping level across the entire reduced sample. These findings on curved crystals demonstrate the importance of defects in shaping the density of states of the substrate, which is an important ingredient when charge transfer processes are considered.

After this preface on $TiO_2$ we considered the problem of chemisorbed isonicotinic acid molecules on a perfect rutile (110) surface in order to explore the effects of structural fluctuations at finite temperatures on molecule-to-surface charge transfer for a prototypical DSSC interface. Applying our DFT-based Green's function technique to snapshots of a CPMD trajectory at 300 K, we found that the inclusion of structural fluctuations at finite temperatures reconciles the extracted elastic charge transfer time with core-hole-clock measurements at room temperature.

The fluctuations of the molecular resonance positions at finite temperatures result in a Gaussian-type broadening of the cumulative spectra, which can be described by a simple semi-classical model of harmonic oscillators assuming linear electron-phonon couplings of the vibrational modes to the molecular levels. Simultaneously, the molecular resonances exhibit Lorentzian-like line shapes of average widths controlled by the available density of acceptor states in the substrate. A mode specific analysis showed that vibrations stretching the carboxyl group anchoring the molecule to the surface contribute most strongly to the temperature-induced broadening. A similar linear coupling of specific vibrations to the elastic linewidths could not be established.

In order to mimic the corresponding core-hole-clock experiments, we included a nitrogen 1s core-hole in our calculations. The presence of the core-hole leads to a down shift of the molecular levels in energy with respect to the substrate's DOS, while simultaneously, the molecular orbitals localize around the attractive core-hole making them less susceptible to structural changes, thus effectively reducing the electron-vibrational coupling at the interface.

Subsequently, we focused on electron injection from Ar towards the ferromagnetic metal substrates Co(0001) and Fe(110) in order to analyze the origin of spin-dependent charge transfer times observed in core-hole-clock measurements. Our calculations confirm the experimental observation that core-excited minority electrons in the 4s state of Ar are injected significantly faster than majority electrons on both substrates. Furthermore, we found in agreement with the experiments faster charge transfer for each spin channel on Fe(110) in comparison with Co(0001), while the majority channel on Fe(110) is as fast as the minority channel on Co(0001). All extracted transfer times are of about a few femtoseconds and hence in near to quan-

titative agreement with the experiments.

We argued that a discussion of the observed spin-dependency of the charge transfer times in terms of the angular momenta of acceptor states as suggested in Ref. 50 is misleading in the case of Ar on Fe(110) or Co(0001). While growing DOS contributions from d-symmetries and from higher angular momenta are to be expected at increasing energies, the highly dispersive character of the surface bands in the energy regions of the resonances is not in line with the common notion that d-bands constitute flat bands pertaining to bound states of d-type atomic character. Therefore, we claim that a correlation of the d-type DOS components with the spin-dependent lifetimes is mostly coincidental in this particular case.

Instead, we found that the source of the observed spin-dependency lies in the variation of the size of the electronic gaps in the spin-dependent surface band structure around the $\bar{\Gamma}$-point at the resonance positions. This was further confirmed by an analysis of the calculations employing a simplified model, which captures the effect of the projected gaps, leading to a consistent picture in comparison with the experiments. These results highlight that taking into account realistic surface band structures as well as the spatial distribution and localization (which translates into a well-defined structure in reciprocal space) of intermediate states can be crucial in interfacial tunneling problems. This puts an interesting perspective on the development of extensions to conventional Tersoff-Hamann STM simulations which account for weighting of the band structure in reciprocal space by a more realistic model of the tip wave-function.

In a final study, we pushed the employed Green's function technique to the limits of its applicability by investigating the sub-femtosecond charge dynamics following an X-ray excitation at the surface of the layered TMD 1T-TaS$_2$. We employed a combined core-hole-clock and first-principles approach, which is tailored to address the directionality of charge-transfer by selectively exciting electronic resonances corresponding to different orientations of S3p orbitals. This is achieved by using linearly polarized light in the experiments and correspondingly preparing intermediate wave-packets with specific S3p-polarizations in our simulations. The analysis of the core-hole-clock data by our experimental collaborators shows that anisotropic two-dimensional charge transfer behavior prevails in the NCDW phase of 1T-TaS$_2$ at room temperature, while in the low temperature CCDW phase charge transfer is isotropic on ultrafast time-scales in spite of the material's layered structure.

Our calculations were able to address the CCDW phase of 1T-TaS$_2$ by setting up a model of the semi-infinite substrate using the known $\sqrt{13}a \times \sqrt{13}a$ reconstruction of the layers in the material. We identified the main spectroscopic features in the theoretically extracted S3p-projected DOSs in direct comparison with the experimental spectra.

The computed lifetimes for a localized initial wave packet formed by the electronic states in the range up to $\sim 2$ eV above the Fermi level are independent on the orbital polarization, and hence in the polarization of light. This is in agreement with the experimentally observed isotropic charge transfer in the CCDW phase. Moreover, this result is independent with respect to variations in the stacking of the CDWs in consecutive layers of the material. However, the absolute time-scales are overestimated by an order of magnitude in comparison with the experiments. Based

on these results we suggest that the transition from anisotropic, two-dimensional charge transfer in the NCDW phase to isotropic, three-dimensional charge transfer in the low-temperature CCDW phase is due to enhanced interlayer coupling and not a consequence of variations in the CDW stacking.

Overall, this thesis demonstrated for the examples of several prototypical interfaces, that the applied Green's function methodology is highly suitable to describe elastic electron transfer at realistic surfaces. Since the calculations are carried out in the energy domain a close and often direct comparison with spectroscopy experiments is possible, while the inclusion of a core-hole inside a modified pseudopotential can effectively be used to mimic core-excitations. This enables a near to quantitative agreement with core-hole-clock measurements of charge transfer times ranging from slightly below a femtosecond up to a few hundred femtoseconds. For the determination of larger charge transfer times numerically very accurate calculations (e.g., using a very small imaginary broadening) need to be performed. For shorter charge transfer times the broad appearance of resonances makes it difficult to identify the relevant resonance features. In such a case time-resolved calculations, as for example by employing a wave-packet propagation method, can give insight about charge transfer dynamics, since these methods are not restricted to the identification of a resonance feature in computed spectra. Furthermore, wave-packet propagations can provide complementary information to the Green's function approach used in this thesis, since they are able to resolve the delocalization of electrons in real space. Beyond the description of elastic charge transfer as in the current work, the inclusion of inelastic scattering processes like electron-phonon scattering (e.g., Eliashberg theory) and electron-electron scattering (e.g., GW approximation) are desirable to obtain an even closer agreement with the experiment. Ultimately, a full description of charge transfer processes including the dynamic preparation of an initial wave-packet by an explicitly modeled incoming light source is of increasing importance at shorter time-scales.

While semi-classical treatments of light are in principle feasible, it is not clear if they provide a realistic account of the photon-absorption by the materials. Here, likely a quantum description of light is inevitable. However, to the best of our knowledge, methods combining such descriptions with first-principles electronic structure methods are not sufficiently developed in order to apply them to large and realistic systems. Current approaches capable of an explicit treatments of excitations are prohibitively demanding in terms of computational resources so that new roads to describe these ultrafast processes and possibly along with this entirely new physics are to be found.

# Appendices

# A. Normalization of Bloch States in an Atomic Orbital Basis

The Bloch-like basis functions

$$\varphi_\nu(\mathbf{k}, \mathbf{r}) = A_\nu(\mathbf{k}) \sum_{\mathbf{R}} \mathrm{e}^{\mathrm{i}\mathbf{k}\mathbf{R}} \varphi_\nu(\mathbf{r} - \mathbf{t}_\nu - \mathbf{R}). \tag{A.1}$$

are normalized within one unit cell of the crystal. The normalization is obtained in the following way

$$\frac{\langle \varphi_\mu(\mathbf{k}') | \varphi_\nu(\mathbf{k}) \rangle}{A_\mu^*(\mathbf{k}') A_\nu(\mathbf{k})} = \tag{A.2}$$

$$= \int_{V_{\mathrm{cell}}} \sum_{\mathbf{R}'} \mathrm{e}^{-\mathrm{i}\mathbf{k}'\mathbf{R}'} \varphi_\mu^*(\mathbf{r} - \mathbf{t}_\mu - \mathbf{R}') \sum_{\mathbf{R}} \mathrm{e}^{\mathrm{i}\mathbf{k}\mathbf{R}} \varphi_\nu(\mathbf{r} - \mathbf{t}_\nu - \mathbf{R}) \, d\mathbf{r} \tag{A.3}$$

$$= \sum_{\mathbf{R}'} \mathrm{e}^{\mathrm{i}(\mathbf{k}-\mathbf{k}')\mathbf{R}'} \sum_{\mathbf{R}} \mathrm{e}^{\mathrm{i}\mathbf{k}(\mathbf{R}-\mathbf{R}')} \int_{V_{\mathrm{cell}}} \varphi_\mu^*(\mathbf{r} - \mathbf{t}_\mu - \mathbf{R}') \varphi_\nu^*(\mathbf{r} - \mathbf{t}_\nu - \mathbf{R}) \, d\mathbf{r} \tag{A.4}$$

$$= \sum_{\mathbf{R}'} \mathrm{e}^{\mathrm{i}(\mathbf{k}-\mathbf{k}')\mathbf{R}'} \sum_{\mathbf{R}} \mathrm{e}^{\mathrm{i}\mathbf{k}(\mathbf{R}-\mathbf{R}')} \int_{V_{\mathrm{cell}}} \varphi_\mu^*(\mathbf{r} - \mathbf{t}_\mu) \varphi_\nu^*(\mathbf{r} - \mathbf{t}_\nu - (\mathbf{R} - \mathbf{R}')) \, d\mathbf{r} \tag{A.5}$$

$$= \sum_{\mathbf{R}'} \mathrm{e}^{\mathrm{i}(\mathbf{k}-\mathbf{k}')\mathbf{R}'} \sum_{\mathbf{T}} \mathrm{e}^{\mathrm{i}\mathbf{k}\mathbf{T}} \int_{V_{\mathrm{cell}}} \varphi_\mu^*(\mathbf{r} - \mathbf{t}_\mu) \varphi_\nu^*(\mathbf{r} - \mathbf{t}_\nu - \mathbf{T}) \, d\mathbf{r} \tag{A.6}$$

$$= \delta_{\mathbf{k},\mathbf{k}'} N_{\mathrm{cell}} \sum_{\mathbf{T}} \mathrm{e}^{\mathrm{i}\mathbf{k}\mathbf{T}} S_{\mu\nu}(\mathbf{T}) = \delta_{\mathbf{k},\mathbf{k}'} N_{\mathrm{cell}} S_{\mu\nu}(\mathbf{k}), \tag{A.7}$$

where the integration in the second line is over the entire volume $V$ of the crystal. $N_{\mathrm{cell}}$ is equal to the number of unit cells with volume $V_{\mathrm{cell}}$ in the supercell making up the crystal so that $V = N_{\mathrm{cell}} V_{\mathrm{cell}}$. $\mathbf{T}$ is the collection of lattice vectors pointing to neighboring unit cells with respect to an arbitrarily chosen central cell at $\mathbf{T} = 0$. In general, the atomic orbitals in neighboring cells overlap with each other. We find for the normalization constant $A_\mu(\mathbf{k})$,

$$A_\mu(\mathbf{k}) = |A_\mu(\mathbf{k})| = \frac{1}{\sqrt{N_{\mathrm{cell}}}} \cdot \frac{1}{\sqrt{1 + \sum_{\mathbf{T} \neq \mathbf{0}} \mathrm{e}^{\mathrm{i}\mathbf{k}\mathbf{T}} S_{\mu\mu}(\mathbf{T})}} \tag{A.8}$$

# B. Defining Equation for Green's Functions in a Non-Orthogonal Basis

To see that the defining equation for the Green's function in a non-orthogonal basis is given by

$$\sum_{\mu}[zS_{\lambda\mu}(\mathbf{k}_{\parallel}) - H^{\sigma}_{\lambda\mu}(\mathbf{k}_{\parallel})]G^{\sigma}_{\mu\nu}(\mathbf{k}_{\parallel}) = \delta_{\lambda\nu}, \tag{B.9}$$

one may start from the general definition of a Green's function in real space

$$[z - \hat{H}^{\sigma}(\mathbf{r})]G(\mathbf{r}, \mathbf{r}'; z) = \delta(\mathbf{r} - \mathbf{r}'). \tag{B.10}$$

Here we consider explicitly the spin dependence of the Hamiltonian. For the sake of clarity we omit here any explicit $\mathbf{k}$-dependence. Using the spectral representation of the Green's function one may first rewrite the expression, so that

$$\delta(\mathbf{r} - \mathbf{r}') = [z - \hat{H}^{\sigma}(\mathbf{r})]\frac{\phi^{\sigma}_i(\mathbf{r})\phi^{\sigma*}_i(\mathbf{r}')}{z - \varepsilon^{\sigma}_i} \tag{B.11}$$

$$= [z - \hat{H}^{\sigma}(\mathbf{r})] \sum_{\mu\nu} \varphi^{\sigma}_{\mu}(\mathbf{r}) \sum_i \frac{c^{\sigma}_{i\mu}c^{\sigma*}_{i\nu}}{z - \varepsilon^{\sigma}_i} \varphi^{\sigma*}_{\nu}(\mathbf{r}') \tag{B.12}$$

$$= [z - \hat{H}^{\sigma}(\mathbf{r})] \sum_{\mu\nu} \varphi^{\sigma}_{\mu}(\mathbf{r})G^{\sigma}_{\mu\nu}\varphi^{\sigma*}_{\nu}(\mathbf{r}'), \tag{B.13}$$

where we have defined the Green's function $G^{\sigma}_{\mu\nu}$ in the atomic basis in the last step. Multiplying from the left with $\varphi^{\sigma}_{\lambda}(\mathbf{r})$ and integrating over $\mathbf{r}$ one receives

$$\int \varphi^{\sigma*}_{\lambda}(\mathbf{r})\delta(\mathbf{r} - \mathbf{r}') \, d\mathbf{r} = \sum_{\mu\nu} \int \varphi^{\sigma}_{\lambda}(\mathbf{r})[z - \hat{H}^{\sigma}(\mathbf{r})]\varphi^{\sigma}_{\mu}(\mathbf{r}) \, d\mathbf{r} \, G^{\sigma}_{\mu\nu}\varphi^{\sigma*}_{\nu}(\mathbf{r}') \tag{B.14}$$

$$\varphi^{\sigma*}_{\lambda}(\mathbf{r}') = \sum_{\mu\nu}[zS_{\lambda\mu} - H^{\sigma}_{\lambda\mu}]G^{\sigma}_{\mu\nu}\varphi^{\sigma*}_{\nu}(\mathbf{r}') \tag{B.15}$$

$$\varphi^{\sigma*}_{\lambda}(\mathbf{r}') = \sum_{\nu} \underbrace{\left(\sum_{\mu}[zS_{\lambda\mu} - H^{\sigma}_{\lambda\mu}]G^{\sigma}_{\mu\nu}\right)}_{= \delta_{\lambda\nu}} \varphi^{\sigma*}_{\nu}(\mathbf{r}'). \tag{B.16}$$

Here, we have identified the Kronecker delta in the last line yielding the definition Eq. (B.9) as desired.

# C. Isonicotinic Acid on TiO₂: Additional Material

This section of the appendix contains additional material regarding the investigations of isonicotinic acid on TiO₂ presented in Chapter 5. In particular, it constitutes the supporting material to the work presented in Section 5.2.[1] Additionally, data with respect to the electron-phonon coupling of isonicotinic acid investigated in Section 5.3 is presented for the core-excited case (see Appendix C.7).

## C.1. Matching Procedure of the Fluctuating Interface to the Fixed Bulk Geometry

The CPMD simulation used in Section 5.2 was obtained employing the plane-wave code Quantum Espresso (QE) and a slab containing four TiO₂ trilayers and the adsorbate attached to one side. This CPMD trajectory was taken from Ref. 206. The electronic structure was subsequently treated with the SIESTA/TranSIESTA code in order to include the effect of a semi-infinite substrate and evaluate properly the width of the molecular states. In order to set-up geometries for the SIESTA/TranSIESTA runs we applied the protocol schematically described in Fig. C.1.
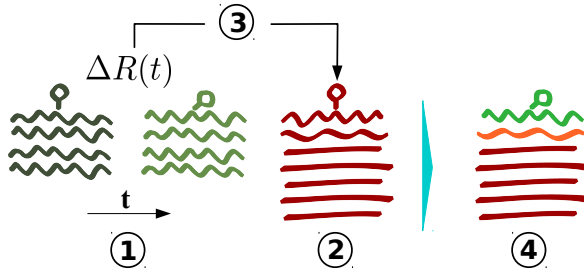


**Figure C.1.:** Schematics of the matching procedure used to match the fluctuating decorated surface to the fixed bulk TiO₂ inside the slab. The four steps are described in the text below.

1. For each time step configuration $\{R_i^{\mathrm{CPMD}}(t)\}$, we calculated the set of displacements $\{\Delta R_i^{\mathrm{CPMD}}(t)\}$ of the atomic coordinates with respect to the QE relaxed equilibrium configuration $\{R_i^{\mathrm{Rel.}}\}$. The displacement of the i-th atom is given by

$$\Delta R_i^{\mathrm{CPMD}}(t) = R_i^{\mathrm{CPMD}}(t) - R_i^{\mathrm{Rel.}} \tag{C.17}$$

   The center of mass of the bottom two trilayers was used as a common reference in order to ensure a proper alignment of all the structures. This only produces a small modification of the coordinates, but ensures a good matching to the fixed bulk geometry. The position of the atoms in those bottom layers is only weakly affected by the vibrational movement of the adsorbate, which is the focus of this work.

---

[1]Reprinted (adapted) with permission from [171]. © 2018 American Chemical Society.

2. Then, we created a thicker slab to perform the SIESTA/TranSIESTA Green's function calculation. This is necessary to have a bulk-like internal region where we can connect the electronic self-energy describing the $TiO_2$ substrate. This structure was obtained from the relaxed structure of a slab containing five trilayers of $TiO_2$ with isonicotinic acid molecules adsorbed on both sides of the slab (dipole canceling configuration). Here, the middle trilayer was kept fixed at bulk configuration during relaxation. Later, four additional bulk layers were added at the center of the slab. This resulted in a slab containing nine trilayers that was used as an equilibrium reference structure $\{R_i^{\text{Ref.}}\}$ for the SIESTA/TranSIESTA runs.

3. Subsequently, one could simply add the displacements $\Delta R_i^{\text{CPMD}}(t)$ to this new reference structure

$$R_i^{\text{new}} = R_i^{\text{Ref.}} + \Delta R_i^{\text{CPMD}}(t), \tag{C.18}$$

obtaining a set of configurations describing the dynamics of the system with a thicker slab. However, such procedure will result in structures exhibiting a discontinuous transition from a fixed bulk geometry to the moving surface.

4. Therefore, we additionally applied a damping to the displacements, smoothening the transition between the second ($z_{max}$) and the third ($z_{min}$) trilayers. We defined the following damping function:

$$f(z) = \begin{cases} 0 & \text{for } z < z_{\min}, \\ \frac{1}{2} \cdot \left[ 1 - \cos\left( \frac{z - z_{\min}}{z_{\max} - z_{\min}} \pi \right) \right] & \text{for } z_{\min} \leq z \leq z_{\max}, \\ 1 & \text{for } z > z_{\max}. \end{cases} \tag{C.19}$$

Applying this damping function we obtain the "matched" configurations $\{R_i^{\text{matched}}\}$,

$$R_i^{\text{matched}} = R_i^{\text{Ref.}} + f(R_{i,z}^{\text{Ref.}}) \cdot \Delta R_i^{\text{CPMD}}(t), \tag{C.20}$$

where $R_{i,z}^{\text{Ref.}}$ is the z-component of the $i$-th atom position in the reference structure.

## C.2.  Imaginary Energy Broadening and Fitting Procedure
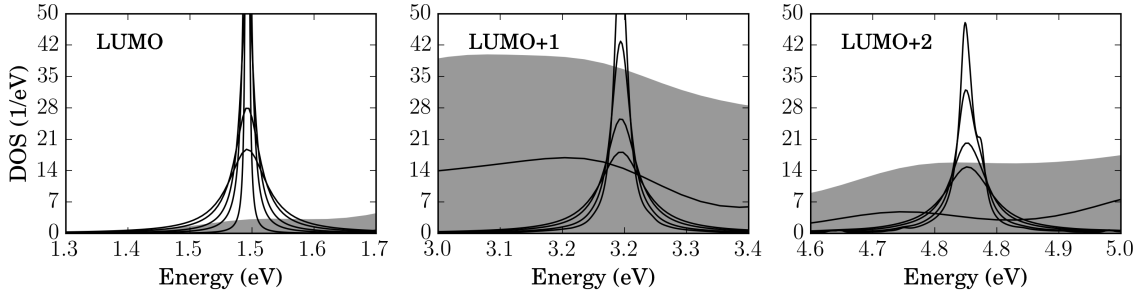


**Figure C.2.:** LUMO to LUMO+2 resonances for $\eta$ values from 1 to 30 meV. Also shown are the DOSs of slab calculations (shaded areas) and of bulk TiO₂ (black line).

We employed in Section 5.2 a parameter of $\eta = 20$ meV entering the complex energy $z = E + i\eta$ in the Green's function to study the linewidth of the molecular resonances. The spectral broadening due to this value is balanced to make the calculations tractable while giving results with the desired accuracy. To illustrate this, the spectra of the resonances from the LUMO to the LUMO+2 for the core-excited case in the equilibrium structure are shown in Fig. C.2 for different values of $\eta$. The corresponding linewidths obtained from Lorentzian fitting are listed in Tab. C.1. The values are virtually independent of $\eta$. This holds up to an accuracy of below 1 meV, as can be read from the data. Since the additional FWHM resulting from the imaginary energy broadening is $2\eta$, distinct resonance features can be distinguished down to this limit. In our case we study single resonances associated with non-degenerate orbitals of the free isonicotinic acid molecule (HOMO to LUMO+2). Only the LUMO in the ground state case is strongly split into anti-bonding and bonding contributions of which we consider the dominant (anti-bonding) component in our analysis. In broad spectral features deviations from Lorentzian line shapes occur and a Lorentzian fitting has a more approximate character, while we still expect to correctly catch the time scale of the decay by such a fitting. In the limit of such broad resonances the dependence of the lifetime on the width is weaker due to their inverse relationship (also the size of the small $\eta$-parameter is less important). Overall we expect to obtain reasonable estimates for peaks with a lifetime of up to $\sim 660$ fs (below $\sim 1$ meV we do not intend to resolve peak widths). Not least, the room temperature values presented in Section 5.2 are averages over 161 snapshots and hence accuracy is improved by statistics.

**Table C.1.:** Extracted linewidths for various $\eta$ values of the imaginary energy $z = E + i\eta$ in the Green's function.

| $\eta$ (meV) | | 30 | 20 | 10 | 5 | 1 |
|---|---|---|---|---|---|---|
| $\Gamma_{\text{LUMO}}$ | (meV) | 0.1 | 0.0 | 0.0 | 0.1 | 0.3 |
| $\Gamma_{\text{LUMO}+1}$ | (meV) | 8.6 | 8.8 | 9.1 | 9.6 | - |
| $\Gamma_{\text{LUMO}+2}$ | (meV) | 14.4 | 14.5 | 15.2 | 15.0 | - |

## C.3. Varying the Core-Hole Charge Inside Pseudopotentials
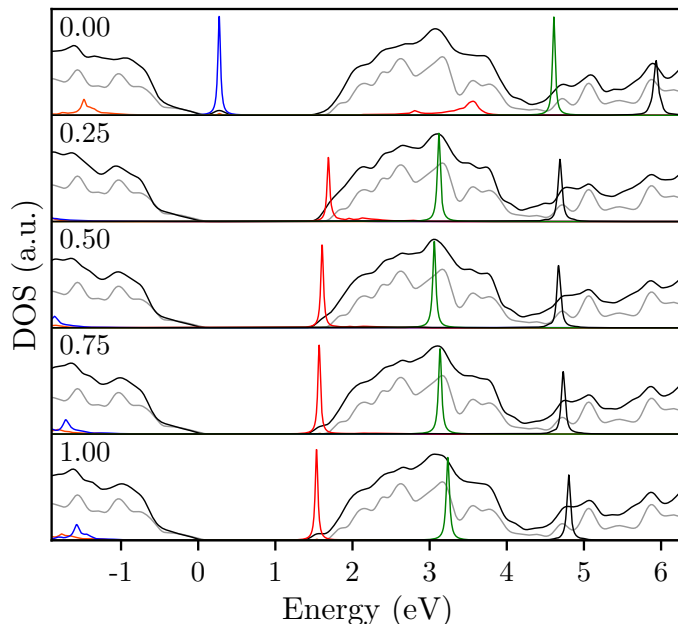


**Figure C.3.:** DOS from a Green's function calculation projected onto different MOs as a function of the nitrogen core-hole charges used in the calculation. Black and gray lines as in Fig. 2c of the main text.

To check the robustness of our calculations with respect to the charge of the hole created in the 1s shell of nitrogen, we performed calculations using pseudopotentials generated from ions with different charges 0 to +1 in steps of 0.25. The removed charge from the N1s was added back to the valence in the calculations in order to neutralize the system (cf. Fig. C.3). Removing zero electrons from the N1s core level is equivalent to the ground state calculation presented in the main text, whereas a full core-hole corresponds to the presented core-excited case. Overall, the unoccupied molecular resonances LUMO to LUMO+2 are only changing marginally after an initial jump between removal of zero and 0.25 electrons (note, that in the core-excited cases the LUMO is at least partly occupied, but the nomenclature of the ground state is kept to maintain consistency). Leaving the ground state case (zero electrons removed) apart, the LUMO downshifts slightly as a function of the core charge, while the HOMO exhibits a larger, but still moderate, upshift. The LUMO+1 and LUMO+2 also show small shifts with a minimum for the case of half a core-hole.

## C.4. Molecular Orbitals Associated with the Resonances

For the assessment of the role of symmetry it is useful to look at the wave-functions and the LDOS around the resonance positions. As commented in the main text, the plots in Fig. C.4 and Fig. C.5 clearly show that LUMO and LUMO+2 have a shape and symmetry particularly appropriate for coupling to the substrate. These MOs have $\pi$ character and a substantial weight on those atoms, which are linked to the substrate.
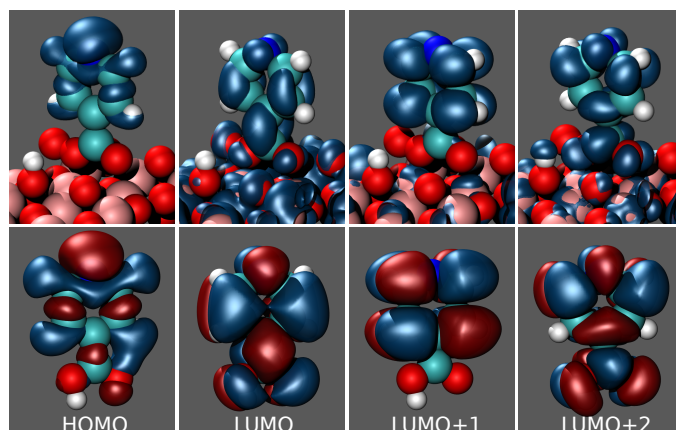


**Figure C.4.:** Lower panels show the MOs for the ground state molecule in the gas phase. Upper panels show the local density of states at the energies of the molecular resonances of the adsorbed molecule in the ground state.
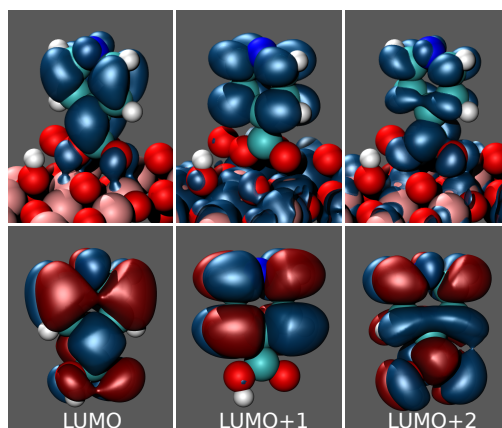


**Figure C.5.:** Orbital shapes analogous to Fig. C.4 but for the core-excited case.

## C.5.   Effect of Spin Polarization in the Core-Excited State

To estimate the consequences of spin polarization after excitation of an electron into the LUMO we performed open shell calculations for several snapshots. The resulting spectra are depicted in Fig. C.6. The figure includes the case of the reference structure (equilibrium structure from ground state calculation) together with some extreme cases of snapshots, where the LUMO is located well inside the gap (at 10.63 ps), or where the LUMO+2 is strongly broadened due to interaction with the substrate (at 12 ps). The other snapshots have been chosen randomly spanning a large range of simulation times to obtain an indication of the effect of spin splitting on the molecular resonances. We note, that for the comparison with experiments, particularly in the LUMO case only the occupied spin channel is of interest (i.e., spin up, here).

The appearance of the line-shapes themselves is only moderately affected by the inclusion of spin and some curves cannot be distinguished at all in the figure. The extracted values of the linewidths can be compared in Tab. C.2. We find a variation for the spin polarized case (spin up) with respect to the unpolarized case (unpol.) of no more than 30%. The only exception is the strongly energy-shifted spectrum at 10.63 ps, where also by visual inspection the LUMO+2 peak appears altered.

Within the scope of the current work, statistical averages are more important than specific configurations. Overall, the average quantities from the set of spin polarized calculations appear in line with the ones from the unpolarized case (see averages in Tab. C.2). Therefore, at the level of semi-local density functional theory the additional collinear spin degree of freedom is not expected to alter the qualitative findings nor to significantly affect the quantitative estimates for elastic lifetimes in the case of isonicotinic acid on rutile(110).

**Table C.2.:** Comparison of spin-polarized and closed shell calculations for the core-excited case. Shown are the extracted values of the linewidths $\Gamma$ and corresponding lifetimes $\tau = \hbar/\Gamma$. The last lines in the table refer to averages $\langle\Gamma\rangle$ and $\hbar/\langle\Gamma\rangle$. The spin polarization $\Delta n_s$ of the molecule is given for each snapshot in terms of the difference between the two spin channels regarding the Mulliken population ($n_s$ with $s =\uparrow,\downarrow$) on the molecule $\Delta n_s = n_\uparrow - n_\downarrow$.

| snapshot | spin | $\Delta n_s$ | $\Gamma_{\text{LUMO}}$ (meV) | $\tau_{\text{LUMO}}$ (fs) | $\Gamma_{\text{LUMO+1}}$ (meV) | $\tau_{\text{LUMO+1}}$ (fs) | $\Gamma_{\text{LUMO+2}}$ (meV) | $\tau_{\text{LUMO+2}}$ (fs) |
|---|---|---|---|---|---|---|---|---|
| reference | unpol. | 0.00 | 0.1 | $\infty$ | 8.8 | 75.0 | 14.5 | 45.3 |
| | up | 0.90 | 0.0 | $\infty$ | 7.3 | 90.7 | 15.4 | 42.7 |
| | down | 0.90 | 65.6 | 10.0 | 4.3 | 152.0 | 17.6 | 37.4 |
| 2.75 ps | unpol. | 0.00 | 0.1 | $\infty$ | 17.6 | 37.4 | 89.5 | 7.4 |
| | up | 0.86 | 0.1 | $\infty$ | 15.1 | 43.6 | 86.7 | 7.6 |
| | down | 0.86 | 61.1 | 10.8 | 8.4 | 78.4 | 101.4 | 6.5 |
| 4.31 ps | unpol. | 0.00 | 0.0 | $\infty$ | 4.4 | 150.6 | 32.9 | 20.0 |
| | up | 0.93 | 0.0 | $\infty$ | 5.1 | 130.0 | 34.9 | 18.9 |
| | down | 0.93 | 18.5 | 35.5 | 4.9 | 134.5 | 480.5 | 1.4 |
| 7.13 ps | unpol. | 0.00 | 0.1 | $\infty$ | 4.7 | 141.1 | 20.1 | 32.8 |
| | up | 0.87 | 0.1 | $\infty$ | 6.0 | 109.5 | 23.9 | 27.5 |
| | down | 0.87 | 60.5 | 10.9 | 3.5 | 188.5 | 67.8 | 9.7 |
| 10.63 ps | unpol. | 0.00 | 0.1 | $\infty$ | 6.6 | 99.1 | 50.4 | 13.1 |
| | up | 0.93 | 0.0 | $\infty$ | 4.9 | 135.5 | 28.2 | 23.3 |
| | down | 0.93 | 2.5 | 259.3 | 3.5 | 186.1 | 51.2 | 12.9 |
| 12.00 ps | unpol. | 0.00 | 0.2 | $\infty$ | 11.0 | 59.6 | 164.8 | 4.0 |
| | up | 0.87 | 0.2 | $\infty$ | 8.7 | 75.3 | 177.7 | 3.7 |
| | down | 0.87 | 83.0 | 7.9 | 7.9 | 83.3 | 134.0 | 4.9 |
| average | unpol. | | 0.1 | $\infty$ | 8.8 | 74.4 | 62.0 | 10.6 |
| | up | | 0.1 | $\infty$ | 7.8 | 83.9 | 61.1 | 10.8 |
| | down | | 48.6 | 13.6 | 5.4 | 121.3 | 142.1 | 4.6 |
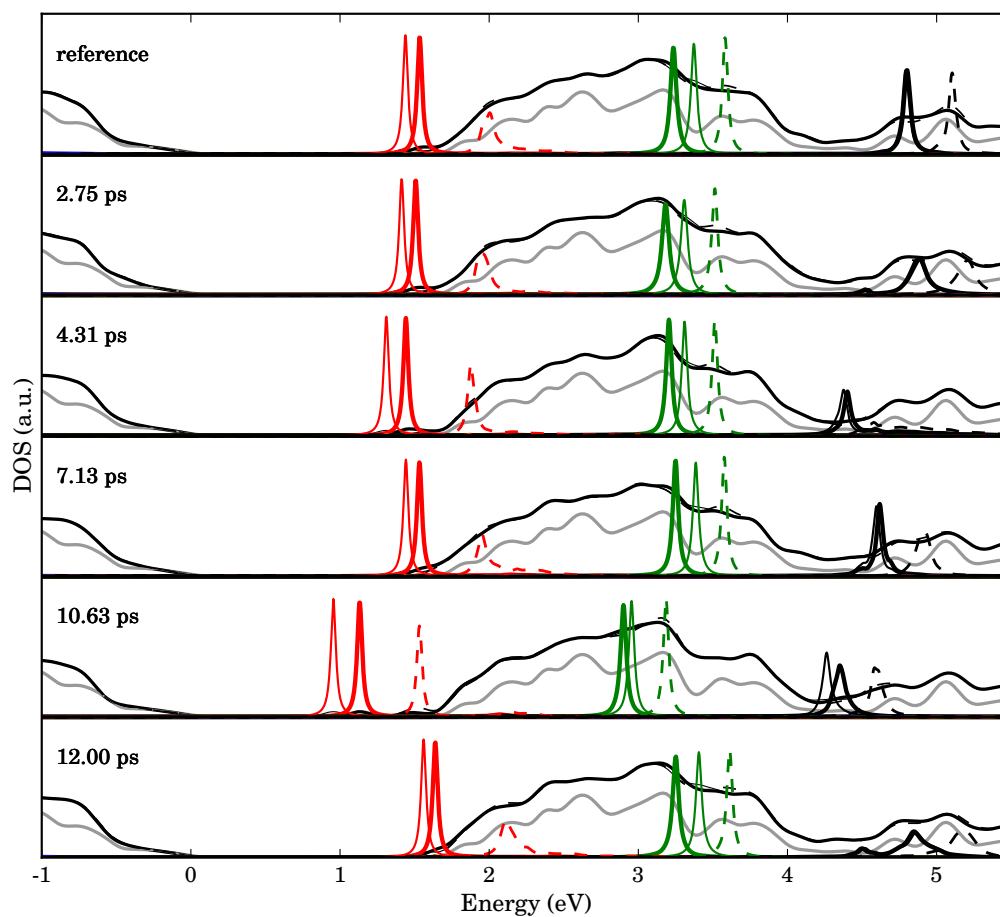
**Figure C.6.:** Spectra for different snapshots from spin-dependent (thin lines, spin up solid lines, spin down dashed lines) and spin-independent (thick lines) calculations. In the background the bulk DOS of the electrodes (gray) and the DOS of the slab with the attached molecules (black) are shown. The line shapes are only weakly affected by the additional complication of spin, for this system.

## C.6.  Effective Voigt-like Profiles

Here we show that the final line shapes of the cumulative spectra (i.e., the spectra shown in Fig. 5.6c and Fig. 5.8c) can be accurately described in terms of Voigt-like curves which are modulated by the density of states of the substrate. First, we approximate the width of the resonances [Eq. (5.2)] at each configuration $i$ as obtained from the Fermi golden rule using an average matrix element and the density of states of the substrate at the instantaneous resonances' energies, i.e.,

$$\Gamma(E_R^i) \approx 2\pi \langle |M_{RS}(E_R^i)|^2 \rangle \rho_S(E_R^i), \qquad (C.21)$$

where for the average matrix element we take the one extracted in the previous Section and given in Table 5.2, i.e., $2\pi \langle |M_{RS}(E_R)|^2 \rangle \approx \langle \Gamma(E_R) \rangle / \langle \rho_S(E_R) \rangle$, and the resulting width is modulated by the substrate density of states. According to this simplification, the cumulative spectra $S(E)$ for the 161 snapshots are approximated as follows:

$$S(E) \equiv \sum_{i=1}^{161} S_i(E) \qquad (C.22)$$

$$\approx \sum_{i=1}^{161} L(E, E_R^i, \Gamma(E_R^i)) = S^{(a)}(E) \qquad (C.23)$$

where $L$ is a Lorentzian function centered at the energy of the instantaneous resonance's energy:

$$L(E, E_R, \Gamma(E_R)) = \frac{1}{\pi} \frac{\Gamma(E_R)/2}{(E - \langle E_R \rangle)^2 + [\Gamma(E_R)/2]^2}. \qquad (C.24)$$

The results $S^{(a)}(E)$ of this approximation, solid lines in Fig. C.7 or Fig. C.8, are in good agreement to the original values of $S(E)$, shaded areas, further confirming the applicability of an average matrix element in our case.

To extend our results to an ergodic sampling of the dynamics, we can further assume that a continuous distribution of values of $E_R$ is obtained, observing a normal distribution around $\langle E_R \rangle$ with standard deviation $\sigma_R$ (we use the values reported in Table 5.1 and Table 5.3:

$$N(E_R, \langle E_R \rangle, \sigma_R) = \frac{1}{\sigma_R \sqrt{2\pi}} \exp\left[ -\frac{(E - \langle E_R \rangle)^2}{2\sigma_R^2} \right], \qquad (C.25)$$

It is interesting to point out that the use of a normal distribution is perfectly justified using the harmonic approximation for the vibrations around the equilibrium position and assuming a linear electron-phonon coupling. Taking such a distribution instead of the summation in Eq. (C.23) results in

$$S^{(b)}(E) = \int N(E_R, \langle E_R \rangle, \sigma_R) L(E, E_R, \Gamma(E_R)) dE_R \qquad (C.26)$$

which, strictly speaking, differs from a Voigt profile (convolution of Gaussian and Lorentzian functions) because here the Lorentzian width $\Gamma(E_R)$ depends on the energy and is modulated by the substrate density of states, see Eq. (C.21). These
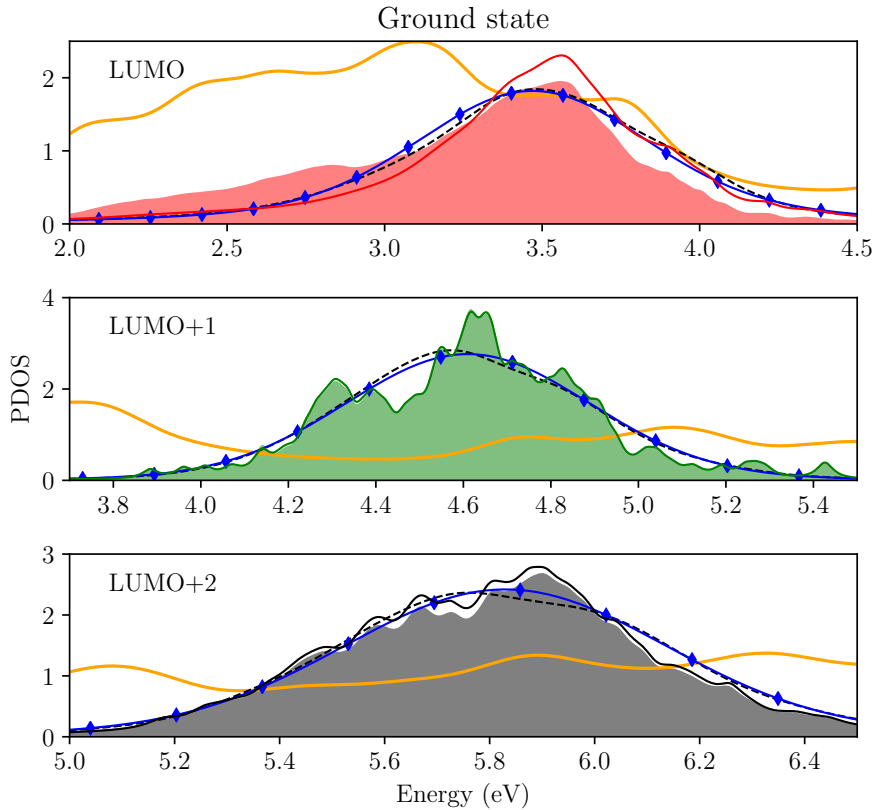
**Figure C.7.:** Cumulative spectra in the electronic ground state for different molecular resonances from 161 snapshots as in Section 5.2 [colored shaded areas, cf. Eq. (C.22)]. Additionally, shown are various approximations to those cumulative spectra: Approximate spectra $S^{(a)}(E)$ [cf. Eq. (C.23)] from Lorentzian line shapes at the 161 resonance positions of the computed cumulative spectra, but assuming their widths are given by an average matrix element modulated by the density of states in the surface (solid lines in colors corresponding to the cumulative spectra). Effective line shapes $S^{(b)}(E)$ [cf. Eq. (C.26)] for an infinite number of normally distributed Lorentzian resonances with their widths given by an average matrix element modulated by the density of the states in the surface (dashed lines). The resulting asymmetric Voigt-like spectra reflect the behavior of the DOS in the substrate $\rho_S(E)$. Symmetric Voigt curves $S^{(c)}(E)$ [cf. Eq. (C.27)] resulting from a Gaussian distribution of an infinite amount of Lorentzians with a constant width (blue diamonds). Note, that for the direct comparison with the computed cumulative spectra the widths of the Lorentzians must be taken as $\Omega(E_R) = \Gamma(E_R)/2 + \eta$, where $\eta$ is the small imaginary component of the energy used for the calculation of the Green's functions. Orange solid lines show the variation of $\rho_S(E)$ as a function of energy in arbitrary units.
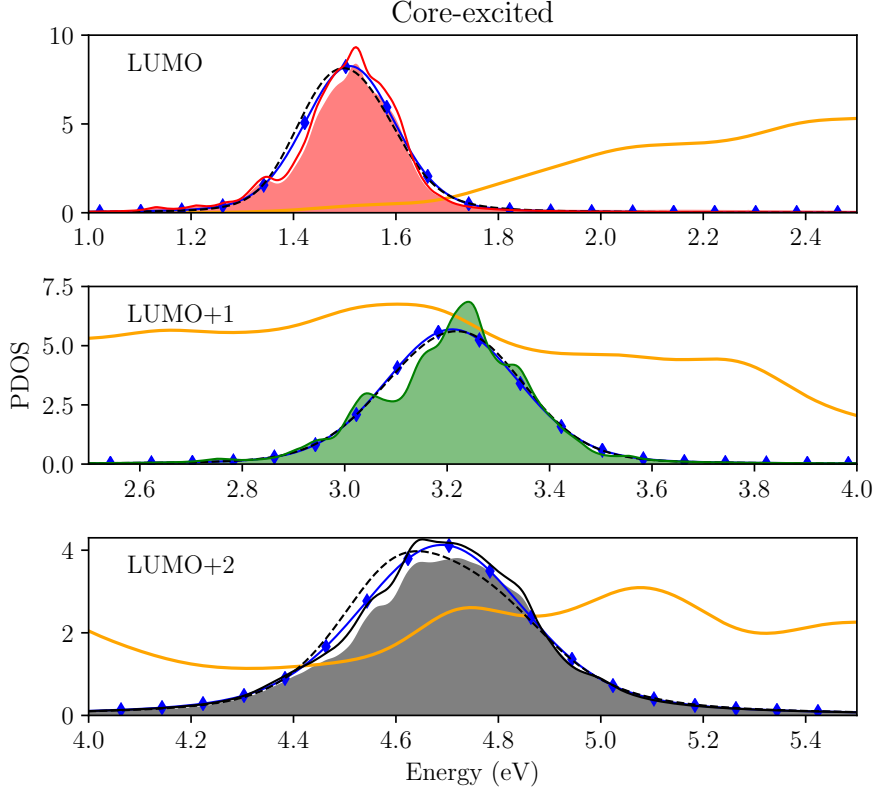
**Figure C.8.:** Cumulative spectra for different molecular resonances in the core excited case and various approximations to those spectra. The figure is organized analogously to Fig. C.7

results are shown as the dashed lines in Fig. C.7 and Fig. C.8. A higher density of states in the substrate results in broader Lorentzian components flattening the resonances, whereas lower density of states results in sharper resonances leading to large peaks in those regions. In the case of the LUMO resonance of the ground state we can clearly see how the structure of the density of states around $\langle E_R \rangle$ gives rise to a very asymmetric peak of the resonance peak. Indeed, the real cumulative spectrum is even more asymmetric, which is probably related to the splitting of the LUMO peak into bonding and antibonding features that is beyond the model used here. In general, the overall agreement is rather good considering the limited sampling of the molecular dynamics trajectories.

Finally, we compare the asymmetric line-shape $S^{(b)}(E)$ due to the modulation of $\Gamma(E_R)$ by $\rho_S(E_R)$ with a completely symmetric Voigt curve, given by

$$S^{(c)}(E) = \int N(E_R, \langle E_R \rangle, \sigma_R) L(E, E_R, \langle \Gamma \rangle) dE_R. \tag{C.27}$$

Here, the fixed average Lorentzian width $\langle \Gamma \rangle$ is used (values shown in Table 5.2) resulting in a symmetric line shape. The curves are shown in Fig. C.7 and Fig. C.8 (blue diamonds). We find that in the current case of isonicotinic acid on rutile(110) the asymmetries are more prevalent in the ground state than in the core-excited case,

where only the LUMO+2 is located in an energy region with a more pronounced variation of $\rho_S(E_R)$.

## C.7. Electron-Vibrational Coupling in the Core-Excited Case
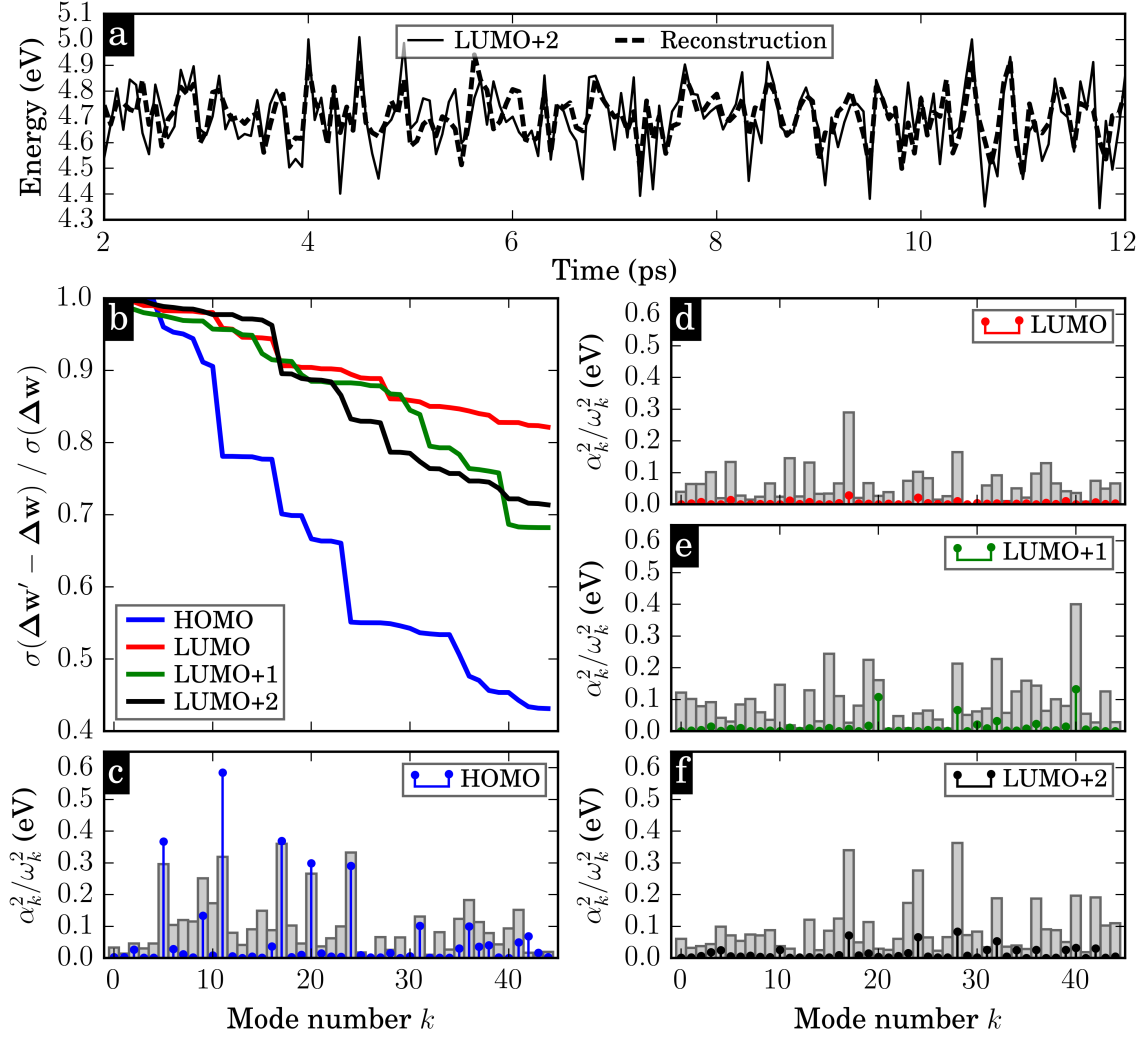


**Figure C.9.:** Analysis of the electron vibrational coupling for the HOMO, LUMO, LUMO+1, and LUMO+2 resonances of core-excited isonicotinic acid on TiO$_2$(110). The figure is organized in the same way as Fig. 5.12 in Section 5.3.3.

We additionally analyzed the diagonal electron-phonon couplings for the core-excited case of isonicotinic acid on TiO$_2$. This analysis was conducted in analogy to the ground state case in Fig. 5.12 of Section 5.3.3. The results for the N1s-core-excited simulations are summarized in Fig. C.9. Overall, the calculations reveal smaller electron-vibrational couplings (c-f) than in the ground state (cf. Fig. 5.12). Furthermore, Fig. C.9b shows that the fluctuations of the LUMO to LUMO+2 resonances are not reproduced as well as in the ground state, while the energetic positions of the HOMO are rather well captured within the applied linear model of electron-phonon coupling (Section 5.3.3).

# D.  Site Dependence of Ar4s-Resonances

We have investigated the site dependence of the resonant linewidths for different adsorption sites of Argon on Fe(110) and on Co(0001). The extracted line widths are listed in Table D.1. Looking at the values in the table apart from weak fluctuations (less than 14 meV) no strong site-dependency of the line widths $\Gamma$ is found.

**Table D.1.:** Extracted linewidths $\Gamma$ in meV for Ar*4s1$\zeta$ resonances with respect to different adsorption sites of Argon on Fe(110) and Co(0001): top position (tp), short bridge (sb), long bridge (lb), bridge position (br), fcc hollow (fcc), and hcp hollow (hcp). The values are shown for different adsorption heights $h$ in Å.

|      |     | Fe(110) | | | Co(0001) | | | |
|------|-----|-----|-----|-----|-----|-----|-----|-----|
|      | $h$ | tp  | sb  | lb  | tp  | br  | fcc | hcp |
| Maj. | 2.7 | 216 | 215 | 212 | 139 | 143 | 143 | 144 |
|      | 3.0 | 244 | 247 | 248 | 120 | 128 | 128 | 128 |
|      | 3.0 | 267 | 273 | 275 | 102 | 107 | 108 | 108 |
| Min. | 2.7 | 736 | 734 | 727 | 189 | 194 | 195 | 195 |
|      | 3.0 | 571 | 584 | 585 | 178 | 191 | 190 | 191 |
|      | 3.3 | 509 | 518 | 520 | 234 | 247 | 247 | 248 |

# E.  Optimization of the Resonance Wave Packet

With the aim to find a better description of the resonance wave packet we consider the possibility to mix different components of the basis set. In this thesis Argon 4s resonances are investigated in Chapter 6. A possible optimization of the resonances wave function by mixing in a polarization due to $4p_z$ components is analyzed there. Here, we derive the expressions for the real coefficients $c_s$ and $c_p$ of a general wave packet consisting of two components $|\phi_1\rangle$ and $|\phi_2\rangle$, which can be chosen as the numerical (real) atomic orbitals of the SIESTA basis set. The resonance wave-packet is then of the form

$$|\tilde{\psi}_R\rangle = c_0 |\phi_0\rangle + c_1 e^{i\varphi} |\phi_1\rangle \,, \tag{E.28}$$

where $\varphi$ is an additional relative phase between the components, which is found to be zero below. The overall phase is irrelevant as expected. The goal is to optimize the projection

$$f(c_0, c_1, \varphi) = \int_a^b \mathrm{Im}\, \langle \tilde{\psi}_R | G(E) | \tilde{\psi}_R \rangle \, dE \,. \tag{E.29}$$

Here, $G$ is the Green's function averaged over all k-points and $a$ and $b$ define an energy interval enclosing the energy position of the resonance. We introduce the following short hand notation

$$f(c_0, c_1, \varphi) = \mathrm{Im}\left[ \begin{pmatrix} c_0 \\ c_1 e^{i\varphi} \end{pmatrix}^\dagger \begin{pmatrix} M_{00} & M_{01} \\ M_{10} & M_{11} \end{pmatrix} \begin{pmatrix} c_0 \\ c_1 e^{i\varphi} \end{pmatrix} \right] \,, \tag{E.30}$$

where the complex matrix elements $M_{\mu\nu}$ are given by

$$M_{\mu\nu} = \int_a^b [SG(E)S]_{\mu\nu} \, dE \tag{E.31}$$

for $\mu, \nu \in 0, 1$. $S$ is the overlap matrix of SIESTA.

Which reduces after some algebra to

$$f(c_0, c_1, \varphi) = c_0^2 \,\mathrm{Im}\, M_{00} + c_1^2 \,\mathrm{Im}\, M_{11} \tag{E.32}$$
$$+ c_0 c_1 [\underbrace{(\mathrm{Im}\, M_{01} + \mathrm{Im}\, M_{10})}_{=B} \cos(\varphi) + \underbrace{(\mathrm{Re}\, M_{01} - \mathrm{Re}\, M_{10})}_{=C} \sin(\varphi)] \,. \tag{E.33}$$

The above expression is then maximized under the constraint $\langle \tilde{\psi}_R | \tilde{\psi}_R \rangle = c_0^2 + c_1^2 = 1$. Substituting $c_1 = \sqrt{1 - c_0^2}$ $\tilde{f}(c_0, \varphi) = f(c_0, \sqrt{1 - c_0^2}, \varphi)$ one obtains

$$\tilde{f}(c_0, \varphi) = \mathrm{Im}\, M_{11} + c_0^2 \underbrace{(\mathrm{Im}\, M_{00} - \mathrm{Im}\, M_{11})}_{=A} \pm c_0 \sqrt{1 - c_0^2}[B \cos(\varphi) + C \sin(\varphi)]\,. \tag{E.34}$$

The optimization is carried out by calculating $\nabla_{c_0, \varphi} \tilde{f}(c_0, \varphi) \stackrel{!}{=} 0$ One finds for the partial derivative with respect to the phase $\varphi$

$$\frac{\partial \tilde{f}}{\partial \varphi} = \mp \sqrt{1 - c_0^2}[B \sin(\varphi) - C \cos(\varphi)] \stackrel{!}{=} 0 \quad \Rightarrow \quad \varphi = \arctan\left(\frac{C}{B}\right). \tag{E.35}$$
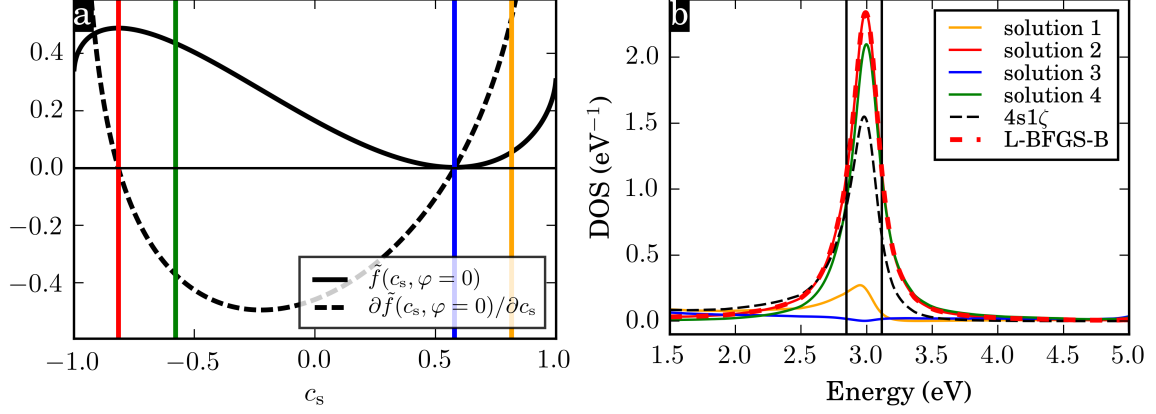
**Figure E.1.:** Example of the optimization of a resonance shape: Majority channel regarding the 4s-resonance of Ar* adsorbed at a distance of 3.6 Å an Fe(110). (a) The four roots of Eq. (E.38) (vertical colored lines) coincide only in two cases with the roots of the derivative of $\tilde{f}(c_s, \varphi = 0)$, where they maximize/minimize $\tilde{f}(c_s, \varphi = 0)$. (b) Spectra corresponding to the four roots in subplot (a). Additionally shown in (b) are the spectrum of the pure Ar*4s resonance (dashed black line) and the spectrum obtained from a numerical optimization (L-BFGS-B, dashed thick red line). The vertical lines highlight the integration range from $a$ to $b$ in Eq. (E.29).

Thereby the phase has been determined. For the derivative with respect to the free coefficient $c_0$ one obtains

$$\frac{\partial \tilde{f}}{\partial c_0} = 2c_0 A \pm \frac{1 - 2c_0^2}{\sqrt{1 - c_0^2}}(B\cos(\varphi) + C\sin(\varphi)) \overset{!}{=} 0. \tag{E.36}$$

Using the expression found above for $\varphi$ one may rewrite the term in brackets as $B\cos\left[\arctan\left(\frac{C}{B}\right)\right] + C\sin\left[\arctan\left(\frac{C}{B}\right)\right] = \text{sgn}(B)\sqrt{B^2 + C^2}$. Finally, we isolate terms containing the coefficient $c_0$ on one side of the equality and take the square resulting in

$$\frac{4c_0^2(1 - c_0^2)}{(1 - 2c_0^2)^2} = \frac{B^2 + C^2}{A^2}. \tag{E.37}$$

This leads to the biquadratic equation

$$c_0^4 - c_0^2 + \frac{B^2 + C^2}{4(A^2 + B^2 + C^2)} = 0, \tag{E.38}$$

which has four formal solutions

$$c_0 = \begin{cases} \frac{1}{2} + \frac{1}{2}\sqrt{D} \\ \frac{1}{2} - \frac{1}{2}\sqrt{D} \\ -\frac{1}{2} + \frac{1}{2}\sqrt{D} \\ -\frac{1}{2} - \frac{1}{2}\sqrt{D} \end{cases} \quad \text{with} \quad D = \frac{A^2}{A^2 + B^2 + C^2}. \tag{E.39}$$

Of those four formal solutions only two optimize the wave packet according to Eq. (E.36). In fact, the actual data presented in Chapter 6 confirms that $C = 0$ and hence $\varphi = 0$. The latter finding simplifies the above equations slightly.

To conclude this section, the optimization procedure described above is applied for the case of Ar attached to Fe(110) at 3.6 Å adsorption height. We consider a wave packet constructed from 4s and $4p_z$ components and analyze the majority channel. Fig. E.1a shows the curves for $\tilde{f}(c_s, \varphi = 0)$ of Eq. (E.35) and $\partial\tilde{f}(c_s, \varphi = 0)/\partial c_s$ of Eq. (E.36). The colored vertical lines in the plot indicate the four formal solutions presented in Eq. (E.39) of which only two relate to the roots of the derivative of $\tilde{f}(c_s, \varphi = 0)$ either maximizing or minimizing $\tilde{f}(c_s, \varphi = 0)$.

In Fig. E.1b the spectral features related to the four roots in Fig. E.1a are displayed in the corresponding colors. The red line visually confirms that solution 2 maximizes the spectral feature inside the energy region of the integration range from $a$ to $b$ [cf. Eq. (E.29)] marked by the vertical black lines in the plot. This result is verified independently by a numerical optimization scheme (L-BFGS-B), which yields a coinciding spectrum (dashed thick red line). The comparison with the spectral feature of a pure 4s resonance state (dashed black line) emphasizes the increase in spectral density around the peak position. Analyzing the widths of the optimized spectra in cf. Table 6.2 and Table 6.3 one finds that the optimized wave packets consistently exhibit longer lifetimes than the pure 4s resonances. In this sense, the optimized states represent an improved account of the resonance wave packets.

# F.   Definitions of Fourier Transforms

The Fourier transform pair in one dimension is defined as

$$f(E) = \mathcal{F}^{-1}[\tilde{f}(t)] = \int_{-\infty}^{\infty} \tilde{f}(t)\mathrm{e}^{iEt}\, dt\,, \tag{F.40}$$

$$\tilde{f}(t) = \mathcal{F}[f(E)] \quad= \frac{1}{2\pi} \int_{-\infty}^{\infty} f(E)\mathrm{e}^{-iEt}\, dE\,. \tag{F.41}$$

In three dimensions we use the definition

$$f(\mathbf{r}) = \mathcal{F}^{-1}[\tilde{f}(\mathbf{k})] = \int_{-\infty}^{\infty} \tilde{f}(\mathbf{k})\mathrm{e}^{i\mathbf{kr}}\, d\mathbf{k}\,, \tag{F.42}$$

$$\tilde{f}(\mathbf{k}) = \mathcal{F}[f(\mathbf{r})] \quad= \frac{1}{(2\pi)^3} \int_{-\infty}^{\infty} f(\mathbf{r})\mathrm{e}^{-i\mathbf{kr}}\, d\mathbf{r}\,. \tag{F.43}$$

The three dimensional Fourier transform of a function $f(\mathbf{r}) = f(|\mathbf{r}|) = f(r)$ which only depends on the radius $r$, can be performed in spherical coordinates. In the following, we use $\mathbf{k} \cdot \mathbf{r} = kr\cos(\theta)$ and the substitution $x = \cos(\theta)$, $dx = -\sin(\theta)\, d\theta$

$$\tilde{f}(\mathbf{k}) = \frac{1}{(2\pi)^3} \int_0^{\infty} \int_0^{\pi} \int_0^{2\pi} f(\mathbf{r})\mathrm{e}^{-i\mathbf{kr}}r^2\, dr \sin(\theta)\, d\theta\, d\phi\,, \tag{F.44}$$

$$= \frac{2\pi}{(2\pi)^3} \int_0^{\infty} f(r) \int_{-1}^{1} \mathrm{e}^{ikrx}\, dx\, r^2\, dr\,, \tag{F.45}$$

$$= \frac{4\pi}{(2\pi)^3} \int_0^{\infty} f(r) \frac{\sin(kr)}{kr} r^2\, dr \tag{F.46}$$

$$= \frac{4\pi}{(2\pi)^3} \int_0^{\infty} f(r) j_0(kr) r^2\, dr\,. \tag{F.47}$$

Here, we have identified the spherical Bessel function $j_0(kr) = \sin(kr)/(kr)$ in the last line. The inverse transformation can be found by using a similar argumentation. These radial transforms are known as the Fourier-Bessel or Hankel transforms. In two dimensions one can write similarly

$$\tilde{f}(\mathbf{k}) = \frac{1}{(2\pi)^2} \int_0^{\infty} \int_0^{2\pi} f(\mathbf{r})\mathrm{e}^{-i\mathbf{kr}}r\, dr\, d\phi\,, \tag{F.48}$$

$$= \frac{1}{(2\pi)^2} \int_0^{\infty} f(r) \int_0^{2\pi} \mathrm{e}^{-ikr\cos(\phi)}\, d\phi\, r\, dr\,, \tag{F.49}$$

$$= \frac{1}{2\pi} \int_0^{\infty} f(r) J_0(kr) r\, dr\,. \tag{F.50}$$

In the last line the inner integral over $\phi$ has been identified as $2\pi J_0(kr)$, where $J_0$ is the zeroth order Bessel function of the first kind.

# Resumen (Summary in Spanish)

Los procesos de transferencia de electrones son fundamentales tanto en la Naturaleza y como para gran cantidad de aplicaciones tecnológicas. Una comprensión detallada de su funcionamiento en la escala atómica es de gran importancia para el diseño de nuevos materiales y dispositivos. En particular, la transferencia de electrones tiene lugar en reacciones catalíticas y foto-catalíticas, así como en celdas electroquímicas y distintos dispositivos generadores de energía solar como las células solares "sensibilizadas" por colorantes (en inglés "dye-sensitized solar cells", DSSCs). En este tipo de situaciones, con frecuencia la transferencia electrónica tiene lugar en una superficie o a través de una interfase, mientras el electrón transferido normalmente procede de una unidad química donora, como un átomo o una molécula absorbidos sobre o cercanos a dicha superficie. Las técnicas experimentales modernas son capaces de estudiar estos procesos en detalle, accediendo a sus escalas espaciales y temporales fundamentales (el nanometro y el femtosegundo). Sin embargo, en sistemas grandes y/o complejos diversos procesos pueden interferir, complicando la descripción. Por dicha razón es preferible estudiar sistemas sencillos que pueden ser estudiados tanto de forma teórica como experimental y comprendidos con modelos relativamente simples.

La presente Tesis se ocupa de describir procesos elásticos de transferencia electrónica en superficies utilizando cálculos de primeros principios. En particular, desarrollamos un método que combina el uso funciones de Green con la información obtenida a partir de cálculos del funcional de la densidad (en inglés "density functional theory", DFT) para realizar una descripción realista de los procesos de transferencia electrónica resonante en superficies. Los tiempos de transferencia de carga así calculados son comparados, con frecuencia de forma muy favorable, con los extraídos de experimentos que utilizan la técnica de espectroscopía "con cronometraje por hueco interno" (en inglés "core-hole-clock spectroscopy").

Dentro de nuestro método consideramos inicialmente capas delgadas que contienen unos pocos planos atómicos y están decoradas por adsorbatos atómicos o moleculares (las unidades donoras). Empleando la aproximación de Born-Oppenheimer los grados de libertad electrónicos y nucleares pueden ser desacoplados y el subsistema electrónico puede ser descrito al nivel de cálculos DFT utilizando funcionales semi-locales ("generalized gradient appoximation", GGA) tal como se implementa en el código SIESTA. Los funcionales GGA proporcionan un buen equilibrio entre su moderado coste computacional y la calidad de la descripción de la estructura de bandas que producen, sobre todo para metales. Por otra parte, los funcionales GGA suelen tener problemas para describir el tamaño del "gap" electrónico tanto en semiconductores

como en sistemas localizados [átomos y moléculas, el "gap" es en este caso la distancia energética entre el último nivel ocupado (HOMO) y el primer nivel desocupado (LU-MO)], que suele ser infravalorado. El alineamiento (posición relativa) de los niveles energéticos en el caso de sistemas que poseen un "gap" también es problemático para este nivel de teoría. Sin embargo, como demostramos en esta Tesis, a pesar de dichas limitaciones y en conjunción con el experimento, este nivel de teoría ya nos permite ahondar en la comprensión de los mecanismos detrás de los procesos de transferencia de carga en muchos sistemas, así como en su dependencia con diversos grados de libertad que describen el sistema como el espín electrónico o la polarización de la luz utilizada en el excitación.

La inyección de carga a través de una interfase se inicia usualmente con un estímulo externo (e.g., la excitación del donor por un haz incidente de luz), preparando al sistema en un estado excitado resonante con los estados electrónicos del sustrato. En una imagen simplificada (mono-electrónica) podemos decir que el electrón excitado es promovido a una resonancia, un estado intermedio entre el estado inicial localizado en el adsorbato y el estado final en el que el electrón se ha deslocalizado en el sustrato. En nuestro trabajo asumimos que este estado intermedio puede ser descrito en términos de un paquete de ondas localizado en el adsorbato, y que puede ser expresado utilizando uno o unos pocos autoestados desocupados del adsorbato. La inyección de carga se corresponde por tanto con el proceso de deslocalización de este paquete de ondas en el sustrato, y puede ser descrito a partir de la evolución temporal del mismo. La función de autocorrelación temporal del paquete de ondas (i.e., la proyección del paquete en cada instante de tiempo sobre el paquete de ondas inicial) se conoce como *amplitud de supervivencia*. El cuadrado de su norma nos da la *probabilidad de supervivencia*, que típicamente describe un decaimiento (reducción) en función del tiempo cuyo análisis nos da la *vida media elástica* de la resonancia. Alternativamente, la transformada de Fourier nos permite expresar la evolución temporal de la probabilidad de supervivencia en términos del espectro de la resonancia en función de la energía. Idealmente, en dicho espectro podremos identificar un pico con forma Lorentziana asociado a cada resonancia. La anchura de cada Lorentziana es la *anchura elástica* del pico $\Gamma$ y está ligada a la vida media elástica $\tau$ por la relación de incertidumbre $\Gamma \times \tau = 1$ (en unidad atómicas). Esto nos permite extraer las vidas medias de los paquetes de onda de cada estado resonante a partir de las anchuras de los correspondiente picos en el espectro energético.

Para una estimación realista de las anchuras y las vidas medias de las resonancias resulta crucial describir con la debida precisión el acomplamiento del paquete de onda del estado excitado intermedio con los estados accesibles en el sustrato a la misma energía. En este punto es importante señalar que el espaciado energético entre niveles en una lámina de anchura finita (cálculo de "slab", habitual utilizando la teoría DFT de primeros principios) resulta un factor limitante para la precisión del cálculo de la vida media. El espaciado entre niveles normalmente escala de forma inversamente proporcional a la anchura de la lámina que representa el sustrato, y siendo esta de pocas distancias atómicas se corre el peligro de que aquel sea comparable o mayor que las anchuras de las resonancias que quieren estimarse. Por tanto, aunque normalmente se puede conseguir una descripción razonable de la interfase (por ejemplo de sus propiedades químicas) utilizando cálculos con láminas delgadas, para estimar las

anchuras de las resonancias correctamente es vital tener en cuenta el acoplo de la región superficial con una número infinito de capas atómicas describiendo el volumen del sustrato. De esta manera tendremos un sustrato semi-infinito con una densidad de estados continua que se asemeja más a la situación experimental. Es posible realizar este tipo de descripción utilizando la técnica de las funciones de Green tal como está implementada en la utilidad *tbtrans* del código SIESTA. Para llevar a cabo los cálculos descritos en esta Tesis hemos realizado una modificación de programa tbtrans para poder proyectar la función de Green dependiente de la energía en la región superficial sobre el paquete de ondas que describe la resonancia en el instante inicial, i.e., justo después de su excitación. Con ello obtenemos el espectro de la resonancia con una resolución en energía en principio arbitraria, sólo limitada por la pequeña parte imaginaria que debe ser sumada a la energía al evaluar la función de Green del material de volumen. Esto es necesario para evitar inestabilidades numéricas y para reducir el tiempo de computación. Sin embargo, esta anchura espuria puede tomar un valor muy pequeño y en la práctica no limita la precisión de nuestros cálculos como se describe en detalle en uno de los apéndices de esta Tesis.

Es importante enfatizar, que los procesos de transferencia de carga descritos en esta Tesis son todos de carácter elástico, es decir no incluimos posible procesos de "scattering" inelástico asociados a pérdida de energía por la excitación de, por ejemplo, fonones, pares electrón-hueco o plasmones. Esperamos que los procesos elásticos dominen la transferencia de carga ultrarrápida que tiene lugar en los sistemas prototípicos que estudiamos en este trabajo.

Como ingrediente final, en la gran mayoría de los casos consideramos que el estado excitado intermedio proviene de la excitación de un estado interno (de "core") en analogía con los experimentos de adsorción de rayos-X y, en particular, con el objeto de comparar nuestra teoría con resultados de experimentos de espectroscopía "con cronometraje por hueco interno". El hueco interno se introduce en el cálculo del pseudopotencial que describirá el átomo donde se localiza la excitación. Esto genera una carga neta positiva en el sistema que neutralizamos añadiendo un electrón de valencia adicional. Este electrón (i.e., el electrón excitado) es constreñido a una región cercana al adsorbato, con una distribución aproximadamente igual a la asociada al paquete de ondas que describe la resonancia objeto de nuestro interés. Por tanto, reproduce la presencia de un electrón poblando la resonancia en los primeros instantes después de la excitación. Esta receta determina el estado inicial de nuestro sistema, a partir del cuya evolución estimaremos los tiempos de transferencia de carga.

Los fundamentos teóricos detrás de los cálculos de estructura electrónica se describen en el Capítulo 2, mientras que el Capítulo 3 se ocupa de forma detallada de las técnicas de funciones de Green. La comparación con el experimento ocupa un papel importante en el trabajo descrito en esta Tesis. Por ello antes de presentar nuestras investigaciones, el Capítulo 4 presenta una descripción básica de las técnicas experimentales utilizadas para obtener información sobre la dinámica electrónica, ocupandonos con especial detalle de la espectroscopía "con cronometraje por hueco interno".

En esta Tesis hemos estudiado una gama de donores de electrones sobre superficies que incluyen desde ad-átomos de argon sobre metales, pasando por moléculas de colorantes quemisorbidas débilmente, y llegando a átomos de azufre enlazados

fuertemente con otro átomos de la superficie. Los correspondientes tiempos de transferencia observados en experimentos de espectroscopía "con cronometraje por hueco interno" disminuyen de forma progresiva desde los pocos femtosegundos a la escala por debajo del femtosegundo (del orden de pocos cientos de attosegundos). En conexión con los distintos adsorbatos, una variedad de sustratos sólidos con diferente carácter han sido explorados incluyendo el semiconductor de "gap" ancho $TiO_2$ (Capítulo 5), las superficies de metales ferromagnéticos Co(0001) y Fe(100) (Capítulo 6), y materiales laminares como el 1T-$TaS_2$ (Capítulo 7). Nuestros resultados ilustran la versatilidad de nuestra metodología para incluir diversos aspectos tales como los efectos de temperatura finita (Capítulo 5), así como la influencia de la polarización de espín del electrón excitado (Capítulo 6) y de la polarización de la luz utilizada en la excitación, que se traduce en una simetría diferente del paquete de ondas inicial (Capítulo 7). Esto nos ha permitido conectar con diversas observaciones experimentales tanto de la literatura como realizadas por colaboradores dentro de trabajos conjuntos teórico-experimentales.

En el Capítulo 5 empezamos presentando un estudio del sustrato semiconductor $TiO_2$, en concreto de las superficies vecinas a la (110) del rutilo con escalones orientados en la dirección [1$\bar{1}$0]. Este trabajo se relaciona con los experimentos realizados en el NanoPhysics Lab del Centro de Física de Materiales de San Sebastián utilizando un sustrato curvado de rutilo con orientación promedio (110). El trabajo explora la relación entre la presencia de escalones en la superficie y la distribución de vacantes de oxígeno. En concreto se explora el grado de reducción de las muestras tal como se obtiene en fotoemisión a partir de la intensidad del estado de defecto que aparece cerca de la banda de conducción, la presencia de vacantes en las terrazas de los escalones a partir de experimentos de microscopía túnel de barrido (en inglés "Scanning Tunneling Microscopy", STM) y la densidad de escalones. Nuestros cálculos teóricos permiten obtener la energía de formación de las vacantes de oxígeno en función de su posición en la terraza. Estos nos permite predecir la tendencia de las vacantes a migrar hacia el borde del escalón. Nuestras simulaciones de las imágenes STM utilizando la teoría de Tersoff-Hamann indican que las vacantes son difíciles de detectar en dichas posiciones cercanas al borde, i.e., el aspecto de la imagen no cambia apreciablemente con respecto al de un escalón estequiométrico. Adicionalmente, análisis de las densidades de estados (en inglés "density of states", DOS) calculadas indican que las vacantes en el borde del escalón contribuyen al dopaje del material de una manera idéntica al de las vacantes en el medio de la terraza o incluso sobre la superficie plana. Por el contrario, la presencia de escalones estequiométricos no lleva aparejada la aparición de ningún estado adicional dentro del "gap" electrónico del material. Por tanto, la tendencia de las vacantes a migrar a los bordes de los escalones puede explicar fácilmente la observación experimental del descenso aparente en la presencia de vacantes de oxígeno en zonas con alta densidad de escalones en los cristales curvados, a pesar de que el nivel de dopaje obtenido a partir de los datos de fotoemisión es similar en toda la muestra. Este estudio para cristales curvados de $TiO_2$ demuestra la importancia de los defectos para conformar la DOS del sustrato, que es uno de los ingredientes fundamentales a la hora de describir los procesos de transferencia de carga.

Después de este prefacio sobre el $TiO_2$, consideramos el problema de las moléculas

de ácido isonicotínico quemisorbidas sobre una superficie perfecta de rutilo (110). Nuestro objetivo será explorar los efectos de las fluctuaciones estructurales a temperaturas finitas en la transferencia de carga de la molécula a la superficie en un ejemplo prototípico de interfase en DSSCs. Aplicando nuestra técnica, que combina cálculos DFT con funciones de Green, a multiples configuraciones instantáneas de una trayectoria de dinámica molecular Car-Parrinello a 300 K, encontramos que la inclusión de fluctuaciones estructurales a temperaturas finitas reconcilia los tiempos de transferencia de carga elástica calculados con aquellos extraídos a partir de medidas utilizando la espectroscopía "con cronometraje por hueco interno" a temperatura ambiente.

Las fluctuaciones a temperatura finita de la energía de cada resonancia molecular dan lugar a una anchura Gaussiana en el promedio térmico del espectro (espectro acumulado). Este efecto puede describirse mediante un sencillo modelo semiclásico de osciladores armónicos que asume acoplamientos electrón-fonón lineales entre los modos vibracionales y los niveles electrónicos de la molécula. Simultáneamente, las resonancias moleculares para cada configuración instantánea muestran formas de línea parecidas a una Lorentziana. En promedio, las anchuras de dichos picos Lorentzianos están controladas por la densidad disponible de estados aceptores en el sustrato a dicha energía. Un análisis de los distintos modos de vibración demuestra que aquellos modos que deforman el grupo carboxilo que ancla la molécula a la superficie contribuyen en mayor medida al ensanchamiento inducido por la temperatura. Por otro lado, en el caso de las anchuras elásticas no se pudo establecer un modelo similar al de la posición energética de los niveles, con un acoplamiento lineal que determina la relación entre la anchura y el grado de excitación de un determinado modo de vibración.

Con el fin de simular los correspondientes experimentos, incluimos en nuestros cálculos un hueco interno en la capa 1s del nitrógeno. La presencia de dicho hueco interno produce un desplazamiento hacia energías más bajas de los niveles moleculares con respecto a la DOS el sustrato. Simultáneamente, los orbitales moleculares se localizan alrededor del centro atractivo creado hueco localizado. Esto hace a los orbitales moleculares menos susceptibles a los cambios estructurales, reduciendo así de forma efectiva el acoplamiento electrón-fonón en la interfase.

En el siguiente trabajo, nos centramos en la inyeccón de electrones desde adátomos de Ar a los sustratos metálicos ferromagnéticos Co(0001) y Fe(110) con el fin de analizar el origen de la dependencia observada experimentalmente de los tiempos de transferencia de carga con el espín del electrón transferido. Nuestros cálculos confirman la observación experimental de que los electrones de espín minoritario excitados desde un estado interno al estado 4s del Ar se inyectan significativamente más rápido que los electrones mayoritarios en ambos sustratos. Además, de nuevo en acuerdo con los experimentos, encontramos una transferencia de carga más rápida para cada canal de espín en Fe(110) que en Co(0001), siendo el canal mayoritario en Fe(110) tan rápido como el canal minoritario en Co(0001). Todos los tiempos de transferencia calculados son de unos pocos femtosegundos y, por lo tanto, están en buen acuerdo cuantitativo con los experimentos.

En nuestro manuscrito argumentamos que la discusión que se realiza en Ref. 50 de la dependencia con el espín de los tiempos de transferencia carga en términos de las

componentes s, p o d de los estados del sustrato alrededor de los átomos metálicos es poco clarificadora en el caso del Ar sobre Fe(110) y Co(0001). En ambos casos la resonancia 4s del Ar excitado se encuentra en una zona de energías correspondiente a bandas altamente dispersivas en dichos sustratos, y claramente por encima de las bandas derivadas de los niveles atómicos 3d del Fe y el Co. Si bien cabe esperar contribuciones crecientes de simetría d y de momentos angulares superiores a medida que la energía aumenta, el carácter altamente dispersivo de las bandas de superficie en la región donde se encuentra la resonancia no concuerda con la noción común de que las bandas d están constituidas por bandas planas derivadas directamente de estados atómicos ligados con simetría d. Por lo tanto, afirmamos que la correlación observada entre la magnitud de la DOS proyectada sobre orbitales de tipo d y los tiempos de vida dependientes del espín es, en este caso, puramente fortuita.

Por el contrario, encontramos que el origen de la dependencia con el espín de los tiempos de transferencia está en la variación para distintas orientaciones del espín de la anchura (en espacio recíproco) de los "gaps" electrónicos en la estructura de bandas de superficie alrededor del punto $\bar{\Gamma}$-point a la energía de resonancia. Esta hipótesis se refuerza mediante un análisis de los cálculos utilizando un modelo simplificado, cuyo principal ingrediente es la posición y forma de los "gaps" proyectados, y que consigue captar las tendencias observadas en el experimento. Estos resultados ponen de manifiesto que se debe tener en cuenta una descripción realista de la estructura de bandas de superficie, así como la distribución espacial y la localización (que se traduce en una estructura bien definida en el espacio recíproco) del paquete de ondas que describe la resonancia, siendo ambos ingredientes cruciales para entender el proceso de transferencia de carga en interfaces. Esto genera una interesante perspectiva para el desarrollo de extensiones a las simulaciones STM convencionales basadas en la teoría de Tersoff-Hamann, estas deben ponderar de forma diferente los distintos estados en la estructura bandas de la superficie utilizando para ello un modelo realista (en espacio recíproco) de las funciones de onda de los estados electrónicos de la punta.

En nuestro último estudio, llevamos nuestra técnica de funciones Green a los límites de su aplicabilidad investigando la dinámica de carga en el rango por debajo del femtosegundo. En este caso nos centramos en la dinámica posterior a excitación con rayos X de la superficie del di-calcogenuro de metal de transición (en inglés "transition metal dichalcogenide", TMD) 1T-TaS$_2$. La excitación se realiza desde el nivel 2s de un azufre superficial hasta una resonancia desocupada con fuerte carácter S 3p. Se trata de un trabajo conjunto experimental (usando espectroscopía "con cronometraje por hueco interno") y teórico (utilizando métodos de primeros principios) que intenta abordar el problema de la direccionalidad de la transferencia de carga en este sistema laminar. Para ello estudiamos la dinámica de resonancias electrónicasc con distinta simetría (p$_\parallel$ o p$_\perp$, i.e., paralelo o perpendicular a la superficie). Esto se consigue utilizando luz polarizada linealmente en los experimentos y, en consecuencia, preparando paquetes de ondas intermedios con distintas polarizaciones en la capa S 3p en nuestras simulaciones. El análisis de los datos obtenidos por nuestros colaboradores experimentales muestra que la anisotrópia de los tiempos de transferencia electrónica, característicos de un sistema con fuerte carácter bidimensional, prevalece en la fase de 1T-TaS$_2$ a temperatura ambiente, correspondiente a la fase de onda de densidad de carga cuasi-conmensurada (en inglés "nearly commensurate charge density

wave", NCDW). Sin embargo en la fase de baja temperatura (onda de densidad de carga conmensuradas, CCDW) el comportamiento es altamente isotrópico en escalas de tiempo ultrarrápidas, a pesar de la estructura por capas del material y, por tanto, indicando un fuerte acoplamiento electrónico en la energía de la resonancia.

Con nuestros cálculos pudimos abordar la fase CCDW del 1T-TaS$_2$. Para ello realizamos un modelo de sustrato semi-infinito utilizando la conocida reconstrucción $\sqrt{13}a \times \sqrt{13}a$ de cada capa del material. Se estudiaron diferentes apilamientos de las capas. Pudimos identificar las principales características espectroscópicas experimentales en la DOS proyectada sobre los orbitales S 3p. Todas la cantidades se promediaron sobre las distintos átomos de azufre no equivalentes en la superficie.

Los tiempos de vida calculados para un paquete de onda inicial localizado en el azufre superficial, formado por estados electrónicos en el rango de hasta $\sim 2$ eV por encima del nivel de Fermi, resultaron ser independientes de la polarización orbital y por lo tanto de la polarización de la luz incidente. Esto está en buen acuerdo con la transferencia de carga isotrópica observada experimentalmente para la fase CCDW. Además, este resultado es independiente con respecto a las variaciones en el apilamiento de la reconstrucción $\sqrt{13}a \times \sqrt{13}a$ en capas consecutivas del material. A pesar de este acuerdo cualitativo, la escala de tiempo absoluta está sustancialmente sobreestimada en comparación con los experimentos. Basadonos en estos resultados, sugerimos que la transición de una transferencia de carga anisotrópica en la fase NCDW, i.e., de carácter bidimensional, a una transferencia de carga isotrópica, i.e., de carácter tridimensional, en la fase de baja temperatura CCDW se debe a un aumento del acoplamiento electrónico entre las capas y no es una consecuencia de variaciones en el apilamiento de las láminas. Esto último podría aventurarse como una explicación si sólo examinásemos las variaciones de la estructura de bandas a energías muy cercanas al nivel de Fermi.

En general, esta Tesis ha demostrado para varias interfases prototípicas que nuestra metodología usando funciones de Green en combinación con cálculos DFT de primeros principios es adecuada para describir la transferencia elástica de electrones en situaciones realistas. Esto lo demuestra el buen acuerdo cualitativo y semi-cuantitativo que obtenemos en la gran mayoría de los casos en comparación con el experimento. Dado que los cálculos utilizan la dependencia con la energía del propagador, es posible realizar una comparación clara con los experimentos de espectroscopía. Además, la inclusión de huecos internos en el pseudopotencial nos permite representar de forma eficaz y eficiente situaciones en las que los electrónes son excitados desde capas atómicas internas. Esto permite un acuerdo casi cuantitativo con las mediciones por espectroscopía "con cronometraje por hueco interno" de tiempos de transferencia de carga que van desde un poco por debajo del femtosegundo hasta unos pocos cientos de femtosegundos. Para la determinación de tiempos de transferencia de carga mayores es necesario realizar cálculos numéricamente muy precisos (por ejemplo, utilizando una parte imaginaria de la energía muy pequeña en el volumen del material), aunque esto no representa en principio ningún problema conceptual. Para tiempos de transferencia de carga más cortos la apariencia general de las resonancias (cada vez más anchas y usualmente menos parecidas a una Lorentziana) dificulta la identificación de las características relevantes de la resonancia, e.g., la definición clara de su anchura. En tal caso, los cálculos realizados en tiempo real, como por ejemplo empleando un

método de propagación de paquetes de ondas, pueden dar una idea más clara de la dinámica de transferencia de carga. Además, la propagación de paquetes de ondas pueden proporcionar información complementaria al enfoque de función de Green utilizado en esta tesis, ya que son capaces de resolver la deslocalización de electrones en el espacio real, mientras en el caso de las funciones de Green nos limitamos a la evolución temporal de la población del paquete de ondas inicial.

Más allá de la descripción de la transferencia de carga elástica como en el trabajo actual, la inclusión de procesos de "scattering" inelásticos asociados a la interacción electrón-fonón (por ejemplo, la teoría de Eliashberg) y la interacción electrón-electrón (por ejemplo, a través de la aproximación GW) son deseables para obtener un acuerdo aún mejor con el experimento. En última instancia, una descripción completa de los procesos de transferencia de carga, incluida la preparación dinámica de un paquete de ondas inicial por un frente de luz incidente incluido de forma explícita es cada vez más importante a medida que los experimentos se adentran en escalas temporales cada vez más cortas. Sin embargo, esto no resulta en absoluto trivial. Aunque los tratamientos semiclásicos de la luz son en principio factibles, no está claro que proporcionen una descripción realista de la absorción de fotones por los materiales en la escala tanto temporal como espacial que aquí nos interesa. Probablemente una descripción cuántica de la luz es probablemente inevitable en este punto. Sin embargo, en nuestra opinión, los métodos que combinan tales descripciones con métodos de estructura electrónica de primeros principios no están hoy en día suficientemente desarrollados para aplicarlos a sistemas grandes y realistas. De hecho se encuentran todavía en su infancia. Los enfoques actuales capaces de un tratamiento explícito de las excitaciones son prohibitivamente exigentes en términos de recursos computacionales, por lo que se deben encontrar nuevas vías para describir estos procesos ultrarrápidos y, posiblemente, junto con ellos una física completamente nueva.

# Bibliography

[1] A. J. Bard. Photoelectrochemistry. *Science*, **207**, 4427, 139 (1980). (see page: 1)

[2] K. J. Young, L. A. Martini, R. L. Milot, R. C. Snoeberger, V. S. Batista, C. A. Schmuttenmaer, R. H. Crabtree, and G. W. Brudvig. Light-driven water oxidation for solar fuels. *Coord. Chem. Rev.*, **256**, 21-22, 2503 (2012). (see pages: 1, 57)

[3] B. O'Regan and M. Grätzel. A low-cost, high-efficiency solar cell based on dye-sensitized colloidal $TiO_2$ films. *Nature*, **353**, 6346, 737 (1991). (see pages: 1, 50, and 57)

[4] M. Grätzel. Dye-sensitized solar cells. *J. Photochem. Photobiol. C Photochem. Rev.*, **4**, 2, 145 (2003).

[5] A. Hagfeldt, G. Boschloo, L. Sun, L. Kloo, and H. Pettersson. Dye-Sensitized Solar Cells. *Chem. Rev.*, **110**, 11, 6595 (2010). (see pages: 1, 49, 50, and 57)

[6] R. A. Marcus. Electron Transfer Reactions in Chemistry: Theory and Experiment (Nobel Lecture). *Angew. Chemie Int. Ed. English*, **32**, 8, 1111 (1993). (see page: 1)

[7] P. Siders and R. A. Marcus. Quantum effects in electron-transfer reactions. *J. Am. Chem. Soc.*, **103**, 4, 741 (1981).

[8] R. Marcus and N. Sutin. Electron transfers in chemistry and biology. *Biochim. Biophys. Acta - Rev. Bioenerg.*, **811**, 3, 265 (1985). (see page: 1)

[9] A. Groß. Theoretical Surface Science: A Microscopic Perspective. Springer, 2nd edition (2009). (see page: 1)

[10] P. M. Echenique and J. B. Pendry. The existence and detection of Rydberg states at surfaces. *J. Phys. C Solid State Phys.*, **11**, 10, 2065 (1978). (see page: 1)

[11] P. Echenique and J. Pendry. Theory of image states at metal surfaces. *Prog. Surf. Sci.*, **32**, 2, 111 (1989). (see page: 1)

[12] K. Giesen, F. Hage, F. J. Himpsel, H. J. Riess, and W. Steinmann. Two-photon photoemission via image-potential states. *Phys. Rev. Lett.*, **55**, 3, 300 (1985). (see page: 1)

[13] T. Fauster and W. Steinmann. Two-Photon Photoemission Spectroscopy of Image States. In Photonic Probes of Surfaces, pages 347–411. Elsevier (1995). (see pages: 1, 46)

[14] R. W. Schoenlein, J. G. Fujimoto, G. L. Eesley, and T. W. Capehart. Femtosecond Studies of Image-Potential Dynamics in Metals. *Phys. Rev. Lett.*, **61**, 22, 2596 (1988). (see page: 1)

[15] U. Hofer, I. L. Shumay, C. Reuß, U. Thomann, W. Wallauer, and T. Fauster. Time-Resolved Coherent Photoelectron Spectroscopy of Quantized Electronic States on Metal Surfaces. *Science (80-. ).*, **277**, 5331, 1480 (1997). (see page: 1)

[16] P. Echenique, R. Berndt, E. Chulkov, T. Fauster, A. Goldmann, and U. Höfer. Decay of electronic excitations at metal surfaces. *Surf. Sci. Rep.*, **52**, 7-8, 219 (2004). (see pages: 1, 3)

[17] E. V. Chulkov, A. G. Borisov, J. P. Gauyacq, D. Sánchez-Portal, V. M. Silkin, V. P. Zhukov, and P. M. Echenique. Electronic excitations in metals and at metal surfaces. *Chem. Rev.*, **106**, 10, 4160 (2006). (see pages: 1, 3)

[18] O. Björneholm, A. Nilsson, A. Sandell, B. Hernnäs, and N. Mårtensson. Determination of time scales for charge-transfer screening in physisorbed molecules. *Phys. Rev. Lett.*, **68**, 12, 1892 (1992). (see pages: 2, 4, 41, and 46)

[19] W. Wurth and D. Menzel. Ultrafast electron dynamics at surfaces probed by resonant Auger spectroscopy. *Chem. Phys.*, **251**, 1-3, 141 (2000). (see pages: 45, 58, 89, 94, and 100)

[20] A. Nilsson. Applications of core level spectroscopy to adsorbates. *J. Electron Spectros. Relat. Phenomena*, **126**, 1-3, 3 (2002).

[21] P. A. Brühwiler, O. Karis, and N. Mårtensson. Charge-transfer dynamics studied using resonant core spectroscopies. *Rev. Mod. Phys.*, **74**, 3, 703 (2002). (see pages: 2, 4, 41, 42, 44, and 58)

[22] A. Föhlisch, P. Feulner, F. Hennies, A. Fink, D. Menzel, D. Sánchez-Portal, P. M. Echenique, and W. Wurth. Direct observation of electron dynamics in the attosecond domain. *Nature*, **436**, 7049, 373 (2005). (see pages: 2, 35, 42, 46, 58, 115, 119, 121, and 124)

[23] P. Hohenberg and W. Kohn. Inhomogeneous Electron Gas. *Phys. Rev.*, **136**, 3B, 864 (1964). (see pages: 2, 10, and 11)

[24] W. Kohn and L. J. Sham. Self-consistent equations including exchange and correlation effects. *Phys. Rev.*, **140**, 4A, 1133 (1965). (see pages: 10, 13, and 15)

[25] W. Kohn. Nobel Lecture: Electronic structure of matter—wave functions and density functionals. *Rev. Mod. Phys.*, **71**, 5, 1253 (1999). (see page: 2)

[26] D. Sánchez-Portal, P. Ordejón, E. Artacho, and J. M. Soler. Density-functional method for very large systems with LCAO basis sets. *Int. J. Quantum Chem.*, **65**, 5, 453 (1997). (see pages: 2, 3)

[27] E. Artacho, D. Sanchez-Portal, P. Ordejon, A. Garcia, and J. M. Soler. Linear-scaling ab-initio calculations for large and complex systems. *Phys. Status Solidi B Basic Solid State Phys.*, **215**, 1, 809 (1999). (see page: 21)

[28] J. M. Soler, E. Artacho, J. D. Gale, A. García, J. Junquera, P. Ordejón, and D. Sánchez-Portal. The SIESTA method for ab initio order- N materials simulation. *J. Phys. Condens. Matter*, **14**, 11, 2745 (2002). (see pages: 23, 52, 59, 60, and 91)

[29] E. Artacho, E. Anglada, O. Diéguez, J. D. Gale, A. García, J. Junquera, R. M. Martin, P. Ordejón, J. M. Pruneda, D. Sánchez-Portal, and J. M. Soler. The SIESTA method; developments and applicability. *J. Phys. Condens. Matter*, **20**, 6, 064208 (2008). (see pages: 2, 3, and 21)

[30] U. Fano. Effects of Configuration Interaction on Intensities and Phase Shifts. *Phys. Rev.*, **124**, 6, 1866 (1961). (see pages: 2, 36)

[31] P. W. Anderson. Localized Magnetic States in Metals. *Phys. Rev.*, **124**, 1, 41 (1961). (see page: 36)

[32] T. B. Grimley. The indirect interaction between atoms or molecules adsorbed on metals. *Proc. Phys. Soc.*, **90**, 3, 751 (1967).

[33] D. M. Newns. Self-Consistent Model of Hydrogen Chemisorption. *Phys. Rev.*, **178**, 3, 1123 (1969). (see pages: 2, 36)

[34] D. Sánchez-Portal. Slab calculations and Green's function recursive methods combined to study the electronic structure of surfaces: application to Cu(111)-(4×4)-Na. *Prog. Surf. Sci.*, **82**, 4–6, 313 (2007). (see pages: 2, 3, 27, 35, 58, 59, 61, 90, 102, and 113)

[35] D. Sánchez-Portal, D. Menzel, and P. M. Echenique. First-principles calculation of charge transfer at surfaces: The case of core-excited $Ar^*(2p_{3/2}^{-1}4s)$ on Ru(0001). *Phys. Rev. B*, **76**, 23, 235406 (2007). (see pages: 2, 3, 27, 35, 37, 61, 90, 93, 102, 107, 113, and 114)

[36] G. Fratesi, C. Motta, M. I. Trioni, G. P. Brivio, and D. Sánchez-Portal. Resonant Lifetime of Core-Excited Organic Adsorbates from First Principles. *J. Phys. Chem. C*, **118**, 17, 8775 (2014). (see pages: 3, 37, 58, 59, 61, 63, 65, 70, 73, and 99)

[37] E. Chulkov, V. Silkin, and P. Echenique. Image potential states on metal surfaces: binding energies and wave functions. *Surf. Sci.*, **437**, 3, 330 (1999). (see page: 3)

[38] E. Chulkov, V. Silkin, and P. Echenique. Image potential states on lithium, copper and silver surfaces. *Surf. Sci.*, **391**, 1-3, L1217 (1997). (see page: 3)

[39] P. Echenique, J. Pitarke, E. Chulkov, and A. Rubio. Theory of inelastic lifetimes of low-energy electrons in metals. *Chem. Phys.*, **251**, 1, 1 (2000). (see page: 3)

[40] K. Niedfeldt, P. Nordlander, and E. A. Carter. Mechanism of enhanced broadening of the ionization level of Li outside transition metal surfaces. *Phys. Rev. B*, **74**, 11, 115109 (2006). (see page: 3)

[41] A. G. Borisov, A. K. Kazansky, and J. P. Gauyacq. Resonant charge transfer in ion-metal surface collisions: Effect of a projected band gap in the $H^-$-Cu(111) system. *Phys. Rev. B*, **59**, 16, 10935 (1999). (see pages: 3, 90, and 102)

[42] F. Martín and M. Politis. Multicenter-Gaussian representation of resonant charge transfer in atom-surface interaction. *Surf. Sci.*, **356**, 1-3, 247 (1996). (see page: 3)

[43] D. Teillet-Billy and J. Gauyacq. Position and width of a negative ion state in front of a surface: formation of $C^-(^4S)$ ions by electron capture. *Surf. Sci.*, **239**, 3, 343 (1990). (see page: 3)

[44] P. Nordlander and J. C. Tully. Energy shifts and broadening of atomic levels near metal surfaces. *Phys. Rev. B*, **42**, 9, 5564 (1990). (see page: 3)

[45] P. Kürpick, U. Thumm, and U. Wille. Close-coupling calculations for ion-surface interactions. *Nucl. Instruments Methods Phys. Res. Sect. B Beam Interact. with Mater. Atoms*, **125**, 1-4, 273 (1997). (see page: 3)

[46] D. Sanchez-Portal, J. Stähler, and X. Zhu. Basic Theory of Heterogeneous Electron Transfer. In Dyn. Solid State Surfaces Interfaces, pages 155–180. Wiley-VCH Verlag GmbH & Co. KGaA, Weinheim, Germany (2012). (see page: 3)

[47] L. A. Miccio, M. Setvin, M. Müller, M. Abadía, I. Piquero, J. Lobo-Checa, F. Schiller, C. Rogero, M. Schmid, D. Sánchez-Portal, U. Diebold, and J. E. Ortega. Interplay between Steps and Oxygen Vacancies on Curved $TiO_2$(110). *Nano Lett.*, **16**, 3, 2017 (2016). (see pages: 4, 50, 51, 52, 55, and 57)

[48] J. Schnadt, J. N. O'Shea, L. Patthey, L. Kjeldgaard, J. Åhlund, K. Nilson, J. Schiessling, J. Krempaský, M. Shi, O. Karis, C. Glover, H. Siegbahn, N. Mårtensson, and P. A. Brühwiler. Excited-state charge transfer dynamics in systems of aromatic adsorbates on $TiO_2$ studied with resonant core techniques. *J. Chem. Phys.*, **119**, 23, 12462 (2003). (see pages: 4, 45, 50, 58, 59, 70, 72, 73, and 76)

[49] P. Feulner, F. Blobner, J. Bauer, R. Han, A. Kim, T. Sundermann, N. Müller, U. Heinzmann, and W. Wurth. Ways to Spin Resolved Core-Hole-Clock Measurements. *e-Journal Surf. Sci. Nanotechnol.*, **13**, 317 (2015). (see pages: 4, 46, 89, and 97)

[50] F. Blobner, R. Han, A. Kim, W. Wurth, and P. Feulner. Spin-Dependent Electron Transfer Dynamics Probed by Resonant Photoemission Spectroscopy. *Phys. Rev. Lett.*, **112**, 8, 086801 (2014). (see pages: 44, 89, 90, 94, 95, 96, 97, 99, 100, 101, 113, 114, 137, and 165)

[51] T. Sundermann, N. Müller, U. Heinzmann, W. Wurth, J. Bauer, R. Han, A. Kim, D. Menzel, and P. Feulner. A universal approach to spin selective core-hole-clock measurement demonstrated for Ar/Co(0001). *Surf. Sci.*, **643**, 190 (2016). (see pages: 4, 46, 89, and 97)

[52] D. Kühn, M. Müller, F. Sorgenfrei, E. Giangrisostomi, R. M. Jay, R. Ovsyannikov, N. Mårtensson, D. Sánchez-Portal, and A. Föhlisch. Directional sub-femtosecond charge transfer dynamics and the dimensionality of 1T-TaS$_2$. *Sci. Rep.*, **9**, 1, 488 (2019). (see pages: 5, 44, 115, 123, and 124)

[53] E. Schrödinger. Quantisierung als Eigenwertproblem. *Ann. Phys.*, **384**, 4, 361 (1926). (see pages: 7, 8)

[54] M. Born and R. Oppenheimer. Zur Quantentheorie der Molekeln. *Ann. Phys.*, **389**, 20, 457 (1927). (see page: 8)

[55] L. S. Cederbaum. Born-Oppenheimer Approximation and Beyond. In W. Domcke, D. R. Yarkony, and H. Köppel (editors), Conical Intersect. Electron. Struct. Dyn. & Spectrosc., volume 15, chapter 1, pages 3–40. World Scientific Publishing (2004). (see pages: 8, 9)

[56] M. V. Berry. Quantal Phase Factors Accompanying Adiabatic Changes. *Proc. R. Soc. A Math. Phys. Eng. Sci.*, **392**, 1802, 45 (1984). (see page: 9)

[57] L. H. Thomas. The calculation of atomic fields. *Math. Proc. Cambridge Philos. Soc.*, **23**, 05, 542 (1927). (see pages: 10, 13)

[58] E. Fermi. Un metodo statistico per la determinazione di alcune priorieta dell'atome. *Rend. Accad. Naz. Lincei*, **6**, 602-607, 32 (1927). (see pages: 10, 13)

[59] R. M. Martin. Electronic Structure: Basic Theory and Practical Methods. Cambridge University Press (2004). (see page: 10)

[60] E. Engel and R. M. Dreizler. Density functional theory : an advanced course. Springer (2011). (see pages: 10, 11, 12, and 16)

[61] M. Levy. Universal variational functionals of electron densities, first-order density matrices, and natural spin-orbitals and solution of the v-representability problem. *Proc. Natl. Acad. Sci. U. S. A.*, **76**, 12, 6062 (1979). (see page: 12)

[62] E. H. Lieb. Density functionals for coulomb systems. *Int. J. Quantum Chem.*, **24**, 3, 243 (1983). (see page: 12)

[63] T. L. Gilbert. Hohenberg-Kohn theorem for nonlocal external potentials. *Phys. Rev. B*, **12**, 6, 2111 (1975). (see page: 12)

[64] Y. A. Wang and E. A. Carter. Orbital-Free Kinetic-Energy Density Functional Theory. In Theor. Methods Condens. Phase Chem., pages 117–184. Kluwer Academic Publishers, Dordrecht (2002). (see page: 13)

[65] V. V. Karasiev, D. Chakraborty, and S. B. Trickey. Progress on New Approaches to Old Ideas: Orbital-Free Density Functionals. In Many-Electron Approaches Physics, Chem. Math. A Multidiscip. View, pages 113–134. Springer, Cham (2014). (see page: 13)

[66] J. C. Slater. The Theory of Complex Spectra. *Phys. Rev.*, **34**, 10, 1293 (1929). (see page: 13)

[67] G. L. Oliver and J. P. Perdew. Spin-density gradient expansion for the kinetic energy. *Phys. Rev. A*, **20**, 2, 397 (1979). (see page: 14)

[68] J. P. Perdew and K. Schmidt. Jacob's ladder of density functional approximations for the exchange-correlation energy. In AIP Conf. Proc., volume 577, pages 1–20. AIP (2001). (see pages: 16, 17)

[69] P. A. M. Dirac. Note on Exchange Phenomena in the Thomas Atom. *Math. Proc. Cambridge Philos. Soc.*, **26**, 03, 376 (1930). (see page: 16)

[70] J. P. Perdew and A. Zunger. Self-interaction correction to density-functional approximations for many-electron systems. *Phys. Rev. B*, **23**, 10, 5048 (1981). (see page: 16)

[71] D. M. Ceperley and B. J. Alder. The ground state of the electron gas by a stochastic method. *Phys. Rev. Lett.*, **45**, 7, 566 (1980). (see page: 16)

[72] S.-K. Ma and K. A. Brueckner. Correlation Energy of an Electron Gas with a Slowly Varying High Density. *Phys. Rev.*, **165**, 1, 18 (1968). (see page: 16)

[73] J. P. Perdew. Accurate Density Functional for the Energy: Real-Space Cutoff of the Gradient Expansion for the Exchange Hole. *Phys. Rev. Lett.*, **55**, 16, 1665 (1985). (see page: 16)

[74] A. D. Becke. Density-functional exchange-energy approximation with correct asymptotic behavior. *Phys. Rev. A*, **38**, 6, 3098 (1988). (see pages: 17, 18, and 117)

[75] J. P. Perdew, K. Burke, and M. Ernzerhof. Generalized Gradient Approximation Made Simple. *Phys. Rev. Lett.*, **77**, 18, 3865 (1996). (see pages: 17, 52, and 60)

[76] J. Tao, J. P. Perdew, V. N. Staroverov, and G. E. Scuseria. Climbing the Density Functional Ladder: Nonempirical Meta-Generalized Gradient Approximation Designed for Molecules and Solids. *Phys. Rev. Lett.*, **91**, 14, 146401 (2003). (see page: 17)

[77] A. D. Becke. Density-functional thermochemistry. IV. A new dynamical correlation functional and implications for exac-exchange mixing. *J. Chem. Phys.*, **104**, 3, 1040 (1996). (see page: 17)

[78] J. P. Perdew, M. Ernzerhof, and K. Burke. Rationale for mixing exact exchange with density functional approximations. *J. Chem. Phys.*, **105**, 22, 9982 (1996). (see page: 17)

[79] J. Klimeš and A. Michaelides. Perspective: Advances and challenges in treating van der Waals dispersion forces in density functional theory. *J. Chem. Phys.*, **137**, 12, 120901 (2012). (see page: 17)

[80] F. London. On Some Properties and Applications of Molecular Forces. In Quantum Chem., pages 400–422. World Scientific (1930). (see page: 17)

[81] M. Dion, H. Rydberg, E. Schröder, D. C. Langreth, and B. I. Lundqvist. Van der Waals Density Functional for General Geometries. *Phys. Rev. Lett.*, **92**, 24, 246401 (2004). (see pages: 17, 18, and 117)

[82] D. C. Langreth, M. Dion, H. Rydberg, E. Schröder, P. Hyldgaard, and B. I. Lundqvist. Van der Waals density functional theory with applications. *Int. J. Quantum Chem.*, **101**, 5, 599 (2005). (see page: 18)

[83] G. Román-Pérez and J. M. Soler. Efficient Implementation of a van der Waals Density Functional: Application to Double-Wall Carbon Nanotubes. *Phys. Rev. Lett.*, **103**, 9, 096102 (2009). (see page: 18)

[84] K. Lee, É. D. Murray, L. Kong, B. I. Lundqvist, and D. C. Langreth. Higher-accuracy van der Waals density functional. *Phys. Rev. B*, **82**, 8, 081101 (2010). (see page: 18)

[85] J. Klimeš, D. R. Bowler, and A. Michaelides. Chemical accuracy for the van der Waals density functional. *J. Phys. Condens. Matter*, **22**, 2, 022201 (2010). (see pages: 18, 117)

[86] S. Grimme. Accurate description of van der Waals complexes by density functional theory including empirical corrections. *J. Comput. Chem.*, **25**, 12, 1463 (2004). (see page: 18)

[87] S. Grimme. Semiempirical GGA-type density functional constructed with a long-range dispersion correction. *J. Comput. Chem.*, **27**, 15, 1787 (2006). (see page: 18)

[88] S. Grimme, J. Antony, S. Ehrlich, and H. Krieg. A consistent and accurate ab initio parametrization of density functional dispersion correction (DFT-D) for the 94 elements H-Pu. *J. Chem. Phys.*, **132**, 15, 154104 (2010). (see page: 18)

[89] A. Tkatchenko and M. Scheffler. Accurate Molecular Van Der Waals Interactions from Ground-State Electron Density and Free-Atom Reference Data. *Phys. Rev. Lett.*, **102**, 7, 073005 (2009). (see page: 18)

[90] F. L. Hirshfeld. Bonded-atom fragments for describing molecular charge densities. *Theor. Chim. Acta*, **44**, 2, 129 (1977). (see page: 18)

[91] A. Tkatchenko, R. a. DiStasio, R. Car, and M. Scheffler. Accurate and efficient method for many-body van der Waals interactions. *Phys. Rev. Lett.*, **108**, 23, 236402 (2012). (see page: 18)

[92] V. G. Ruiz, W. Liu, E. Zojer, M. Scheffler, and A. Tkatchenko. Density-Functional Theory with Screened van der Waals Interactions for the Modeling of Hybrid Inorganic-Organic Systems. *Phys. Rev. Lett.*, **108**, 14, 146103 (2012). (see page: 18)

[93] C.-O. Almbladh and U. von Barth. Exact results for the charge and spin densities, exchange-correlation potentials, and density-functional eigenvalues. *Phys. Rev. B*, **31**, 6, 3231 (1985). (see page: 18)

[94] E. J. Baerends, O. V. Gritsenko, and R. van Meer. The Kohn-Sham gap, the fundamental gap and the optical gap: the physical meaning of occupied and virtual Kohn-Sham orbital energies. *Phys. Chem. Chem. Phys.*, **15**, 39, 16408 (2013). (see page: 19)

[95] L. Hedin. New Method for Calculating the One-Particle Green's Function with Application to the Electron-Gas Problem. *Phys. Rev.*, **139**, 3A, A796 (1965). (see page: 19)

[96] E. E. Salpeter and H. A. Bethe. A Relativistic Equation for Bound-State Problems. *Phys. Rev.*, **84**, 6, 1232 (1951). (see page: 19)

[97] J. F. Janak. Proof that $\delta E/\delta n_i = \varepsilon$ in density-functional theory. *Phys. Rev. B*, **18**, 12, 7165 (1978). (see page: 20)

[98] J. C. Slater. Statistical Exchange-Correlation in the Self-Consistent Field. *Adv. Quantum Chem.*, **6**, C, 1 (1972). (see page: 20)

[99] J. Gavnholt, T. Olsen, M. Engelund, and J. Schiøtz. $\Delta$ self-consistent field method to obtain potential energy surfaces of excited molecules on surfaces. *Phys. Rev. B*, **78**, 7, 075441 (2008). (see page: 20)

[100] R. J. Maurer and K. Reuter. Excited-state potential-energy surfaces of metal-adsorbed organic molecules from linear expansion $\Delta$-self-consistent field density-functional theory ($\Delta$SCF-DFT). *J. Chem. Phys.*, **139**, 1, 014708 (2013). (see page: 20)

[101] L. Triguero, L. G. M. Pettersson, and H. Ågren. Calculations of near-edge x-ray-absorption spectra of gas-phase and chemisorbed molecules by means of density-functional and transition-potential theory. *Phys. Rev. B*, **58**, 12, 8097 (1998). (see page: 20)

[102] A. Baby, G. Fratesi, S. R. Vaidya, L. L. Patera, C. Africh, L. Floreano, and G. P. Brivio. Anchoring and Bending of Pentacene on Aluminum (001). *J. Phys. Chem. C*, **119**, 7, 3624 (2015). (see page: 20)

[103] K. Diller, R. J. Maurer, M. Müller, and K. Reuter. Interpretation of x-ray absorption spectroscopy in the presence of surface hybridization. *J. Chem. Phys.*, **146**, 21, 214701 (2017). (see page: 20)

[104] J. Junquera, Ó. Paz, D. Sánchez-Portal, and E. Artacho. Numerical atomic orbitals for linear-scaling calculations. *Phys. Rev. B*, **64**, 23, 235111 (2001). (see pages: 21, 60, and 118)

[105] F. Bloch. Über die Quantenmechanik der Elektronen in Kristallgittern. *Zeitschrift für Phys.*, **52**, 7-8, 555 (1929). (see page: 21)

[106] E. Antončík. Approximate formulation of the orthogonalized plane-wave method. *J. Phys. Chem. Solids*, **10**, 4, 314 (1959). (see page: 23)

[107] J. Phillips and L. Kleinman. New method for calculating wave functions in crystals and molecules. *Phys. Rev.*, **116**, 2, 287 (1959). (see page: 23)

[108] D. Hamann, M. Schlüter, and C. Chiang. Norm-conserving pseudopotentials. *Phys. Rev. Lett.*, **43**, 20, 1494 (1979). (see page: 24)

[109] N. Troullier and J. L. Martins. Efficient pseudopotentials for plane-wave calculations. *Phys. Rev. B*, **43**, 3, 1993 (1991). (see pages: 24, 25, 60, 91, and 117)

[110] L. Kleinman and D. Bylander. Efficacious form for model pseudopotentials. *Phys. Rev. Lett.*, **48**, 20, 1425 (1982). (see pages: 24, 25)

[111] S. Froyen, N. J. Troullier, J. L. Martins, L. C. Balbás, J. M. Soler, and A. Garcia. ATOM Program Version 4.2.0 (2017). (see page: 25)

[112] S. G. Louie, S. Froyen, and M. L. Cohen. Nonlinear ionic pseudopotentials in spin-density-functional calculations. *Phys. Rev. B*, **26**, 4, 1738 (1982). (see page: 24)

[113] D. Vanderbilt. Soft self-consistent pseudopotentials in a generalized eigenvalue formalism. *Phys. Rev. B*, **41**, 11, 7892 (1990). (see page: 24)

[114] E. N. Economou. Green's Functions in Quantum Physics. Springer, Berlin, Heidelberg (2006). (see page: 27)

[115] A. Williams, P. Feibelman, and N. Lang. Green's-function methods for electronic-structure calculations. *Phys. Rev. B*, **26**, 10, 5433 (1982). (see page: 33)

[116] J. Neugebauer and M. Scheffler. Adsorbate-substrate and adsorbate-adsorbate interactions of Na and K adlayers on Al(111). *Phys. Rev. B*, **46**, 24, 16067 (1992). (see page: 33)

[117] M. Brandbyge, J.-L. Mozos, P. Ordejón, J. Taylor, and K. Stokbro. Density-functional method for nonequilibrium electron transport. *Phys. Rev. B*, **65**, 16, 165401 (2002). (see pages: 34, 35, and 61)

[118] N. Papior, N. Lorente, T. Frederiksen, A. García, and M. Brandbyge. Improvements on non-equilibrium and transport Green function techniques: The next-generation transiesta. *Comput. Phys. Commun.*, **212**, 8 (2017). (see pages: 34, 35)

[119] E. J. Mele and J. D. Joannopoulos. Electronic states at unrelaxed and relaxed GaAs(110) surfaces. *Phys. Rev. B*, **17**, 4, 1816 (1978). (see page: 34)

[120] M. P. L. Sancho, J. M. L. Sancho, and J. Rubio. Quick iterative scheme for the calculation of transfer matrices: application to Mo(100). *J. Phys. F Met. Phys.*, **14**, 5, 1205 (1984). (see page: 35)

[121] M. P. L. Sancho, J. M. L. Sancho, J. M. L. Sancho, and J. Rubio. Highly convergent schemes for the calculation of bulk and surface Green functions. *J. Phys. F Met. Phys.*, **15**, 4, 851 (1985). (see page: 35)

[122] R. D. Muiño, D. Sánchez-Portal, V. M. Silkin, E. V. Chulkov, and P. M. Echenique. Time-dependent electron phenomena at surfaces. *Proc. Natl. Acad. Sci. U. S. A.*, **108**, 3, 971 (2011). (see pages: 35, 89, 99, and 100)

[123] M. Deppe, A. Föhlisch, F. Hennies, M. Nagasono, M. Beye, D. Sánchez-Portal, P. M. Echenique, and W. Wurth. Ultrafast charge transfer and atomic orbital polarization. *J. Chem. Phys.*, **127**, 17, 174708 (2007). (see pages: 35, 42, 46, 115, and 121)

[124] A. Bohm, M. Gadella, and G. B. Mainland. Gamow vectors and decaying states. *Am. J. Phys.*, **57**, 12, 1103 (1989). (see page: 39)

[125] A. Bohm, N. L. Harshman, and H. Walther. Relating the Lorentzian and exponential: Fermi's approximation, the Fourier transform, and causality. *Phys. Rev. A*, **66**, 1, 012107 (2002). (see page: 39)

[126] A. Bohm, P. W. Bryant, H. Uncu, S. Wickramasekara, and W. P. Schleich. The beginning of time observed in quantum jumps. *Fortschritte der Phys.*, **65**, 6-8, 1700015 (2017). (see page: 39)

[127] A. J. Britton, M. Weston, and J. N. O'Shea. Charge transfer from an aromatic adsorbate to a semiconductor $TiO_2$ surface probed on the femtosecond time scale with resonant inelastic x-ray scattering. *Phys. Rev. Lett.*, **109**, 1, 017401 (2012). (see page: 41)

[128] M. Piancastelli. Auger resonant Raman studies of atoms and molecules. *J. Electron Spectros. Relat. Phenomena*, **107**, 1, 1 (2000). (see page: 42)

[129] L. Cao, X.-Y. Gao, A. T. S. Wee, and D.-C. Qi. Quantitative Femtosecond Charge Transfer Dynamics at Organic/Electrode Interfaces Studied by Core-Hole Clock Spectroscopy. *Adv. Mater.*, **26**, 46, 7880 (2014). (see pages: 45, 46)

[130] C. Keller, M. Stichler, G. Comelli, F. Esch, S. Lizzit, W. Wurth, and D. Menzel. Ultrafast Charge Transfer Times of Chemisorbed Species from Auger Resonant Raman Studies. *Phys. Rev. Lett.*, **80**, 8, 1774 (1998). (see page: 46)

[131] A. Föhlisch, S. Vijayalakshmi, F. Hennies, W. Wurth, V. Medicherla, and W. Drube. Verification of the core-hole-clock method using two different time references: Attosecond charge transfer in c(4×2)S/Ru(0001). *Chem. Phys. Lett.*, **434**, 4, 214 (2007). (see page: 46)

[132] L. Cao, Y.-Z. Wang, J.-Q. Zhong, Y.-Y. Han, W.-H. Zhang, X.-J. Yu, F.-Q. Xu, D.-C. Qi, and A. T. S. Wee. Molecular Orientation and Site Dependent Charge Transfer Dynamics at PTCDA/TiO$_2$(110) Interface Revealed by Resonant Photoemission Spectroscopy. *J. Phys. Chem. C*, **118**, 8, 4160 (2014). (see page: 46)

[133] J. Ben Taylor, L. C. Mayor, J. C. Swarbrick, J. N. O'Shea, C. Isvoranu, and J. Schnadt. Adsorption and charge transfer dynamics of bi-isonicotinic acid on Au(111). *J. Chem. Phys.*, **127**, 13, 134707 (2007). (see page: 46)

[134] A. J. Britton, M. Weston, J. B. Taylor, A. Rienzo, L. C. Mayor, and J. N. O'Shea. Charge transfer interactions of a Ru(II) dye complex and related ligand molecules adsorbed on Au(111). *J. Chem. Phys.*, **135**, 16, 164702 (2011).

[135] A. J. Gibson, R. H. Temperton, K. Handrup, M. Weston, L. C. Mayor, and J. N. O'Shea. Charge transfer from an adsorbed ruthenium-based photosensitizer through an ultra-thin aluminium oxide layer and into a metallic substrate. *J. Chem. Phys.*, **140**, 23, 234708 (2014). (see page: 46)

[136] J. Schnadt, P. A. Brühwiler, L. Patthey, J. N. O'Shea, S. Södergren, M. Odelius, R. Ahuja, O. Karis, M. Bässler, P. Persson, H. Siegbahn, S. Lunell, and N. Mårtensson. Experimental evidence for sub-3-fs charge transfer from an aromatic adsorbate to a semiconductor. *Nature*, **418**, 6898, 620 (2002). (see page: 46)

[137] L. C. Mayor, J. Ben Taylor, G. Magnano, A. Rienzo, C. J. Satterley, J. N. O'Shea, and J. Schnadt. Photoemission, resonant photoemission, and x-ray absorption of a Ru(II) complex adsorbed on rutile TiO$_2$(110) prepared by in situ electrospray deposition. *J. Chem. Phys.*, **129**, 11, 114701 (2008).

[138] M. Weston, A. J. Britton, and J. N. O'Shea. Charge transfer dynamics of model charge transfer centers of a multicenter water splitting dye complex on rutile TiO$_2$(110). *J. Chem. Phys.*, **134**, 5, 054705 (2011). (see page: 46)

[139] S. Lizzit, R. Larciprete, P. Lacovig, K. L. Kostov, and D. Menzel. Ultrafast Charge Transfer at Monolayer Graphene Surfaces with Varied Substrate Coupling. *ACS Nano*, **7**, 5, 4359 (2013). (see page: 46)

[140] Y. Garcia-Basabe, A. R. Rocha, F. C. Vicentin, C. E. P. Villegas, R. Nascimento, E. C. Romani, E. C. de Oliveira, G. J. M. Fechine, S. Li, G. Eda, and D. G. Larrude. Ultrafast charge transfer dynamics pathways in two-dimensional $MoS_2$-graphene heterostructures: a core-hole clock approach. *Phys. Chem. Chem. Phys.*, **19**, 44, 29954 (2017). (see page: 46)

[141] A. Ravikumar, G. Kladnik, M. Müller, A. Cossaro, G. Bavdek, L. L. Patera, D. Sánchez-Portal, L. Venkataraman, A. Morgante, G. P. Brivio, D. Cvetko, and G. Fratesi. Tuning ultrafast electron injection dynamics at organic-graphene/metal interfaces. *Nanoscale*, **10**, 17, 8014 (2018). (see page: 46)

[142] C. N. Eads, D. Bandak, M. R. Neupane, D. Nordlund, and O. L. A. Monti. Anisotropic attosecond charge carrier dynamics and layer decoupling in quasi-2D layered $SnS_2$. *Nat. Commun.*, **8**, 1, 1369 (2017). (see pages: 46, 116, and 125)

[143] P. Kao, S. Neppl, P. Feulner, D. L. Allara, and M. Zharnikov. Charge Transfer Time in Alkanethiolate Self-Assembled Monolayers via Resonant Auger Electron Spectroscopy. *J. Phys. Chem. C*, **114**, 32, 13766 (2010). (see page: 46)

[144] A. Batra, G. Kladnik, H. Vázquez, J. S. Meisner, L. Floreano, C. Nuckolls, D. Cvetko, A. Morgante, and L. Venkataraman. Quantifying through-space charge transfer dynamics in π-coupled molecular systems. *Nat. Commun.*, **3**, 1, 1086 (2012). (see page: 46)

[145] G. Kladnik, M. Puppin, M. Coreno, M. de Simone, L. Floreano, A. Verdini, A. Morgante, D. Cvetko, and A. Cossaro. Ultrafast Charge Transfer Pathways Through A Prototype Amino-Carboxylic Molecular Junction. *Nano Lett.*, **16**, 3, 1955 (2016). (see page: 46)

[146] O. Adak, G. Kladnik, G. Bavdek, A. Cossaro, A. Morgante, D. Cvetko, and L. Venkataraman. Ultrafast Bidirectional Charge Transport and Electron Decoherence at Molecule/Surface Interfaces: A Comparison of Gold, Graphene, and Graphene Nanoribbon Surfaces. *Nano Lett.*, **15**, 12, 8316 (2015). (see page: 46)

[147] D. Cvetko, G. Fratesi, G. Kladnik, A. Cossaro, G. P. Brivio, L. Venkataraman, and A. Morgante. Ultrafast electron injection into photo-excited organic molecules. *Phys. Chem. Chem. Phys.*, **18**, 32, 22140 (2016). (see page: 61)

[148] R. H. Temperton, A. J. Gibson, K. Handrup, and J. N. O'Shea. Adsorption and charge transfer interactions of bi-isonicotinic acid on Ag(111). *J. Chem. Phys.*, **147**, 5, 054703 (2017). (see page: 46)

[149] T. Fauster. Time-resolved two-photon photoemission. In W. Schattke and M. A. Van Hove (editors), Solid-State Photoemiss. Relat. Methods, chapter Time-resol, pages 247–268. Wiley-VCH GmbH, Weinheim, Germany (2003). (see page: 46)

[150] H. Petek and S. Ogawa. Femtosecond time-resolved two-photon photoemission studies of electron dynamics in metals. *Prog. Surf. Sci.*, **56**, 4, 239 (1997).

[151] M. Weinelt. Time-resolved two-photon photoemission from metal surfaces. *J. Phys. Condens. Matter*, **14**, 43, R1099 (2002). (see page: 46)

[152] M. Bauer, S. Pawlik, and M. Aeschlimann. Decay dynamics of photoexcited alkali chemisorbates: Real-time investigations in the femtosecond regime. *Phys. Rev. B*, **60**, 7, 5016 (1999). (see page: 46)

[153] S. Neppl, A. Shavorskiy, I. Zegkinoglou, M. Fraund, D. S. Slaughter, T. Troy, M. P. Ziemkiewicz, M. Ahmed, S. Gul, B. Rude, J. Z. Zhang, A. S. Tremsin, P.-A. Glans, Y.-S. Liu, C. H. Wu, J. Guo, M. Salmeron, H. Bluhm, and O. Gessner. Capturing interfacial photoelectrochemical dynamics with picosecond time-resolved X-ray photoelectron spectroscopy. *Faraday Discuss.*, **171**, 0, 219 (2014). (see page: 46)

[154] D. Menzel. Ultrafast charge transfer at surfaces accessed by core electron spectroscopies. *Chem. Soc. Rev.*, **37**, 10, 2212 (2008). (see pages: 46, 58)

[155] A. A. Zholents and M. S. Zolotorev. Femtosecond X-Ray Pulses of Synchrotron Radiation. *Phys. Rev. Lett.*, **76**, 6, 912 (1996). (see pages: 47, 76)

[156] A. A. Zholents and W. M. Fawley. Proposal for Intense Attosecond Radiation from an X-Ray Free-Electron Laser. *Phys. Rev. Lett.*, **92**, 22, 224801 (2004).

[157] F. Krausz and M. Ivanov. Attosecond physics. *Rev. Mod. Phys.*, **81**, 1, 163 (2009). (see page: 76)

[158] K. C. Prince, E. Allaria, C. Callegari, R. Cucini, G. De Ninno, S. Di Mitri, B. Diviacco, E. Ferrari, P. Finetti, D. Gauthier, L. Giannessi, N. Mahne, G. Penco, O. Plekan, L. Raimondi, P. Rebernik, E. Roussel, C. Svetina, M. Trovò, M. Zangrando, M. Negro, P. Carpeggiani, M. Reduzzi, G. Sansone, A. N. Grum-Grzhimailo, E. V. Gryzlova, S. I. Strakhova, K. Bartschat, N. Douguet, J. Venzke, D. Iablonskyi, Y. Kumagai, T. Takanashi, K. Ueda, A. Fischer, M. Coreno, F. Stienkemeier, Y. Ovcharenko, T. Mazza, and M. Meyer. Coherent control with a short-wavelength free-electron laser. *Nat. Photonics*, **10**, 3, 176 (2016). (see pages: 47, 76)

[159] N. Hartmann, G. Hartmann, R. Heider, M. S. Wagner, M. Ilchen, J. Buck, A. O. Lindahl, C. Benko, J. Grünert, J. Krzywinski, J. Liu, A. A. Lutman, A. Marinelli, T. Maxwell, A. A. Miahnahri, S. P. Moeller, M. Planas, J. Robinson, A. K. Kazansky, N. M. Kabachnik, J. Viefhaus, T. Feurer, R. Kienberger, R. N. Coffee, and W. Helml. Attosecond time-energy structure of X-ray free-electron laser pulses. *Nat. Photonics*, **12**, 4, 215 (2018). (see page: 47)

[160] U. Diebold. The surface science of titanium dioxide. *Surf. Sci. Rep.*, **48**, 5–8, 53 (2003). (see pages: 49, 56)

[161] X. Chen and S. S. Mao. Titanium Dioxide Nanomaterials: Synthesis, Properties, Modifications, and Applications. *Chem. Rev.*, **107**, 7, 2891 (2007). (see page: 49)

[162] M. A. Henderson. A surface science perspective on $TiO_2$ photocatalysis. *Surf. Sci. Rep.*, **66**, 6-7, 185 (2011). (see page: 49)

[163] J. Schneider, M. Matsuoka, M. Takeuchi, J. Zhang, Y. Horiuchi, M. Anpo, and D. W. Bahnemann. Understanding $TiO_2$ Photocatalysis: Mechanisms and Materials. *Chem. Rev.*, **114**, 19, 9919 (2014). (see page: 49)

[164] M. Ni, M. K. Leung, D. Y. Leung, and K. Sumathy. A review and recent developments in photocatalytic water-splitting using $TiO_2$ for hydrogen production. *Renew. Sustain. Energy Rev.*, **11**, 3, 401 (2007). (see page: 49)

[165] W. R. Duncan and O. V. Prezhdo. Theoretical Studies of Photoinduced Electron Transfer in Dye-Sensitized $TiO_2$. *Annu. Rev. Phys. Chem.*, **58**, 1, 143 (2007). (see pages: 49, 65)

[166] K. Vos and H. Krusemeyer. Low temperature electroreflectance of $TiO_2$. *Solid State Commun.*, **15**, 5, 949 (1974). (see page: 49)

[167] H. Tang, F. Lévy, H. Berger, and P. E. Schmid. Urbach tail of anatase $TiO_2$. *Phys. Rev. B*, **52**, 11, 7771 (1995). (see page: 49)

[168] R. Zallen and M. Moret. The optical absorption edge of brookite $TiO_2$. *Solid State Commun.*, **137**, 3, 154 (2006). (see page: 49)

[169] R. H. Tait and R. V. Kasowski. Ultraviolet photoemission and low-energy-electron diffraction studies of $TiO_2$ (rutile) (001) and (110) surfaces. *Phys. Rev. B*, **20**, 12, 5178 (1979). (see page: 49)

[170] B. J. Morgan and G. W. Watson. A Density Functional Theory + U Study of Oxygen Vacancy Formation at the (110), (100), (101), and (001) Surfaces of Rutile $TiO_2$. *J. Phys. Chem. C*, **113**, 17, 7322 (2009). (see page: 49)

[171] M. Müller, D. Sánchez-Portal, H. Lin, G. P. Brivio, A. Selloni, and G. Fratesi. Effect of Structural Fluctuations on Elastic Lifetimes of Adsorbate States: Isonicotinic Acid on Rutile(110). *J. Phys. Chem. C*, **122**, 14, 7575 (2018). (see pages: 50, 57, and 143)

[172] U. Diebold, J. F. Anderson, K.-O. Ng, and D. Vanderbilt. Evidence for the Tunneling Site on Transition-Metal Oxides: $TiO_2$(110). *Phys. Rev. Lett.*, **77**, 7, 1322 (1996). (see page: 51)

[173] M. Setvin, C. Franchini, X. Hao, M. Schmid, A. Janotti, M. Kaltak, C. G. de Walle, G. Kresse, and U. Diebold. Direct View at Excess Electrons in $TiO_2$ Rutile and Anatase. *Phys. Rev. Lett.*, **113**, 8, 86402 (2014). (see page: 51)

[174] T. Luttrell, W.-K. Li, X.-Q. Gong, and M. Batzill. New Directions for Atomic Steps: Step Alignment by Grazing Incident Ion Beams on TiO$_2$(110). *Phys. Rev. Lett.*, **102**, 16, 166103 (2009). (see pages: 51, 52, and 56)

[175] S. Wendt, P. T. Sprunger, E. Lira, G. K. H. Madsen, Z. Li, J. Ø. Hansen, J. Matthiesen, A. Blekinge-Rasmussen, E. Lægsgaard, B. Hammer, and F. Besenbacher. The Role of Interstitial Sites in the Ti3d Defect State in the Band Gap of Titania. *Science (80-. ).*, **320**, 5884, 1755 (2008). (see pages: 51, 56)

[176] C. Di Valentin, G. Pacchioni, and A. Selloni. Electronic Structure of Defect States in Hydroxylated and Reduced Rutile TiO$_2$(110) Surfaces. *Phys. Rev. Lett.*, **97**, 16, 166803 (2006). (see page: 52)

[177] B. J. Morgan and G. W. Watson. A DFT+U description of oxygen vacancies at the TiO$_2$ rutile (110) surface. *Surf. Sci.*, **601**, 21, 5034 (2007). (see page: 52)

[178] J. Stausholm-Møller, H. H. Kristoffersen, U. Martinez, and B. Hammer. A density functional theory study of atomic steps on stoichiometric rutile TiO$_2$(110). *J. Chem. Phys.*, **139**, 23, 234704 (2013). (see page: 52)

[179] T. P. Hardcastle, C. R. Seabourne, R. M. D. Brydson, K. J. T. Livi, and A. J. Scott. Energy of Step Defects on the TiO$_2$ Rutile (110) Surface: An ab initio DFT Methodology. *J. Phys. Chem. C*, **117**, 45, 23766 (2013). (see page: 52)

[180] H. J. Monkhorst and J. D. Pack. Special points for Brillouin-zone integrations. *Phys. Rev. B*, **13**, 12, 5188 (1976). (see pages: 53, 91)

[181] U. Martinez, L. B. Vilhelmsen, H. H. Kristoffersen, J. Stausholm-Møller, and B. Hammer. Steps on rutile TiO$_2$(110): Active sites for water and methanol dissociation. *Phys. Rev. B*, **84**, 20, 205434 (2011). (see page: 55)

[182] U. Martinez, J. Ø. Hansen, E. Lira, H. H. Kristoffersen, P. Huo, R. Bechstein, E. Lægsgaard, F. Besenbacher, B. Hammer, and S. Wendt. Reduced Step Edges on Rutile TiO$_2$(110) as Competing Defects to Oxygen Vacancies on the Terraces and Reactive Sites for Ethanol Dissociation. *Phys. Rev. Lett.*, **109**, 15, 155501 (2012). (see page: 55)

[183] I. Horcas, R. Fernández, J. M. Gómez-Rodríguez, J. Colchero, J. Gómez-Herrero, and A. M. Baro. WSXM : A software for scanning probe microscopy and a tool for nanotechnology. *Rev. Sci. Instrum.*, **78**, 1, 013705 (2007). (see page: 55)

[184] J. Tersoff and D. R. Hamann. Theory of the scanning tunneling microscope. *Phys. Rev. B*, **31**, 2, 805 (1985). (see pages: 56, 114)

[185] C. J. Chen. Introduction to scanning tunneling microscopy. Oxford University Press (1993). (see page: 56)

[186] A. Kojima, K. Teshima, Y. Shirai, and T. Miyasaka. Organometal Halide Perovskites as Visible-Light Sensitizers for Photovoltaic Cells. *J. Am. Chem. Soc.*, **131**, 17, 6050 (2009). (see page: 57)

[187] L. Calió, S. Kazim, M. Grätzel, and S. Ahmad. Hole-Transport Materials for Perovskite Solar Cells. *Angew. Chemie Int. Ed.*, **55**, 47, 14522 (2016). (see page: 57)

[188] M. K. Nazeeruddin, F. De Angelis, S. Fantacci, A. Selloni, G. Viscardi, P. Liska, S. Ito, B. Takeru, and M. Grätzel. Combined Experimental and DFT-TDDFT Computational Study of Photoelectrochemical Cell Ruthenium Sensitizers. *J. Am. Chem. Soc.*, **127**, 48, 16835 (2005). (see page: 57)

[189] J. Schnadt, J. N. O'Shea, L. Patthey, J. Krempaský, N. Mårtensson, and P. A. Brühwiler. Alignment of valence photoemission, x-ray absorption, and substrate density of states for an adsorbate on a semiconductor surface. *Phys. Rev. B*, **67**, 23, 235420 (2003). (see page: 58)

[190] J. Schnadt, J. O'Shea, L. Patthey, J. Schiessling, J. Krempaský, M. Shi, N. Mårtensson, and P. Brühwiler. Structural study of adsorption of isonicotinic acid and related molecules on rutile TiO$_2$(110) II: XPS. *Surf. Sci.*, **544**, 1, 74 (2003).

[191] J. Schnadt, J. Schiessling, J. O'Shea, S. Gray, L. Patthey, M.-J. Johansson, M. Shi, J. Krempaský, J. Åhlund, P. Karlsson, P. Persson, N. Mårtensson, and P. Brühwiler. Structural study of adsorption of isonicotinic acid and related molecules on rutile TiO$_2$(110) I: XAS and STM. *Surf. Sci.*, **540**, 1, 39 (2003).

[192] J. N. O'Shea, J. Schnadt, P. A. Brühwiler, H. Hillesheimer, N. Mårtensson, L. Patthey, J. Krempasky, C. Wang, Y. Luo, and H. Ågren. Hydrogen-Bond Induced Surface Core-Level Shift in Isonicotinic Acid. *J. Phys. Chem. B*, **105**, 10, 1917 (2001). (see page: 58)

[193] D. R. Jones and A. Troisi. A method to rapidly predict the charge injection rate in dye sensitized solar cells. *Phys. Chem. Chem. Phys.*, **12**, 18, 4625 (2010). (see page: 58)

[194] N. Martsinovich and A. Troisi. Theoretical studies of dye-sensitised solar cells: from electronic structure to elementary processes. *Energy Environ. Sci.*, **4**, 11, 4473 (2011). (see pages: 58, 67)

[195] O. V. Prezhdo and P. J. Rossky. Mean-field molecular dynamics with surface hopping. *J. Chem. Phys.*, **107**, 3, 825 (1997). (see page: 58)

[196] C. F. Craig, W. R. Duncan, and O. V. Prezhdo. Trajectory Surface Hopping in the Time-Dependent Kohn-Sham Approach for Electron-Nuclear Dynamics. *Phys. Rev. Lett.*, **95**, 16, 163001 (2005).

[197] A. V. Akimov and O. V. Prezhdo. The PYXAID Program for Non-Adiabatic Molecular Dynamics in Condensed Matter Systems. *J. Chem. Theory Comput.*, **9**, 11, 4959 (2013). (see page: 58)

[198] S. Hammes-Schiffer and J. C. Tully. Proton transfer in solution: Molecular dynamics with quantum transitions. *J. Chem. Phys.*, **101**, 6, 4657 (1994). (see page: 58)

[199] W. Stier and O. V. Prezhdo. Nonadiabatic Molecular Dynamics Simulation of Light-Induced Electron Transfer from an Anchored Molecular Electron Donor to a Semiconductor Acceptor. *J. Phys. Chem. B*, **106**, 33, 8047 (2002). (see pages: 58, 65)

[200] L. G. C. Rego and V. S. Batista. Quantum Dynamics Simulations of Interfacial Electron Transfer in Sensitized $TiO_2$ Semiconductors. *J. Am. Chem. Soc.*, **125**, 26, 7989 (2003). (see page: 58)

[201] S. G. Abuabara, L. G. C. Rego, and V. S. Batista. Influence of Thermal Fluctuations on Interfacial Electron Transfer in Functionalized $TiO_2$ Semiconductors. *J. Am. Chem. Soc.*, **127**, 51, 18234 (2005). (see page: 58)

[202] H. Wang and M. Thoss. Multilayer formulation of the multiconfiguration time-dependent Hartree theory. *J. Chem. Phys.*, **119**, 3, 1289 (2003). (see page: 59)

[203] M. Thoss, I. Kondov, and H. Wang. Theoretical study of ultrafast heterogeneous electron transfer reactions at dye-semiconductor interfaces. *Chem. Phys.*, **304**, 1, 169 (2004).

[204] I. Kondov, M. Čížek, C. Benesch, H. Wang, and M. Thoss. Quantum Dynamics of Photoinduced Electron-Transfer Reactions in Dye-Semiconductor Systems: First-Principles Description and Application to Coumarin 343-$TiO_2$. *J. Phys. Chem. C*, **111**, 32, 11970 (2007).

[205] J. Li, I. Kondov, H. Wang, and M. Thoss. Quantum dynamical simulation of photoinduced electron transfer processes in dye-semiconductor systems: theory and application to coumarin 343 at $TiO_2$. *J. Phys. Condens. Matter*, **27**, 13, 134202 (2015). (see page: 59)

[206] H. Lin, G. Fratesi, S. Selçuk, G. P. Brivio, and A. Selloni. Effects of Thermal Fluctuations on the Structure, Level Alignment, and Absorption Spectrum of Dye-Sensitized $TiO_2$: A Comparative Study of Catechol and Isonicotinic Acid on the Anatase(101) and Rutile(110) Surfaces. *J. Phys. Chem. C*, **120**, 7, 3899 (2016). (see pages: 59, 60, 63, and 143)

[207] J. E. Inglesfield. A method of embedding. *J. Phys. C Solid State Phys.*, **14**, 26, 3795 (1981). (see page: 61)

[208] G. A. Benesh and J. E. Inglesfield. An embedding approach for surface calculations. *J. Phys. C Solid State Phys.*, **17**, 9, 1595 (1984).

[209] G. P. Brivio and M. I. Trioni. The adiabatic molecule-metal surface interaction: Theoretical approaches. *Rev. Mod. Phys.*, **71**, 1, 231 (1999). (see page: 61)

[210] L. Kleinman. Comment on the average potential of a Wigner solid. *Phys. Rev. B*, **24**, 12, 7412 (1981). (see page: 61)

[211] J. Junquera, M. Zimmer, P. Ordejón, and P. Ghosez. First-principles calculation of the band offset at BaO/BaTiO$_3$ and SrO/SrTiO$_3$ interfaces. *Phys. Rev. B*, **67**, 15, 155327 (2003). (see page: 61)

[212] J. Junquera, M. H. Cohen, and K. M. Rabe. Nanoscale smoothing and the analysis of interfacial charge and dipolar densities. *J. Phys. Condens. Matter*, **19**, 21, 213203 (2007). (see page: 61)

[213] R. Zwanzig. Rate processes with dynamical disorder. *Acc. Chem. Res.*, **23**, 5, 148 (1990). (see page: 62)

[214] W. Stier and O. V. Prezhdo. Thermal effects in the ultrafast photoinduced electron transfer from a molecular donor anchored to a semiconductor acceptor. *Isr. J. Chem.*, **42**, 2-3, 213 (2002). (see page: 65)

[215] W. R. Duncan, W. M. Stier, and O. V. Prezhdo. Ab Initio Nonadiabatic Molecular Dynamics of the Ultrafast Electron Injection across the Alizarin-TiO$_2$ Interface. *J. Am. Chem. Soc.*, **127**, 21, 7941 (2005). (see page: 65)

[216] E. Maggio, N. Martsinovich, and A. Troisi. Evaluating Charge Recombination Rate in Dye-Sensitized Solar Cells from Electronic Structure Calculations. *J. Phys. Chem. C*, **116**, 14, 7638 (2012). (see page: 67)

[217] T. Ida, M. Ando, and H. Toraya. Extended pseudo-Voigt function for approximating the Voigt profile. *J. Appl. Crystallogr.*, **33**, 6, 1311 (2000). (see page: 70)

[218] F. Giustino. Electron-phonon interactions from first principles. *Rev. Mod. Phys.*, **89**, 1, 015003 (2017). (see pages: 77, 81)

[219] E. B. Wilson, J. C. Decius, and P. C. Cross. Molecular vibrations: the theory of infrared and Raman vibrational spectra. Dover Publications (1980). (see page: 77)

[220] H. M. Sevian and J. L. Skinner. A molecular theory of inhomogeneous broadening, including the correlation between different transitions, in liquids and glasses. *Theor. Chim. Acta*, **82**, 1-2, 29 (1992). (see page: 80)

[221] M. Martinez, M.-P. Gaigeot, D. Borgis, and R. Vuilleumier. Extracting effective normal modes from equilibrium dynamics at finite temperature. *J. Chem. Phys.*, **125**, 14, 144106 (2006). (see page: 81)

[222] W. Press, S. Teukolsky, W. Vetterling, and B. Flannery. Numerical Recipes: The Art of Scientific Computing. Cambridge University Press, 3rd edition (2007). (see pages: 83, 85)

[223] A. Föhlisch, D. Menzel, P. Feulner, M. Ecker, R. Weimar, K. Kostov, G. Tyuliev, S. Lizzit, R. Larciprete, F. Hennies, and W. Wurth. Energy dependence of resonant charge transfer from adsorbates to metal substrates. *Chem. Phys.*, **289**, 1, 107 (2003). (see page: 89)

[224] J.-P. Gauyacq, A. G. Borisov, G. Raseev, and A. K. Kazansky. Long-lived adsorbate states on metal surfaces. *Faraday Discuss.*, **117**, 0, 15 (2000). (see pages: 90, 102)

[225] A. G. Borisov, A. K. Kazansky, and J. P. Gauyacq. Finite Time Effect in the Charge Transfer Process during an Ion-Metal Surface Collision. *Phys. Rev. Lett.*, **80**, 9, 1996 (1998).

[226] J. P. Gauyacq and A. G. Borisov. Excited electron transfer between a core-excited $Ar^*(2p_{3/2}^{-1}4s)$ atom and the metal substrate in the Ar/Cu(111) system. *Phys. Rev. B*, **69**, 23, 235408 (2004). (see pages: 90, 102)

[227] C. Kittel. Introduction to solid state physics. Wiley, 8th edition (2005). (see page: 91)

[228] D. J. Singh, W. E. Pickett, and H. Krakauer. Gradient-corrected density functionals: Full-potential calculations for iron. *Phys. Rev. B*, **43**, 14, 11628 (1991). (see page: 91)

[229] M. Battocletti, H. Ebert, and H. Akai. Influence of gradient corrections to the local-density-approximation on the calculation of hyperfine fields in ferromagnetic Fe, Co, and Ni. *Phys. Rev. B*, **53**, 15, 9776 (1996). (see page: 91)

[230] M. Asato, A. Settels, T. Hoshino, T. Asada, S. Blügel, R. Zeller, and P. H. Dederichs. Full-potential KKR calculations for metals and semiconductors. *Phys. Rev. B*, **60**, 8, 5202 (1999).

[231] S. Shallcross, A. E. Kissavos, V. Meded, and A. V. Ruban. An ab initio effective Hamiltonian for magnetism including longitudinal spin fluctuations. *Phys. Rev. B*, **72**, 10, 104437 (2005). (see page: 91)

[232] R. Hoffmann. Solids and surfaces : a chemist's view of bonding in extended structures. VCH Publishers, New York (1988). (see page: 94)

[233] A. G. Borisov, J. P. Gauyacq, A. K. Kazansky, E. V. Chulkov, V. M. Silkin, and P. M. Echenique. Long-Lived Excited States at Surfaces: Cs/Cu(111) and Cs/Cu(100) Systems. *Phys. Rev. Lett.*, **86**, 3, 488 (2001). (see page: 102)

[234] M. Chhowalla, H. S. Shin, G. Eda, L.-J. Li, K. P. Loh, and H. Zhang. The chemistry of two-dimensional layered transition metal dichalcogenide nanosheets. *Nat. Chem.*, **5**, 4, 263 (2013). (see page: 115)

[235] G. Liu, B. Debnath, T. R. Pope, T. T. Salguero, R. K. Lake, and A. A. Balandin. A charge-density-wave oscillator based on an integrated tantalum disulfide–boron nitride–graphene device operating at room temperature. *Nat. Nanotechnol.*, **11**, 10, 845 (2016).

[236] W. Choi, N. Choudhary, G. H. Han, J. Park, D. Akinwande, and Y. H. Lee. Recent development of two-dimensional transition metal dichalcogenides and their applications. *Mater. Today*, **20**, 3, 116 (2017).

[237] D. Svetin, I. Vaskivskyi, S. Brazovskii, and D. Mihailovic. Three-dimensional resistivity and switching between correlated electronic states in 1T-TaS$_2$. *Sci. Rep.*, **7**, 1, 46048 (2017). (see page: 115)

[238] R. Roldán, M. P. López-Sancho, F. Guinea, E. Cappelluti, J. A. Silva-Guillén, and P. Ordejón. Momentum dependence of spin–orbit interaction effects in single-layer and multi-layer transition metal dichalcogenides. *2D Mater.*, **1**, 3, 034003 (2014). (see page: 115)

[239] J. R. Schaibley, H. Yu, G. Clark, P. Rivera, J. S. Ross, K. L. Seyler, W. Yao, and X. Xu. Valleytronics in 2D materials. *Nat. Rev. Mater.*, **1**, 11, 16055 (2016).

[240] S. Manzeli, D. Ovchinnikov, D. Pasquier, O. V. Yazyev, and A. Kis. 2D transition metal dichalcogenides. *Nat. Rev. Mater.*, **2**, 8, 17033 (2017). (see page: 115)

[241] B. Sipos, A. F. Kusmartseva, A. Akrap, H. Berger, L. Forró, and E. Tutiš. From Mott state to superconductivity in 1T-TaS$_2$. *Nat. Mater.*, **7**, 12, 960 (2008). (see pages: 115, 117)

[242] K. Rossnagel. On the origin of charge-density waves in select layered transition-metal dichalcogenides. *J. Phys. Condens. Matter*, **23**, 21, 213001 (2011). (see pages: 115, 117)

[243] T. Ritschel, J. Trinckauf, K. Koepernik, B. Büchner, M. v. Zimmermann, H. Berger, Y. I. Joe, P. Abbamonte, and J. Geck. Orbital textures and charge density waves in transition metal dichalcogenides. *Nat. Phys.*, **11**, 4, 328 (2015). (see pages: 116, 118, 125, 126, and 127)

[244] T. Ritschel. Electronic self organization in layered transition metal dichalcogenides. Ph.D. thesis, Technische Universität Dresden (2015). (see pages: 116, 118, and 125)

[245] G. Grüner. Density Waves in Solids. Addison-Wesley Publishing Company (1994). (see page: 117)

[246] R. E. Peierls. Quantum Theory of Solids. Clarendon Press, Oxford (1955). (see page: 117)

[247] H. Fröhlich. On the Theory of Superconductivity: The One-Dimensional Case. *Proc. R. Soc. A Math. Phys. Eng. Sci.*, **223**, 1154, 296 (1954). (see page: 117)

[248] J. A. Wilson, F. J. Di Salvo, and S. Mahajan. Charge-density waves and superlattices in the metallic layered transition metal dichalcogenides. *Adv. Phys.*, **50**, 8, 1171 (1974). (see pages: 117, 118)

[249] A. Spijkerman, J. L. de Boer, A. Meetsma, G. A. Wiegers, and S. van Smaalen. X-ray crystal-structure refinement of the nearly commensurate phase of 1T-TaS$_2$ in (3+2)-dimensional superspace. *Phys. Rev. B*, **56**, 21, 13757 (1997). (see pages: 117, 118, 119, and 125)

[250] D. Cho, G. Gye, J. Lee, S.-H. Lee, L. Wang, S.-W. Cheong, and H. W. Yeom. Correlated electronic states at domain walls of a Mott-charge-density-wave insulator 1T-TaS$_2$. *Nat. Commun.*, **8**, 1, 392 (2017). (see page: 117)

[251] S. A. Tawfik, T. Gould, C. Stampfl, and M. J. Ford. Evaluation of van der Waals density functionals for layered materials. *Phys. Rev. Mater.*, **2**, 3, 034005 (2018). (see page: 117)

[252] C. Lee, W. Yang, and R. G. Parr. Development of the Colle-Salvetti correlation-energy formula into a functional of the electron density. *Phys. Rev. B*, **37**, 2, 785 (1988). (see page: 117)

[253] B. Dardel, M. Grioni, D. Malterre, P. Weibel, Y. Baer, and F. Lévy. Temperature-dependent pseudogap and electron localization in 1T-TaS$_2$. *Phys. Rev. B*, **45**, 3, 1462 (1992). (see page: 118)

[254] J. A. Wilson, F. J. Di Salvo, and S. Mahajan. Charge-Density Waves in Metallic, Layered, Transition-Metal Dichalcogenides. *Phys. Rev. Lett.*, **32**, 16, 882 (1974). (see page: 118)

[255] R. Brouwer and F. Jellinek. The low-temperature superstructures of 1T-TaSe$_2$ and 2H-TaSe$_2$. *Phys. B+C*, **99**, 1-4, 51 (1980). (see pages: 119, 120)

[256] R. Brouwer. Incommensurability in Crystal Structures. Ph.D. thesis, University of Groningen, Netherlands (1978). (see pages: 119, 120)

[257] A. S. Ngankeu, S. K. Mahatha, K. Guilloy, M. Bianchi, C. E. Sanders, K. Hanff, K. Rossnagel, J. A. Miwa, C. Breth Nielsen, M. Bremholm, and P. Hofmann. Quasi-one-dimensional metallic band dispersion in the commensurate charge density wave of 1T-TaS$_2$. *Phys. Rev. B*, **96**, 19, 195147 (2017). (see page: 125)

[258] T. Ritschel. Disrupted orbital order and the pseudogap in layered 1T-TaS$_2$. *Phys. Rev. B* (2018). (see page: 125)

[259] Y. Ge and A. Y. Liu. First-principles investigation of the charge-density-wave instability in 1T-TaSe$_2$. *Phys. Rev. B*, **82**, 15, 155133 (2010). (see pages: 125, 126)

[260] M. B. Walker and R. L. Withers. Stacking of charge-density waves in 1T transition-metal dichalcogenides. *Phys. Rev. B*, **28**, 5, 2766 (1983). (see page: 126)

[261] K. Nakanishi and H. Shiba. Theory of Three-Dimensional Orderings of Charge-Density Waves in 1T-TaS$_2$ (X: S, Se). *J. Phys. Soc. Japan*, **53**, 3, 1103 (1984). (see page: 126)

[262] C. B. Scruby, P. M. Williams, and G. S. Parry. The role of charge density waves in structural transformations of 1T-TaS$_2$. *Philos. Mag.*, **31**, 2, 255 (1975). (see page: 126)

[263] S. Tanda, T. Sambongi, T. Tani, and S. Tanaka. X-Ray Study of Charge Density Wave Structure in 1T-TaS$_2$. *J. Phys. Soc. Japan*, **53**, 2, 476 (1984).

[264] L. Le Guyader, T. Chase, A. H. Reid, R. K. Li, D. Svetin, X. Shen, T. Vecchione, X. J. Wang, D. Mihailovic, and H. A. Dürr. Stacking order dynamics in the quasi-two-dimensional dichalcogenide 1T-TaS$_2$ probed with MeV ultrafast electron diffraction. *Struct. Dyn.*, **4**, 4, 044020 (2017). (see page: 126)

[265] R. Claessen, B. Burandt, H. Carstensen, and M. Skibowski. Conduction-band structure and charge-density waves in 1T-TaS$_2$. *Phys. Rev. B*, **41**, 12, 8270 (1990). (see page: 126)

[266] H. Sato, M. Arita, Y. Utsumi, Y. Mukaegawa, M. Sasaki, A. Ohnishi, M. Kitaura, H. Namatame, and M. Taniguchi. Conduction-band electronic structure of 1T-TaS$_2$ revealed by angle-resolved inverse-photoemission spectroscopy. *Phys. Rev. B*, **89**, 15, 155137 (2014). (see page: 126)

[267] W. Drube, R. Treusch, and G. Materlik. Density of State Effects in Ag $L_3M_{4,5}M_{4,5}$ Threshold Auger Spectra. *Phys. Rev. Lett.*, **74**, 1, 42 (1995). (see page: 129)

[268] A. Föhlisch, O. Karis, M. Weinelt, J. Hasselström, A. Nilsson, and N. Mårtensson. Auger Resonant Raman Scattering in Itinerant Electron Systems: Continuum Excitation in Cu. *Phys. Rev. Lett.*, **88**, 2, 027601 (2001). (see page: 129)